Ocean Optics

RICHARD W. SPINRAD
KENDALL L. CARDER
MARY JANE PERRY

OXFORD UNIVERSITY PRESS

OXFORD MONOGRAPHS ON GEOLOGY AND GEOPHYSICS

Series editors

OXFORD MONOGRAPHS ON GEOLOGY AND GEOPHYSICS

1. DeVerle P. Harris: *Mineral resources appraisal: mineral endowment, resources, and potential supply: concepts, methods, and cases*
2. J. J. Veevers (ed.): *Phanerozoic earth history of Australia*
3. Yang Zunyi, Cheng Yugi and Wang Hongzhen (eds.): *The geology of China*
4. Lin-gun Liu and William A. Bassett: *Elements, oxides and silicates: high pressure phases with implications for the earth's interior*
5. Antoni Hoffman and Matthew H. Nitecki (eds.): *Problematic fossil taxa*
6. S. Mahmood Naqvi and John J. W. Rogers: *Precambrian geology of India*
7. Chih-Pei Chang and T. N. Krishnamurti (eds.): *Monsoon meteorology*
8. Zvi Ben-Avraham (ed.): *The evolution of the Pacific Ocean margins*
9. Ian McDougall and T. Mark Harrison: *Geochronology and thermochronology by the $^{40}Ar/^{39}Ar$ method*
10. Walter C. Sweet: *The Conodonta: morphology, taxonomy, paleoecology, and evolutionary history of a long-extinct animal phylum*
11. H. J. Melosh: *Impact cratering: a geologic process*
12. J. W. Cowie and M. D. Brasier (eds.): *The Precambrian–Cambrian boundary*
13. C. S. Hutchinson: *Geological evolution of southeast Asia*
14. Anthony J. Naldrett: *Magmatic sulfide deposits*
15. D. R. Prothero and R. M. Schoch (eds.): *the evolution of perissodactyls*
16. M. Menzies (ed.): *Continental mantle*
17. R. J. Tingey (ed.): *Geology of the Antarctic*
18. Thomas J. Crowley and Gerald R. North: *Paleoclimatology*
19. Gregory J. Retallack: *Miocene paleosols and ape habits of Pakistan and Kenya*
20. Kuo-Nan Liou: *Radiation and cloud processes in the atmosphere: theory, observation, and modeling*
21. Brian Bayly: *Chemical change in deforming materials*
22. Allan K. Gibbs and Christopher N. Barron: *The geology of the Guiana Shield*
23. Peter J. Ortoleva: *Geochemical self-organization*
24. Robert G. Coleman: *Geologic evolution of the Red Sea*
25. Richard W. Spinrad, Kendall L. Carder, and Mary Jane Perry: *Ocean Optics*
26. Clinton M. Case: *Physical principles of flow in unsaturated porous media*
27. Eric B. Kraus and Joost A. Businger: *Atmosphere-ocean interaction*, second edition

Ocean Optics

RICHARD W. SPINRAD

Director, Ocean Biology/Optics/Chemistry Division
Office of Naval Research

KENDALL L. CARDER

Department of Marine Sciences,
University of South Florida

MARY JANE PERRY

School of Oceanography,
University of Washington at Seattle

OXFORD UNIVERSITY PRESS New York
CLARENDON PRESS Oxford
1994

Oxford University Press

Oxford New York Toronto
Delhi Bombay Calcutta Madras Karachi
Kuala Lumpur Singapore Hong Kong Tokyo
Nairobi Dar es Salaam Cape Town
Melbourne Auckland Madrid

and associated companies in
Berlin Ibadan

Published by Oxford University Press, Inc.,
200 Madison Avenue, New York, New York 10016

Oxford is a registered trademark of Oxford University Press

Library of Congress Cataloging-in-Publication Data
Spinrad, Richard W.
Ocean optics/Richard W. Spinrad, Kendall L. Carder, Mary Jane Perry
p. cm. – (Oxford monographs on geology and geophysics ; no. 25)
Includes bibliographical references and index.
ISBN 0-19-506843-2
1. Optical oceanography–Congresses. I. Carder, Kendall L.
II. Perry, Mary Jane, 1948– . III. Title. IV. Series.
GC177.6.S65 1994
551.46'01–dc20 93-7840

1 3 5 7 9 8 6 4 2
Printed in the United States of America
on acid-free paper

DEDICATION

This volume was strongly inspired by the works and careers of three unique scientists: Nils Jerlov, John Tyler, and Rudolph Preisendorfer. As a group, the contributors to this book owe a strong debt of gratitude and respect to these three men. Jerlov is considered by many "the father of ocean optics." Preisendorfer established the basis for much of the modern theoretical treatment of the field. Tyler was a technological pioneer, catalyzing ideas for and the development of optical oceanographic instrumentation and experimental techniques.

As scientists we have all been wonderfully influenced by the lives and the works of Jerlov, Tyler, and Preisendorfer. This book is dedicated to them and the legacies they have left.

This page intentionally left blank

PREFACE

Oceanography is inherently a multidisciplinary science. Similarly, optical variability in the ocean is driven by a combination of physical, biological, chemical, and geological processes. When the original concept for this book was discussed, it was clear that the focus of the contributions should be on the strongly interactive nature of radiative transfer in the sea and the processes that control the sources and fates of dissolved and particulate material in the sea. It is *oceanography* that unites these studies, and *optics* that provides the answers. Our field has evolved extensively from the days when optics was considered an esoteric and mysterious arm of the ocean sciences community.

This revelation is supported by any number of metrics of the community. Optical theory is now firmly embedded in studies of mixed layer dynamics. Productivity analyses of the ocean are incomplete without a firm understanding of the spectral nature of the radiance field. Photochemistry, by definition, is linked to the time- and space-dependent nature of radiative transfer. While it is true that the community of scientists who use optical techniques has grown, it is even more significant that the number of optical oceanographers has also increased in the last several decades. This book is authored by a cross-section of that population of optical oceanographers.

This volume builds on the wealth of historical information on light in the sea and is indicative of the present state of the science of optical oceanography. In the same way that modern texts in the field of geophysical fluid dynamics can harken back to the principles documented in the classical physical oceanographic volumes, this book follows from the pages of the classic tomes of Jerlov, van de Hulst, Preisendorfer, and Kirk. The reader will find that familiarity with these works (see the list of references) is very useful. But, even without the benefit of the knowledge presented in those classic works, the reader will undoubtedly appreciate the richly multidisciplinary aspect of modern research in optical oceanography as represented here.

The themes of *closure* and *inversion* permeate the chapters of this book. Closure is a concept that takes three fundamental forms in the field of optical oceanography: scale closure, experimental closure, and instrumental closure. Scale closure addresses the issue of agreement between measurements made on individual particles and measurements made on bulk water samples. Experimental closure implies that theoretical predictions of the behavior of the light field should agree or "close" with measurements (either of bulk water samples or of individual particles). The concept of instrumental closure is exemplified by the

requirement that the sum of the measured coefficients of absorption and scattering should equal the measured coefficient of attenuation. These closure concepts are, clearly, not independent, but the reader will find that the research community tends to address the issues in a manner analogous to that described above.

Inversion is a classical problem in almost every science. Simply, the concept is one of discriminating theoretically, from measurements of the light field, the fundamental sources of variability within a given system. An example might be the determination of the absorption coefficient from measurement of the underwater radiance distribution. Closure and inversion are the means to specific scientific ends. As such they are often the techniques used in optical oceanography to understand the most fundamental principles of natural variability.

The reader who follows the outline of this book will find that he or she is being led through a forest of wide technical diversity. The editors have endeavored to preserve the strong flavor of diversity that is uniquely characteristic of optical oceanography. As such, terminology is not necessarily standardized (and should not be). Researchers, for example, working with *in vitro* absorption know the β term as the filter pad optical pathlength amplification factor, but the same term for the theoretical physicist is the volume scattering function. It is inappropriate for the relatively small community of optical oceanographers to dictate standard nomenclature. The reader should be aware of the consequent admixture of terminology found in this volume.

The layout of the book is intended to carry the reader from the state of the science in theoretical treatments through direct analyses of sources of variability in the optics of the sea. The path continues to include many of the secondary processes controlling variability—processes that were, until very recently, considered unimportant, but that are now clearly recognized as potentially strong contributors to variability.

The chapters by Gordon, Kirk, and Zaneveld are the theoretical framework for much of the experimentation described in the book. The physical foundation for radiative transfer described by Howard Gordon is a nearly seamless continuation of the classical treatments provided by Jerlov, van de Hulst, and Preisendorfer. He provides an elegant application of numerical methods as a demonstration of one of the more powerful modern modeling capabilities in optical oceanography. John Kirk provides some of the essential concepts defining the highly interactive nature of optics and biology, especially for the confused—and highly topical—coastal regions. Ron Zaneveld's treatment of apparent and inherent optical properties is central to the definition of the issues of inversion and closure as described above.

The issue of scale closure is at the heart of the chapters by Morel and Perry. André Morel presents some of the theory of optical variability of individual algal cells. The link to large-scale optical variability is identified with respect to implications for remote sensing. Mary Jane Perry couples Morel's chapter with a discussion of methodologies for analysis of the absorption properties of individual phytoplankton cells.

The general subject of field experimentation is discussed in detail by Højerslev, Yentsch, Kiefer, and Marra. Niels Højerslev provides an historical perspective, emphasizing the experimental methodologies developed in Scandinavia (for many years the bastion of optical oceanographic research) in the early part of the 20th century. Many of these techniques served as conceptual predecessors for the most modern optical oceanographic instruments. Charlie Yentsch defines natural particle diversity as it is manifested in fluorescence variability, identifying particle size as something of a segregator of optical properties. Dale Kiefer expands on some of these same concepts to look into the environmental controls on optical properties of phytoplankton cells, and some of the consequent relationships among inherent optical properties. John Marra describes what is considered the state of the art in attacking issues of long-term variability in optics in the sea: deep water moorings that incorporate bio-optical and physical instrumentation.

The final section of this book includes three very different approaches to addressing secondary sources of optical variability. George Kattawar's chapter, dealing with polarization in the sea, represents the vector treatment of the radiative transfer equation. His results suggest a new thinking with respect to the definition of the radiance distribution in the ocean. Similarly, Ray Smith and Bruce Marshall have put into quantitative terms an important aspect of transspectral scattering: Raman scattering. This revelationary area of research has begun to identify an important source of spectral variability underwater. Ken Carder and Dave Costello describe a technique for studying the variability in shape of marine hydrosols. Their work also impinges strongly on the issue of scale closure, by virtue of the attention they have given to the nature of large particles in the sea.

All of these chapters were presented at a conference on Optical Oceanography in 1989 at Friday Harbor, Washington. The attendees represented a major cadre of the "free world" optical oceanographers at that time. Since the time of that meeting, the "New World Order" has opened many doors for collaboration and cooperation for scientists from around the world. It is exciting to think how this volume may spawn powerful interactions among optical oceanographers. Even more exciting is to think how the next version of a collection of state-of-the-science chapters such as these may manifest itself in the future.

November, 1992

R.W.S.
K.L.C.
M.J.P.

This page intentionally left blank

CONTENTS

This page intentionally left blank

CONTRIBUTORS

Kendall L. Carder
Department of Marine Sciences
University of South Florida
140 7th Ave. S.
St. Petersburg, FL 33701

David K. Costello
Department of Marine Sciences
University of South Florida
140 7th Ave. S.
St. Petersburg, FL 33701

Howard R. Gordon
Department of Physics
University of Miami
Coral Gables, FL 33124

Niels K. Højerslev
Institute of Physical Oceanography
University of Copenhagen
2200 Copenhagen, DENMARK

George W. Kattawar
Department of Physics
Texas A & M University
College Station, TX 77843

Dale A. Kiefer
Department of Biological Sciences
University of Southern California
University Park
Los Angeles, CA 90089

John T. O. Kirk
CSIRO
Division of Plant Industry
P.O. Box 1600
Canberra ACT 2601 AUSTRALIA

Motoaki Kishino
The Institute of Physical and Chemical Research
Wako-shi, Saitama 351-01 JAPAN

John Marra
Lamont-Doherty Geological Observatory
Columbia University
Palisades, NY 10964

Bruce R. Marshall
Geography Department
University of California
Santa Barbara, CA 93106

André Morel
Laboratoire de Physique et Chemie
Université Pierre et Marie Curie
06230 Villefranche-sur-Mer FRANCE

Mary Jane Perry
School of Oceanography
WB-10
University of Washington
Seattle, WA 98195

Raymond C. Smith
Geography Department
University of California
Santa Barbara, CA 93106

Charles S. Yentsch
Bigelow Laboratory for Ocean Sciences
McKown Point
West Boothbay Harbor, ME 04575

J. Ronald V. Zaneveld
College of Oceanography
Oregon State University
Corvallis, OR 97331

Ocean Optics

This page intentionally left blank

1

MODELING AND SIMULATING RADIATIVE TRANSFER IN THE OCEAN

Howard R. Gordon
University of Miami

Introduction

The propagation of light in the sea is of interest in many areas of oceanography: light provides the energy that powers primary productivity in the ocean; light diffusely reflected by the ocean provides the signal for the remote sensing of subsurface constituent concentrations (particularly phytoplankton pigments); light absorbed by the water heats the surface layer of the ocean; light absorbed by chemical species (particularly dissolved organics) provides energy for their dissociation; and the attenuation of light with depth in the water provides an estimate of the planktonic activity. Engineering applications include the design of underwater viewing systems. The propagation of light in the ocean–atmosphere system is governed by the integral–differential equation of radiative transfer, which contains absorption and scattering parameters that are characteristic of the particular water body under study. Unfortunately, it is yet to be shown that these parameters are measured with sufficient accuracy to enable an investigator to derive the in-water light field with the radiative transfer equation (RTE). Furthermore, the RTE has, thus far, defied analytical solution, forcing one to resort to numerical methods. These numerical solutions are referred to here as "simulations."

In this chapter, simulations of radiative transfer in the ocean–atmosphere system are used (1) to test the applicability of approximate solutions of the RTE, (2) to look for additional simplifications that are not evident in approximate models, and (3) to obtain approximate inverse solutions to the transfer equation, e.g., to derive the ocean's scattering and absorption properties from observations of the light field. The chapter is based on a lecture presented at the Friday Harbor Laboratories of the University of Washington directed to both students and experts. For the students, I have tried to make the material as self-contained as possible by including the basics, i.e., by providing the basic definitions of the optical properties and radiometry for absorbing–scattering media, developing the approximate solutions to the RTE for testing the simulations, detailing the model used for scattering and

absorbing properties of ocean constituents in the simulations, and briefly explaining the simulation method employed. For the experts, I hope I have provided some ideas worthy of experimental exploration.

Basic concepts

The basic concepts of radiative transfer will be developed in this section. Excellent texts are available on this subjects. Three that I have found particularly useful are Chandrasekhar (1950), Preisendorfer (1965), and van de Hulst (1980). To introduce the subject, I find it more convenient to emphasize the particle nature of light as opposed to the wave aspects. Thus, we consider light of wavelength λ (SI unit: nm) to be composed of a stream of particles (photons) each of which possesses an energy hc/λ, where h is Planck's constant and c is the speed of light. The fundamental quantity in radiometry is the spectral radiant power $P(\lambda)$. When a detector viewing light through a filter transmitting a spectral bandwidth $\Delta\lambda$ centered on λ records N photons per second, the *spectral radiant power* is

$$P(\lambda) = \frac{hc}{\lambda}\frac{N}{\Delta\lambda} \tag{1.1}$$

The SI unit for $P(\lambda)$ is watts nm^{-1}.

The light field

When one speaks of the "light field," what is generally meant is a quantity known as the radiance. Consider a detector of spectral radiant power. Let the detector have an area A_D and be equipped with a spectral filter which passes a range of wavelengths $\Delta\lambda$ centered on λ. Place the detector at the end of a long hollow cylindrical tube, e.g., a paper towel roll, which restricts the field of view of the detector to a solid angle (SI unit: sr) $\Delta\Omega = A/l^2$, where A is the cross-sectional area of the tube and l is the distance from the end of the tube to the detector. Such an arrangement constitutes a radiometer. If the detector records a power $P(\lambda,\hat{\xi})$ when the open end of the tube is aimed in a direction to receive photons traveling toward $\hat{\xi}$, i.e., the open end of the tube points in the direction of the unit vector $\hat{\xi}$, the radiometer records, at its position, a *radiance* $L(\lambda,\xi)$ defined by

$$L(\lambda,\hat{\xi}) = \frac{P(\lambda,\hat{\xi})}{A_D\,\Delta\Omega} \tag{1.2}$$

(The SI unit for radiance is W m^{-2} nm^{-1} sr^{-1}). To be rigorous, a limiting procedure should be used in which $\Delta\Omega$ and $\Delta\lambda$ both $\to 0$. In practice, they need only be sufficiently small that a further reduction in their size would result in no change in the radiance. It should also be noted that the physical size of the radiometer must be sufficiently small that it does not significantly perturb the light field by its presence. The radiance is a function of the position of the radiometer as well as the direction in which it is aimed and the wavelength of the light.

In this chapter we adopt a cartesian coordinate system in which the x and y axes are along the sea surface and the z axis is directed into the water. Direction is specified by the polar angle (θ) and the azimuth angle (ϕ) of a spherical coordinate system built on the cartesian system. Thus, photons traveling toward the ocean from the atmosphere have $0 \leq \theta < 90°$, while photons exiting the ocean surface have $90 < \theta \leq 180°$. The radiance in the ocean is a much weaker function of horizontal position (x,y) than depth of (z), so L is taken to be a function of depth, direction, and wavelength, i.e., $L = L(z,\theta,\phi,\lambda)$. At a given depth and wavelength, $L(\theta,\phi)$ is usually referred to as the *radiance distribution.*

Because the radiance is very difficult to measure routinely, most light field measurements involve integrals of the radiance distribution. The integrals of interest here are the downwelling irradiance

$$E_d(z,\lambda) = \int_{\Omega_d} L(z,\theta,\phi,\lambda) \cos\theta \, d\Omega = \int_0^{2\pi} d\phi \int_0^{\pi/2} L(z,\theta,\phi,\lambda) \cos\theta \sin\theta \, d\theta \tag{1.3}$$

and the upwelling irradiance

$$E_u(z,\lambda) = -\int_{\Omega_u} L(z,\theta,\phi,\lambda) \cos\theta \, d\Omega = -\int_0^{2\pi} d\phi \int_{\pi/2}^{\pi} L(z,\theta,\phi,\lambda) \cos\theta \sin\theta \, d\theta \tag{1.4}$$

where Ω_d and Ω_u refer to integration over the downward and upward hemispheres, respectively. These represent the energy or photon flux (energy or photons per unit time per unit area) across a horizontal surface at depth z associated with the downwelling and upwelling light fields, respectively. Another pair of useful integrals are the downwelling and upwelling scalar irradiances $E_{0d}(z,\lambda)$ and $E_{0u}(z,\lambda)$ defined by

$$E_{0d}(z,\lambda) = \int_{\Omega_d} L(z,\theta,\phi,\lambda) \, d\Omega = \int_0^{2\pi} d\phi \int_0^{\pi/2} L(z,\theta,\phi,\lambda) \sin\theta \, d\theta \tag{1.5}$$

and

$$E_{0u}(z,\lambda) = \int_{\Omega_u} L(z,\theta,\phi,\lambda) \, d\Omega = \int_0^{2\pi} d\phi \int_{\pi/2}^{\pi} L(z,\theta,\phi,\lambda) \sin\theta \, d\theta \tag{1.6}$$

The scalar irradiance, $E_0(z,\lambda) = E_{0d}(z,\lambda) + E_{0u}(z,\lambda)$, is proportional to the energy or photon density (energy or photons per unit volume) associated with the light field at depth z. The SI unit for all of the irradiance functions above is $\mathrm{W\,m^{-2}\,nm^{-1}}$.

Other quantities associated with the irradiances are

(i) the reflectance

$$R(z,\lambda) = \frac{E_u(z,\lambda)}{E_d(z,\lambda)} \tag{1.7}$$

(ii) the downwelling distribution function

$$D_d(z,\lambda) = \frac{E_{0d}(z,\lambda)}{E_d(z,\lambda)} \tag{1.8}$$

and (iii) the upwelling distribution function

$$D_u(z,\lambda) = \frac{E_{0u}(z,\lambda)}{E_u(z,\lambda)} \tag{1.9}$$

The reflectance just beneath the surface is of central interest in ocean color remote sensing (Gordon and Morel, 1983). The reciprocal of the distribution functions are referred to as the *average cosines*, e.g.,

$$\bar{\mu}_d = \frac{1}{D_d} \tag{1.10}$$

is the downwelling average cosine. The reason for this name is seen from the definition in terms of the radiance distribution:

$$\bar{\mu}_d = \frac{\int_{\Omega_d} L(z,\theta,\phi,\lambda)\ \cos\theta\, d\Omega}{\int_{\Omega_d} L(z,\theta,\phi,\lambda)\, d\Omega} \tag{1.11}$$

i.e. $\bar{\mu}_d$ is the average value of $\cos\theta$ for the downwelling radiance distribution.

Apparent optical properties

Experimental measurements of the irradiances E_d, E_u, etc., reveal that they decay approximately exponentially with depth. Thus, it is natural to define attenuation coefficients associated with the decay, i.e.,

$$K_x(z,\lambda) = -\frac{d\left(\ln\left[E_x(z,\lambda)\right]\right)}{dz} \tag{1.12}$$

where $x = d$, u, or 0. These are called the downwelling, upwelling, and scalar irradiance attenuation coefficients for $x = d$, u, and 0, respectively. In a homogeneous medium these irradiance (or "diffuse") attenuation coefficients

depend weakly on depth and are therefore, in some sense, characteristic of the medium. However, their actual value depends on the surface illumination, i.e., the sun angle, the ratio of sky light to direct sunlight, and cloud conditions, and are thus not properties of the medium *alone*. Because of this they are referred to as *apparent optical properties* (Preisendorfer, 1961, 1976). In the same spirit, R, D_d, and D_u, which also depend only weakly on depth, are apparent optical properties.

Inherent optical properties

Our aim is to understand the propagation of light in the sea, i.e., the variation in the radiance distribution with depth and direction, etc., so we cannot be satisfied with the apparent optical properties that simply document the variations. Thus, we look for more fundamental means of characterizing the medium. This is accomplished by probing samples of the medium with a well-defined beam of light. Consider a small volume Δv of length Δl illuminated by a parallel beam of light traveling in a direction specified by the unit vector $\hat{\xi}$ as shown in Fig. 1-1.

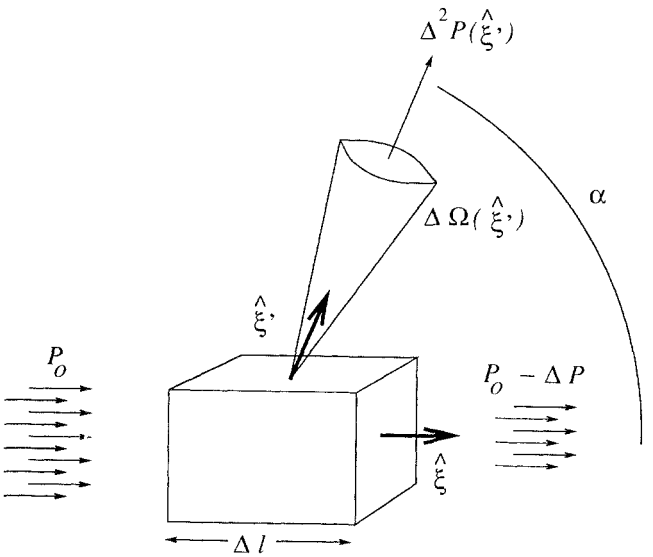

$$c = \frac{l}{P_o}\frac{\Delta P}{\Delta l}$$

$$\beta(\hat{\xi} \to \hat{\xi}') = \frac{\Delta^2 P(\hat{\xi}') / P_o}{\Delta l \, \Delta\Omega(\hat{\xi}')}$$

Fig. 1-1. Definition of the inherent optical properties.

$P_0(\lambda)$ is the spectral radiant power entering the volume. In traversing the volume some photons are removed from the parallel beam by *absorption* within Δv, while other photons are removed from the parallel beam by virtue of their change in direction (*scattering*) within Δv, i.e. they exit Δv traveling in directions other than $\hat{\xi}$. If $\Delta P(\lambda)$ is the spectral radiant power removed from the parallel beam by virtue of scattering and absorption, then the *beam attenuation coefficient*, $c(\lambda)$ is defined by

$$c(\lambda) = \frac{1}{\Delta l}\left(\frac{\Delta P(\lambda)}{P_0(\lambda)}\right) \tag{1.13}$$

i.e., the fraction of the power removed from the beam per unit length. The SI unit for $c(\lambda)$ is m^{-1}. If $\Delta^2 P(\lambda,\hat{\xi}')$ is the spectral radiant power scattered into a small solid angle $\Delta\Omega(\hat{\xi}')$ containing the direction $\hat{\xi}'$, the *volume scattering function* (VSF) $\beta(\lambda,\hat{\xi}\rightarrow\hat{\xi}')$ is defined according to

$$\beta(\lambda,\hat{\xi}\rightarrow\hat{\xi}') = \frac{1}{\Delta l\,\Delta\Omega(\hat{\xi}')}\left(\frac{\Delta^2 P(\lambda,\hat{\xi}')}{P_0(\lambda)}\right) \tag{1.14}$$

i.e., the fractional power scattered from $\hat{\xi}$ into the direction $\hat{\xi}'$ per unit length per unit solid angle around $\hat{\xi}'$. [The "2" on $\Delta^2 P(\lambda,\hat{\xi}')$ indicates that it is of second order in smallness; i.e., small because Δl is small and also small because $\Delta\Omega(\hat{\xi}')$ is small.] The SI unit for β is $m^{-1}\,sr^{-1}$. In Eqs. (1.13) and (1.14) Δl and $\Delta\Omega(\hat{\xi}')$ must be sufficiently small that reduction in their sizes produces negligible changes in c and β. For the size of the scattering volume this means that it must be sufficiently small that photons have a negligible probability of scattering more than once in Δv. For seawater and for the particles suspended in the water in random orientation, β depends on direction only through the angle α between $\hat{\xi}$ and $\hat{\xi}'$ given by $\alpha = \cos^{-1}(\hat{\xi}\cdot\hat{\xi}')$. If we sum the contributions from each $\Delta\Omega(\hat{\xi}')$ over the entire sphere surrounding Δv, i.e., sum the light scattered into all directions, the result is

$$\int_{4\pi} \beta(\lambda,\hat{\xi}\rightarrow\hat{\xi}')\,d\Omega(\hat{\xi}') = \frac{1}{\Delta l}\left(\frac{\Delta P_s(\lambda)}{P_0(\lambda)}\right) \tag{1.15}$$

where

$$\Delta P_s(\lambda) = \sum_{\text{all } \Delta\Omega(\hat{\xi}')} \frac{\Delta^2 P(\lambda,\hat{\xi}')}{\Delta\Omega(\hat{\xi}')}\Delta\Omega(\hat{\xi}') \tag{1.16}$$

Comparison of Eq. (1.15) with Eq. (1.13) shows that the right-hand side of Eq. (1.15) is the contribution to the right-hand side of Eq. (1.13) resulting from scattering. Thus, the *scattering coefficient* $b(\lambda)$ is given by

$$b(\lambda) = \int_{4\pi} \beta(\lambda,\hat{\xi}\rightarrow\hat{\xi}')\, d\Omega(\hat{\xi}') \tag{1.17}$$

where the 4π on the integral means that it is to be taken over 4π sr. The scattering processes we deal with here are *elastic*, i.e., there is no wavelength (energy) change upon scattering. Fluorescence and Raman scattering are two examples of important processes in the ocean in which the "scattered" photons have longer wavelength (lower energy) than the incident photon. These *inelastic* scattering processes can be formulated in a manner similar to that above; however, they are not considered in this chapter (see Chapters 8 and 11).

Finally, since $\Delta P(\lambda)$ - $\Delta P_s(\lambda)$ is the power absorbed in Δv, we must have

$$c(\lambda) - b(\lambda) = \frac{1}{\Delta l}\left(\frac{\Delta P(\lambda) - \Delta P_s(\lambda)}{P_0(\lambda)}\right) = a(\lambda) \tag{1.18}$$

where $a(\lambda)$ is the *absorption coefficient*. The quantities $a(\lambda)$, $b(\lambda)$, $c(\lambda)$, and $\beta(\lambda,\hat{\xi}\rightarrow\hat{\xi}')$ are referred to as the *inherent optical properties* of the medium (Preisendorfer, 1961, 1976). From the definitions of the inherent optical properties (which require the absence of multiple interactions within Δv) it is clear that they must be additive over the constituents of the medium. For example, if β_w is the volume scattering function of pure seawater, and β_p is the volume scattering function of the particles suspended in the water, then

$$\beta(\lambda,\alpha) = \beta_w(\lambda,\alpha) + \beta_p(\lambda,\alpha) \tag{1.19}$$

Similar relationships hold for each of the inherent optical properties. This is a form of the Lambert–Beer law. Another form of the Lambert–Beer law is that the inherent optical properties due to the ith constituent of the medium are proportional to the concentration of the ith constituent—C_i. For example,

$$a(\lambda) = a_w(\lambda) + \sum_i a_i^*(\lambda) C_i \tag{1.20}$$

where $a_w(\lambda)$ is the absorption coefficient of pure seawater, and $a_i^*(\lambda)$ is the *specific* absorption coefficient of the ith constituent.

There are several convenient parameters that are defined in terms of the inherent optical properties. These are the scattering phase function $P \equiv \beta/b$, the single scattering albedo $\omega_0 \equiv b/c$, the backscattering coefficient

$$b_b \equiv 2\pi \int_{\pi/2}^{\pi} \beta(\alpha) \sin\alpha \, d\alpha \tag{1.21}$$

the forward scattering coefficient $b_f \equiv b - b_b$, the backscattering probability, $\tilde{b}_b \equiv b_b/b \equiv \mathrm{B}$ and the forward scattering probability $\tilde{b}_f \equiv b_f/b \equiv \mathrm{F}$.

In general the inherent optical properties are very difficult to measure routinely (an exception is c at 660 nm for which commercially available instrumentation exists.) They are, however, easy to interpret in terms of the constituents by virtue of satisfying the Lambert–Beer law. In contrast, the apparent optical properties, in particular $K_d(z,\lambda)$, $K_u(z,\lambda)$, and $R(z,\lambda)$, are easily measured with commercially available instrumentation. Unfortunately, the apparent optical properties are very difficult to interpret because of their dependence on the surface illumination, the sea state, and depth. Furthermore, they do not, in general, satisfy the Lambert–Beer law.

The radiative transfer equation

The radiance distribution is related to the inherent optical properties through the radiative transfer equation (RTE). In a medium in which the inherent optical properties depend only on depth, inelastic processes are ignored, and there are no internal sources, e.g., bioluminescence, the RTE is

$$\cos\theta \frac{dL(z,\lambda,\theta,\phi)}{dz} = -c(z,\lambda)\, L(z,\lambda,\theta,\phi) + \int_{4\pi} \beta(z,\lambda,\theta',\phi' \rightarrow \theta,\phi)\, L(z,\lambda,\theta',\phi')\, d\Omega' \tag{1.22}$$

where $d\Omega' = \sin\theta'\, d\theta'\, d\phi'$, and the 4π on the integral means that the integration is to be carried out over all θ' and ϕ'. The first term on the right-hand side represents the loss of radiance in the direction (θ,ϕ) by scattering and absorption, while the second term provides the gain in radiance due to scattering of radiance from all other directions (θ',ϕ') into the direction (θ,ϕ). In what follows, we shall omit the explicit dependence of the various quantities on λ. In terms of the auxiliary inherent optical properties, the RTE becomes

$$\cos\theta \frac{dL(z,\theta,\phi)}{c(z)\, dz} = -L(Z,\theta,\phi) + \omega_0(z) \int_{4\pi} P(z,\theta',\phi' \rightarrow \theta,\phi)\, L(z,\theta',\phi')\, d\Omega' \tag{1.23}$$

It has been shown by Case (1957) that, given the radiance incident on the upper and lower boundaries of the medium, the solutions to the RTE are unique if $\omega_0 < 1$, i.e., there is *some* absorption (which, in the ocean, is always supplied by the water itself). Except in the case of very shallow water, the ocean can be considered to be infinitely deep, and as such, the radiance within the ocean depends on the radiance incident on the sea surface, i.e., $L(0,\theta,\phi)$ for $\theta \leq 90°$.

Note that in Eq. (1.23) $c(z)$ occurs only in the combination $c(z)\, dz$. This suggests that it may be useful to introduce a dimensionless depth τ—the *optical depth*—such that $d\tau = c(z)\, dz$. In a homogeneous ocean $\tau = cz$, and the RTE becomes

$$\cos\theta \frac{dL(\tau,\theta,\phi)}{d\tau} = -L(\tau,\theta,\phi) + \omega_0 \int_{4\pi} P(\theta',\phi' \rightarrow \theta,\phi)\, L(\tau,\theta',\phi')\, d\Omega' \tag{1.24}$$

which shows that all homogeneous media with the same ω_0, $P(\alpha)$, and incident radiance distributions, will have the same values of $L(\tau,\theta,\phi)$ at each τ within the media.

The direct and inverse problems

Given the radiance distribution incident on the sea surface, or incident on the top of the atmosphere in the case of the ocean–atmosphere system, the RTE can be solved for the radiance given the inherent optical properties. Thus, from the constituent concentrations C_i, the specific absorption and scattering coefficients a_i^* and b_i^*, and the phase functions P_i derived by laboratory measurements, the

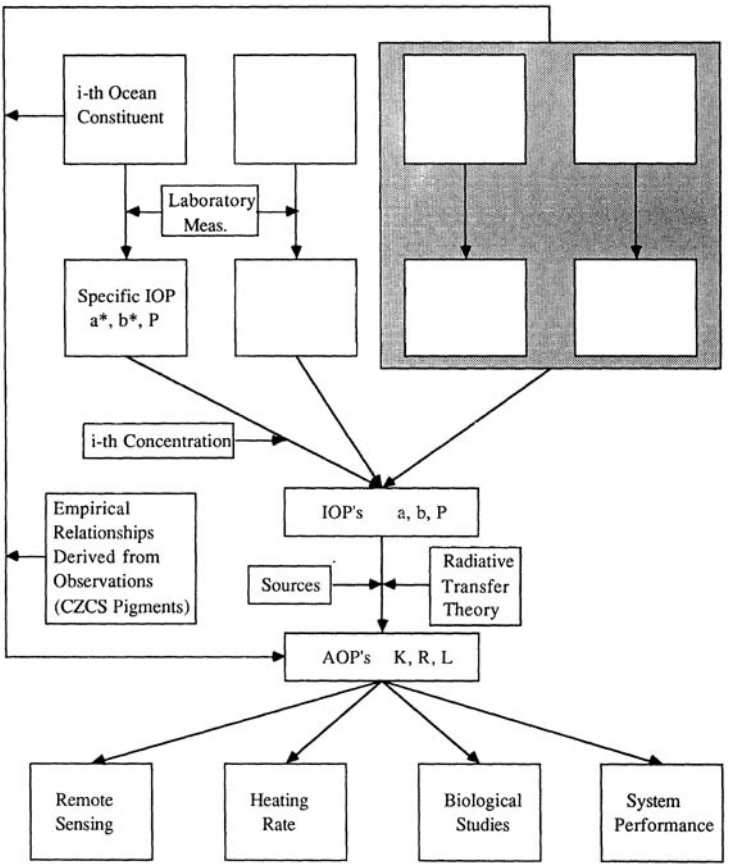

Fig. 1-2. The central position of radiative transfer theory in marine optics.

inherent optical properties are determined. Radiative transfer theory then provides the apparent optical properties for application to specific problems. This procedure is illustrated in Fig. 1-2. This figure also illustrates an empirical method that has been used in some applications, i.e., directly relating the constituent concentrations to the apparent optical properties. Examples of this are relating the near-surface $K_d(\lambda)$ or the ratio of reflectances at two wavelengths to the phytoplankton pigment concentration. Also shown is an example in which constituents cannot be easily separated, e.g., several species of phytoplankton, and are therefore pooled to form a single constituent (the shaded box). With the exception of the empirical loop, all of the arrows flow from top to bottom through the radiative transfer segment. This is referred to as the *direct problem.* If the arrows are reversed—i.e., apparent optical properties → inherent optical properties → constituents, we have the *inverse problem* of radiative transfer. The inverse problem is of interest for several reasons: (1) the apparent optical properties sample very large volumes (tens to hundreds of cubic meters) of the medium and thus include large particles that might be missed with classical instruments for measuring the inherent optical properties (recall that inherent optical property measurements are carried out on very small volumes to avoid multiple scattering within the sample volume); (2) the long effective path length in the medium (tens of meters) that are possible in the case of K_d measurements enable the detection of very small concentrations of constituents; and (3) the apparent optical properties are directly measured in remote sensing applications. Solving the inverse problem, i.e., reversing the arrow through the radiative transfer segment in Fig. 1-2, is the ultimate goal of the modeling and simulation described in this paper.

Single and quasi-single scattering theory

Unfortunately, analytical solutions to the RTE are possible only in the simplest cases, e.g. $\omega_0 = 0$, and one must resort to numerical solutions. Often, researchers seek approximate solutions and test their validity by comparison with "exact" numerical computations. This approach is used here. In this section we provide an algorithm for solving the RTE and use it to develop the solution in single scattering. This solution is then modified to the quasi-single scattering approximation, which is useful in media with strong forward scattering, e.g., the ocean.

The successive order of scattering solution

The successive order of scattering technique is the most straightforward method of solving the RTE. The basic idea is to successively compute the radiance that is scattered once, twice, etc., and then to sum these contributions to obtain the total radiance. The development is simplified if we let the medium be homogeneous with $\omega_0 < 1$. Then the RTE becomes

$$\cos\theta \frac{dL(z,\theta,\phi)}{c\,dz} = -L(z,\theta,\phi) + \omega_0 \int_{4\pi} P(\theta',\phi' \rightarrow \theta,\phi)\, L(z,\theta',\phi')\, d\Omega' \tag{1.25}$$

We then assume that the radiance can be expanded in a power series in ω_0, i.e.,

$$L(z,\theta,\phi) = L^{(0)}(z,\theta,\phi) + \omega_0 L^{(1)}(z,\theta,\phi) + \omega_0^2 L^{(2)}(z,\theta,\phi) + \cdots \tag{1.26}$$

put this into the RTE, and group like powers of ω_0. The RTE is then satisfied if the individual $L^{(n)}$ satisfy

$$\begin{aligned}
\cos\theta \frac{dL^{(0)}}{c\,dz} &= -L^{(0)} \\
\cos\theta \frac{dL^{(1)}}{c\,dz} &= -L^{(1)} + \int P L^{(0)'}\, d\Omega' \\
\cos\theta \frac{dL^{(2)}}{c\,dz} &= -L^{(2)} + \int P L^{(1)'}\, d\Omega' \\
&\vdots \\
\cos\theta \frac{dL^{(n)}}{c\,dz} &= -L^{(n)} + \int P L^{(n-1)'}\, d\Omega' \\
&\vdots
\end{aligned} \tag{1.27}$$

These represent a simplification in that the single integral–differential equation has been transformed into a set of ordinary differential equations (the integrals can now be evaluated in principle since each integrand is furnished by the preceding equation). If the medium is illuminated from above by a radiance $L_{\text{inc}}(0,\theta,\phi)$, and we choose the simplest among the many ways of satisfying the boundary condition at $z=0$ by taking

$$\begin{aligned}
L^{(0)}(0,\theta,\phi) &= L_{\text{inc}}(0,\theta,\phi) \\
L^{(n)}(0,\theta,\phi) &= 0 \text{ for } n > 0
\end{aligned} \tag{1.28}$$

the resulting $L(z,\theta,\phi)$ will satisfy the RTE and the boundary conditions at $z=0$ and, as such, is the *unique* solution.

The single scattering approximation

In the *single scattering* approximation (SSA), the series is terminated at $n=1$, i.e., $L = L^{(0)} + \omega_0 L^{(1)}$. To develop this solution we ignore refraction at the sea surface and the presence of the atmosphere, and we also assume that the ocean is infinitely deep. The radiance incident on the sea surface is

$$L_{\text{inc}}(0,\theta,\phi) = F_0\, \delta(\cos\theta - \cos\theta_0)\, \delta(\phi - \phi_0) \tag{1.29}$$

where θ_0 and ϕ_0 are the solar zenith and azimuth angles, respectively, and δ is the Dirac delta function. F_0 is the solar irradiance on a plane normal to the sun's rays. The equation for $L^{(0)}$ can be solved immediately, yielding

$$L^{(0)}(z,\theta,\phi) = F_0\delta(\cos\theta - \cos\theta_0)\,\delta(\phi - \phi_0)\exp(-cz/\cos\theta_0) \tag{1.30}$$

The equation for $L^{(1)}$ then becomes

$$\cos\theta\frac{dL^{(1)}}{c\,dz} = -L^{(1)} + \int PL^{(0)'}\,d\Omega' = -L^{(1)} + P(\theta_0,\phi_0\rightarrow\theta,\phi)F_0\exp(-cz/\cos\theta_0) \tag{1.31}$$

The solution to this equation is

$$\begin{aligned}\frac{L_u^{(1)}(z,\theta,\phi)}{E_d(0)} &= \frac{P(\alpha)}{\cos\theta_0 - \cos\theta}\exp(-cz/\cos\theta_0)\\ \frac{L_d^{(1)}(z,\theta,\phi)}{E_d(0)} &= \frac{P(\alpha)}{\cos\theta_0 - \cos\theta}[\exp(-cz/\cos\theta_0) - \exp(-cz/\cos\theta)]\end{aligned} \tag{1.32}$$

where

$$E_d(0) = F_0\cos\theta_0 \tag{1.33}$$

and

$$\cos\alpha = \cos\theta\,\cos\theta_0 + \sin\theta\,\sin\theta_0\cos\phi \tag{1.34}$$

The subscripts u and d in Eq. (1.32) mean "up" ($\theta > 90°$) and "down" ($\theta < 90°$), respectively. From these we can compute the first-order or single scattering approximation to the apparent optical properties. As an example we compute $K_d(0)$, the downwelling irradiance attenuation coefficient just beneath the surface. For $cz \ll 1$,

$$L_d^{(1)}(z,\theta,\phi) = \frac{E_d(0)P(\alpha)}{\cos\theta_0\cos\theta}cz \tag{1.35}$$

Then

$$\begin{aligned}E_d^{(0+1)} &= \int_0^{2\pi}\int_0^{\pi/2}(L_d^{(0)} + \omega_0 L_d^{(1)})\cos\theta\,\sin\theta\,d\theta\,d\phi\\ &= F_0\cos\theta_0\,e^{-cz/\cos\theta_0} + \omega_0\int_0^{2\pi}\int_0^{\pi/2}\cos\theta\,L_d^{(1)}(z,\theta,\phi)\sin\theta\,d\theta\,d\phi\end{aligned} \tag{1.36}$$

or, for small cz,

$$E_d^{(0+1)} \to F_0 \cos\theta_0 (1 - cz/\cos\theta_0) + F_0 \omega_0 cz \int_0^{2\pi} \int_0^{\pi/2} P(\alpha) \sin\theta \, d\theta \, d\phi \tag{1.37}$$

The first-order $K_d(0)$ is

$$\begin{aligned} K_d^{(1)}(0) &= \lim_{z \to 0} -\frac{1}{E_d^{(0+1)}} \frac{dE_d^{(0+1)}}{dz} \\ &= \frac{c - b \int_0^{2\pi} \int_0^{\pi/2} P(\alpha) \sin\theta \, d\theta \, d\phi}{\cos\theta_0} \end{aligned} \tag{1.38}$$

When $\theta_0 = 0$, i.e., light is incident normally on the surface, $\alpha = \theta$ and $\iint P(\alpha) \sin\theta \, d\theta \, d\phi = \tilde{b}_f = F$. In this case

$$K_d^{(1)}(0) = c - bF = c - b + b_b = a + b_b = c(1 - \omega_0 F) \tag{1.39}$$

and to first order $K_d(0)$ depends only on absorption and *backscattering*. We shall see later that the volume scattering functions for the ocean are very strongly peaked in the forward direction, which implies that the integral in Eq. (1.38) is only slightly less than 1 for moderate values of θ_0. In this case, $K_d^{(1)}(0)$ depends mostly on a and varies with θ_0 in proportion to $1/\cos\theta_0$.

As a second example, we compute the single scattering approximation to $R(0)$. From Eq. (1.32) we have

$$\frac{L_u^{(1)}(0,\theta,\phi)}{E_d(0)} = \frac{P(\alpha)}{\cos\theta_0 - \cos\theta} \tag{1.40}$$

so

$$\begin{aligned} R^{(1)}(0) &= \frac{E_u^{(1)}(0)}{E_d(0)} \\ &= -\int_0^{2\pi} \int_{\pi/2}^{\pi} \frac{L_u^{(1)}(0,\theta,\phi)}{E_d(0)} \cos\theta \, d\Omega \\ &= -\omega_0 \int_0^{2\pi} \int_{\pi/2}^{\pi} \frac{P(\alpha)}{\cos\theta_0 - \cos\theta} \cos\theta \sin\theta \, d\theta \, d\phi \end{aligned} \tag{1.41}$$

Letting $\mu = -\cos\theta$ and $\mu_0 = \cos\theta_0$, we have

$$R^{(1)}(0) = \omega_0 \int_0^{2\pi} d\phi \int_0^1 \frac{\mu}{\mu + \mu_0} P(\alpha)\, d\mu$$
$$= \frac{1}{c} \int_0^{2\pi} d\phi \int_0^1 \frac{\mu}{\mu + \mu_0} \beta(\alpha)\, d\mu \tag{1.42}$$

where

$$\cos\alpha = -\mu\mu_0 + \sqrt{(1-\mu^2)(1-\mu_0^2)}\,\cos\phi \tag{1.43}$$

For the specific case of isotropic scattering (β independent of α), $P = 1/4\pi$ and the integrals above are easy to evaluate to obtain

$$R^{(1)}(0) = \frac{\omega_0}{2}\left[1 - \mu_0 \ln\left(\frac{1+\mu_0}{\mu_0}\right)\right] \tag{1.44}$$

Because of refraction at the sea surface (ignored here), the value of θ_0 in the water is restricted to be less than approximately 48.6°, thus for a flat ocean μ_0 is between approximately 0.66 and 1. Evaluation of $R^{(1)}(0)$ over this range shows that it is almost a linear function of $1/\mu_0$. We shall use this observation later.

The quasi-single scattering approximation

We shall see below that the single scattering approximation works well for $K_d(0)$, i.e. Eq. (1.38), but Eq. (1.42) is a very poor approximation to $R(0)$. Thus, we look for a way to approximate multiple scattering in the computation of $R(0)$. The *quasi-single scattering* approximation (QSSA) achieves this (Gordon, 1973). The basic idea of the quasi-single scattering approximation is that in the ocean, as remarked earlier, the volume scattering function is very strongly peaked in the forward direction. This implies that photons are usually scattered through very small angles. However, when photons scatter through small angles there is little difference between this and not scattering at all! In the quasi-single scattering approximation the phase function is modified so that all of the scattering in $0 \le \alpha \le 90°$ is concentrated into $\alpha = 0°$ and the resulting RTE is solved in the single scattering approximation. The beam attenuation coefficient then becomes $a + b_b$, i.e.,

$$c = a + b \rightarrow a + b_b = K_d^{(1)}(0) \qquad \text{for } \theta_0 = 0 \tag{1.45}$$

Thus, the quasi-single scattering approximation approximation for $R^{(1)}(0)$ is found by replacing β/c in Eq. (1.42) by $\beta/K_d^{(1)}(0)$:

$$\frac{\beta}{c} \rightarrow \frac{\beta}{K_d^{(1)}(0)} = \frac{bP/c}{K_d^{(1)}(0)/c} = \frac{\omega_0 P}{1 - \omega_0 F} \tag{1.46}$$

The reflectance is then approximated by

$$R(0) = \frac{\omega_0}{1 - \omega_0 F} \int_0^{2\pi} d\phi \int_0^1 \frac{\mu}{\mu + \mu_0} P(\alpha)\, d\mu \tag{1.47}$$

In Eq. (1.47) α can be $< 90°$ for $\mu_0 \neq 1$. In this case, the actual phase function $P(\alpha)$ is to be used in the integration (even though this procedure is inconsistent with the derivation of the approximation) so that the quasi-single scattering approximation will reduce to the single scattering approximation as $\omega_0 \rightarrow 0$. Figure 1-3 compares "exact" numerical computations of the reflectance just beneath the sea surface (points) with that predicted by the single scattering approximation and the quasi-single scattering approximation. In the computations the sun is at the zenith so $\mu_0 = 1$. Also, all of the refraction effects associated with the sea surface are included in the exact computations. The phase function used in this example is labeled "T" in Fig. 1-5 below. The quasi-single scattering approximation provides reasonable values of $R(0)$ for ω_0 less than approximately 0.85, while, in contrast, the single scattering approximation is very poor for ω_0 greater than approximately 0.35. The quasi-single scattering approximation (and single scattering approximation) prediction for $K_d(0)$ is of course $a + b_b$ if $\theta_0 = 0$. Fig. 1-4 compares exact and quasi-single scattering approximation (and single scattering approximation) computations of $K_d(0)$ for the same situation as in Fig. 1-3. For $\theta_0 \neq 0$, we take the suggestion offered in Eq. (1.38) and assume

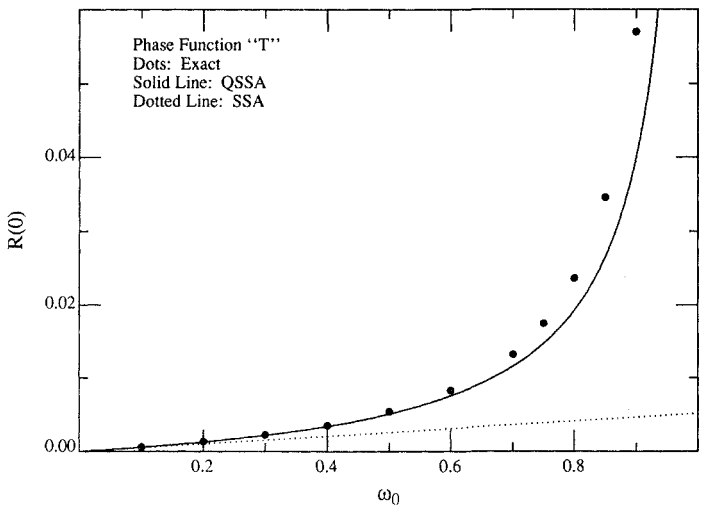

Fig. 1-3. Comparison between exact, quasi-single scattering approximation, and single scattering approximation computations of $R(0)$.

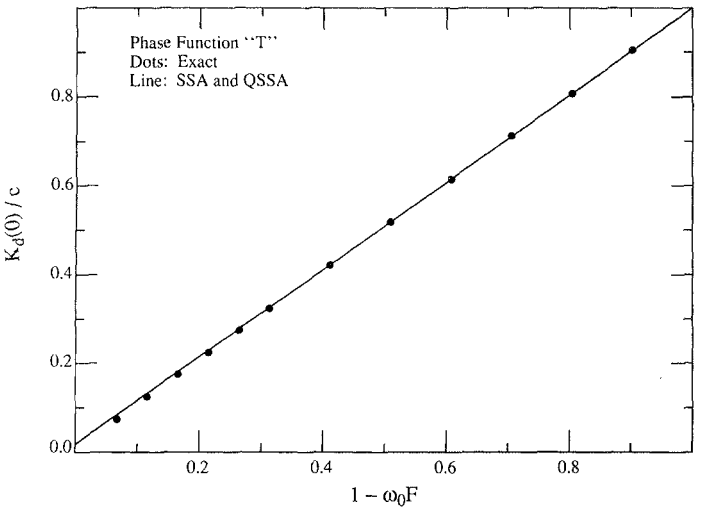

Fig. 1-4. Comparison between exact, quasi-single scattering approximation, and single scattering approximation computations of $K_d(0)$.

$$K_d(0) = \frac{a + b_b}{\mu_0} \tag{1.48}$$

The quasi-single scattering approximation clearly provides excellent values of K_d and R very near the surface.

These simple approximate solutions of the RTE suggest several questions to be examined. Among these are (1) the validity of the approximations in the presence of the atmosphere, (2) the influence of the refracting, *rough*, air–sea interface, and (3) the possibility of extending Eq. (1.48) to depths greater than $z \approx 0$. They can also be used as a guide to look for other simplifications, e.g., does the relationship

$$\frac{R(\mu_0)}{R(1)} \approx \frac{\text{Const.}}{\mu_0} \tag{1.49}$$

which resulted from the single scattering approximation for an isotropic scattering phase function, have more general validity? We shall investigate these questions by *simulating* radiative transfer in a hypothetical ocean–atmosphere system, i.e., we shall solve Eq. (1.24) for a semi-infinite, homogeneous ocean with realistic values of P and ω_0. To do this we need realistic values of c and $\beta(\alpha)$.

Bio-optical model of the inherent optical properties

In this section we develop a realistic model of the optical properties of Case 1 waters (Morel and Prieur, 1977), i.e., waters for which phytoplankton and their

immediate detrital material play a dominant role in determining the optical properties—thus the term *bio-optical* model. Only two constituents are considered here—water and a combined constituent, phytoplankton and detrital particles, as in the shaded box in Fig. 1-2. This combined "constituent," which is particulate, we denote by the subscript p. Thus, $c = c_w + c_p$ and $\beta = \beta_w + \beta_p$. It is a matter of simple algebra to show that

$$\omega_0 P = \frac{\omega_p P_p (c_p/c_w) + \omega_w P_w}{c_p/c_w + 1} \tag{1.50}$$

and given ω_w, ω_p, P_w, and P_p, representing the inherent optical properties of the water and of the suspended particles, $\omega_0 P$ in Eq. (1.24) is specified by the single parameter c_p/c_w. Since it is customary to parameterize Case 1 waters by the pigment concentration C, defined to be the sum of the concentrations of chlorophyll a and phaeophytin a, we will relate c_p to C. First, however, we must model the inherent optical properties.

The absorption coefficient a_w has been inferred from measurements of downwelling and upwelling irradiance in oligotrophic waters such as the Sargasso Sea (Morel and Prieur, 1977; Prieur and Sathyendranath, 1981; Smith and Baker, 1981), and the scattering coefficient b_w and the volume scattering function $\beta_w(\alpha)$ have been measured directly for pure water and for saline solutions of pure water corresponding to salinities between 35 and 39 parts per thousand by Morel (1974). The resulting a_w, b_w and ω_w are given in Table 1-1 for the wavelengths used in the present computations, and $P_w(\alpha)$ is provided in Fig. 1-5.

The scattering coefficient of particles at 550 nm, $b_p(550)$, is *statistically* related to the pigment concentration C through (Morel, 1980)

$$b_p = B_c C^{0.62} \tag{1.51}$$

where $b_p(550)$ is in m^{-1} and C is in mg m^{-3} (see also Gordon and Morel, 1983). The constant B_C, the scattering coefficient at a pigment concentration of 1 mg m^{-3}, ranges from 0.12 to 0.45 and has an average value of 0.30. The variation in B_C is due to the natural variability of scattering over the various species of phytoplankton, as well as a variability in scattering by the detrital

Table 1-1. Absorption and scattering coefficients of pure seawater

λ (nm)	a_w (m^{-1})	b_w (m^{-1})	ω_w
440	0.0145	0.0049	0.253
480	0.0176	0.0034	0.162
550	0.0638	0.0019	0.029

Source: Gordon (1989b).

particles associated with the phytoplankton. Similarly, the absorption coefficient of the particles has been statistically studied as a function of C by Prieur and Sathyendranath (1981) yielding for $C < 10\,\mathrm{mg\,m^{-3}}$:

$$a_p(\lambda) = 0.06\, A_c(\lambda)\, C^{0.602} \tag{1.52}$$

where $a_p(\lambda)$ is in $\mathrm{m^{-1}}$ and C is in $\mathrm{mg\,m^{-3}}$. In this equation $A_C(\lambda)$ is the absorption coefficient of the particles normalized to 440 nm, i.e.,

$$A_C(\lambda) = \frac{a_p(\lambda)}{a_p(440)} \tag{1.53}$$

The relative absorption of particles $A_C(\lambda)$ deduced by Prieur and Sathyendranath (1981) agrees well with absorption measurements made on phytoplankton cultures by Sathyendranath (1981). Note that $a_p(\lambda)$ and $b_p(\lambda)$ include both phytoplankton and their detrital material and thus represent the absorption and scattering of all the components considered here, other than the water itself. These nonlinear relationships between a_p and C and b_p and C are believed to be due to a systematic variation in the ratio of the concentration of phytoplankton to that of detrital material as a function of the concentration of phytoplankton (Hobson et al., 1973; Smith and Baker, 1978a). Since $a_p(\lambda)$ and $b_p(\lambda)$ vary with pigment concentration in nearly the same manner, $\omega_p(\lambda)$ must, in the first approximation, be *independent* of the pigment concentration. At 550 nm, where an average B_C is known, these relationships provide $\omega_p(550) = 0.933$, in good agreement with the range measured by Bricaud et al. (1983) for four species of cultured phytoplankton: $0.89 \le \omega_p(550) \le 0.97$. In order to fix reasonable values of $\omega_p(\lambda)$ at the other wavelengths of interest, we assume $B_C(\lambda)$ obeys a power law with wavelength, i.e., $B_C(\lambda) \propto \lambda^{-n}$, and take $n = +1$. This yields $B_C(480) \approx 0.34$ and $B_C(440) \approx 0.38$. The resulting values of $\omega_p(\lambda)$ and $\omega_w(\lambda)$ used in the computations are provided in Table 1-2. It should be noted that the marine particulate component is far better at scattering light than at absorbing it. In fact, even near the phytoplankton absorption maximum, $b_p/a_p \approx 6$. To ensure that departures of ω_p from those used in Table 1-2 do not influence the results of this work, simulations also have been carried out at 480 nm for $\omega_p = 0.5$, 0.7, and 0.99. For a more complete description of the bio-optical model, see Gordon (1987) and Gordon (1989b).

Table 1-2. Model values of ω_w and ω_p

λ (nm)	ω_w	ω_p
440	0.253	0.86
480	0.162	0.88
550	0.029	0.93

Source: Gordon (1989b).

For the particle phase function we use measurements of the volume scattering function at 530 nm made for waters in several locations with very different turbidities (total scattering coefficients) by Petzold (1972). After subtracting the scattering by pure seawater, the resulting particle phase functions are very similar, having a standard deviation that is within about 30% of the mean, over waters for which the particle scattering coefficient varied over a factor of 50. The mean particle phase function derived from Petzold's measurements is adopted for this study and is designated by the symbol *M*. Also, two other particle phase functions are used to represent the extremes of the phase functions given by Petzold's measurements. These are the mean of three phase functions measured in the turbid waters of San Diego Harbor and designated by *T*, and a phase function measured in the clear waters of the Tongue of the Ocean, Bahamas, and designated by *C*. The three particle phase functions are shown in Fig. 1-5 along with the phase function for scattering by the water itself. It is seen that these model particle phase functions differ principally in their scattering at angles greater than 25°.

This completes the specification of the quantities needed for the simulation: ω_w, ω_p, $P_w(\alpha)$, and $P_p(\alpha)$. Varying the parameter c_p/c_w from 0 to ∞ results in models that range from a particle-free ocean to an ocean in which the optical properties of the particles are completely dominant. This parameter is now easily related to the pigment concentration, e.g.,

$$\frac{c_p(550)}{c_w(550)} \approx 4.9C^{0.6} \tag{1.54}$$

etc.

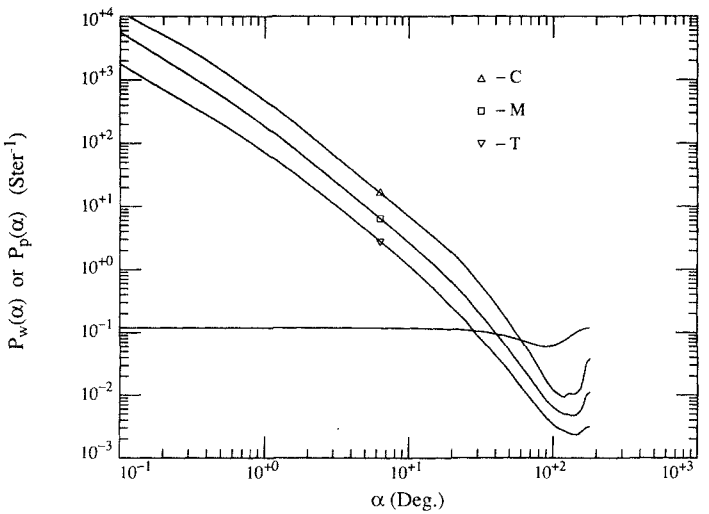

Fig. 1-5. Phase functions *C*, *M*, and *T* for particles derived from Petzold (1972) and for water derived from Morel (1974). $P_p(\alpha)$ for *M* and *C* have been multiplied by 2 and 4, respectively. (Taken from Gordon 1989b.)

The atmosphere influences the in-water light field by distributing a portion of the near-parallel solar beam over the entire upward hemisphere, i.e., in producing sky light from direct sunlight, which is incident on the sea surface. In order to simulate the angular distribution of radiation entering the ocean we solve the RTE for the atmosphere as well. In fact, we solve the RTE for the coupled ocean–atmosphere system. This requires an atmospheric model. This model atmosphere consisted of 50 layers and included the effects of aerosols, ozone, and Rayleigh scattering, vertically distributed according to data taken from the work of Elterman (1968). The aerosol phase functions were computed by Fraser (R. Fraser, NASA/Goddard Space Flight Center, personal communication) from Mie theory using the Deirmendjian (1969) Haze C size distribution. This model simulates optical properties of the cloud-free atmosphere.

Simulations and analysis

Using the inherent optical properties modeled above for the ocean–atmosphere system, the applicability of the single scattering approximation and the quasi-single scattering approximation was examined by comparing their predictions with the results of exact solutions (including all orders of multiple scattering) of the RTE. Rather than using the successive order of scattering method developed earlier, we choose the Monte Carlo method of solution.

The Monte Carlo method

In the Monte Carlo method of radiative transfer, the solution to Eq. (1.24) is developed by following the life histories of a very large number of photons, beginning with their entry at the top of the atmosphere from the sun and ending when they leave the system either by absorption in the ocean or the atmosphere or by reflection out of the atmosphere. A very readable description of the method (along with a sample computer code in FORTRAN) has been provided by Kirk (1981a). Briefly, a photon enters the atmosphere and travels a distance l before interacting with the medium. The interaction is either absorption or scattering. If it is absorption, the photon disappears and another photon is started. If it is scattered, the scattering angles must be found from the phase function in order to determine the direction of the scattered photon. The process is then repeated, i.e., the distance to the next interaction, the type of interaction, and if necessary the new direction, are determined. When a photon crosses a given horizontal surface (z) it contributes one unit to the downwelling (upwelling) irradiance if its direction of flight is downward (upward). Likewise it contributes $1/|\cos\theta|$ units of scalar irradiance. Accumulating the irradiances for a large number of photons yields estimates of the associated values of $E_d(z)$, etc. The irradiance estimate is N/N_0, where N is the number of photons contributing to the irradiance and N_0 is the number of photons injected into the atmosphere from the sun. The variance in a given irradiance estimate is $1/N$, so the relative error in the irradiance is

$1/\sqrt{N}$. The simulation described is called a *direct* simulation. In the computations discussed here, methods have been used to reduce the variance in the Monte Carlo estimate; however, these technical aspects will not be discussed.

To implement the Monte Carlo scheme, one needs to determine three unknowns: (1) the distance l between photon interactions; (2) whether the interaction was absorption or scattering; and (3) the scattering angles. These are chosen from a sequence of random numbers (actually pseudo-random numbers) in the following manner. Let $\rho_0, \rho_1, \ldots, \rho_{i-1}, \rho_i, \rho_{i+1}, \ldots$ be a sequence of random numbers between 0 and 1. Then after any scattering interaction, the distance to the next interaction is given by

$$l = \frac{-1}{c} \ln(\rho_j) \tag{1.55}$$

The type of interaction is determined from another random number ρ_{j+1}:

$$\begin{aligned} \rho_{j+1} \leq \omega_0 &\Rightarrow \text{scattering} \\ \rho_{j+1} > \omega_0 &\Rightarrow \text{absorption} \end{aligned} \tag{1.56}$$

Finally the polar Θ and azimuth Φ scattering angles relative to the photon's direction are determined from ρ_{j+2} and ρ_{j+3} by

$$\begin{aligned} \rho_{j+2} &= 2\pi \int_0^{\Theta} P(\alpha) \sin\alpha \, d\alpha \\ \rho_{j+3} &= 2\pi\Phi \end{aligned} \tag{1.57}$$

When a photon encounters the air–sea interface the laws of geometrical optics are applied to determine the photon's fate—reflection or transmission—and the reflected or transmitted directions. In simulations in which the interface is roughened by the wind, the sea surface is modeled as a collection of individual facets. The direction of the normal to an individual facet is determined from the Cox and Munk (1954) probability density for slopes regardless of wind direction; i.e., if θ_n is the angle the surface normal makes with the z axis, and ϕ_n is the angle the projection of the normal on the x–y plane makes with the x axis, then

$$\begin{aligned} \rho_{j+4} &= 2\pi\phi_n \\ \rho_{j+5} &= \frac{1}{2\pi} \frac{1}{\sqrt{\pi\sigma^2}} \int_0^{\theta_n} \exp[-\tan^2\gamma/\sigma^2] \tan\gamma \sec^2\gamma \, d\gamma \end{aligned} \tag{1.58}$$

where $\sigma^2 = 0.003 + 0.00512V$, and V is the wind speed. The specular (Fresnel) reflectance of the facet is

$$r(\Psi_i,\Psi_r) = \frac{1}{2}\left(\frac{sin^2(\Psi_i - \Psi_r)}{\sin^2(\Psi_i + \Psi_r)} + \frac{\tan^2(\Psi_i - \Psi_r)}{\tan^2(\Psi_i + \Psi_r)}\right) \tag{1.59}$$

where Ψ_i and Ψ_r are the angles the incident and refracted rays make with the surface normal, respectively. They are related by Snell's law, $m_i \sin\Psi_i = m_r \sin\Psi_r$, where m_i and m_r are the refractive indices in the incident and refracted media, respectively. If $\sin\Psi_r > 1$ then the photon is reflected, otherwise, the next random number in the sequence, ρ_{j+6}, is selected and

$$\begin{aligned} \rho_{j+6} &\leq r \Rightarrow \text{reflection} \\ \rho_{j+6} &> r \Rightarrow \text{transmission} \end{aligned} \tag{1.60}$$

The simulation set

To test the efficacy of simple models such as the quasi-single scattering approximation in realistic situations, a large set of simulations (334) of radiative transfer in the ocean-atmosphere system have been carried out in which all of the important parameters are varied over wide ranges. The simulations include solar zenith angles of 0°, 20°, 25°, 30°, 40°, 60°, and 80° as well as a uniform incident radiance distribution to simulate an overcast sky. Pigment concentrations of 0, 0.01, 0.05, 0.1, 0.5, 1.0, and 4.6 mg m^{-3} were used along with phase functions *C*, *M*, and *T* and ω_p from Table 1-2 to characterize the particles. The surface roughness was provided by varying the parameter σ over 0, 0.1, 0.2, and 0.3 for a few simulations. The simulations were carried out at wavelengths of 440, 480, and 550 nm. The simulated light field was used to compute the apparent optical properties. The resulting apparent optical properties were treated as experimental data, albeit data collected under carefully controlled conditions, a cloud-free sky and a homogeneous ocean of *precisely known* inherent optical properties.

Sample simulations of K and R

In this section examples of simulations of K_d and R are provided. As delineated above, given the bio-optical model of the ocean, the quantities necessary to specify a simulation are λ, C (or equivalently c_p/c_w), the particle phase function (C, M, or T), θ_0, and σ (or equivalently the wind speed V). Figures 1-6 and 1-7 show simulations of K_d and R as a function of depth in the ocean at 550 nm using particle phase function T and a pigment concentration of 0.35 mg m^{-3} (c_p/c_w = 2.6). For this value of c_p/c_w, $c = 0.237$ m^{-1}. In these particular examples there is no atmosphere. The left-most curve on each figure corresponds to $\theta_0 = 0$ and $\sigma = 0$, the center curve to $\theta_0 = 80°$ and $\sigma = 0$, and the right-most curve to $\theta_0 = 80°$ and $\sigma = 0.2$ ($V \approx 7.5$ m s^{-1}). A simulation was also carried out for $\theta_0 = 0$ and $\sigma = 0.2$ and the results were virtually identical to the corresponding $\sigma = 0$ case. These figures demonstrate why $K_d(z)$ and $R(z)$ are apparent optical properties:

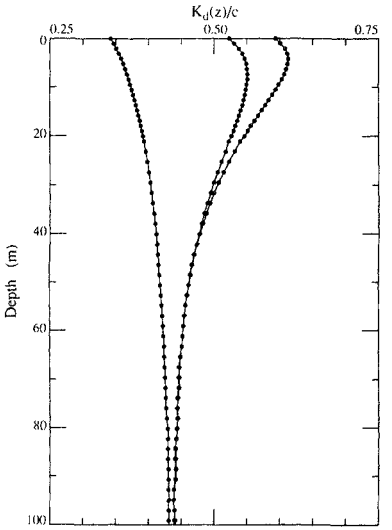

Fig. 1-6. $K_d(z)$ as a function of z at 550 nm with $C = 0.35\,\text{mg m}^{-3}$.

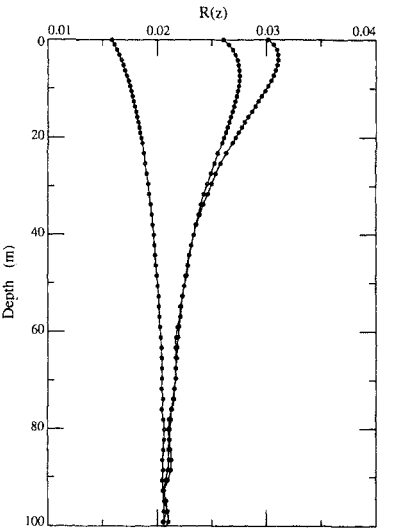

Fig. 1-7. $R(z)$ as a function of z at 550 nm with $C = 0.35\,\text{mg m}^{-3}$.

their values depend on depth, the incident light field (θ_0), and the surface roughness (σ), and are therefore *not* characteristic of the medium alone. The figures suggest three light field regimes. The first is the upper ~25 m, where the light field depends strongly on all three variables z, θ_0, and σ. The second is $25 \leq z \leq 70$ m in which K_d and R retain their dependence on z and θ_0, but become independent of σ. Thus, in the second regime the state of roughness of the sea surface is irrelevant. Finally, for $z \geq 70$ m, K_d and R become nearly independent

of θ_0 and z. In fact, as z increases further, K_d and R do become constants (independent of all three variables), and thus become characteristic of the medium alone. This is the *asymptotic* light field in which K_d, R, and the other apparent optical properties become inherent optical properties (Preisendorfer, 1959). Notice that $R(z)$ becomes noisy after approximately 80 m. This is due to the statistical fluctuations in the Monte Carlo computation of $E_u(z)$. Since $E_u \approx E_d/50$ in these examples, $N_u/N_d \approx 1/50$, where N_u and N_d are the number of upwelling and downwelling photons, respectively. If ${\sigma_u}^2$ and ${\sigma_d}^2$ are the variances associated with N_u and N_d, then $\sigma_u/\sigma_d \approx 7$ and the statistical fluctuation in the upwelling field is roughly an order of magnitude larger than in the downwelling field.

Analysis of K_d

The $K_d(z)$ set from the simulations is used here to study the applicability of the quasi-single scattering approximation value to realistic oceans. Since Eq. (1.48) provides the quasi-single scattering approximation $K_d(0)$, we will first examine

$$K \equiv \lim_{z \to 0} K_d(z) \tag{1.61}$$

i.e., K_d just beneath the sea surface. The μ_0 term in Eq. (1.48) accounts for the direction of the incident beam in the medium, i.e., the incident radiance distribution. For a flat ocean with no atmosphere μ_0 should be replaced by $\mu_{0w} = \cos\theta_{0w}$, where θ_{0w} is the *refracted* angle of the solar beam. However, in the simulations the incident radiance distribution consists of skylight as well as direct sunlight. Furthermore, even in the absence of the atmosphere, the rough surface will cause the solar beam to become diffuse in the water. Thus, we need to generalize μ_0 with a parameter that describes the incident radiance distribution and reduces to μ_{0w} in the case of a flat ocean in the absence of the atmosphere. Preisendorfer (1961) showed that when $\omega_0 \to 0$, $K_d(z) \to aD_d(z)$. This suggests that a candidate parameter is $D_d(0)$ for the *transmitted* radiance distribution (Gordon, Brown and Jacobs, 1975). This is the value of $D_d(0)$ that would be measured just beneath the surface *if the medium did not scatter*, i.e., if $b = 0$. To emphasize that $\omega_0 = 0$ in its definition, I refer to it as D_0. For a flat ocean with no atmosphere, the transmitted incident radiance distribution is

$$L_{\text{inc}} = F_0 t(\theta_0)\delta(\theta_{0w} - \theta_0)\,\delta(\phi - \phi_0) \tag{1.62}$$

where $t(\theta_0)$ is the Fresnel transmittance of the sea surface. From the definitions of E_d, E_u, and D_d it is easy to see that this leads to

$$D_0 = \frac{1}{\cos\theta_{0w}} \tag{1.63}$$

Table 1-3. D_0 just beneath the (flat) sea surface

θ_0°	440 nm	480 nm	550 nm	$1/\cos\theta_{0w}$
0	1.034	1.027	1.019	1.000
20	1.074	1.065	1.055	1.035
25	1.088	1.077	1.067	1.054
30	1.105	1.100	1.093	1.079
40	1.158	1.154	1.149	1.142
60	1.286	1.293	1.299	1.315
80	1.284	1.311	1.346	1.484
Diffuse	1.197	1.197	1.197	

source: Gordon (1989b).

as desired. D_0^{-1} is, of course, the "average cosine" of the *transmitted* light field. With this generalization, Eq. (1.48) applied to the ocean becomes

$$K = D_0(a + b_b) \tag{1.64}$$

or

$$\frac{K}{cD_0} = 1 - \omega_0 F \tag{1.65}$$

D_0 has been computed at each wavelength and for each solar zenith angle by directly solving the RTE for the given λ and θ_0 with $\omega_0 = 0$. The results of this computation for D_0 are provided in Table 1-3. Note that, as expected, D_0 usually increases with increasing θ_0; however, for 440 nm the contribution from the increasing amount of skylight compared to direct sunlight from $\theta_0 = 60°$ to $\theta_0 =$

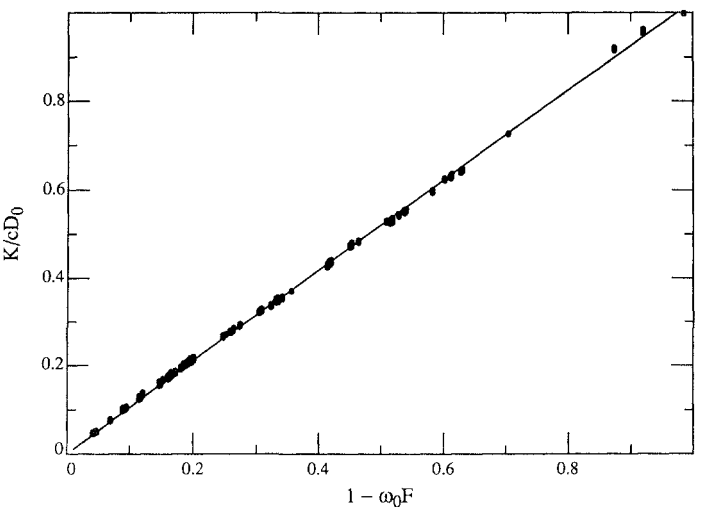

Fig. 1-8. K/cD_0 as a function of $1-\omega_0 F$.(Taken from Gordon 1989b.)

80° actually causes a small decrease in D_0. Also, for $\theta_0 \leq 60°$ the difference between D_0 and $1/\cos\theta_{0w}$ is usually less than about 3%.

Figure 1-8 from Gordon (1989b) shows K/cD_0 as a function of $1-\omega_0 F$ for the simulation set delineated above (points). These quantities are nearly linearly related. In fact, linear regression yields

$$\frac{K}{cD_0} = 1.0395(1 - \omega_0 F) \tag{1.66}$$

with an average error of only 2.5%; however, a slightly better fit (average error 1.8%) is obtained using

$$\frac{K}{cD_0} = \sum_{n=1}^{2} k_n (1 - \omega_0 F)^n \tag{1.67}$$

with $k_1 = 1.0617$ and $k_2 = -0.0370$ determined through least-squares analysis. The term "average error" as used here (and below) is defined to be

$$\frac{1}{N} \sum_{i=1}^{N} \frac{|y_i^{\text{estimated}} - y_i^{\text{true}}|}{|y_i^{\text{true}}|} \times 100\% \tag{1.68}$$

where y is the dependent variable, and N is the number of observations. The line through the points on Fig. 1-8 is the quadratic least-squares fit. The excellent fit provided by these relationships demonstrates the value of the single scattering approximation and quasi-single scattering approximation: they suggested the relationship between K/c and $1-\omega_0 F$, which provides the dependence on ω_0 and the phase function; and they led the way to D_0, which provides the dependence on the geometric structure of the incident radiance distribution and the sea surface roughness.

It is natural to inquire whether these ideas can be extended to K_d at other depths. We investigate this by applying the ideas used for K to $\langle K \rangle$,

$$\frac{\langle K \rangle}{c} = -\frac{\ln[E_d(z_{10})/E_d(0)]}{z_{10}} = \frac{2.3026}{z_{10}} \tag{1.69}$$

where z_{10} is the depth for which E_d falls to 10% of its value just beneath the surface $[E_d(z_{10})/E_d(0) = 0.1]$. In contrast to K, which is difficult to measure because of the presence of wave-induced light field fluctuations, $\langle K \rangle$ is relatively easy to measure. Fig. 1-9 provides $\langle K \rangle / cD_0$ as a function of $1-\omega_0 F$ for the individual simulations (points). The line is a least-squares fit to

$$\frac{\langle K \rangle}{cD_0} = \sum_{n=1}^{3} \langle k \rangle_n (1 - \omega_0 F)^n \tag{1.70}$$

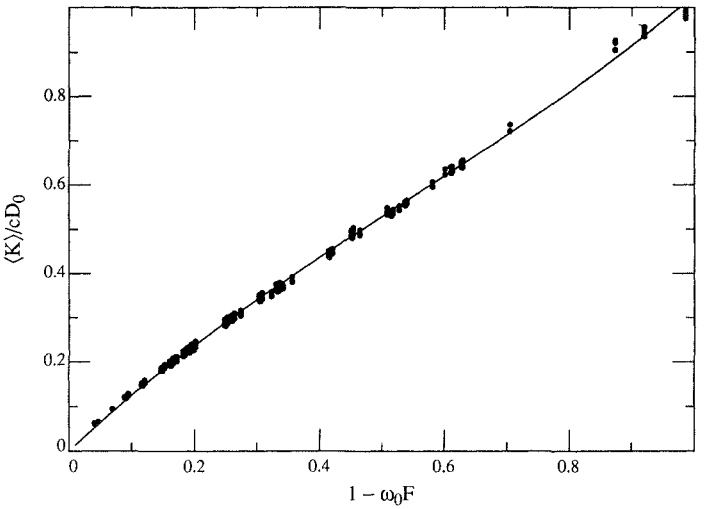

Fig. 1-9. $\langle K \rangle / cD_0$ as a function of $1-\omega_0 F$.(Taken from Gordon 1989b.)

with $\langle k \rangle_1 = 1.3197$, $\langle k \rangle_2 = -0.7559$, and $\langle k \rangle_3 = 0.4655$. The average error in the least-squares fit is 2.2%.

The above analysis shows that, with good accuracy, K/D_0 and $\langle K \rangle / D_0$ can be written as *explicit* algebraic functions of the inherent optical properties c, ω_0 and F (independent of the geometry of the incident light field and surface roughness). In fact, the accuracy is likely better than the accuracy with which K or $\langle K \rangle$ can be measured. Therefore we are justified in regarding the quantities K/D_0 and $\langle K \rangle / D_0$ as inherent optical properties. It should be noted that if the mode of illumination of the ocean never varied, the distinction between the inherent optical properties and the apparent optical properties would blur, i.e., for a given set of inherent optical properties the apparent optical properties would always be the same at a given depth in the water. A particular setting, wherein the (flat) sea surface is illuminated by the sun at the zenith with the atmosphere absent, is unique as far as $K_d(z)$ is concerned. For a given z the value of $K_d(z)$ in this setting is a minimum over all possible modes of illumination (see Fig. 1-6, left-most curve). Thus, it is reasonable to refer to $K_d(z)$ in this situation as the *inherent* irradiance attenuation coefficient and give it the special symbol $K_d^I(z)$. Likewise, K^I and $\langle K \rangle^I$ are the inherent values of K and $\langle K \rangle$, i.e. the values that would be measured in imaginary setting above. The quantities K/D_0 and $\langle K \rangle / D_0$ represent excellent *approximations* to K^I and $\langle K \rangle^I$, that is, the results of measurements in real situations can be transformed to this ideal setting through the simple division by D_0.

An important application of Eqs. (1.66), (1.67), and (1.70) is the examination of the application of the Lambert–Beer law, Eq. (1.20), which holds for all of the standard inherent optical properties, i.e., a, b, c, and β, to the inherent irradiance attenuation coefficients K^I and $\langle K \rangle^I$. Many investigators (Baker and Smith, 1982;

Morel, 1988; Smith and Baker, 1978a, 1978b) have had considerable success in assuming that K_d satisfies a similar equation, i.e.,

$$K_d = K_w + \sum_i K_i = K_w + \sum_i k_i^* C_i \tag{1.71}$$

where K_d is the mean $K_d(z)$ over the euphotic depth or some fraction thereof, K_i is the irradiance attenuation coefficient for the ith component, and k_i^* is the specific irradiance attenuation coefficient for the ith component. K_w is obtained from measurements in very clear ocean water, e.g., the Sargasso Sea. Equation (1.71) has become a standard tool for relating irradiance data to biological activity, and as such it is important to assess its validity for K and $\langle K \rangle$. Since K^I and $\langle K \rangle^I$ are effectively inherent optical properties, it seems natural to test these. In the case of K, the test is simple if Eq. (1.66) is used:

$$\begin{aligned} K^I &= \frac{K}{D_0} = 1.0395(a + b_b) \\ &= 1.0395(a_w + \sum_i a_i^* C_i + (b_b)_w + \sum_i (b_b)_i^* C_i) \\ &= 1.0395(a_w + (b_b)_w) + \sum_i 1.0395(a_i^* + (b_b)_i^*)C_i \\ &= K_w^I + \sum_i (k_i^I)^* C_i = K_w^I + \sum_i K_i^I \end{aligned} \tag{1.72}$$

where, K_w^I and K_i^I are the inherent K's for pure water and for the ith constituent, respectively. $(k_i^I)^*$ is the specific inherent K for the ith constituent. Thus, the linear dependence of K^I on the inherent optical properties suggests that the Lambert–Beer law is valid for this quantity to high accuracy. It also suggests that deviations from Lambert–Beer law must result from a nonlinear dependence of K_d on the inherent optical properties. In the case of $\langle K \rangle$ the relationship between $\langle K \rangle^I$ and the inherent optical properties is clearly not linear (Fig. 1-9). How does this nonlinearity affect the Lambert–Beer law? To analyze this, consider a two-component mixture of water and particles, as in the bio-optical model described earlier. The true value of $\langle K \rangle^I$ for the mixture is easily found to be

$$\frac{\langle K \rangle_T^I}{c} = \frac{\langle K \rangle_T}{cD_0} = \sum_{n=1}^{3} \langle k \rangle_n (1 - \omega_0 F)^n \tag{1.73}$$

where from Eq. (1.50)

$$\omega_0 F = \frac{\omega_p F_p c_p + \omega_w F_w c_w}{c_p + c_w}$$

or

$$1 - \omega_0 F = (1 - \omega_w F_w) \frac{c_w}{c} + (1 - \omega_p F_p) \frac{c_p}{c} \tag{1.74}$$

The $\langle K\rangle^I$ predicted by the Lambert–Beer law for the mixture is

$$\langle K\rangle^I_{LB} = \langle K\rangle^I_w + \langle K\rangle^I_p$$

or (1.75)

$$\frac{\langle K\rangle_{LB}}{cD_0} = \left(\frac{\langle K\rangle_w}{c_wD_0}\right)\frac{c_w}{c} + \left(\frac{\langle K\rangle_p}{c_pD_0}\right)\frac{c_p}{c}$$

where

$$\frac{\langle K\rangle_w}{c_wD_0} = \sum_{n=1}^{3}\langle k\rangle_n(1-\omega_wF_w)^n$$

$$\frac{\langle K\rangle_p}{c_pD_0} = \sum_{n=1}^{3}\langle k\rangle_n(1-\omega_pF_p)^n \qquad (1.76)$$

The interpretation of these relationships is provided in the schematic in Figure 1-10 in which the curvature of the $\langle K\rangle/cD_0$ versus $(1\text{-}\omega_0F)$ relationship (solid curve) has been greatly exaggerated. On the figure the points marked w and p refer to conditions in which the medium consists of only water ($c_p = 0$) and only particles ($c_w = 0$), respectively. Mixing the values of $(1\text{-}\omega_0F)$ for each component yields a value for the mixture indicated by the vertical dotted line. The resulting (true) value of $\langle K\rangle/cD_0$ is that corresponding to the point marked "true" on the $\langle K\rangle/cD_0$ versus $(1\text{-}\omega_0F)$ curve. In contrast, the Lambert–Beer law mixes the values of $\langle K\rangle_w/c_wD_0$ and $\langle K\rangle_p/c_pD_0$ in the same proportion as $(1\text{-}\omega_wF_w)$ and $(1\text{-}\omega_pF_p)$, respectively (compare Eqs. 1.74 and 1.75), and therefore, yields the value corresponding to the point on the (dashed) straight line from w to p marked

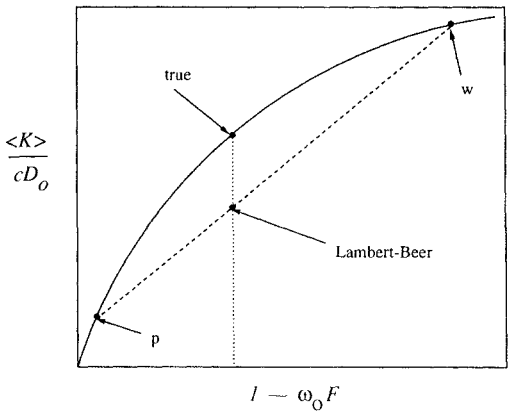

Fig. 1-10. Comparison between the true and the Lambert–Beer values of $\langle K\rangle/cD_0$ for a mixture of water and particles.

"Lambert–Beer." Thus, $\langle K \rangle_{LB}$ is always less than $\langle K \rangle_T$. Using this technique it is easy to estimate the errors in the Lambert–Beer law for any situation. For example, if white sand ($\omega_p \approx 1$) is added to water and the result is examined in the red region of the spectrum ($\omega_w \approx 0$), application of this technique to Fig. 1-9 suggests that the Lambert–Beer law should work rather well until $(1\text{-}\omega_0 F)$ for the mixture becomes ≈ 0.5, or $c_p \approx c_w$. Since c_w is large in the red, this could represent a significant sediment load. This analysis technique also reveals that, in the case of the mixture of water and phytoplankton-detritus utilized earlier, the Lambert–Beer law applied to $\langle K \rangle^I$ should be a better approximation within the strong absorption bands, e.g., 440 nm, than outside them, e.g., 550 nm.

It should be noted that this analysis assumes that the Lambert–Beer law is applied to K^I and $\langle K \rangle^I$. Application to K and $\langle K \rangle$ directly will lead to increased error, however, Table 1-3 shows that D_0 varies from the mean by only ±10% when $\theta_0 \leq 40°$ or the sky is completely overcast. This explains why the Lambert–Beer law has been found to be approximately valid for K_d. Also, note that the fact that K^I and $\langle K \rangle^I$ are inherent optical properties is *not* sufficient to insure the validity of the Lambert–Beer law, i.e., their dependence on the inherent optical properties must be linear as well. Finally, as z increases, and the asymptotic regime is approached, K_d rigorously becomes an inherent optical property (and is independent of D_0); however, the nonlinearity in the K_d/c versus $(1\text{-}\omega_0 F)$ relationship increases with depth (compare Figs. 1-8 and 1-9). Thus, it is to be expected that deviations from the Lambert–Beer law will increase with depth.

Analysis of R(0)

The success of the quasi-single scattering approximation in approximating the reflectance of the ocean (Fig. 1-3) suggests that it may be capable of explaining the dependence of R as a function of θ_0 on the scattering phase function. Indeed, when computations of R as function of θ_0 for several phase functions are compared with the "exact" Monte Carlo simulations for a flat ocean, in the absence of the atmosphere, it is found that the quasi-single scattering approximation (and single scattering approximation) value of $R(\theta_0)/R(\theta_0 = 0)$ agrees with the Monte Carlo value with an error < 5% for $\omega_0 \leq 0.8$ and ≤ 10% for $\omega_0 = 0.9$ (Gordon, 1989a). Furthermore, as in the case of isotropic scattering, the Monte Carlo computations show a near-linear variation of R with μ_{0w}^{-1} (Eq. 1.49) (also seen by Jerome et al., 1988). Thus, the quasi-single scattering approximation (and single scattering approximation) explains the dependence of the R-variation with θ_0 on the phase function with reasonable accuracy. Conversely, it should be possible to retrieve information about the phase function from measurements of the variation of R with θ_0. However, as in the case of K_d, in a realistic ocean the incident light field transmitted through the (rough) air–sea interface depends on, in addition to θ_0, the relative amount of sky light and direct sunlight, and the surface slope variance, σ^2, characterizing the surface roughness. Also, when the sky is totally overcast, there is no dependence on θ_0. Thus a generalization of μ_0 is required to specify the incident radiance distribution. Following the generalization employed with K_d, i.e., replacing Eq. (1.48) by Eq.

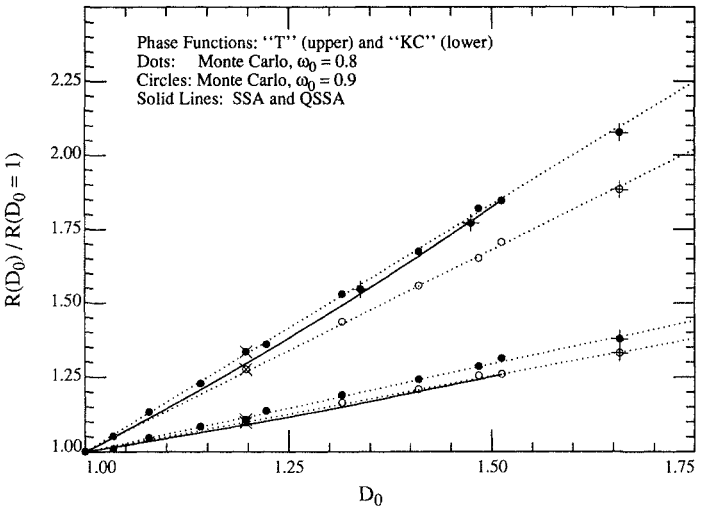

Fig. 1-11. R as a function of D_0. Symbols with +'s are for a rough surface and symbols with x's are for a diffuse incident irradiance. (Taken from Gordon 1989a.)

(1.65), we examine the variation of R with D_0 rather than μ_{0w}^{-1}. This variation is shown in Fig. 1-11, in which Monte Carlo and quasi-single scattering approximation (and single scattering approximation) values of $R(D_0)/R(D_0 = 1)$ are shown as a function of D_0 for two scattering phase functions and two values of ω_0. In the figure, the dots are for $\omega_0 = 0.8$, while the open circles for $\omega_0 = 0.9$. The symbols with +'s are for a rough surface ($V \approx 7.5\,\mathrm{m\,s^{-1}}$) and the symbols with $\times$'s are for a diffuse incident irradiance (overcast sky). The solid curves are the result of the quasi-single scattering approximation (and single scattering approximation) computations for a flat ocean with no atmosphere, for which $D_0 = \mu_{0w}^{-1}$. The bio-optical model is not used here, rather, the phase function is fixed (independently of ω_0) and ω_0 is varied. The phase function is taken to be either T or KC tabulated in Gordon, Brown, and Jacobs (1975) from measurements made by Kullenberg (1968) in the Sargasso Sea. These are shown in Fig. 1-12 below. The upper curve on Fig. 1-11 is for phase function T, while the lower is for KC. Note that the Monte Carlo simulations are linearly related to D_0 with a high degree of accuracy, even when surface roughness and overcast conditions are included. Thus, for a given ω_0,

$$R(D_0) = [m(D_0 - 1) + 1]\,R(1) \tag{1.77}$$

where the slope m depends on just the phase function for $\omega_0 \leq 0.8$, but it depends on both the phase function and ω_0 for $\omega_0 \geq 0.8$. Also, the quasi-single scattering approximation (and single scattering approximation) approximations, found by inserting the actual phase functions into Eq. (1.47) and varying μ_0 (actually

varying μ_{0w}) provide good approximations to the linear relationships, and as such can be used to estimate m given the phase function.

Clearly, m in Eq. (1.77) contains information on the scattering phase function. Can this information be extracted? To perform the extraction, it is convenient to have an analytical approximation to the phase function. For this we choose

$$P(\alpha) = \frac{P(90°)}{(1 - e_f \cos\alpha)^4 (1 + e_b \cos\alpha)^4} \tag{1.78}$$

where e_f and e_b are adjustable parameters. This was first used by Beardsley and Zaneveld (1969) and is excellent for reproducing P for $\alpha \geq 40°$; however, it is a very poor approximation at scattering angles less than 25 - 30° and, for the phase functions in Fig. 1-5 it is in error by a factor of 10^3 or more near 0°. Fortunately, because of refraction at the air-sea interface, Eq. (1.47) does not require $\alpha \leq 40°$. The inversion question is now examined by assuming that $R(\theta_0)$ is measured (in this case Monte Carlo *simulated*) at 10° increments from 0° to 89°. This "data" is then fitted to Eq. (1.47) with $P(\alpha)$ given by Eq. (1.78), using a nonlinear least-squares technique to determine the unknown parameters e_f and e_b. Since this procedure can only yield an estimate of $P(\alpha)/P(90°)$ over the angular range $41° \leq \alpha \leq 180°$, the value of P(90°) must be estimated independently. For reasons that will become evident below, it is required that the inverted and true phase functions have the same value of B, i.e. the same backscattering probability. The resulting retrieved phase functions for $\omega_0 = 0.8$ (solid curves) and 0.9 (dashed curves) are presented in Fig. 1-12. This exercise demonstrates that in this

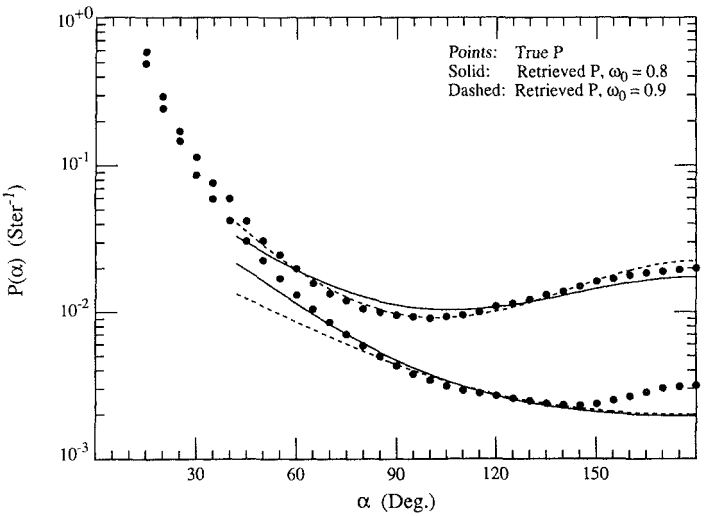

Fig. 1-12. Retrieved phase functions KC (upper) and T (lower) from $R(\theta_0)$ using Eq.(1.47) and Eq. (178). The dots are the true values. The solid and dashed curves are for $\omega_0 = 0.8$ and 0.9, respectively. (Taken from Gordon 1989a.)

restricted case, i.e., measurement of $R(\theta_0)$ for the full domain of θ_0, the absence of an atmosphere, and a flat surface, an estimate of the general shape of $P(\alpha)$ for $60°–70° \leq \alpha \leq 180°$ can be retrieved.

Retrieval of inherent optical properties from K, R, and c

Equation (1.47) for the quasi-single scattering approximation approximation to R involves an integral over the phase function. Given $P(\alpha)$ the integral can be evaluated, and for $\mu_0 = 1$ the values cluster around $0.3B$, i.e.

$$\int_0^{2\pi} d\phi \int_0^1 \frac{\mu}{\mu + 1} P(\alpha)\, d\mu \approx 0.3B \tag{1.79}$$

For example, for phase function T the integral is $0.284B$, for KC it is $0.334B$, and for pure water it is $0.335B$. This suggests that

$$R(\mu_0 = 1) \approx 0.3 \frac{\omega_0 B}{1 - \omega_0 F} \tag{1.80}$$

i.e., that for $\mu_0 = 1$, R depends on the phase function only though B. Indeed, Gordon et al. (1975) found that writing

$$R(\mu_0 = 1) = \sum_{n=1}^{3} r_n \left(\frac{\omega_0 B}{1 - \omega_0 F} \right)^n \tag{1.81}$$

reproduced Monte Carlo simulations with excellent accuracy when the value of the r_n were determined by least-squares. Combining Eq. (1.80) with Eq. (1.65) we have

$$R(\mu_0 = 1) \approx 0.3 \frac{\omega_0 B}{K^l/c} = 0.3 \frac{b_b}{K^l} \tag{1.82}$$

suggesting that it would be useful to write

$$R(\mu_0 = 1) = \sum_{n=1}^{3} r_{K_n} \left(\frac{b_b}{K^l} \right)^n \tag{1.83}$$

or, more usefully,

$$\frac{b_b}{K^l} = \frac{\omega_0 B}{K^l/c} = \sum_{n=1}^{3} r'_{K_n} \left[R(D_0 = 1) \right]^n \tag{1.84}$$

Table 1-4. Expansion coefficients for Eqs. (1.84) and (1.85)

n	k'_{Kn}	r'_{Kn}
1	+0.89670	+2.8264
2	+0.20271	−3.8947
3	−0.13506	−36.232

Source: Gordon (1991).

Similarly, Eq. (1.67) can be inverted:

$$1 - \omega_0 F = \sum_{n=1}^{3} k'_{K_n} \left(\frac{K^I}{c} \right)^n \tag{1.85}$$

The expansion coefficients r_{Kn}' and k_{Kn}' derived from the appropriate simulations are given in Table 1-4. Thus, if measurements of K^I, c, and $R(D_0)$ as a function of D_0 are carried out, $R(D_0 = 1)$ can be estimated by linearly extrapolating $R(D_0)$ to $D_0 = 1$, and Eq. (1.84) can be used to estimate b_b or $\omega_0 B$. ω_0 can then be found from

$$\begin{aligned} \omega_0 &= \omega_0(F + B) \\ &= -(1 - \omega_0 F) + 1 + \omega_0 B \end{aligned} \tag{1.86}$$

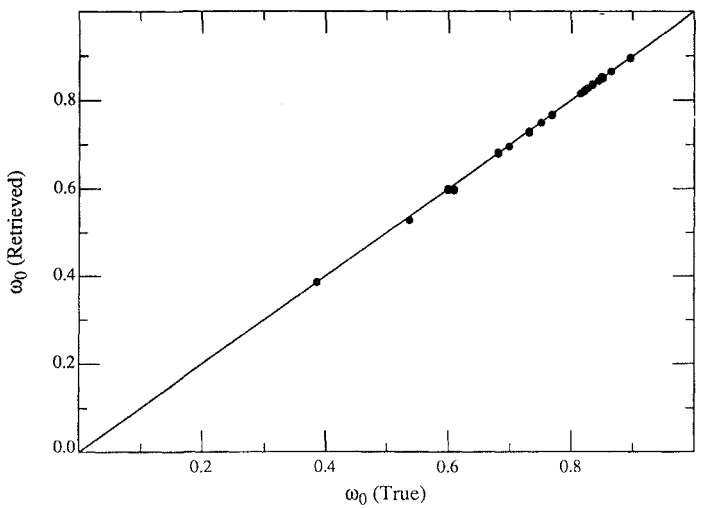

Fig. 1-13. Comparison of retrieved and true ω_0.

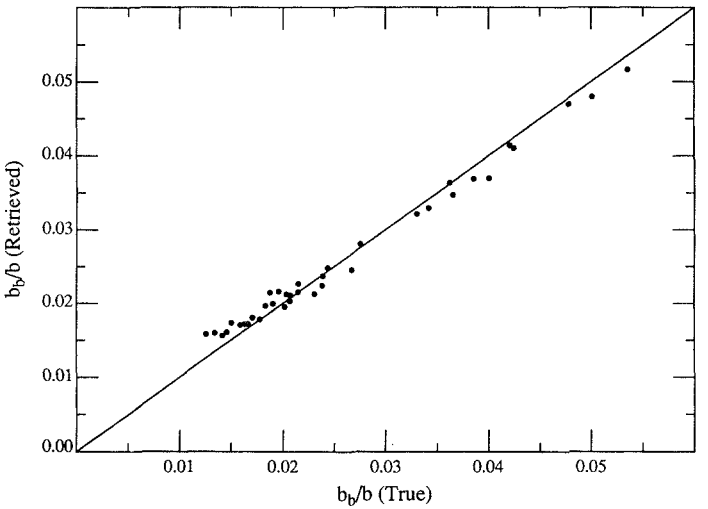

Fig. 1-14. Comparison of retrieved and true B.

($1-\omega_0 F$ is from K^I/c and $\omega_0 B$ is from K^I and R) and B is found from $B = \omega_0 B/\omega_0$. Finally, a and b are found from $b = c\omega_0$ and $a = c - b$. Since $F \approx 1$ for most oceanic situations, the estimation of ω_0 is determined principally by K, while, in contrast, B is determined principally by $R(D_0 = 1)$. Equation (1.85) fits the Monte Carlo simulations far better than Eq. (1.84) (not shown), thus, we expect that this scheme will yield a very accurate estimate of ω_0 and a less accurate estimate of B. It is important to note that if measurements of c are unavailable, then Eq. (1.85) is unavailable and ω_0 cannot be found; however, Eq. (1.84) can still be used to estimate b_b.

I have tested the method derived above for estimating the inherent optical properties for the 42 model oceans in the simulation set described earlier. Briefly, K and $R(D_0)$ were determined from Monte Carlo simulations for the ocean–atmosphere system illuminated with $\theta_0 = 20°$, 40°, and 80° with a flat sea surface. The $R(D_0)$ values were used to find $R(D_0 = 1)$ by extrapolation (Eq. 1.77). K was used with Eq. (1.85) to find $(1-\omega_0 F)$ and combined with $R(D_0 = 1)$ to find $\omega_0 B$ using Eq. (1.84). ω_0 was then determined from Eq. (1.86). Figure 1-13 compares the estimated values of ω_0 with the actual values. The mean error over the 42 model oceans in the estimation of ω_0 was 0.33%. Figure 1-14 compares the estimated with the true values of B. Although the figure covers only the range $0 < B < 0.06$, compared with the full range of possible values from 0 to 0.5 ($c_p = 0$), it does encompass most ocean situations since $B > 0.06$ is very rare in the visible. The mean error in the retrieved value of B is 5.8%. The methods of the previous section can also be used to retrieve the phase function. For low C, the retrievals are excellent; for high C the quality of the retrievals is similar to those for T on Fig. 1-12. For phase functions M and C the high-C

retrievals are much poorer due to the inability of Eq. (1.78) to reproduce the strong maximum in $P(\alpha)$ near $\alpha = 180°$ (Fig. 1-5) for these particle phase functions. For a more complete discussion of this subject, including utilizing $\langle K \rangle$ as well as K, the reader is referred to Gordon (1991).

Equation (1.84) can also be used to shed light on an important question in marine optics mentioned earlier. In the direct problem described earlier, measured values of the inherent optical properties are used to predict the apparent optical properties. However, the inherent optical properties are usually measured at significantly different spatial scales from the apparent optical properties. For example, classical measurements of $\beta(\alpha)$, from which b_b is determined, are usually carried out with sampling volumes $\sim 1\,\text{cm}^3$, while K and R sample volumes of the order of $10–1000\,\text{m}^3$ or larger. Do the classical scattering instruments sufficiently adequately sample the few-in-number larger particles, particularly in clear water, to be useful in the estimation of the apparent optical properties? Equation (1.84) can be used to directly address this question with field measurements.

It should be clear that D_0 has been central to the entire analysis. I have presented a simple technique for estimating this quantity from irradiance measurements above the surface. A complete discussion is provided in Gordon (1989b).

Discussion

In this chapter I have tried to provide a self-contained discussion on modeling and simulation of radiative transfer in the ocean. The obvious goal of the simulation is to provide a solution to the direct problem—derivation of the apparent optical properties from $\beta(\alpha)$ and c for given external variables θ_0 and σ. To do this, the inherent optical properties have been modeled statistically in terms of the pigment concentration which, in Case 1 waters, should be sufficient. This bio-optical model for the inherent optical properties should lead to simulated apparent optical properties that are realistic, at least in a statistical sense. I have used the results of such simulations to test simple models and/or discover new relationships between the inherent optical properties and the apparent optical properties. The simulated "data" are perhaps more valuable than experimental measurements for this purpose because *all* of the variables can be *known* and *controlled*, in the simulation.

The radiative transfer model that we examined here was the very simple single scattering approximation–quasi-single scattering approximation. It was found that the quasi-single scattering approximation provided a reasonable approximation to $K_d(0)$ and $R(0)$ (Figs. 1-3 and 1-4). However, its real importance was in suggesting the parameter groupings $(1 - \omega_0 F)$ and $\omega_0 B/(1 - \omega_0 F)$ as variables for power-series expansions of K_d and R, respectively, in indicating the need to generalize μ_{0w}^{-1} to D_0, and in providing a simple explanation of the variation of $R(0)$ with θ_0 in terms of the volume scattering function. This led to much more precise (and general) relationships between K, $\langle K \rangle$, R, and the inherent optical

properties. These new models, in turn, provide a means of effecting a partial solution of the inverse problem–estimating a, b, b_b, and $\beta(\alpha)$ from near-surface measurements of the apparent optical properties and c. They also furnished an explanation of the success of the Lambert–Beer law when applied to the near-surface K_d, provided a simple graphical means of estimating the error in the Lambert–Beer law in given situations, and suggested that the law will become less useful at larger values of z. Finally, they provided a *direct* relationship between an inherent optical property and the apparent optical properties, Eq. (1.84), that can be used to estimate the efficacy of classical measurements of the inherent optical properties in providing quantities of sufficient accuracy to determine the apparent optical properties.

It is important to note that *inelastic* processes such as Raman scattering (Marshall and Smith, 1990; Stavn and Weidemann, 1988b, and Chapter 12 this volume) and solar-induced fluorescence (Gordon, 1979; Chapters 6, 8, 9, and 10 this volume) have been ignored in this work, and therefore, the conclusions reached are valid only when such processes make a negligible contribution to the apparent optical properties near the sea surface. Although these processes are likely to have a negligible affect on K and $\langle K \rangle$, they can significantly increase R, e.g., the chlorophyll a fluorescence at ~685 nm. The polarization property of light has also been ignored in this analysis (see Chapter 11 this volume). Investigations of the importance of polarization have been carried out in optically thick atmospheres. Kattawar et al. (1976) found that for Rayleigh scattering atmospheres the neglect of polarization could lead to significant errors in the radiance (~25%), while for atmospheres with a strongly forward scattering phase function only a small error in the radiance (~0.1%) was incurred. Also, Kattawar (1990) found that in the case of a Rayleigh scattering atmosphere, even though there can be considerable errors incurred in the radiance by neglecting polarization, there is *no* error in the irradiances. Since this chapter centered on irradiance, I believe that the neglect of polarization will not result in significant error. Finally, the ocean has been assumed to be homogeneous. This is reasonable in the mixed layer and the results should be applicable there; however, it should be recognized that application of the equations involving R also requires homogeneity from the surface to a depth $\approx 1/K_d$ (Gordon and Clark, 1980).

Acknowledgment

This work received support from the Office of Naval Research under Contract N00014-84-K-0451 and Grant N00014-89-J-1985, and from the National Aeronautics and Space Administration under Grant NAGW-273.

2

THE RELATIONSHIP BETWEEN THE INHERENT AND THE APPARENT OPTICAL PROPERTIES OF SURFACE WATERS AND ITS DEPENDENCE ON THE SHAPE OF THE VOLUME SCATTERING FUNCTION

John T.O. Kirk
CSIRO Division of Plant Industry, Canberra, Australia

Introduction

Let us begin by reminding ourselves just what we mean by "the inherent optical properties" and "the apparent optical properties" of surface waters. The inherent optical properties are those that belong to the aquatic medium itself: properties that belong to a small sample of the aquatic medium taken out of the water body just as much as they belong to a great mass of the medium existing within the water body itself. The properties of particular concern to us are the absorption coefficient, a, the scattering coefficient, b, and the volume scattering function, $\beta(\theta)$.

The absorption coefficient at a given wavelength is a measure of the intensity with which the medium absorbs light from a parallel beam per unit pathlength of medium (see Eq. 1.18). The scattering coefficient at a given wavelength is a measure of the intensity with which the medium scatters light from a parallel beam per unit pathlength of medium (see Eq. 1.17). Both a and b have the units, m^{-1}. The normalized volume scattering function specifies the angular (θ) distribution of single-event scattering around the direction of a parallel incident beam. It is often normalized to total scattering and referred to as the *scattering phase function*, $P(\theta)$ (see Eq. 1.21).

Since these properties belong, as I have already said, to a small sample of the medium, just as much as they do to a great slab of ocean, they can be measured in the laboratory. The absorption coefficients at various wavelengths can be measured with a suitable spectrophotometer: the scattering coefficient and the volume scattering function can be measured with a light scattering photometer.

The apparent optical properties are not properties of the aquatic medium as such although they are closely dependent on the nature of the aquatic medium. In reality they are properties of the light field that, under the incident solar radiation stream, is established within the water body. The particular properties

in this class of present concern to us are the vertical attenuation coefficient for downward irradiance, K_d (see Eq. 1.12), which is of course a measure of the rate at which the downward flux of light in a particular waveband diminishes per unit vertical distance downwards; and the irradiance reflectance, R, sometimes called the irradiance ratio, which is the ratio at any specified depth of the upward irradiance, E_u, to the downward irradiance, E_d (see Eq. 1.7). K_d, like a and b, has units of m^{-1}; R is a dimensionless ratio.

These and other apparent optical properties are inseparable from the water body itself. They cannot be measured on samples. The light field set up within a small aliquot taken out of the ocean is quite different from that existing within the ocean itself, even at the surface, because that small sample while it is still present within the ocean receives not only the downward solar flux, but also light coming from all directions, and from a range of distances within the water body, as a result of scattering within the water body.

Nevertheless, although, as I have emphasized, the apparent optical properties are properties of the total light field set up within the water body, the actual values they take up are largely determined by the inherent optical properties of the aquatic medium, and are not very much altered by changes in the incident radiation field such as a change in the solar elevation or in cloud cover (see Chapter 1). We can say for example that a particular location in the sea, or a particular lake, has a certain K_d or R value for some specified waveband, and this statement will remain approximately valid, independent of the time of day or the weather conditions, so long as the composition of the water (and therefore the inherent optical properties) remain about the same.

It was in recognition of this useful aspect of field properties such as K_d and R, that the late Rudolf Preisendorfer suggested many years ago that they be referred to as apparent optical properties. For many purposes, he was implying, we can treat them as though they are properties of the water. And when limnologists or oceanographers say, for example, that this lake has a high K_d, or that oceanic water mass has a low K_d, or that a certain turbid estuary has a high reflectance, this is exactly what they are doing.

The apparent optical properties of a water body are the resultant, the product, of the interaction between the incident solar flux and the inherent optical properties of the water. For a given incident solar radiation field – a particular solar altitude, a certain angular distribution of the diffuse sky light – the apparent optical properties are entirely determined by the inherent optical properties of the water. This naturally leads us to the question. In precisely what way are they so determined? What is the actual nature of the relationship between the apparent and the inherent optical properties? Or, to put it another way, what mathematical form do our hypothesized relationships

$$\begin{aligned} K_d &= f_1\,[a,\, b,\, \beta(\theta)] \\ R &= f_2\,[\mathrm{a},\, b,\, \beta(\theta)] \end{aligned} \tag{2.1}$$

take?

Why is this question worth addressing? First of all, to anyone interested in the physics of underwater radiation transfer, this is an important question in its own right. Physics, after all, essentially consists of seeking explanations of observed phenomena in terms of the underlying, more fundamental, physical laws. And if we can quantitatively describe in mathematical form the manner in which the inherent optical properties determine the light field, and thus the apparent optical properties, then we have advanced our understanding of the physics of the system.

Secondly, the question is of considerable practical importance because answering it would greatly increase our predictive capability. It would enable us to proceed from any anticipated change in the composition of the water to the consequent change in the apparent optical properties, and thus in the underwater light field available for photosynthesis or visibility, or in the emergent light flux, which is used for remote sensing. The reason why knowledge of these relationships would enable us to make such predictions is that the value of an inherent optical property, such as the absorption or the scattering coefficient, due to a particular component of the medium, is linearly related to the concentration of that component. Thus from the anticipated changes in the concentrations of various components of the medium, we can calculate from the values of the specific absorption coefficient and specific scattering coefficient what the new values of total absorption and scattering coefficients in various wavebands are. And then using whatever relationships we have found to exist between inherent and apparent optical properties we can determine how the apparent optical properties, and hence the light field, change.

Now it might be argued that really all we need is an empirical relationship between the concentration of a given component and the value of the apparent optical property of interest. In the case of K_d, the vertical attenuation coefficient for irradiance, perhaps all we need is the average increase in K_d for the waveband of interest per unit increase in concentration of any given component. We might, for example, use k_c, the average increase in vertical attenuation coefficient for the photosynthetic waveband per mg phytoplankton chlorophyll per cubic meter. To a first approximation this is indeed often a useful approach. There are problems with it, however. The first is that we may not have the empirical relationship we need. While we may have one for phytoplankton, we probably will not have one for any other component of the medium.

The second problem is that an apparent optical property such as K_d need not increase linearly with the concentration of any particular component, and furthermore this approach will be even less accurate when more than one component of the system is changing, and not necessarily in the same direction. This simple empirical approach would, for example, yield particularly inaccurate predictions if there were simultaneous changes in two components, one of which contributed mainly to absorption and the other mainly to scattering. Working at the more fundamental level of the inherent optical properties, and calculating from these (assuming we are in possession of the appropriate relationships) the associated apparent properties, circumvents these problems.

The ecosystem processes for which we might use this anticipated predictive capability might be of a natural or an unnatural kind. A phytoplankton ecologist might, for example, wish to calculate in what way the underwater light climate might be changed by a bloom of a particular algal species, or by seasonal changes in dissolved humic color in river water entering the ecosystem. Alternatively, and this is already of immediate practical concern in many places around the globe, an environmental protection authority or an industrial water user may wish to know in advance what effect a particular effluent would have on the light field, as specified through the apparent optical properties, in a surface water body to which the effluent may be discharged.

Let me give the reader as an example the waste water discharge from a particular power station in Australia. The waste water combines water from cooling tower purges, power station site drainage, and runoff from the overburden dump—the overburden being that layer of soil and rock that has to be removed to get at the coal in the open-cast coal mine that supplies the power station. The water is passed through settling ponds and a flocculating agent is added to promote settling of the particles. The final effluent is discharged to a creek. The water above the discharge point is reasonably clear, and the optical water quality is quite good. Despite the treatment it has had, the settling pond discharge is much more turbid and colored than the creek water, and below the discharge point the optical character of the creek is completely altered—it is now very turbid and colored.

The next example is an outfall from which the effluent from the sewage treatment works of a town in New South Wales is discharged to the ocean. This is not raw sewage—it has had secondary treatment—but the waste water is colored, and imparts color to the ocean water in the vicinity of the outfall.

In cases such as these, industrial water users can measure the inherent optical properties of their effluent and, of course, of the receiving water. They can readily calculate for any given dilution, the resultant inherent optical properties of the receiving water body with the effluent mixed in. Thus, if they have a relationship between the inherent and apparent optical properties they can proceed to calculate how environmentally relevant parameters, such as the K_d for the photosynthetic waveband, will be altered. And if, for example, the relevant environmental agency had specified that penetration of the photosynthetic waveband should not be diminished by, let us say, more than 10%, then the effluent discharger will be able to determine the values of the inherent optical properties of his effluent that should not be exceeded if he is to meet this standard.

So, the kinds of relationships we are talking about are not only scientifically interesting but are also powerful tools to assist us in minimizing the unavoidable impact of human activity on the environment.

Deriving relationships by modeling

Having discussed at some length why it would be desirable to know the relationships between the inherent and apparent optical properties, let us now go on to consider how such relationships might be arrived at.

One approach that is possible in theory but difficult in practice is to actually set up working models, i.e., to establish artificial bodies of water, to control the composition of the water in such a way as to achieve particular values of absorption coefficient and scattering coefficient, and then measure the characteristics of the light field existing within the water body under a natural or an artificial light field. By systematically varying the inherent optical properties of the water, and measuring the consequent changes in the apparent optical properties expressed within the water body, one might hope to arrive at the desired relationships.

The problem with this approach would be that of scale, of avoiding boundary effects, of ensuring that the light field within the artificial water body did correspond to that in a similar slab of water in a real water body. The criterion would be that the vertical and horizontal dimensions of the artificial water body should be substantially greater than the length scale within which most of the attenuation is taking place. For clear colorless marine waters, the working model would have to be impractically large. For some of the more highly colored and turbid inland waters, however, a realistic working model might not be beyond the bounds of possibility.

Of course, if you deliberately make the absorption and/or scattering very high indeed then you can have a water body that is effectively of infinite optical depth while being of a size that will fit inside the laboratory. Timofeeva in Russia, in fact, carried out many studies of the light field established within laboratory systems of this type (Timofeeva, 1974), and arrived at a number of interesting relationships, but not, as it happens, the ones we are specifically seeking today.

An alternative to setting up artificial water bodies is to carry out numerous measurements, of both inherent and apparent optical properties, in existing water bodies, and hope that over time you accumulate enough data to make a search for relationships feasible. This would, however, be vastly time-consuming, as well as expensive, and there is no guarantee that you would ever encounter some of the more extreme optical situations, the ones that are most likely to reveal the underlying relationships. No one, to my knowledge, has taken this path.

Given that the real world presents well-nigh insuperable problems, our only remaining hope is to retreat to the unreal world: that is to say, to develop mathematical models of imaginary, idealized water bodies, and see what properties they exhibit. There are various ways of achieving this, but conceptually the simplest is the Monte Carlo method (see Chapter 1). This approach has been used a great deal in nuclear physics: its application to underwater light fields was pioneered by Kattawar and Plass, and by Howard Gordon and coworkers (Plass and Kattawar, 1972; Gordon et al., 1975).

In the Monte Carlo method the computer follows the fate of a large number of photons, one at a time, passing into an imaginary body of water of specified inherent optical properties. The values of the inherent optical properties determine the probabilities of the various things that can happen to the photons, so that with the use of random numbers and appropriate cumulative frequency

distributions, each photon can be followed throughout its lifetime in the water body. Then, from the behavior of all the photons—say a million of them in a typical simulation—a complete picture of the underwater radiation field can be arrived at.

From the underwater field thus calculated, the apparent optical properties that are of interest—say the K_d value, or the reflectance—can readily be extracted. We can systematically vary the values of the inherent optical properties of the water, that are used as inputs for the calculation—the absorption coefficient, for example, or the scattering coefficient. From the manner in which the apparent optical properties behave in response to the changing values of the inherent optical properties, we may then hope to discern the nature of the dependence of the former on the latter: in short, to arrive at the relationships we have been seeking.

Some years ago I carried out a study of this type. It was meant to apply to the kinds of waters that I am most concerned with, namely, inland waters, estuarine, and coastal waters. One of the choices that has to be made is what scattering phase function, or normalized volume scattering function, to use in the calculation. All the waters I have to deal with are moderately to very turbid, and scattering is dominated by particles: the density-fluctuation scattering of pure molecular water makes no significant contribution.

Volume scattering functions for waters in which scattering is particle-dominated have a strong family likeness in respect to their shape. Most of the scattering is within a few degrees of the forward direction. There is in the region of 1–2% backscattering.

Calculations carried out with a single $\beta(\theta)$ data set, reasonably typical for waters of this type, should therefore yield results of wide applicability to water bodies of moderate to high turbidity such as those of interest to me. Accordingly, for all that original set of calculations I chose to use the normalized volume scattering function data that Theodore Petzold, of the Visibility Laboratory of the Scripps Institution, obtained at the beginning of the 1970s for what he called the "very turbid" but that I would describe as only moderately turbid waters of San Diego Harbor (Petzold, 1972).

From these calculations, by varying the inherent optical properties as I have described, determining the consequent apparent optical properties from the characteristics of the simulated light field, and seeking to fit the data to various mathematical forms, I eventually found (Kirk 1981a,b, 1984a) that the dependence of K_d, the vertical attenuation coefficient for downward irradiance, on the absorption and scattering coefficients is very well described by the equation

$$K_d = \frac{1}{\mu_0} [a^2 + G(\mu_0)\, ab]^{1/2} \tag{2.2}$$

where μ_0 is the cosine of the refracted solar photons just beneath the surface.

$G(\mu_0)$ may be regarded as a coefficient determining the relative contribution of scattering to vertical attenuation of irradiance. It is a linear function of μ_0 in accordance with

$$G(\mu_0) = g_1\mu_0 - g_2 \tag{2.3}$$

The particular values of g_1 and g_2 are slightly different according to whether we are talking about K_d(av), the average K_d over the whole euphotic zone, i.e., the average from the surface down to the 1% light level, or about K_d (z_m), the localized value that K_d has at depth z_m, the mid-point of the euphotic zone. The two corresponding forms of Eq. (2.2) are

$$K_d(\text{av}) = \frac{1}{\mu_0}[a^2 + (0.425\ \mu_0 - 0.190)ab]^{1/2} \tag{2.4}$$

and

$$K_d(z_m) = \frac{1}{\mu_0}[a^2 + (0.473\ \mu_0 - 0.218)\ ab]^{1/2} \tag{2.5}$$

To make them of greater generality, the equations can all be rearranged so that they express the ratio of the vertical attenuation coefficient to the absorption coefficient,K_d/a, as a function of b/a, the ratio of the scattering to the absorption coefficient e.g.,

$$\frac{K_d}{a} = \frac{1}{\mu_0}\left(1 + G(\mu_0)\ \frac{b}{a}\right)^{1/2} \tag{2.6}$$

Figure 2-1 shows how accurately these equations describe the relationship between K_d and a and b. The points are the K_d/a values arising directly out of the Monte Carlo simulations. The curves are calculated from the equation. Over a wide range of b/a values and solar zenith angles, the agreement is very good.

Now that we have arrived at an explicit relationship between the apparent optical property of interest to us, namely K_d, and the inherent optical properties that determine it, then for any given situation, where we have a particular value of a and a particular value of b, while we can still run a complete Monte Carlo simulation of the field if we want to, it is no longer necessary if we only need the K_d value. We simply substitute the appropriate values of a, b and μ_0 into the equation.

This equation, or set of equations, applies to monochromatic light. For real-world applications we are often more interested in the attenuation of broad bands of radiation, such as for example the photosynthetic waveband, 400–700 nm. This presents no problem. A simple desk computer program can carry out the calculation sequentially for a series of narrow wavebands, and combine the results to calculate vertical attenuation of the whole photosynthetic, or other, waveband (Kirk, 1984b).

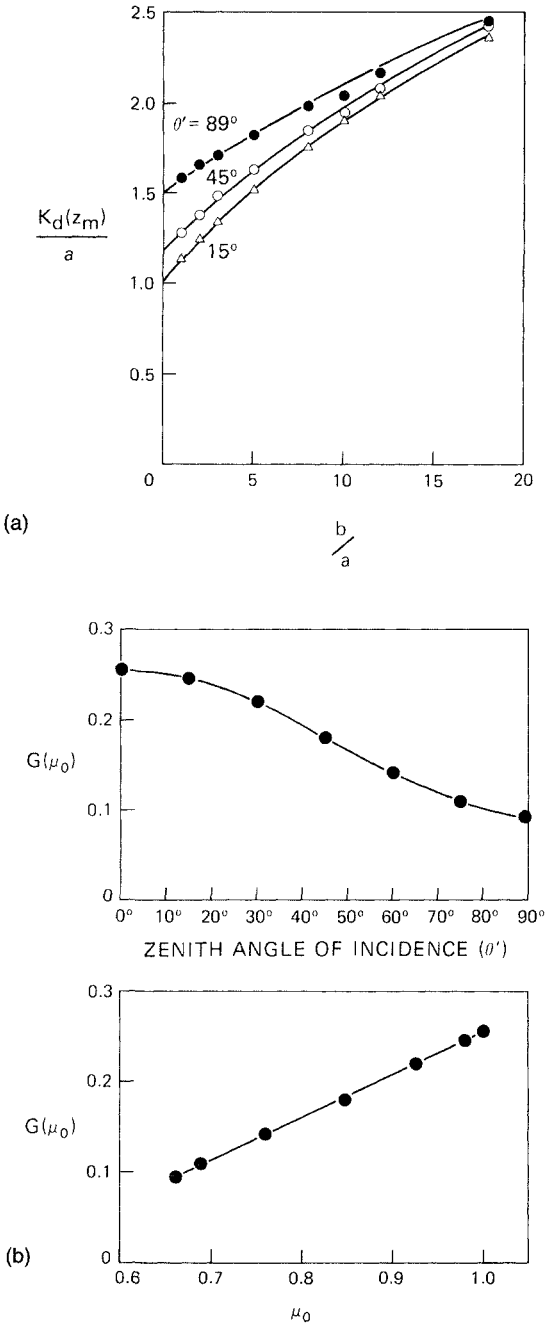

Fig. 2-1. (a) Ratio of vertical attenuation coefficient to absorption coefficient as a function of b/a at different angles of incidence. The zenith angle of the incident flux above the surface is indicated next to each curve. The points are the values obtained in Monte Carlo simulations; the curves were calculated using Eq. (2.6). (b) Variation of the coefficient $G(\mu_0)$ with (upper) zenith angle of incidence, and (lower) cosine (μ_0) of the incident photons after refraction at the surface.

Handled in this way the equation can readily be used, either as a tool for ecological investigation or for dealing with practical problems of optical water quality. For example, returning again to the problem of the effects of waste water discharge on optical water quality in the receiving water body, an industrial water user who has measured the absorption and scattering properties of his effluent and of the receiving water can readily, using this simple computer program, predict the effect of the effluent, at any anticipated dilution, on the penetration of solar radiation in the water body. I have in fact carried out such calculations for industrial water users in Australia.

The other apparent optical property that is of present concern to us is the irradiance reflectance. Howard Gordon and coworkers in their 1975 Monte Carlo study were able to fit the results to a polynomial function of the absorption coefficient, and the backscattering coefficient, b_b, which, by ignoring all terms other than the dominant first one, can be simplified to (cf. Eq. 1.47)

$$R(0) = C \frac{b_b}{a + b_b} \tag{2.7}$$

where, for zenith sun, the coefficient C has the value 0.32 (Gordon et al., 1975; Gordon and Morel, 1983). Since b_b is usually much smaller than a, this can be further simplified to

$$R(0) \approx C \frac{b_b}{a} \tag{2.8}$$

By a different computer modeling procedure, Louis Prieur (1976), in André Morel's laboratory, arrived at the same relationship, with C having the value 0.33.

The coefficient C is a function of solar altitude, and in my own Monte Carlo studies I found that it could reasonably well be expressed as a linear function of μ_0, the cosine of the zenith angle of the refracted photons:

$$C(\mu_0) = -0.629\mu_0 + 0.975 \tag{2.9}$$

As the equation implies, and Fig. 2-2 shows, reflectance decreases as the solar altitude increases. For zenith sun, this relationship predicts that $C = 0.346$, in reasonable agreement with other workers' values.

The existence of a relationship between reflectance and inherent optical properties is useful in two ways. On the one hand it makes it possible to predict the effect of a waste water discharge on the reflectance of the receiving water body. The relevance of this is that the reflectance of a water body strongly influences our perception of the aesthetic quality of that water body. We have learnt to associate high reflectance with muddy, turbid waters. Thus, here we have a tool for the management of another aspect of environmental quality.

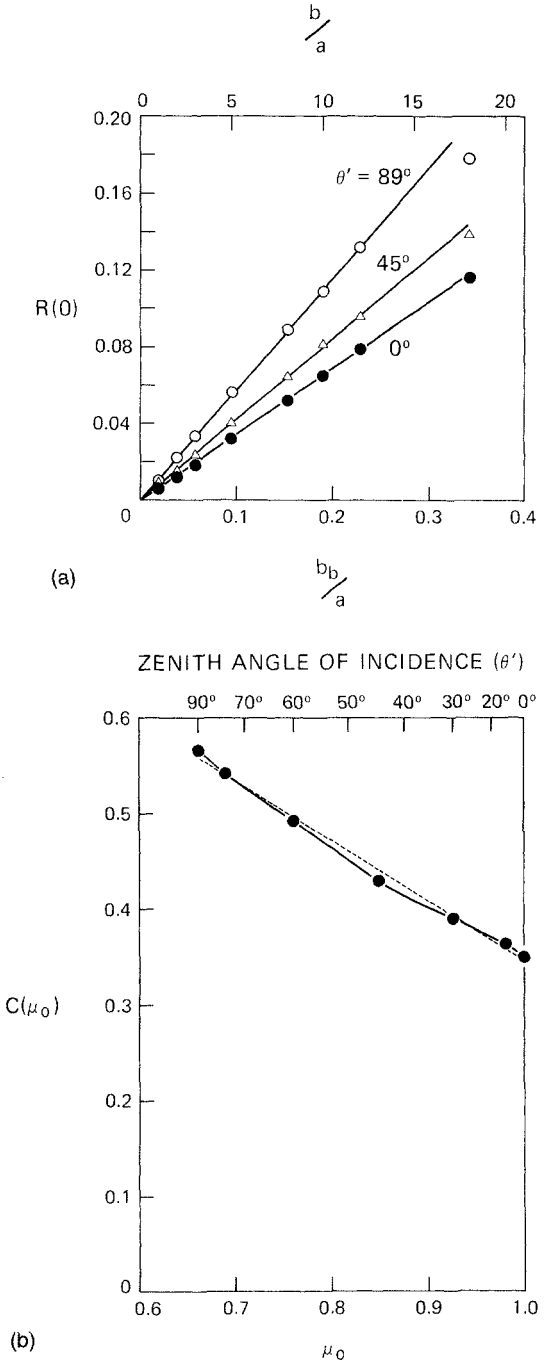

Fig. 2-2. (a) Linear relationship between irradiance reflectance and the ratio of the backscattering (b_b) to the absorption (a) coefficient at three different zenith angles of incidence. (b) Variation of the coefficient $C(\mu_0)$ with zenith angle of incidence and with the cosine (μ_0) of the refracted photons.

The other way in which a relationship between reflectance and inherent optical properties is useful, of course, is that if we measure the reflectance, whether by remote sensing or, for that matter, sea-level sensing, we can derive information about the inherent optical properties, and hence about the water composition. But this is a large and important topic in its own right that other contributors will no doubt address, and that I shall not pursue further here.

Variation in the shape of the volume scattering function and its consequences

All my Monte Carlo modeling of the underwater light field that I have described so far was carried out, as I made clear, using the normalized volume scattering function obtained by Petzold for the moderately turbid water of San Diego Harbor. This was, as the reader will recall, with the intention of making the results applicable to the kind of waters that I mainly have to deal with.

However, once you get away from the inland, estuarine, and coastal waters, into the clear waters of the ocean proper, where light scattering by particles, in some regions at least, diminishes to the point that scattering by water itself contributes significantly to the total, then the shape of the volume scattering function does begin to differ noticeably from that of particle-dominated waters such as those of San Diego Harbour. Partly because of the need to establish relationships applicable to these oceanic waters, but also because of its intrinsic theoretical interest, I have now carried out a systematic exploration of the effects of changes in the shape of the volume scattering function on the relationships between the inherent and apparent optical properties.

As the source of the scattering data I have used virtually the complete set of measurements published by Petzold (1972) for a range of water types, of which San Diego Harbor happened to be the most turbid. There are 12 different waters altogether, and these are listed, together with some of the optical characteristics, in Table2-1. The reader need not worry about most of this data for the present. Looking at the first two columns the reader will get some idea of the kinds of water involved.

They include two moderately turbid seawaters, with scattering coefficients in excess of $1.0\,m^{-1}$; two waters that we might describe as being from the continental shelf, with scattering coefficients between 0.2 and $0.3\,m^{-1}$; and three oceanic type waters with scattering coefficients approximately in the $0.04–0.1\,m^{-1}$ range. In addition, to widen the range of water optical types, Petzold used both fresh water and seawater, treated in various ways. A fresh water sample was filtered until its scattering coefficient was reduced all the way down to $0.009\,m^{-1}$. To some of this he added colorless scattering particles to raise its scattering coefficient to about $0.5\,m^{-1}$. The seawater sample, initially moderately turbid, he subjected to three different periods of continued filtration, reducing its scattering coefficient progressively to 0.4, 0.08, and $0.008\,m^{-1}$.

We thus have here waters that cover an approximately 200-fold range of scattering intensity, but which, more importantly, include waters with such low levels of particle scattering that scattering by water itself contributes substantially

Table 2-1. Light scattering characteristics of the different water types

Water Type	Scattering coefficient[a] $b(m^{-1})$	Backscattering ratio[a] b_b/b	Average cosine of scattering $\bar{\mu}_s$	Coefficient determining contribution of scattering to attenuation, $\bar{G}(1.0)$
1. San Diego Harbor	1.54 (av)	0.019	0.922	0.231
2. Bahama Islands (Sta. no. 7)	0.117	0.025	0.915	0.235
3. Bahama Islands (Sta. no. 8)	0.037	0.044	0.867	0.341
4. Bahama Islands (Sta. no. 9)	0.043	0.038	0.885	0.309
5. Offshore, S. California (Sta. no. 5)	0.275	0.014	0.947	0.157
6. Offshore, S. California (Sta. no. 11)	0.219	0.013	0.947	0.160
7. Filtered fresh water	0.009	0.119	0.726	0.671
8. Filtered fresh water + $Al(OH)_3/Mg(OH)_2$ (scattering)	0.547	0.018	0.926	0.221
9. Seawater	1.284	0.015	0.929	0.200
10. Seawater, filtered 40 min	0.407	0.017	0.931	0.206
11. Seawater, filtered 1 hr 40 min	0.081	0.025	0.918	0.225
12. Seawater, filtered 18 h	0.008	0.146	0.660	0.851

[a]Taken from the data of Petzold (1972).
[b]Calculated from the volume scattering function as described in Kirk (1991).

to the total and markedly influences the shape of the volume scattering function. As one indication of the change in shape of the volume scattering function, consider the backscattering ratio, which is the proportion of the total scattering that occurs at angles greater than 90°. Note that all those waters with scattering coefficients in excess of $0.2\,m^{-1}$ have backscattering ratios in the range 0.013–0.019, i.e., they have 1–2% backscattering. Once the scattering coefficient falls below $0.2\,m^{-1}$ the backscattering ratio begins to rise, eventually reaching about 12% and 15% in the highly filtered fresh water, and seawaters, respectively. This is an indication of the increased contribution of density fluctuation scattering by water itself, for which the backscattering ratio is 50% (Morel, 1974).

Dependence of K_d on a and b in waters of different scattering function

With the help of Petzold's measurements, let us now turn our attention to the possible effect of changes in the shape of the scattering function on the relationship between inherent and apparent optical properties. The first question to be addressed is: Does the dependence of K_d on the absorption and scattering

coefficients, specified in Eq. (2.2), apply in waters of widely varying normalized volume scattering function? Note that we are talking here primarily about the form of this relationship: the value of the coefficient $G(\mu_0)$, is a separate matter to which we shall return later.

To answer this question I have used the rearranged, more general, form of the equation, namely, Eq. (2.6) which expresses the ratio of K_d to a as a function of the ratio of b to a. For simplicity I here confine my attention to vertically incident light, that is, for $\mu_0 = 1.0$. For any given pair of values of a and b, and the value of K_d arising from the Monte Carlo simulation, we obtain the corresponding value of the coefficient $G(\mu_0)$ [which we indicate by $G(1.0)$ since $\mu_0 = 1.0$] using the inverted form of Eq. (2.6)

$$G(1.0) = \frac{a}{b}\left[\left(\frac{K_d \mu_0}{a}\right)^2 - 1\right] \tag{2.10}$$

The average value of $G(1.0)$ for any given water we obtain from a series of seven computer runs, all with the scattering phase function appropriate for that water, and covering the range $b/a = 1$ to 18. This average value of $G(1.0)$,

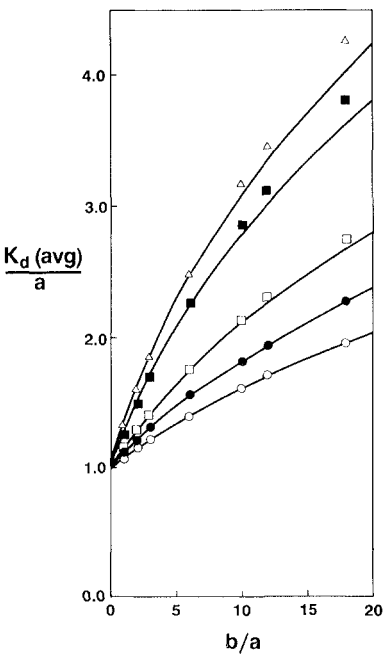

Fig. 2-3. Ratio of vertical attenuation coefficient to absorption coefficient as a function of *b/a* for five different water types. The light is vertically incident. From the top downward the waters are: seawater, filtered 18 h △); filtered fresh water (■); Bahama Islands, station 8 (□); San Diego harbor (●); offshore S. California, station 11 (○). The points arise directly from the Monte Carlo calculations; the curves are calculated using Eq. (2.6).

corresponding to that particular scattering function, we indicate by $\bar{G}(1.0)$. The values of this coefficient for the different waters are listed in Table 2-1, and you can see that they vary quite strongly from one scattering function to another. The reason for this is a matter we shall return to later.

The question now is: If we put this average value of $G(1.0)$ into Eq. (2.6) how well does this predict the variation of K_d/a as a function of b/a? Figure 2-3 shows the results for 5 of the 12 water types, chosen so as to span, at appropriate intervals, the complete range of variation in shape of the volume scattering function. The points are the K_d/a values arising directly out of the Monte Carlo simulations. The lines are the theoretical curves obtained from Eq. (2.6), using our best estimate of G, derived in the manner I have just indicated.

As you can see, the values of K_d derived from Monte Carlo modeling lie close to the corresponding theoretical curves, indicating that our equation is a reasonable representation of the relationship between K_d, b, and a for a range of waters varying widely in the shape of their volume scattering function – more widely, in fact, than would be encountered in nature.

For the two least "natural" waters – with particle scattering greatly reduced by filtration and consequently greatly increased backscattering and wide-angle scattering – the equation somewhat underpredicts the values of K_d/a at high b/a ratios, but the errors are not more than about 5%.

The data I have presented so far apply only to vertically incident light, but Eq. (2.2) predicts a dependence of K_d also on the angle of the incident light, expressed in terms of μ_0, the cosine of the refracted solar beam beneath the surface. In addition to the dependence of K_d on the reciprocal of μ_0, the coefficient $G(\mu_0)$ increases linearly with μ_0 in accordance with Eq. (2.3). These equations were arrived at by calculations for the San Diego water. We must

Table 2-2. Values of the coefficients g_1 and g_2 in Eq. (2.3) for the different water types, determined by linear regression of $\bar{G}(\mu_0)$ against μ_0

Water type[a]	g_1	g_2
1	0.425	0.190
2	0.412	0.173
3	0.580	0.230
4	0.539	0.222
5	0.292	0.133
6	0.308	0.144
7	1.018	0.337
8	0.432	0.203
9	0.382	0.177
10	0.391	0.181
11	0.407	0.176
12	1.329	0.459

[a]As listed in Table 2-1.

Table 2-3. Tests of the applicability of Eq. (2.2). Compared here for three of the different water types are the values of K_d(av) (m^{-1}) arising directly out of the Monte Carlo simulation with those calculated by substitution of the corresponding values of μ_0 and $\bar{G}(\mu_0)$ into Eq. (2.2). In every case $b/a = 6$

Water Type		Bahama Islands Sta. no. 9		Offshore, S. Calif. Sta. no. 11		Seawater, filtered 18 h	
Zenith angle of incident light (degrees)	μ_0	K_d (av) Monte Carlo	K_d (av) Eq. (2.2)	K_d (av) Monte Carlo	K_d (av) Eq. (2.2)	K_d (av) Monte Carlo	K_d (av) Eq. (2.2)
0	1	1.703	1.704	1.406	1.409	2.493	2.494
15	.981	1.708	1.718	1.419	1.423	2.509	2.511
30	.927	1.767	1.762	1.470	1.468	2.562	2.561
45	.848	1.837	1.831	1.550	1.538	2.646	2.639
60	.760	1.933	1.919	1.640	1.633	2.732	2.730
75	.689	1.993	1.997	1.725	1.722	2.813	2.808
89	.661	2.020	2.032	1.747	1.764	2.826	2.836

therefore ask if a similar dependence on μ_0 holds for these other waters with their different scattering phase functions.

The answer is that it does. I shall not burden the reader with the details of the calculations. Suffice it to say that Eqs. (2.2) and (2.3) apply to all the waters, with respect to variation in μ_0 as well as a and b. The actual values of the constants g_1 and g_2 in Eq. (2.3) do vary as the normalized volume scattering function varies. Table 2-2 lists the values of g_1 and g_2 for all 12 water types, but we need not dwell on these data.

As a final check on the general applicability of Eq. (2.2), Table 2-3 compares, for three of these waters, the values for K_d(av) arising directly out of the Monte Carlo simulation with those calculated by substitution of the corresponding values of $G(\mu_0)$ (obtained from Eq. (2.3) with the appropriate g_1 and g_2 values from Table 2-2) and μ_0 into Eq. (2.2). Each water was assumed to have a b/a ratio of 6, and the calculations were carried out for a wide range of solar angles. It is clear that the K_d(av) values calculated by Eq. (2.2) are in very good agreement with those derived directly from the irradiance data.

Dependence of the coefficient $G(\mu_0)$ on the shape of the volume scattering function

It is evident from the findings so far that the coefficient $G(\mu_0)$, which, in the manner specified by Eq. (2.2), determines the extent to which the vertical attenuation coefficient is influenced by scattering, is markedly influenced by the shape of the volume scattering function. One is led naturally to inquire whether

this influence, this relationship, can be put on a quantitative basis. Can we perhaps find some single parameter that in some measure represents, or corresponds to, the shape of the volume scattering function, and establish a relationship between this parameter and $G(\mu_0)$? If we can, then all we need in order to find the correct form of Eq. (2.2) for any optical water type is the value of this hypothetical shape parameter for the volume scattering function of that water, and we can arrive at the appropriate $G(\mu_0)$ for use in Eq. (2.2).

After a certain amount of experimentation I have concluded that there is a shape parameter that fills the bill, and it is the average cosine of scattering. It could alternatively be referred to as the average cosine of the singly scattered light field. The reader will recall, of course, that the average cosine of a light field at a point is the average value, in an infinitesimally small volume element at that point in the field, of the cosine of the zenith angle of all the photons in the volume element (see Eq. 1.11). Suffice it to say that from any set of data for the normalized volume scattering function of a water, the average cosine of scattering may be obtained. I have given it the symbol $\bar{\mu}_s$, and the calculated values of this parameter for all twelve optical water types are given in Table 2-1. Not surprisingly, it is the two waters with the lowest total scattering, the two that are least dominated by particle scattering at very narrow forward angles, which have the lowest values of the average cosine of scattering.

Having chosen our scattering function shape parameter, and evaluated it for the different waters, we can examine in what way, if at all, it is related to the coefficient $G(\mu_0)$, which determines the contribution of scattering to vertical attenuation. In Fig. 2-4, $\bar{G}(1.0)$—the best estimate of the value of $G(\mu_0)$ for vertically incident light—for each of the 12 waters is plotted against the average cosine of scattering for these waters. It is clear that, as we might expect, the dependence of vertical attenuation on scattering, expressed through $\bar{G}(1.0)$,

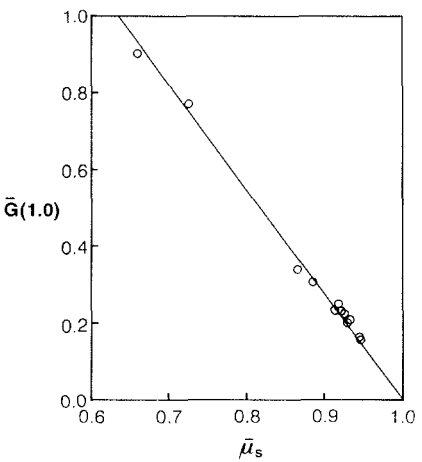

Fig. 2-4. Variation of $\bar{G}(1.0)$ with the average cosine of scattering of the water.

diminishes steeply as the scattering becomes increasingly concentrated within narrow forward angles. In the limit, when photons are all scattered forward without any change of direction, that is to say when $\bar{\mu}_s = 1.0$, there is of course no longer any effect of scattering on attenuation, i.e. $\bar{G}(1.0)$ equals zero.

As I remarked earlier, what we really want is to be able to express the dependence of $G(\mu_0)$ on the scattering shape factor in simple mathematical form. The inverse dependence of $\bar{G}(1.0)$ on $\bar{\mu}_s$ indicated in Fig. 2-4 suggests the possibility of a simple relationship between $G(\mu_0)$ and the reciprocal of $\bar{\mu}_s$. Or, to extend this a little, since $G(\mu_0)$ is actually a function of μ_0, and since when we so express it we do so with help of two other terms, g_1 and g_2, in accordance with Eq. (2.3), what we must in fact explore is the dependence of g_1 and g_2 on $1/\bar{\mu}_s$.

The values of g_1 and g_2 have already been determined for each water type and are listed in Table 2-2. In Fig. 2-5 these values are plotted as functions of the reciprocal of the average cosine of scattering for the 12 waters. The relationship is in each case approximately linear, and using linear regression may be represented as

$$g_1\,(\bar{\mu}_s) = \frac{2.127}{\bar{\mu}_s} - 1.895 \tag{2.11}$$

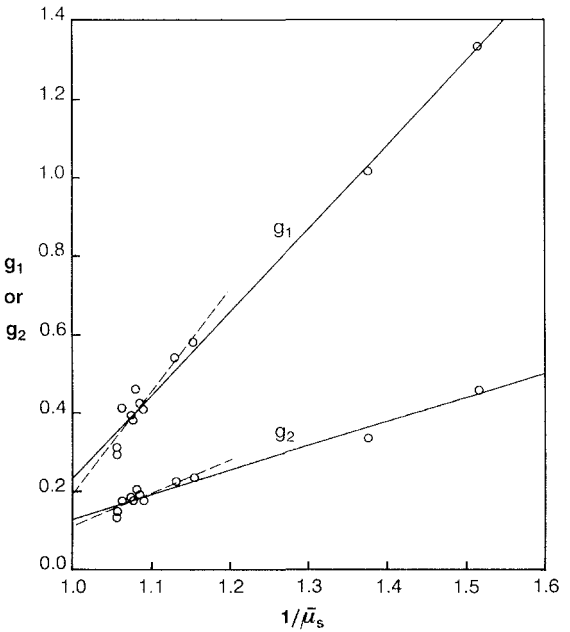

Figure 2-5. The values of the coefficients g_1, and g_2, as a function of the reciprocal of the average cosine of scattering of the water. Regression lines for all 12 waters (solid lines) and for the 10 waters excluding the two extremely low scattering examples (dashed lines).

$$g_2(\bar{\mu}_s) = \frac{0.618}{\bar{\mu}_s} - 0.490 \tag{2.12}$$

with r values of 0.995 and 0.983, respectively. Substituting back into Eq. (2.3), we can now express the dependence of the coefficient $G(\mu_0)$ on the shape of the volume scattering function by means of the relationship

$$G(\mu_0, \bar{\mu}_s) = \mu_0 \left(\frac{2.127}{\bar{\mu}_s} - 1.895 \right) - \frac{0.618}{\bar{\mu}_s} + 0.490 \tag{2.13}$$

What this means is that for any water for which we know the shape factor, $\bar{\mu}_s$, of the volume scattering function, we can find the appropriate formulation of $G(\mu_0)$ for incorporation in Eq. (2.2). That is to say, we can now with reasonable accuracy express the apparent optical property, K_d, as a function of all the inherent optical properties by which it is determined.

Irradiance reflectance in waters with different scattering functions

Let me now briefly turn to the other apparent optical property of particular interest to us, namely the irradiance reflectance, R, and consider to what extent this might be affected by variation in the shape of the volume scattering function. Earlier work, you will recall, had shown that $R(0)$, the reflectance just beneath the surface is approximately proportional to b_b/a, and the constant of proportionality, $C(\mu_0)$, is a function of solar altitude expressed through μ_0, in accordance with Eq. (2.9). In comparing waters with different scattering phase functions we shall for simplicity confine our attention to vertically incident light, for which $\mu_0 = 1.0$, i.e., we shall consider specifically $C(1.0)$.

There are now two questions to be asked: Does a linear dependence of $R(0)$ on b_b/a occur in all the waters under consideration? And if so, to what extent does the value of the coefficient, $C(1.0)$, vary with the shape of the volume scattering function? The values of $R(0)$ for values of b_b/a in the range 0.0–0.4, for all 12 water types are plotted in Fig. 2-6. There are many data points which have been omitted simply because they coincide closely with other data points.

It can be seen that for ratios of b_b/a up to about 0.25, the data for all the waters can be satisfactorily fitted to a single straight line, and linear regression yields the relationship

$$R(0) = 0.331 \frac{b_b}{a} \tag{2.14}$$

At higher values of b_b/a, in the range 0.4–2.6, $R(0)$ increases less than linearly with b_b/a. Furthermore the points for different waters separate out and fall on different lines. However, taking into account the ratios of scattering to absorption that normally exist in the real world, I think it likely that a value of about 0.33 for $C(1.0)$ should be applicable to most ocean waters. Given that a constant of

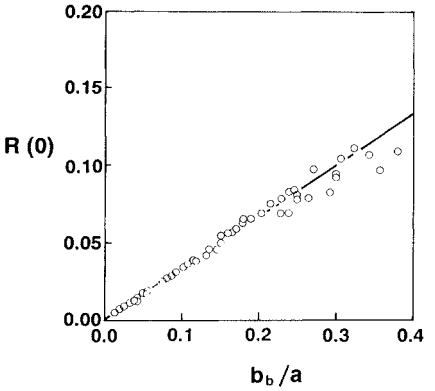

Figure 2-6. The relationship between the irradiance reflectance and the ratio of the backscattering (b_b) to the absorption (a) coefficient. The data for all 12 water types for b_b/a values up to 0.4 have been plotted. Data points in this range have been omitted only where they coincide too closely with other points. The line was obtained by linear regression through all data points in the range $0 < b_b < 0.25$.

proportionality of about this size between $R(0)$ and b_b/a has commonly been assumed in the past, anyway, it does not seem that for vertically incident light possible variation in the shape of volume scattering functions need cause any revision in existing interpretations of underwater irradiance reflectance.

When the sun is not at the zenith, differences do, however, emerge. The extent to which reflectance increases as the solar angle departs from the vertical does depend on the shape of the volume scattering function (Gordon, 1989a), tending in fact to increase with $\bar{\mu}_s$ (Kirk, 1991).

3

OPTICAL CLOSURE: FROM THEORY TO MEASUREMENT

J. Ronald V. Zaneveld
Oregon State University

Introduction

The intensity and spectrum of the light in the ocean have a major influence on the biological processes. These processes in turn determine the concentrations of much of the suspended and dissolved matter in the ocean, which affect the way in which the light is scattered and absorbed. These relationships can perhaps be most easily illustrated schematically as in Fig. 3-1. At the upper boundary we have the sun and sky radiances and the surface transmission conditions that combine to provide the energy entering through the surface. The ocean itself

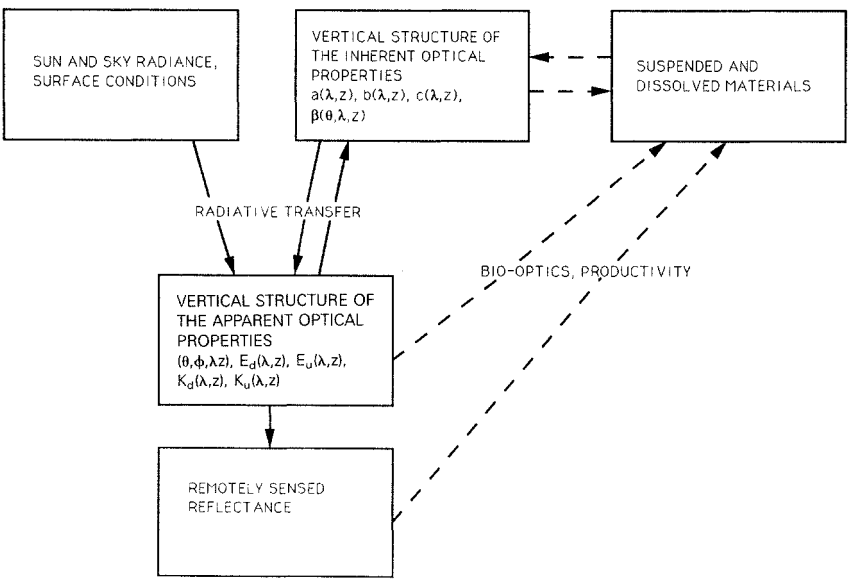

Fig. 3-1. Relationships between the various concepts in optical oceanography

contains the vertical structure of those optical properties that do not depend on the structure of the light field, but depend only on the properties of the suspended and dissolved materials: the absorption coefficient $a(\lambda,z)$, the beam attenuation coefficient $c(\lambda,z)$, and the volume scattering function $\beta(\theta,\lambda,z)$. These are known as *inherent* optical properties, because they do not depend on the source radiance field (Preisendorfer, 1976). They are a function only of the suspended and dissolved materials in the water, and of the water itself.

How does the vertical structure of the inherent optical properties affect the vertical structure of the radiance field in the ocean itself? This is the problem of radiative transfer in which we try to predict the intensity, direction, and spectrum of the light (spectral radiance) in the ocean, based on a set of given inherent optical properties. Those properties of the light field in the ocean that depend on the radiance are known as the *apparent* optical properties. Radiance field integrals, such as the vector irradiance, $E(\lambda,z)$, the scalar irradiance $E_0(\lambda,z)$, and their attenuation coefficients are also apparent optical properties (see Table 3-1).

Table 3-1. Radiative transfer definitions

$a(\lambda,z)$	Absorption coefficient	=	fraction of power lost to absorption per distance Δr of propagation of a parallel beam of light
$b(\lambda,z)$	Scattering coefficient	=	fraction of beam energy lost to scattering per distance Δr of propagation of a parallel beam of light
$c(\lambda,z)$	Attenuation coefficient	=	$a(\lambda,z) + b(\lambda,z)$

Also,

$$b(\lambda,z) = 2\pi \int_0^{\pi} \beta(\gamma,\lambda,z) \sin\gamma \, d\gamma = b_f(\lambda,z) + b_b(\lambda,z)$$

where

$\beta(\gamma)$ = $dI(\gamma)/E\,dV$ = volume scattering function, where

$dI(\gamma)$ = radiant intensity scattered in direction γ relative to the beam direction from volume element dV and the subscripts f and b represent scattering in the forward and backward hemispheres, respectively

$L(\theta,\phi,\lambda,z)$ = radiance distribution of the light field = flux of photon energy of wavelength λ from direction (θ,ϕ) per nm per unit solid angle per unit projected cross-sectional area of a receiver at depth z

Downwelling scalar irradiance

$$E_{0d}(\lambda,z) = \int_0^{2\pi} d\phi \int_0^{\pi/2} L(\theta,\phi,\lambda,z) \sin\theta \, d\theta$$

Table 3-1. Continued

Upwelling scalar irradiance

$$E_{0u}(\lambda,z) = \int_0^{2\pi} d\phi \int_{\pi/2}^{\pi} L(\theta,\phi,\lambda,z) \sin\theta \, d\theta$$

Scalar irradiance

$$E_0 = E_{0u} + E_{0d}$$

Downwelling irradiance

$$E_d(\lambda,z) = \int_0^{2\pi} d\phi \int_0^{\pi/2} L(\theta,\phi,\lambda,z) \cos\theta \sin\theta \, d\theta$$

Upwelling irradiance

$$E_u(\lambda,z) = \int_0^{2\pi} d\phi \int_{\pi/2}^{\pi} L(\theta,\phi,\lambda,z) \cos\theta \sin\theta \, d\theta$$

Net downwelling irradiance

$$E = E_d + E_u$$

EQUATION OF RADIATIVE TRANSFER

This equation describes the change of radiance per unit depth dz along direction (θ,ϕ) for a horizontally stratified medium. The first term on the right side is the loss of radiance, while the second and third terms are the gains of radiance per unit depth dz due to scattering from direction (θ',ϕ') toward (θ,ϕ) by inelastic and elastic (e.g. fluorescence, Raman) processes, respectively.

$$\cos\theta \frac{dL(\theta,\phi,\lambda,z)}{dz} = -c(\lambda,z) L(\theta,\phi,\lambda,z) + \int_0^{2\pi} \int_0^{\pi} \beta(\theta,\theta',\phi,\phi',\lambda,z) L(\theta',\phi',\lambda,z) \sin\theta' \, d\theta' \, d\phi' + F(\lambda,\lambda_1)$$

Analytical solutions abound: Given $L(\theta,\phi,\lambda,0)$, $c(\lambda,z)$, and $\beta(\gamma,\lambda,z)$, we can calculate $L(\theta,\phi,\lambda,z)$ and hence $E(\lambda,z)$ and $E_0(\lambda,z)$.

Optical oceanographers are particularly interested in being able to derive the vertical structure of the apparent optical properties through radiative transfer theory, given the vertical structure of the inherent optical properties and the input radiance field. They are also interested in reversing this process. That is, we have potential linkages in both directions. As we shall see, some apparent optical properties and inherent optical properties are easier to measure than others, so that in reality one measures a mixture of both. The task is then to derive other, unmeasured parameters with sufficient accuracy. The light levels in the ocean feed back via bio-optics and primary productivity to the concentration and nature of suspended and dissolved materials. This is the bio-optics loop. We thus see that underwater optics and biology are very tightly linked. The biology determines the structure of the inherent optical properties, which in turn determines the structure of the light field, which governs along with biochemical parameters the rate at which photosynthesis takes place.

One can think of closing the bio-optics loop when radiative transfer predictions and measurements are consistent, and when the predictions of primary productivity and resultant concentrations of particles and dissolved materials match reality. This type of "closure" is not expected any time soon. However, if the biological portion of the loop is not considered at this time, optical closure between the inherent optical properties and apparent optical properties is feasible.

What then is optical closure? One can think of it as the simultaneous verification of a mathematical relationship and a set of parameters by means of the independent measurement of the parameters. This requires an underlying theory or definition and a set of measurable parameters. One would like to test theories and definitions in such a sequence that one is eventually able to answer the question that arises in all experimental work: is the theory wrong or are the instruments wrong? By initially testing only expressions that are exact, we limit ourselves at first to instrument validation. The classical example of an exact expression is

$$a + b = c \tag{3.1}$$

This is really just the definition that the attenuation coefficient c consists of the sum of the absorption coefficient a and the scattering coefficient b. The relation is thus exact and any test using this relation is a test of the instrumentation only. Thus if one were able to measure a independently, b independently, and c independently, and were then able to satisfy this equation to within an acceptable accuracy, closure of the relationship would have been satisfied. Such closure would provide a great deal of confidence that these measurements are being performed correctly. Since the inherent optical properties a, b, and c are central to the verification of radiative transfer theories, let us have a look at how one might determine these parameters and how one would approach closure for Eq. (3.1).

Closure of the inherent optical properties

We will look at the instruments in reverse order, i.e., c, b, and a, as historically these parameters have been measured with decreasing accuracy in that order (see Chapter 7 for an early history of some of these measurements).

Jerlov (1976) describes the principle of transmissometers, which are used to measure the beam attenuation coefficient. The task of the modern transmissometer is to measure in situ, rapidly, and accurately a beam attenuation spectrum. Such a transmissometer is under development at Sea Tech, Inc. The Sea Tech, Inc. transmissometer uses a xenon-arc flashlamp light source. This light source is ideal because of its high output in the blue and blue-green portion of the spectrum. A portion of the light from the flashlamp passes through a 1-mm pinhole and intermediate light stop to a collimating lens. The collimated light beam passes through an interference filter wheel that selects the wavelengths of the instrument. The filtered beam is then directed toward a quartz-cube beam splitter. Approximately one half of the monochromatic light is reflected to a reference detector. The other half of the light passes through the beam splitter to a quartz window and into the enclosed water path. It passes through the water path, which is enclosed in a Celcon® plastic, nonreflective tube. The tube walls remain outside the path of the light interaction with the water, so that no reflections of the direct beam are observed by the receiver.

At the end of the 25-cm water path, the light beam (diminished in intensity by attenuation in the water path) passes through another quartz window and is focused onto the receiver detector. The receiver detector then measures the intensity of the transmitted light. Under the control of its internal microprocessor, the instrument measures and records the intensity of the light pulse at the reference and signal detectors. It also measures and subtracts the intensity of ambient light at the two detectors and the temperatures of the detectors. When it receives the signal values from the instrument, the host computer stores the values and computes the ratio of the signal to the reference light intensity. The ratio is linearly related to the transmissivity of the water path by a constant that is determined during calibration. Corrections due to the response of the instrument to variations in detector temperatures must be determined and applied.

Part of the error in a transmission measurement is due to the inclusion of forward scattered light. If $\beta(\theta)$ is the volume scattering function and γ is the half-angle of the receiver, the attenuation coefficient will be underestimated by:

$$b_e = 2\pi \int_0^{\gamma} \beta(\theta) \sin\theta \, d\theta \tag{3.2}$$

where the lower integration limit is 0 and the upper limit is γ. The measured transmission will then be overestimated by a factor of e^{be}. It is thus possible to correct for the finite half-angle of the receiver if either the forward scattering is

known or if the nature of the particles is known, so that the particulate scattering function can be calculated from Mie scattering theory.

At the present time the total scattering coefficient can be determined only by measuring the volume scattering function, $\beta(\theta)$, at a sufficient number of angles θ, and integrating using the following equation:

$$b = 2\pi \int_0^{\pi} \beta(\theta) \sin\theta \, d\theta \tag{3.3}$$

where $\beta(\theta)$ is the fraction of collimated irradiance incident on a sample volume of water that is scattered as radiant intensity in the direction θ. Using the value of b determined in this way together with independent measurements of a and c allows us to test closure of the inherent optical properties via Eq. (3.1). Satisfying closure of measurements with this equation provides confidence that b can be determined in the future by accurate measurements of a and c. This is important because measurements of $\beta(\theta)$ over all θ are difficult to perform accurately.

In situ instruments for the measurement of the volume scattering function were developed at the former Visibility Laboratory of the Scripps Institution of Oceanography. This type of instrumentation is still in existence (now under control of Dr. K. Voss at the University of Miami) and can be used to obtain a measurement of b by means of integration over the scattering function. Spinrad et al. (1978) showed that the scattering function in the near-forward direction is flat as predicted by Mie scattering. The shape observed by Petzold (1972) is quite different in that the scattering continues to increase towards 0. This difference must be further studied. It may be due to turbulence, as suggested by the work of Honey and Sorenson (1970). Petzold states that the resolution of the devices is 2% of scattering and that the integrated b values are accurate to within about 5%.

Another approach to determining b uses Morel's (1973) analysis of calculated scattering functions, in which he concludes that the scattering at 4° is proportional to the total scattering coefficient b. An instrument based on this principle was constructed by Carder et al. (1984). Verification of Morel's principle by means of direct measurements would be of interest, as it would set error limits on the use of $\beta(4°)$ for the measurement of b.

The absorption coefficient has been hardest to measure directly in situ. A method occasionally used depends on Gershun's (1939) equation. This equation is obtained by integration of the equation of radiative transfer (see Table 3-1) over all directions. We then get

$$-\frac{dE(\lambda,z)}{dz} = aE_0(\lambda,z) \tag{3.4}$$

where E_0 and E are the scalar and vector irradiances as defined in Table 3-1. The scalar irradiance $E_0(\lambda,z)$, is simply the integration of the radiance over 4π

steradians. This integral can be broken up into the sum of an upwelling irradiance $E_{ou}(\lambda,z)$, and a downwelling irradiance $E_{od}(\lambda,z)$. Vector irradiance $E(\lambda,z)$, the integral over 4π steradians of the radiance multiplied by the cosine of the zenith angle, provides a measure of the total flux of light crossing a horizon.

Due to intercalibration problems, it is not easy to measure the apparent optical properties E_0 and E simultaneously and accurately. Special instruments to do this were built by Honey and Sorenson (1970) and Højerslev (1974).

Another way of measuring a in situ is to use a reflecting tube as proposed by Zaneveld and Bartz (1984) and implemented in the laboratory by Zaneveld et al. (1990). It is similar to a transmissometer except that it has a wide-angle detector instead of a collimated detector and that the light beam is surrounded by a reflecting tube. The principle behind the device is that all the directly transmitted light and all of the forward scattered light is collected. The instrument thus measures in theory $c - b_f$ ($= a + b_b$). In reality there are errors that represent a larger fraction of b due to imperfect reflection at the walls of the reflecting tube (Zaneveld et al., 1990). For the first generation device the error was approximately 14% of b. It turns out that this percentage is only weakly a function of the shape of the volume scattering function (see Chapter 2 and Table 2-1), so that the overall error in a is reasonably predictable and should be less than 2% of b.

Another error to be considered is the inclusion of fluoresced light in the detected light of inherent optical property sensors. A typical value for the fluorescent efficiency of phytoplankton in the red is 4% of the light absorbed in the blue. The fluoresced light is nearly uniform directionally, so that the amount of light that is detected depends on the solid angle of the receiver. Since the receiver angle of transmissometers is very small, only a very small fraction of the fluoresced light is detected, and has no influence on the measured value of c. The absorption meter, however, has a large receiver angle and in theory could detect up to 50% of the fluoresced light. The amount of fluoresced light detected thus amounts to a maximum of 2% of the absorbed light. Fluorescence introduces an error of at most 2% in the measured value of a. The actual error is much less, as only part of the energy absorbed can be used for fluorescence. Furthermore, in a closure experiment, if one were to measure spectral a one could deduce with reasonable accuracy the amount of light absorbed by pigments such as chlorophyll and correct a accordingly.

In addition to fluorescence in the red part of the spectrum there is fluorescence in the green (Shapiro et al., 1989b), but this is even weaker than the red fluorescence and will have no significant influence on the measurement of the inherent optical properties by direct means.

Another effect to be considered in the transfer of energy from one wavelength to another is Raman scattering by water itself. This effect is approximately one order of magnitude below the Rayleigh scattering of pure water, and so also will not affect measurements made in small volumes of seawater. Fluorescence and Raman scattering have a major influence on the measurement of the apparent optical properties above 500 nm, however (see Chapter 12 and Stavn and

Weidemann 1988a). This is so because one measures the apparent optical properties for the longer wavelengths in the presence of much larger amounts of radiation at the shorter wavelengths, which excite the transspectral effects. A proper inherent optical property device has the filter at the light source, so that attenuation or absorption at the longer wavelengths is not measured in the presence of the shorter excitation wavelengths. For this reason, white light source inherent optical property devices with filters at the detector end may produce significant errors.

When we combine the errors of the various instruments we see that if we determine c from Eq. (3.1) we should have errors that are less than 7% of b. If we know b to within 10%, the measurement of c can be corrected to within about 2% of b. It is thus reasonable to expect Eq. (3.1) to be satisfied to within a few percent of b. A significant advantage will be the simultaneous measurement of all the parameters, so that corrections can be made by iteration. Knowledge of the shape of the scattering function will allow a correction for the measurements of a and c. Having carried out simultaneous measurements of the inherent optical properties one can study how one would correct measurements of a and c when the shape of the scattering function is not available, but a first estimate of b via Eq. (3.1) is available.

In the future, when it has been shown that it is possible to determine b from measurements of a and c, it might be possible to determine the shape of the volume scattering function far more simply than by measurement over a large number of angles. The backscattering coefficient could be determined using an instrument based on the work of Oishi (1990). Oishi contends that the value of the volume scattering coefficient at 120° is directly proportional to b_b, with an average error of about 6%. Validation of this sort of device can be carried out by simultaneous measurements of the scattering function using Petzold's (1972) devices. If the backscattering can be measured and if b is known from $c - a$, the degrees of freedom left in the shape of the scattering function in the forward direction are limited. Measurement of the scattering function at a few angles in the forward direction might be sufficient to determine the shape of the scattering function with sufficient accuracy for radiative transfer calculations.

Closure of the apparent optical properties

We have thus seen that it is conceptually possible in the near future to carry out experimental closure of the inherent optical properties without involvement of the apparent optical properties. A different kind of closure is required in order to satisfy the entire equation of radiative transfer (see Table 3-1 and Fig. 3-1). This equation links radiance, the beam attenuation coefficient, and the volume scattering function. In addition, transpectral functions are also shown because Raman scattering and fluorescence can be important for certain wavelengths and optical domains. Because of the importance of the shape of the light field in the ocean, efforts to experimentally satisfy the equation of radiative transfer are a very important form of optical closure.

The radiance distribution and the volume scattering function are very difficult (but not impossible) to measure. Therefore we will first consider closure using an integrated form of the equation of radiative transfer, Gershun's equation (Eq. 3.4), introduced earlier. We will then consider approximate expressions involving the inherent optical properties and apparent optical properties, whereafter we return to closure of the full equation of radiative transfer.

The apparent optical properties can be routinely determined at present. The most commonly used instruments are built by Biospherical Instruments. These devices can measure the vector and scalar irradiances at a number of discrete wavelengths. They can similarly measure the upwelling nadir radiance. As in the other devices described above, calibration and temperature effects must be carefully considered.

The most frequently used apparent optical property is K, the diffuse attenuation coefficient of the vector irradiance, defined by

$$K(\lambda,z) = -\frac{1}{E(\lambda,z)}\frac{dE(\lambda,z)}{dz} = \frac{d}{dz}\ln E(\lambda,z) \tag{3.5}$$

We thus wish to intercalibrate K with the inherent optical properties. This can be done via Gershun's equation. Gershun's equation links the depth derivative of the vector irradiance, the scalar irradiance and the absorption coefficient. Gershun's equation is exact if one can ignore the effects of Raman scattering and fluorescence. This is the case only for the shortest wavelengths in the visible spectrum, 400–450 nm. The average cosine of the light field, $\bar{\mu}$ is defined as the ratio of E and E_0. Substitution into Eq. (3.5) then gives

$$K = \bar{\mu}a \tag{3.6}$$

We thus see that K and a differ only by a factor of $\bar{\mu}$, which in the ocean ranges from 0.6 to 1. K can therefore be determined from a with an accuracy of better than 20% and vice versa, without any knowledge of the shape of the light field. Near the surface the average cosine can be determined quite accurately from the refracted solar zenith angle, providing a direct comparison of K and a. Closure of K and a can thus be accomplished near the surface independent of the intercalibration of E_0 and E. It is in general difficult to measure K near the surface, however, due to wave effects, ship shadow, etc. In the future it may thus be easier to determine K at the surface from a measurement of a and an estimate of the average cosine, than from the vertical structure of E.

A further comparison of K and the inherent optical properties without prior calibration of E_0 and E can be obtained in the asymptotic region. The asymptotic region occurs at great optical depths where the light field has undergone sufficient scattering to be no longer related to the surface light field (see Chapter 1). The shape of the light field, K, and the average cosine then all become inherent optical properties (Preisendorfer, 1959; Hojerslev and Zaneveld, 1977). Prieur and Morel (1971) calculated the relationship of K_∞/c and

b/c. Their relationship is described by the following expression (Zaneveld, 1989)

$$K_\infty/c = 1 - 0.52(b/c) - 0.44(b/c)^2 \tag{3.7}$$

Gordon (personal communication) has shown that at asymptotic depths the relationship between K_∞/c and b/c becomes nearly independent of the shape of the volume scattering function, provided this function is within the range of shapes normally encountered in the ocean. We thus see that our ability to derive K from the vertical structure of E can be tested in the asymptotic region. Derivation of K from the vertical structure of E may seem straightforward, but is complicated by the fact that a relatively large depth increment is required to accurately calculate K. This results in a trade-off between the accuracy of K and its vertical resolution. Mueller's (1991) approach using Hermitian polynomials is a major improvement in this regard.

An important aspect of K is that it can be obtained without having an absolute calibration of E. K_0 is the diffuse attenuation coefficient for the scalar irradiance, and it can similarly be obtained without having an absolute calibration of E_0. The differential form of Gershun's equation (Zaneveld, 1989) is given by

$$K_a(z) = K(z) - K_0(z) + K_k(z) \tag{3.8}$$

where $K_a(z)$ and $K_k(z)$ are defined as in Eq. (3.5), replacing E by a and K, respectively. This expression is very useful to test our ability to accurately determine K and K_0 from the vertical structure of the irradiances, without knowledge of the absolute calibration of the irradiances, as it relates K and K_0 only to the vertical structure of a. The absorption coefficient in turn also does not need to be known in absolute terms in order to test closure using this relationship. We are particularly interested in testing the algorithms used to derive K and K_0 from E and E_0 and in verifying that these algorithms adequately predict the vertical structure. Equation (3.8) again does not include Raman scattering or fluorescence and must be used in this form only in the region of 400–450 nm. Once we are satisfied that K and K_0 can be determined with acceptable accuracy, we will wish to test in situ the internal consistency of determinations of the scalar and vector irradiances.

The intercalibration of E_0 and E can best be tested by use of Gershun's equation (Eq. 3.4) rewritten as follows

$$K = \frac{E}{E_0}\, a \tag{3.9}$$

In this form, having previously satisfied our ability to determine a and K, we can directly test the intercalibration of the vector and scalar iradiances. Another way of testing the intercalibration of the irradiances is by direct integration of the radiance distribution.

Voss (1989) describes the use of his electro-optics radiance camera system (RADS) in which E, E_0, and K are derived from the vertical structure of the radiance. He then uses Gershun's equation in several forms to obtain a. Since all apparent optical properties are based on the radiance and its derivative with depth, a direct measurement of the radiance allows calculation of all apparent optical properties, and subsequent intercomparison with devices that directly measure integrals of the radiance such as E and E_0.

Having introduced the measurement of radiance as a realistic option, we can now proceed to the unpolarized equation of radiative transfer (Table 3-1). For the shorter wavelengths of the visible spectrum (up to 450 nm) fluorescence and Raman scattering effects are not expected to have a major influence, so that $F(\lambda_1,\lambda_2)$ can be set equal to zero. The measurements required to verify closure of the simplest form of the equation of radiative transfer are thus the radiance, the volume scattering function and the beam attenuation coefficient. These observations would allow one to verify closure via the many solutions to the unpolarized equation of radiative transfer with no internal sources and transspectral effects (Chandrasekhar, 1950; Preisendorfer, 1976).

A solution that is well adapted to the actual measurements of radiance that are made with the RADS device is the quad-averaged approach of Mobley (1989). Closure via Monte Carlo models can also be tested using the measurements of radiance, scattering, and beam attenuation.

An important question is the error generated by ignoring the polarization of the radiance and by using only the unpolarized element of the Mueller scattering matrix. Kattawar and Adams (1989) carried out a calculation using a Monte Carlo formulation for Rayleigh scattering and showed that significant polarization effects exist even at great depths (see also Chapter 11). Since it is not possible at present to measure in situ either the full Mueller scattering matrix or the Stokes radiance vector, the extent to which closure can be satisfied using the unpolarized formulations will be a test not only of the accuracy of the solution but also of the assumption that polarization effects can be ignored.

Since it is a difficult task to measure all parameters required to test even the unpolarized equation of radiative transfer, many approximate solutions have been developed. These typically involve only the up- and downwelling vector and scalar irradiances and their derivatives, the nadir radiance, $L(\pi)$, and a subset of the inherent optical properties consisting of a, c, and b_b. One must bear in mind that all approximate methods are wrong. The question is just "How wrong are they?"

A commonly used approximate method for calculating the vertical structure of the irradiances from the inherent optical properties and vice versa involves the two-stream models originated by Schuster (1905). Recent examples of this approach can be found in the papers by Preisendorfer and Mobley (1984), Aas (1987), and Stavn and Weidemann (1989). The primary problem with these models lies in the formulation of the backscattering of the irradiance streams. Inversion to obtain the true backscattering coefficient is therefore difficult. If closure of the inherent optical properties and apparent optical properties has been

tested using exact relationships, instrumental error budgets will have been determined. One can then proceed with examination of approximate relations and estimate errors associated with the various approximations as set forth in the cited papers.

A different approach was taken by Zaneveld (1982), who derived the following approximate expression directly from the equation of radiative transfer

$$\frac{2\pi L_u}{E_{0d}} = \frac{b_b}{k(\pi) + a + b_b} \tag{3.10}$$

This, then, would allow a combination of the inherent properties and $k(\pi)$, the attenuation coefficient for the nadir radiance, to derive the upwelling radiance. This method could provide a very interesting way of verifying upwelling radiance just beneath the surface. In a practical sense, there is always an instrument package above the sensor, which shades the measurement. Thus, upwelling radiance is a very difficult parameter to measure accurately, but it is extremely important because it provides the ocean color, water-leaving radiance signal viewed from space. In terms of closure, then, it is important to learn how upwelling radiance can be measured and predicted correctly. Equation (3.10) was estimated to be accurate to within 30% for most oceanic situations. This was recently confirmed by Monte Carlo calculations (Weidemann, personal communication).

A number of approximate expressions are used in algorithms for the inversion of remotely sensed radiance to obtain the oceanic pigment concentrations. We will mention here two examples that form the basis of models of the relationship of upper ocean optics and pigment content. The first relation is

$$R = \frac{E_u}{E_d} = 0.33\,\frac{b_b}{a} \tag{3.11}$$

This expression was initially derived by Gordon et al. (1975) (see also Chapters 1 and 2) and used by Morel (1988) in his extensive model. Clearly an expression such as this contains assumptions regarding the average shape of the light field and the average shape of the volume scattering function. Investigation of this sort of relation thus makes most sense in a statistical way. Individual situations can readily be constructed in which Eq. (3.11) is off by large amounts. It is more meaningful to examine the mean and standard deviation of the error. This implies a relatively large number of measurements in a number of different environments.

A second, more complicated expression, is

$$\frac{R}{Q} = \sum_{i=1}^{2} l_i \left(\frac{b_b}{a + b_b}\right)^i \tag{3.12}$$

(Gordon, 1986), where $l_1 = 0.0949$ and $l_2 = 0.0794$, and Q is the ratio of the upwelling vector irradiance and the upwelling nadir radiance. This expression was deduced from extensive Monte Carlo calculations. Examination of this sort of expression using intercalibrated sets of inherent optical properties and apparent optical properties will be an interesting aspect of descriptive optical oceanography in the next decade.

Discussion and conclusions

The purpose of this chapter was to provide an outline of the instrumentation and relationships that could be used to test optical closure. The primary concern initially is the generation of an intercalibrated set of measured parameters that includes both inherent optical properties and apparent optical properties. Generation of such a set is of interest primarily because it would prove that the optical properties are being measured correctly. This in itself is expected to take several years. Confidence in the measurements is a prerequesite for analysis of approximate expressions; hence the emphasis initially on the few exact relationships (Eqs. 3.1, 3.2, and 3.4). These relations could be examined using instrumentation that is already in existence or is projected to be in the next several years. One aspect that could complicate closure of the inherent optical properties and the irradiances is the scale problem. The inherent optical properties are measured using very small volumes (on the order of $100\,cm^3$), whereas the apparent optical properties are obtained using volumes that include the entire water column. Clearly, very large particles are ignored in the small volume inherent optical property measurements, and are included in the apparent optical properties measurements. Due to the ratio of cross-sectional area to volume, it is unlikely however, that in normal oceanic situations, particles larger than $50\,\mu m$ play a significant role in radiative transfer. The scale problem nevertheless needs to be examined carefully in any closure experiment.

Raman scattering and spectral fluorescence require further consideration (see Chapters 8, 9 and 12). Calibration of the instrumentation can be verified in those parts of the spectrum that are not influenced by those effects. They are important, however, for the verification of radiative transfer solutions. Raman scattering and spectral fluorescence are actually inherent optical properties, although they have classically not been regarded as such. In the future these parameters should be measured in absolute units and included in radiative transfer experiments. It is now possible to measure aspects of spectral fluorescence in situ (Cowles et al., 1990). This is not yet done in absolute units as would be required for radiative transfer. Calibration of fluorescence measurements should be possible in the future. Cowles et al. measure both the Raman scattering and the fluorescence, so that the fluorescence could be calibrated using Raman scattering, once its values have been determined. Inclusion of both the Raman scattering and spectral fluorescence in radiative transfer experiments would be very interesting.

A further concern is the inclusion of polarization effects (see Chapter 11). The results of Kattawar and Adams (1989) were obtained using a Rayleigh scattering

phase function. Results should be different for a phase function that is more realistic for oceanic particle assemblages. Nevertheless, polarization effects are important in the ocean and must be included for a complete description of the radiative transfer. Such measurements will be very difficult to make, and will probably not be carried out until the unpolarized measurements have been examined in detail.

Bioluminescence has not been considered in the sequence of closure experiments. While imbedded light sources can be handled theoretically with some confidence (Gordon, 1987), they are a transient effect, and are therefore not included. The prudent optical oceanographer, however, should be aware of the possible existence of bioluminescence that was stimulated by passage of the instrument package through the water. Such bioluminescence would alter the relationship between the apparent optical properties and inherent optical properties. This altered relationship could not be unraveled unless independent measurements of stimulated bioluminescence were made.

In conclusion, we have seen that in the next several years closure of the inherent optical properties and apparent optical properties in the blue part of the spectrum can be tested. Discrepancies between the apparent optical properties and inherent optical properties must be carefully studied and can be due to instrumental errors, transspectral effects, polarization effects, and bioluminescence. The development of instrumentation and theories to fully describe the optics in the oceans will be a formidable but important task.

Acknowledgment

This work was supported by the Office of Naval Research through contract N00014-90J1132.

4

INTERRELATIONSHIPS BETWEEN LIGHT AND PHYTOPLANKTON IN THE SEA

Motoaki Kishino
The Institute of Physical and Chemical Research, Japan

Introduction

Light energy penetrating the sea is diminished almost exponentially with depth with an accompanying drastic change in the energy spectrum as the result of absorption by various components in the seawater. Such a change in the light environment will affect phytoplankton life directly. Accordingly, in the study of light in the sea, much attention has been drawn toward the contribution of phytoplankton to the light field and also how much energy or which parts of the light spectrum are utilized at various depths by phytoplankton.

Spectral distribution of underwater irradiance is determined by the processes of absorption and scattering from various components of the seawater. Since absorption plays a much more important role in spectral variation than scattering (Preisendorfer, 1961), the spectral absorption of each component should be studied in order to adequately interpret the variation of spectral irradiance in the sea. The materials absorbing light are phytoplankton, other particles, dissolved organic substances, and the water itself. Spectral characteristics of the light environment in the sea are determined by the variable ratios of these components.

Several authors have attempted to measure directly the spectral absorption of individual components in seawater (Kirk, 1980; Okami et al., 1982; Kishino et al., 1984; Carder and Steward, 1985; Weidemann and Bannister, 1986). However, the determination of the absorption coefficient of natural phytoplankton is quite difficult, because no suitable technique is available for the direct measurement of absorption. Accordingly, there is still considerable uncertainty about light absorption by phytoplankton under natural conditions.

Phytoplankton photosynthetic efficiency is important for the algae as well as the other organisms in the same ecosystem. Photosynthetic efficiency can be estimated fundamentally from quantum yield, which is obtained by measuring three parameters: photosynthetic rate, spectral downward irradiance, and the spectral absorption coefficient of phytoplankton.

Underwater spectral irradiance

The optical system of a recently designed spectral irradiance meter is shown in Fig. 4-1. The meter has two independent cosine collectors that receive downward and upward spectral irradiance, respectively, by rotation of the mirror placed behind the collectors. After collimation, light reflected by the mirror is separated by a beam splitter. One beam travels towards the monochromator grating grid (600 lines/mm), which sweeps over the range from 350 to 750 nm within 1 s. The second beam is monitored for incident light intensity at one wavelength (either 482, 531 or 569 nm) after passing through respective interference filters. This monochromatic signal controls the high voltage supply to the photomultiplier tube in order to increase the accuracy of the determination of the spectral distribution, even at depths where irradiance is low. Total time required for a set of spectral downward and upward irradiance data is about 4 s.

Measurements were carried out in Tokyo Bay, Sagami Bay, and in the area south of Honshu (Fig. 4-2). Some results obtained from three typical water columns are shown in Fig. 4-3. There is no major difference in the energy spectrum of solar radiation reaching the sea surface in various water types. The 1% (of surface photosynthetically available radiation, PAR, between 350 nm and 700 nm) depth was about 83 m in open water (Stn. F), about 29.5 m in coastal water (Stn. J6) and about 4.8 m in the turbid water (Stn. 05).

The energy spectrum at the 1% depth for each water type varied considerably. In the open water (Stn. F), the maximum penetration of irradiance was centered around 480–490 nm with a half-bandwidth of approximately 60 nm. The energy decreased sharply around 510–520 nm and orange and red light at wavelengths longer than 550 nm largely disappeared. On the other hand, shorter-wavelength irradiance diminished gradually and irradiance at 440 nm was still about 30% of the maximum. In the coastal water (Stn. J6), maximum penetration occurred between 500 and 550 nm with a half-bandwidth of about 100 nm. There was a sharp drop around 590–600 nm, and red light (>600 nm) was greatly attenuated. There was also a small decrease around 510 to 520 nm. Irradiance at shorter wavelengths diminished faster than in the open water, and energy at 440 nm was about 10–15% of the peak energy. In the turbid shallow water (Stn. 05),

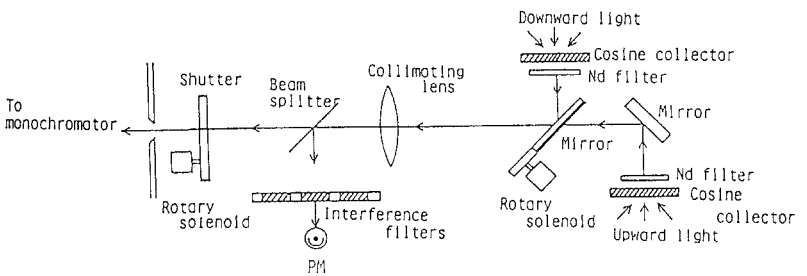

Fig. 4-1. Optical system of newly designed underwater spectral irradiance meter. Nd, neutral density filter; PM, photomultiplier tube. (From Kishino and Okami, 1984.)

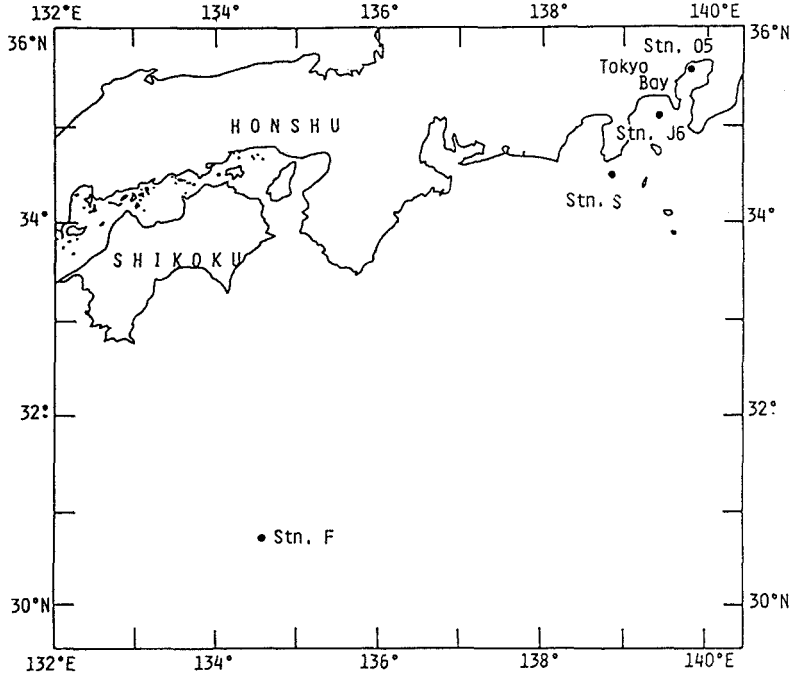

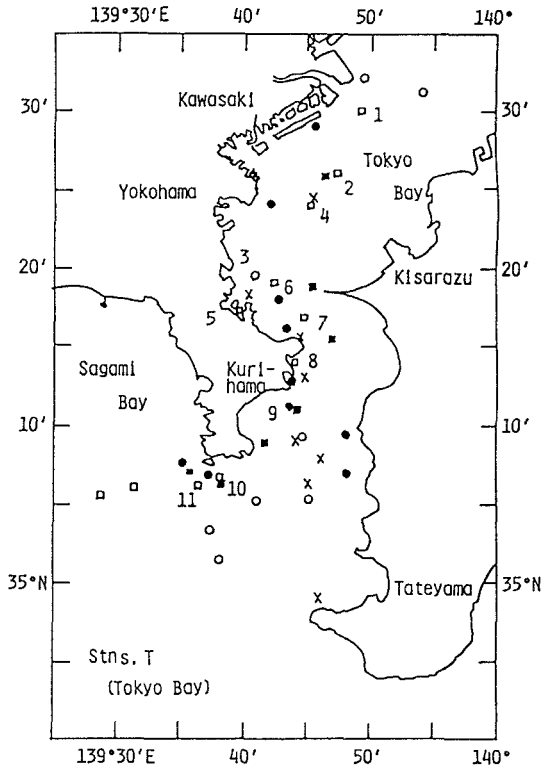

Fig..4-2. Location of stations.

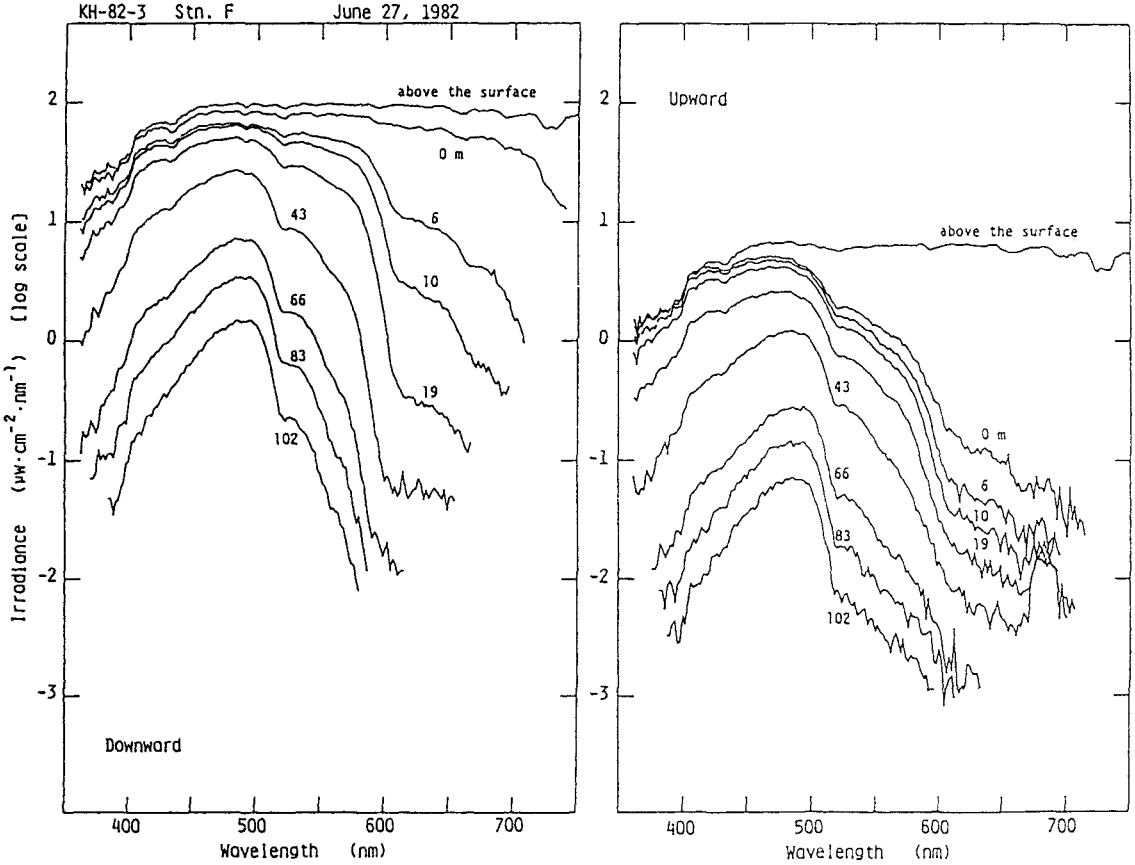

Fig. 4-3a. Distribution of downward and upward spectral irradiance at various depths.

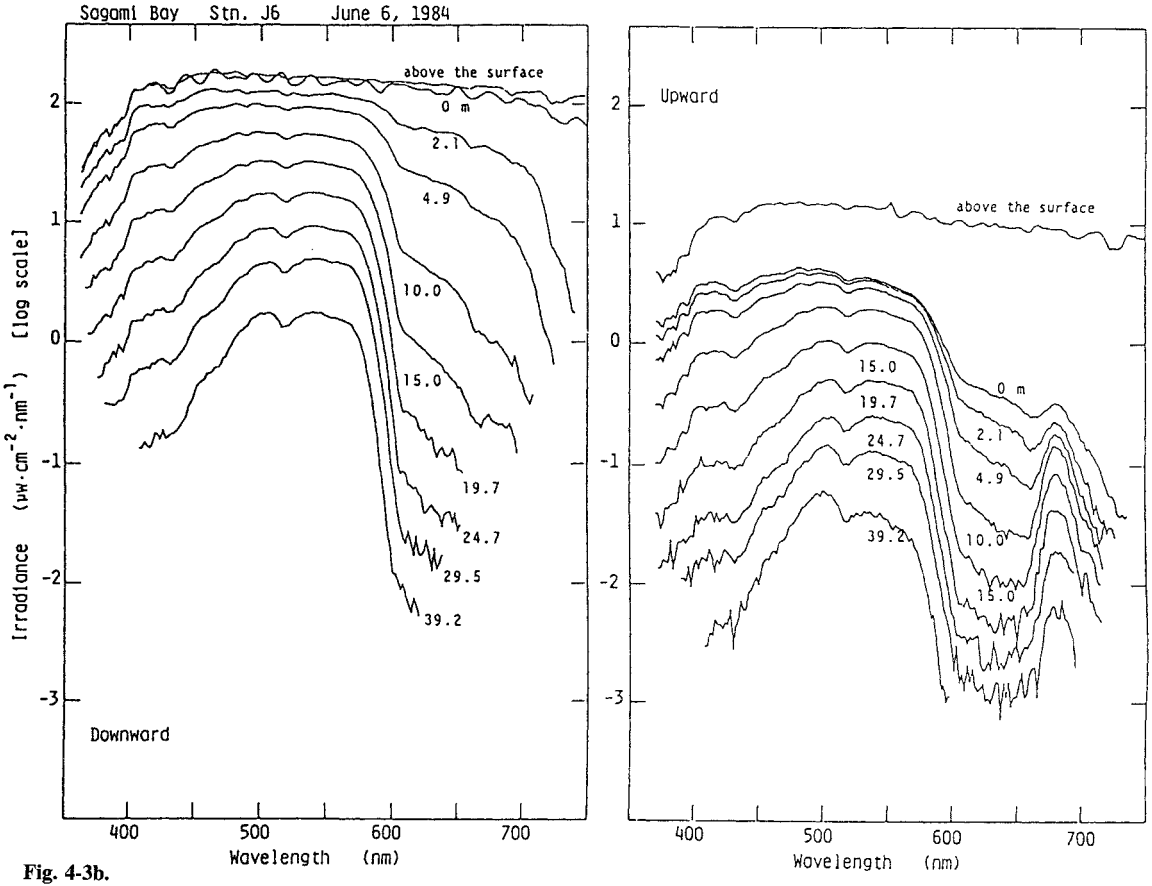
Sagami Bay Stn. J6 June 6, 1984
above the surface
0 m
2.1
4.9
10.0
15.0
19.7
24.7
29.5
39.2
Downward
Irradiance (μW·cm⁻²·nm⁻¹) [log scale]
Wavelength (nm)
Upward
above the surface
0 m
2.1
4.9
10.0
15.0
15.0
19.7
24.7
29.5
39.2
Wavelength (nm)

Fig. 4-3b.

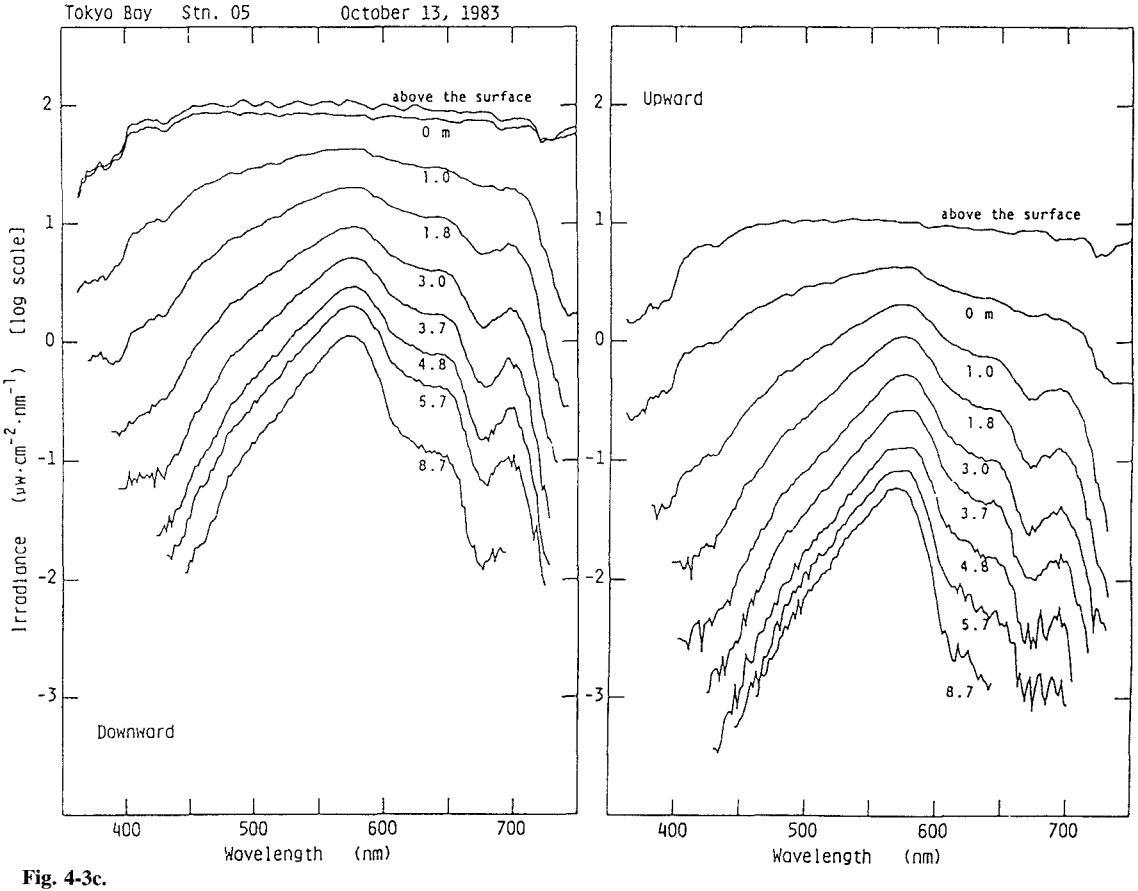
Tokyo Bay Stn. 05 October 13, 1983
above the surface
0 m
1.0
1.8
3.0
3.7
4.8
5.7
8.7
Downward
Upward
Irradiance (μw·cm⁻²·nm⁻¹) [log scale]
Wavelength (nm)
400
500
600
700
2
1
0
-1
-2
-3

Fig. 4-3c.

maximum penetration was found at around 570 nm with a half-bandwidth of about 60 nm. There was a sharp drop between 590 and 600 nm, but irradiance at longer wavelengths still remained at a significant level (about 30% of the peak energy at 650 nm). On the other hand, energy attenuation at shorter wavelengths was quite high and violet light (<450 nm) was not detected.

Spectral absorption coefficient of phytoplankton

In early studies, the values of the absorption coefficient of phytoplankton were taken from either the measured absorption spectrum of cultured phytoplankton (Bannister, 1979), direct measurement of whole suspended particles (Takematsu et al., 1981; Dubinsky et al., 1984; Lewis et al., 1985), indirect estimation using the attenuation coefficient (Tyler, 1975; Morel and Prieur, 1977; Smith and Baker, 1978b; Prieur and Sathyendranath, 1981), or literature (Bannister, 1974; Dubinsky and Berman, 1976). A much-improved method for the measurement of the absorption coefficient of phytoplankton (Kishino et al., 1985) is the modified opal glass technique combined with methanol extraction treatment. This method is described below.

Water samples containing phytoplankton particles are filtered onto a 24-mm glass fiber filter (Whatman GF/F) and the light absorbance of the particles retained on the filter, A_p, is measured directly using a spectrophotometer (Shimadzu MPS-5000) relative to a wetted glass fiber filter paper for reference (Fig. 4-4a). The spectrophotometer is equipped with matched end-on type photomultiplier tubes. Samples are placed immediately in front of each photomultiplier tube. Because of this design, all transmitted and most of the

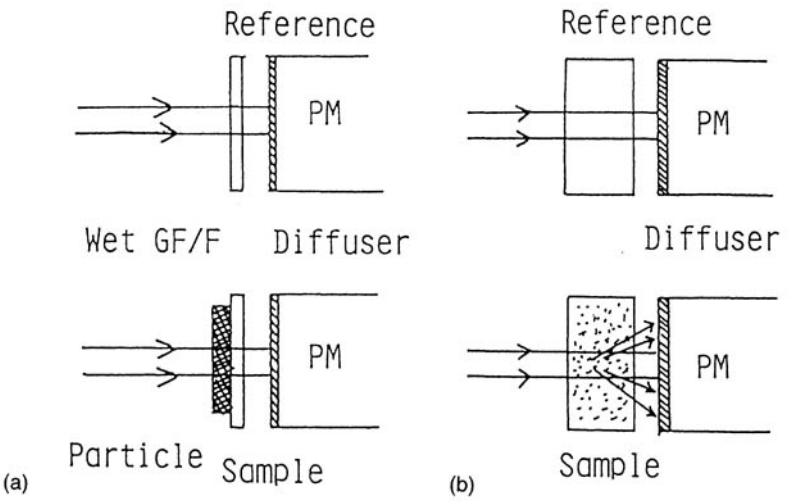

Fig. 4-4. Schematic diagram of system used to measure the absorption coefficient of particles: (a) on the filter; (b) in the cell.

scattered light is collected and measured. Spectral light absorption by all particles $a_p(\lambda)$, is derived from the following relation

$$a_p(\lambda) = 2.3 \frac{A_p(\lambda)}{X} \tag{4.1}$$

where X is the effective pathlength in meters, obtained from V/S (V is the volume of the seawater sample filtered; S is the surface area of the filter) and 2.3 is a conversion factor from common to natural logarithms. After the measurement is made the filter paper is extracted with methanol for 30–60 min and the decolorized filter paper is used again to measure the light absorbance spectrum, A_d, in the same manner as before. Light absorption due to particles without their pigments, $a_d(\lambda)$, is obtained identically

$$a_d(\lambda) = 2.3 \frac{A_d(\lambda)}{X} \tag{4.2}$$

The difference, $a_{ph}(\lambda)$, between $a_p(\lambda)$ and $a_d(\lambda)$ is considered to be the light absorption of the phytoplankton

$$a_{ph}(\lambda) = a_p(\lambda) - a_d(\lambda) \tag{4.3}$$

Light absorption of suspended particles, $a_s(\lambda)$, can also be determined directly in the medium using a cylindrical cell against a filtered water sample as a reference (Fig. 4-4b). In many tests there were no major spectral changes in light absorption by particles between suspended samples and filtered samples, although the actual light absorption was much greater on the filter (Kiefer and SooHoo, 1982). One can therefore make use of a pathlength amplification factor, β, as follows

$$\beta = \frac{\bar{a}_p}{\bar{a}_s} \tag{4.4}$$

where $\bar{a}_p$ and $\bar{a}_s$ represent the wavelength-averaged values of $a_p(\lambda)$ and $a_s(\lambda)$ between 350 and 700 nm, respectively. Assuming that the value obtained from the total suspended particles was the same as that of phytoplankton cells, the specific absorption coefficient of phytoplankton, $k_c(\lambda)$, can be estimated as follows

$$k_c(\lambda) = \frac{a_{ph}(\lambda)}{\beta \times \text{Chl}} \tag{4.5}$$

in which Chl is the chlorophyll concentration.

Three different species of cultured phytoplankton and peat moss suspension were used to test this technique (Fig. 4-5). Methanol treatment removed more

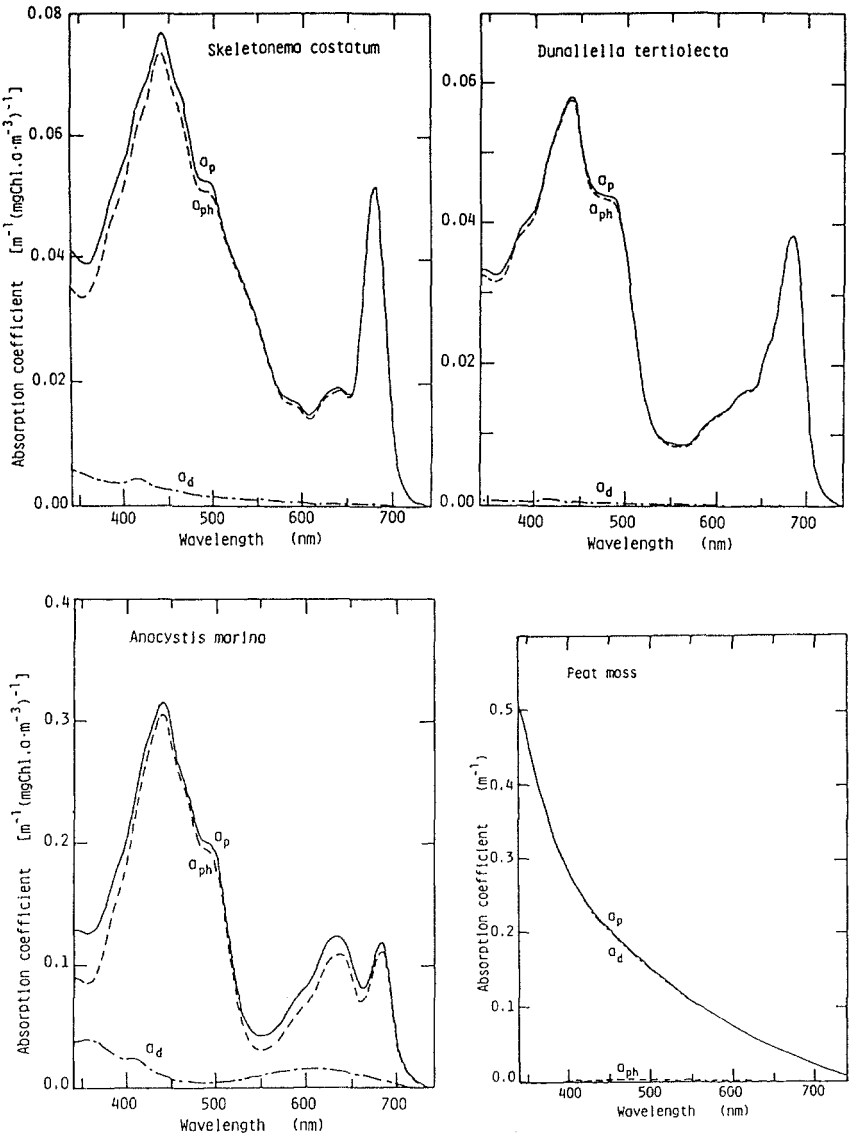

Fig. 4-5. Light absorption spectra of cultured phytoplankton cells and peat moss before (a_p) and after (a_d) methanol treatment; a_{ph} is light absorption by phytoplankton. (From Kishino et al., 1985.)

than 95.5% of photosynthetic pigments from *Skeletonema costatum* and *Dunaliella tertiolecta*. *Anacystis marina*, whose major accessory pigments are water-soluble phycobiliproteins, also had most of its photosynthetic pigments extracted (90.4%) by the methanol treatment. The absorption of a peat moss sample, which contained only detrital particles, is consistently higher at the

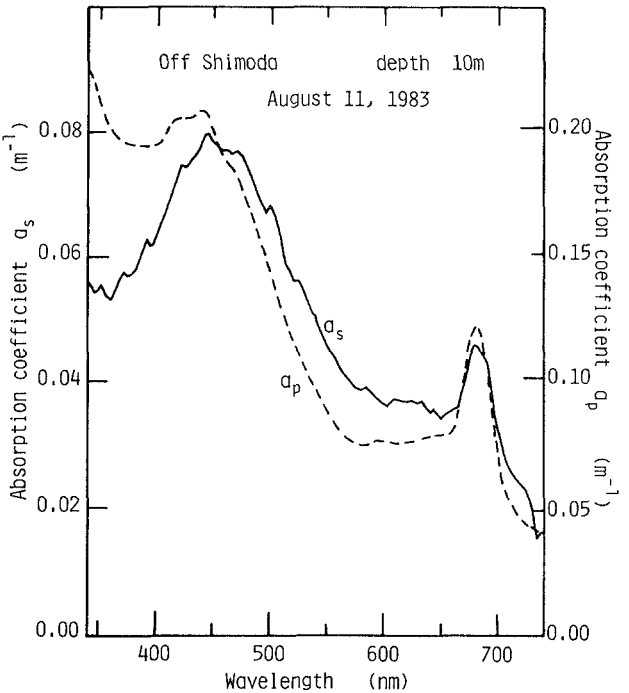

Fig. 4-6. Light absorption spectra of suspended particles in natural seawater determined by modified opal glass technique (a_p) and by direct determination in suspension (a_s). (From Kishino et al., 1985.)

shorter wavelengths. It is obvious that there is no difference in the absorption spectrum before and after the methanol treatment. This suggests that detrital particles in the seawater do not change the absorption spectrum obtained by methanol treatment.

Figure 4-6 shows the absorption spectra of suspended particles in natural seawater determined by the modified opal glass technique and by direct determination in suspension. Both spectra show a similar pattern, although a slight difference is noticed between 550 and 600 nm and at wavelengths shorter than 400 nm. The averaged pathlength amplification factor obtained for the sample is 2.45. These results confirm that the modified opal glass technique gives an excellent spectrum of absorption for particles suspended in water.

Figure 4-7 shows the light absorption spectra of suspended particles determined by the modified opal glass technique for seawater samples collected from the euphotic and disphotic (i.e. below 1% surface irradiance level) zones. The spectrum of a_p in the euphotic zone shows a pattern indicating light absorption by chlorophyll *a* and various photosynthetic pigments around 680 nm and between 400 and 500 nm. After methanol treatment, the filter paper becomes pale yellow, and a simple spectrum, a_d, with a consistent increase towards shorter wavelengths is obtained, and a characteristic phytoplankton absorption curve,

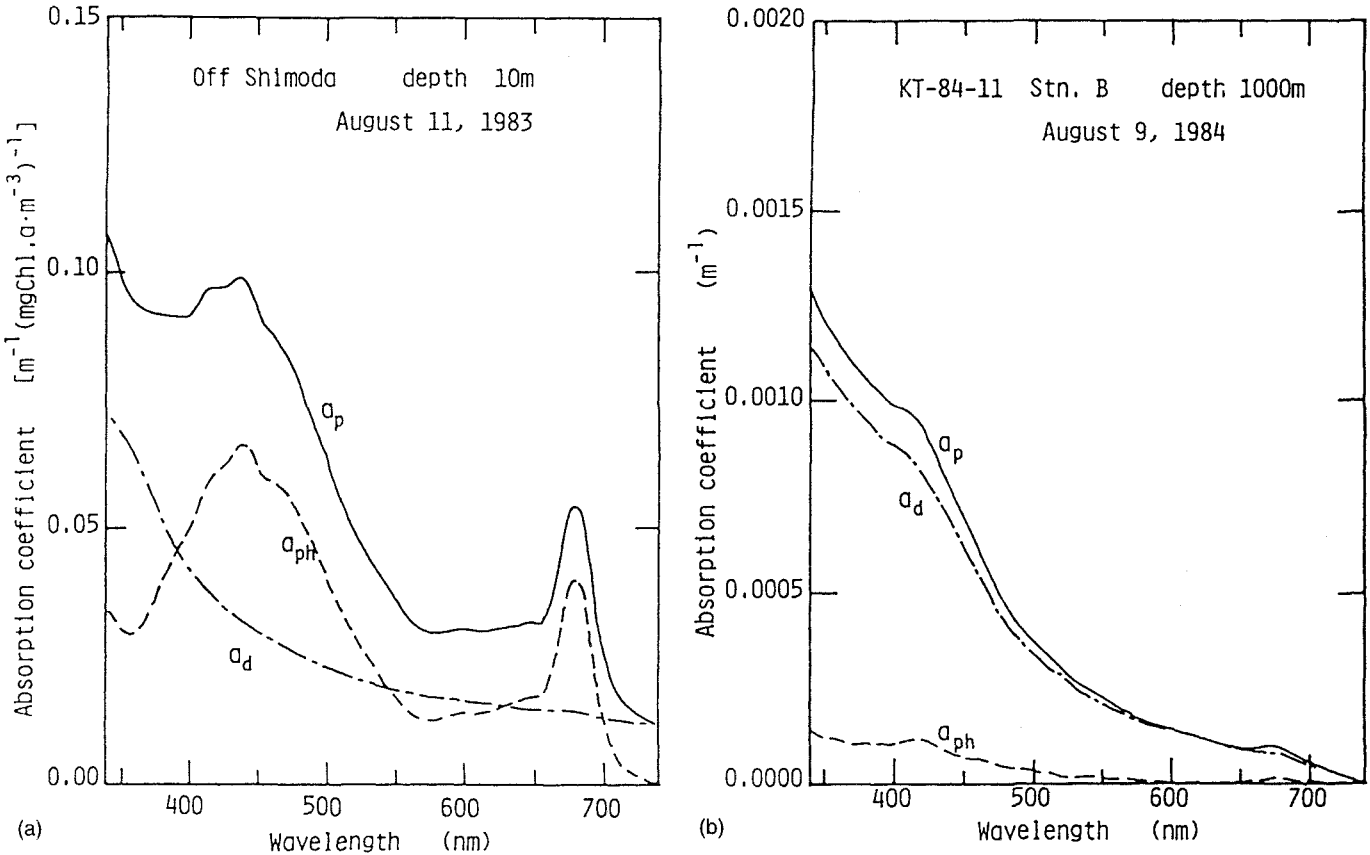

Fig. 4-7. Light absorption spectra of suspended particles in the euphotic zone (a) and disphotic zone (b). (From Kishino et al., 1985.)

a_{ph}, is obtained. The absorption spectra of the disphotic zone sample show little difference in the patterns before and after the methanol treatment, suggesting negligible contribution by algae.

The major portion of photosynthetic pigments in natural phytoplankton can be extracted by methanol. Consequently it is suggested that the specific spectral absorption coefficient of phytoplankton in natural seawater can be measured by the modified opal glass technique combined with methanol extraction treatment.

Contribution of phytoplankton and other components to the light field in the sea

Measurements of the absorption coefficient of seawater were carried out at various stations covering a wide range of optical water types in the study area (Fig. 4-2). The spectral absorption coefficient of phytoplankton, $a_{ph}(\lambda)$, and other living and nonliving particles, $a_d(\lambda)$, were measured by the modified opal glass technique. The absorption of filtered seawater, $a_y(\lambda)$, was measured relative to that of distilled water using the spectrophotometer (Shimadzu MPS-5000). Total light absorption coefficient, $a(\lambda)$, was calculated as follows:

$$a(\lambda) = a_{ph}(\lambda) + a_d(\lambda) + a_y(\lambda) + a_w(\lambda) \tag{4.6}$$

where $a_w(\lambda)$ is the absorption coefficient of pure water (Smith and Baker, 1981).

Figure 4-8 shows the light absorption spectra measured at two stations: S-1 and T-1. At Stn. S-1 in the coastal water, the total absorption coefficient was $0.20\,m^{-1}$ and light absorption by water was significant at wavelengths longer 500 nm. Phytoplankton absorbed light energy at wavelengths between 400 and 500 nm and absorption of dissolved matter mainly contributed at wavelengths shorter than 400 nm. Light absorption by particles other than phytoplankton was minor at wavelengths shorter than 500 nm. At Stn. T-1, in the turbid water of Tokyo Bay, the total absorption coefficient was $1.3\,m^{-1}$. Water absorbed light significantly at wavelengths longer than 600 nm, and dissolved matter absorbed mostly at wavelengths shorter than 400 nm. Absorption of light by phytoplankton was striking at wavelengths between 400 and 500 nm and around 680 nm.

Table 4-1 indicates the relative contribution of each component to total light absorption measured at various locations in the study area. All figures in the table are values integrated over the wavelength of PAR (Photosynthetically available radiation from 350–700 nm). Light absorption by water was more than 90% in the clearest water and decreased with increases in total absorption, dropping to roughly 10% in the highly turbid water. In contrast, the contribution by phytoplankton to light absorption was only 1.4% in the clearest water and 40% in extremely turbid water. Light absorption by particles other than phytoplankton ranged from 2.9% to 43.8%, depending on the character of water mass. The contribution of dissolved matter to total absorption was 3.1% in the clearest

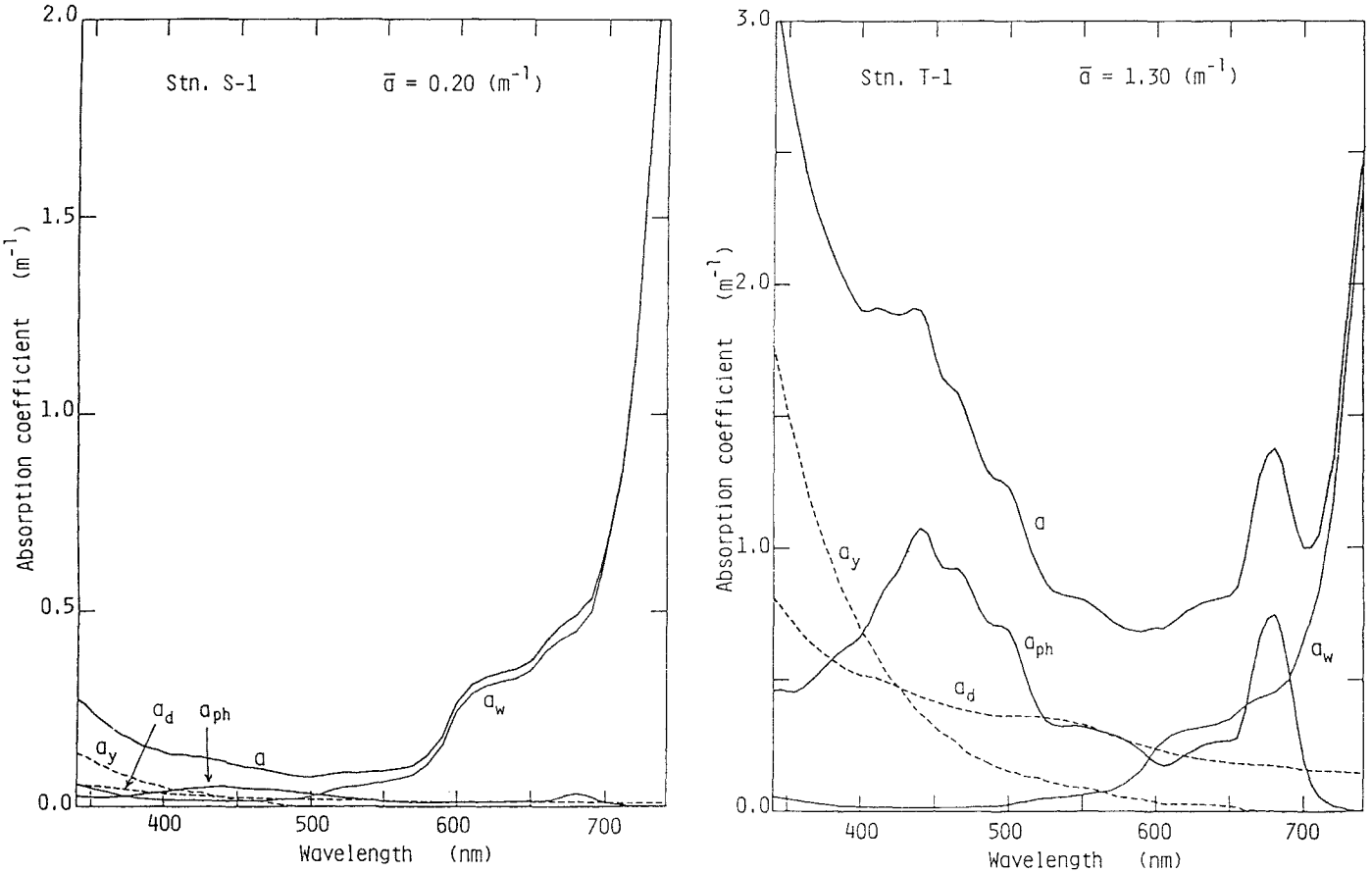

Fig. 4-8. Absorption spectra of raw sample water (a), water (a_w), phytoplankton (a_{ph}), other particles (a_d), and dissolved matter(a_y).

Table 4-1. Relative contribution of light absorption coefficients of water ($\bar{a}_w$), phytoplankton ($\bar{a}_{ph}$), other particles ($\bar{a}_d$) and dissolved matter ($\bar{a}_y$) to total light absorption ($\bar{a}$) integrated over the range of PAR

Station	Sampling depth (m)	$\bar{a}$	$\bar{a}_w$	$\bar{a}_{ph}$	$\bar{a}_d$	$\bar{a}_y$	Chl *a*
Pure water		0.14	100.0	0.0	0.0	0.0	0.0
F	0	0.15	92.6	1.4	2.9	3.1[a]	0.081
F	30	0.16	91.1	2.0	3.6	3.3[a]	0.102
F	75	0.18	80.5	7.3	6.3	5.9[a]	0.464
S-2	10	0.19	73.5	9.2	8.4	8.9	1.21
S-1	10	0.20	68.7	12.7	10.1	8.5	1.89
T-11	0	0.27	51.9	5.5	29.1	13.5	0.66
T-10	0	0.38	37.3	20.4	30.0	12.3	3.42
T-9	0	0.40	35.5	6.6	39.0	18.8	1.77
T-8	0	0.43	32.8	12.7	38.5	16.0	2.27
T-7	0	0.52	27.3	9.8	39.1	23.8	4.32
T-6	0	0.54	26.1	13.1	30.5	30.2	4.85
T-5	0	0.62	22.7	15.1	29.7	32.4	7.64
T-4	0	0.68	20.7	17.4	41.3	20.6	7.72
T-3	0	0.82	17.2	24.6	43.8	14.3	13.6
T-2	0	0.84	16.8	27.9	30.7	24.6	13.5
T-1	0	1.30	10.8	40.5	27.1	21.6	39.1

[a]Estimated from $K(\lambda)$.

water, increasing to over 30% in the turbid water. This confirms that the contribution of phytoplankton to the light field is small in chlorophyll-poor clear water and large in chlorophyll-rich turbid water.

Quantum yield of photosynthesis in a thermally stratified sea

The quantum yield of photosynthesis, ϕ, is derived from the photosynthetic rate based on chlorophyll *a*, P, divided by the quanta absorbed by the phytoplankton, PUR (Morel, 1978),

$$\phi = P/\mathrm{PUR}$$

Photosynthetic rate can be measured experimentally. PUR is estimated from PAR multiplied by the mean specific absorption coefficient, $\bar{k}_c$

$$\mathrm{PUR} = \mathrm{PAR} \times \bar{k}_c$$

where $\bar{k}_c$ is estimated from the specific spectral absorption coefficient.

In the present study, the quantum yield of phytoplankton was estimated under natural conditions. A well-stratified, open-ocean environment was chosen for the

experimental site, where phytoplankton were considered to be well-adapted to the light environment.

Total irradiance at the sea surface was monitored continuously with a pyranometer on the ship's upper deck. Underwater downward spectral irradiance was determined with the underwater irradiance meter (Fig. 4-1). The specific absorption coefficient of phytoplankton was determined by the modified opal glass technique. The photosynthetic rate of phytoplankton was measured by the in situ method using a ^{13}C-technique (Hama et al., 1983). Samples were collected with a 20-liter Niskin bottle before sunrise and dispensed into 500-ml Pyrex glass bottles. Following the addition of $NaH^{13}CO_3$, the bottles were suspended at given depths. Incubation was conducted from sunrise to noon, noon to sunset, and sunrise to sunset. After incubation, all samples were immediately filtered onto glass fiber filters (Whatman GF/F) and ^{13}C content was determined using a mass spectrometer (ANELBA, TE-150).

Temporal variations in the profile of PAR in terms of percent of surface irradiance at different times of the day are shown in Fig. 4-9. Light energy decreases rapidly in the top 5 m because of rapid absorption of red light, followed by an almost exponential decrease with depth. The 10% light depth occurs between 40 and 47 m, and the 1% light level is between 79 and 92 m. The downward spectral irradiance at this station is shown in Fig. 4-3a.

Light absorption by suspended particles collected from 20 and 70 m depths at this station is shown in Fig. 4-10. The curve of a_{ph} shows two major peaks at 440 and 680 nm.

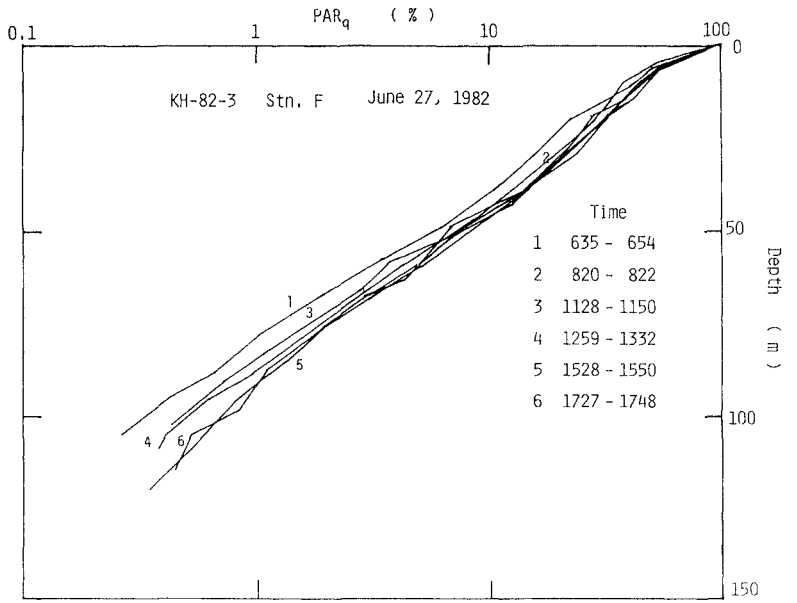

Fig. 4-9. Relative light intensity of PAR in the water column. (From Kishino et al., 1986.)

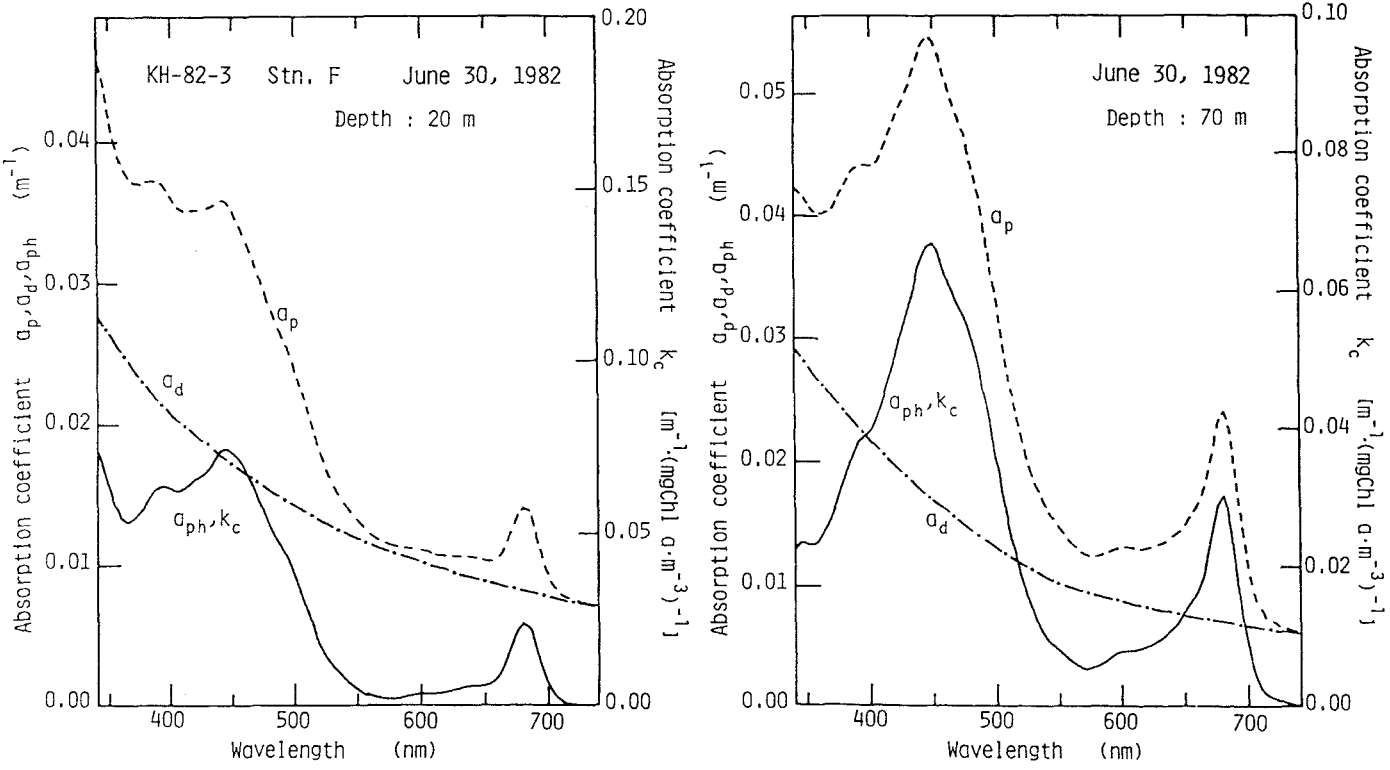

Fig. 4-10. Absorption spectra of suspended particles retained on glass fiber filter. (From Kishino et al., 1986.)

The mean specific absorption coefficient, $\bar{k}_c$, which is weighted for spectral irradiance, and $\tilde{k}_c$ which is not weighted for spectral irradiance, are calculated for the range of PAR as follows:

$$\bar{k}_c = \frac{\int_{350}^{700} k_c(\lambda)(\lambda/\hbar c)E_d(\lambda)\,\partial\lambda}{\int_{350}^{700} (\lambda/\hbar c)E_d(\lambda)\,\partial\lambda} \tag{4.7}$$

$$\tilde{k}_c = \int_{350}^{700} \frac{k_c(\lambda)\,d\lambda}{(700 - 350)} \tag{4.8}$$

Figure 4-11 shows $\bar{k}_c$ and $\tilde{k}_c$ plotted as functions of depth. The values of $\tilde{k}_c$ vary from 0.0222 to 0.03 m^{-1} (mgChl*a* m^{-3})$^{-1}$. There is no consistent trend with depth. However the value of $\bar{k}_c$ increases rapidly with depth from 0.022 at the surface

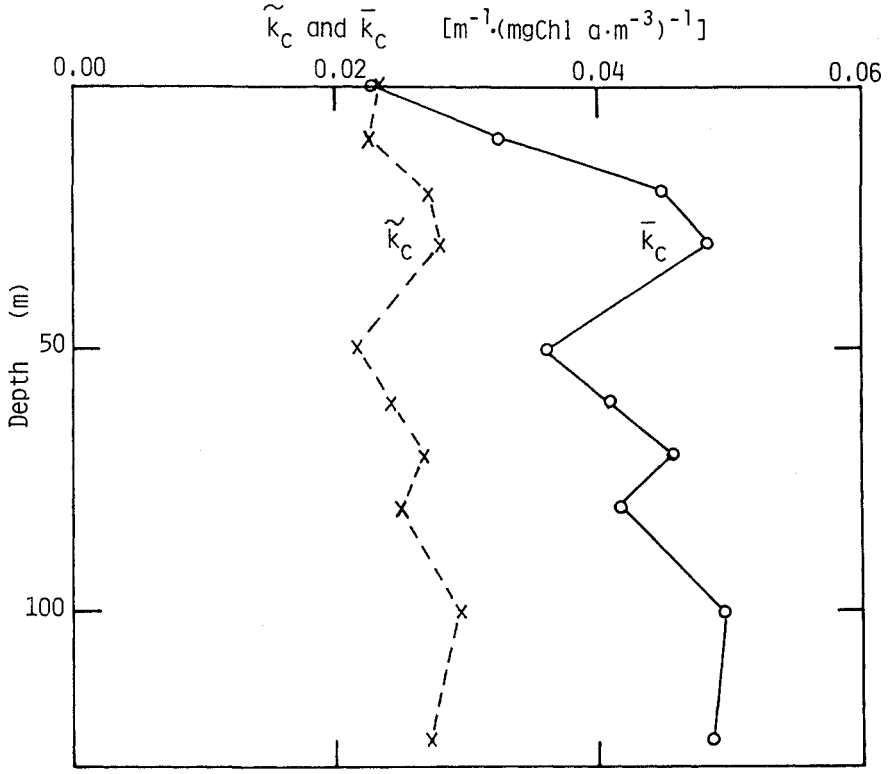

Fig. 4-11. Vertical changes of $\bar{k}_c$ and $\tilde{k}_c$ of phytoplankton. (From Kishino et al., 1986.)

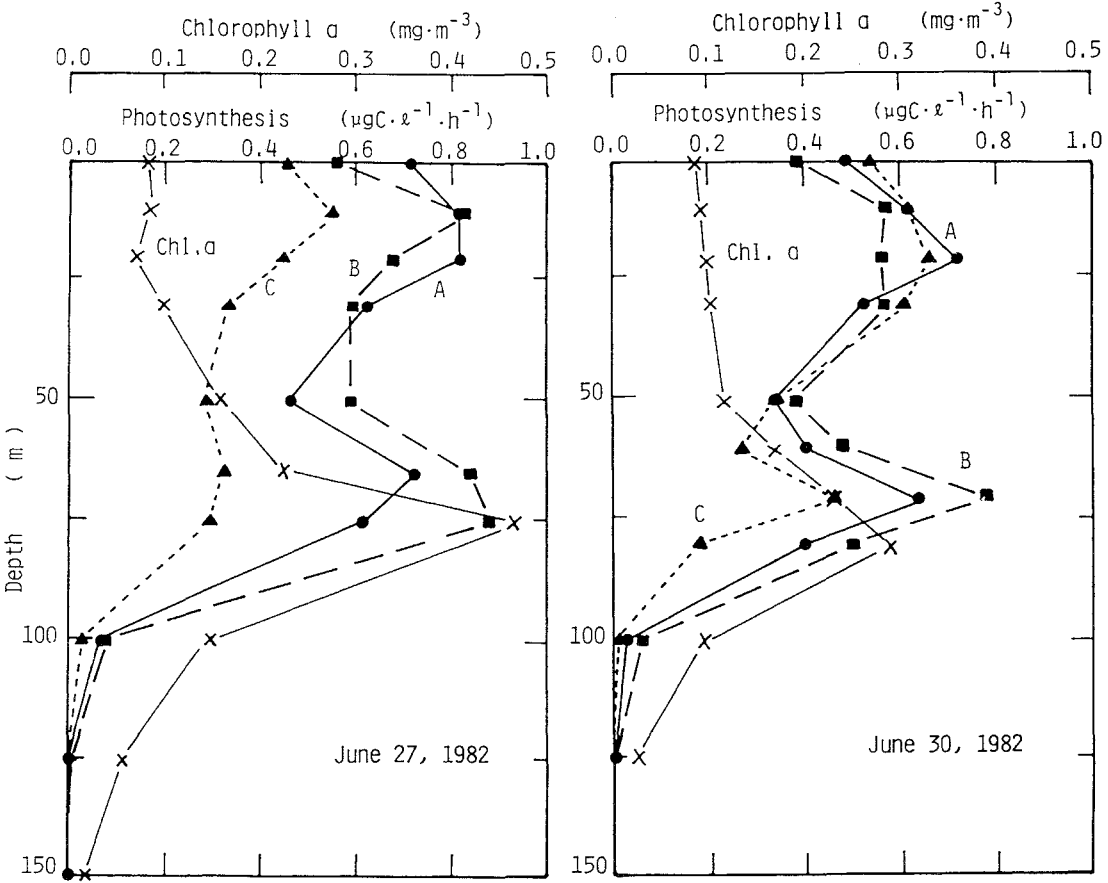

Fig. 4-12. Vertical profiles of chlorophyll *a* and in situ photosynthesis. Curves A, B and C represent sunrise to sunset, sunrise to noon, and noon to sunset segments, respectively. (From Kishino et al., 1986.)

to 0.044 at 30 m and fluctuates between 0.036 and 0.050 m^{-1} $(mgChl\,a\,m^{-3})^{-1}$. The high $\bar{k}_c$ is due to the combined effects of the high specific light absorption by phytoplankton at wavelengths <500 nm and the increase in the relative proportion of blue light.

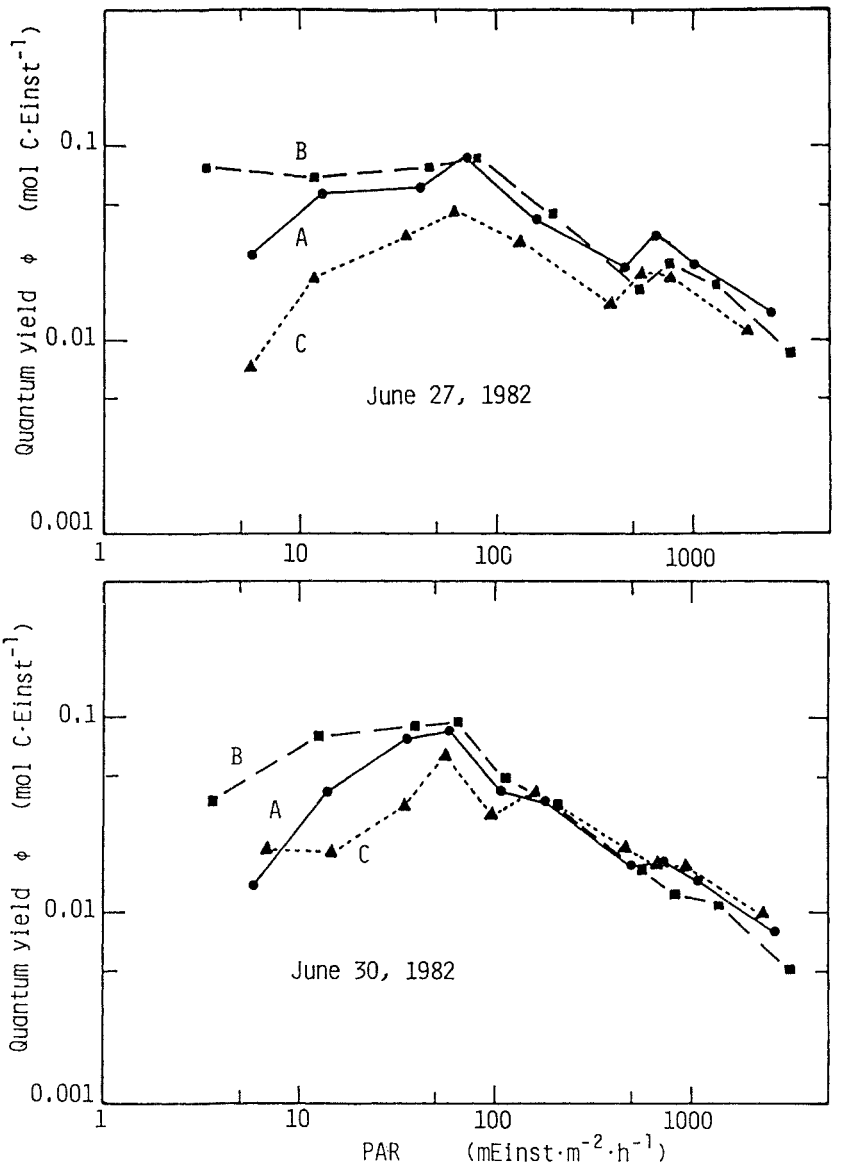

Fig. 4-13. Quantum yield of phytoplankton occurring in different light intensities at various depths. Curves A, B and C as in Fig. 4-12. (From Kishino et al., 1986.)

Vertical profiles of in situ photosynthesis and chlorophyll *a* are shown in Fig. 4-12. Chlorophyll profiles show a distinct peak at 75 or 80 m. However, there was no chlorophyll peak in the top of 30 m. Two peaks are noted in the profiles of in situ photosynthesis, one near the surface and other at 75 m depth. Photosynthesis in the morning (B) is higher than in the afternoon (C); this is more pronounced at the depth of the subsurface chlorophyll maximum.

The resultant photosynthetic quantum yield of phytoplankton is plotted in Fig. 4-13 against PAR measured at each depth. Quantum yields are 0.005–0.013 at the surface (right-hand side of figure), 0.013–0.033 at the surface photosynthesis maximum, 0.033–0.094 at the subsurface chlorophyll maximum, and 0.007–0.077 mol C $Einst^{-1}$ below 100 m. Yields at the depth of the subsurface maximum are very close to the maximum yield obtained experimentally in the laboratory (Kok, 1960; 0.1 mol C $Einst^{-1}$). However, the irradiance measured in this case is the *downward* irradiance (with a cosine collector), which is expected to show about 20% less energy than the scalar irradiance (with a spherical collector) in the sea. Consequently, the quantum yield under scalar irradiance will be reduced to about 80% of the value obtained here. Nevertheless, it is obvious that phytoplankton at the subsurface chlorophyll maximum depth have a high photosynthetic activity. This result strongly suggests that phytoplankton inhabiting the bottom of the euphotic zone apply the greatest effort to absorb light energy.

5

OPTICS FROM THE SINGLE CELL TO THE MESOSCALE

André Morel
Université Pierre et Marie Curie

Introduction

The inherent optical properties of a water body (mesoscale), namely, the absorption coefficient, the scattering coefficient, and the volume scattering function combine with the radiant distribution above the sea to yield the apparent optical properties (Preisendorfer, 1961). The radiative transfer equation is the link between these two classes of optical properties.

Locally, the inherent properties of seawater are governed by, and strictly result from, the sum of the contributions of the various components, namely, the water itself, the various particles in suspension able to scatter and absorb the radiant energy, and finally the dissolved absorbing compounds. Analyzing these contributions is an important goal of optical oceanography. Among these particles, the phytoplanktonic cells, with their photosynthetic pigments, are of prime importance, in particular in oceanic waters far from terrestrial influence. They also are at the origin of other kinds of particles, such as their own debris, as well as other living "particles" grazing on them (bacteria, flagellates and other heterotrophs). Studying optics at the level of single cells and particles is therefore a requirement for a better understanding of bulk optical properties of oceanic waters.

Independently of this goal, the study of the individual cell optics per se is fundamental when analyzing the pathways of radiant energy, in particular the light harvesting capabilities and the photosynthetic performances of various algae or their fluorescence responses.

The following presentation is a guidline for readers who will find detailed studies in the classic books *Light Scattering by Small Particles* by van de Hulst (1957) and *Light and Photosynthesis in Aquatic Ecosystems* by Kirk (1983), as well as in a paper dealing specifically with the optics of phytoplankton by Morel and Bricaud (1986).

This chapter is organized according to the title, with first a summary of the relevant theories to be applied when studying the interaction of an

electromagnetic field with a particle, and then, as a transition between this scale and that of in vitro experiments, some results concerning the optical behavior of pure algal suspensions; finally the more complicated situations encountered in natural environments are briefly described to introduce the "nonlinear biological" effect (Smith and Baker, 1978a) upon the optical coefficients for oceanic waters, and to examine some of the empirical relationships, as presently available, between the pigment concentration and the optical properties of the upper ocean at mesoscale and global scale.

Single-particle optics and optical coefficients

The dimensionless efficiency factors for absorption, Q_a, and for scattering, Q_b, are defined as the ratios of the radiant energy absorbed within or scattered by the particle to the radiant energy impinging upon its geometrical cross-section, s. The efficiency factor for attenuation, Q_c, is defined as $Q_c = Q_b + Q_a$. In addition, the factor Q_b can be split into $Q_b = Q_{bf} + Q_{bb}$, where the subscripts b and f refer to the backscattering and forward-scattering components, respectively. In turn, multiplying these dimensionless factors by the geometrical cross-section of the particle, s, yields the optical cross-section for a given process (absorption or scattering). Note that in a similar way and by ratioing emitted energy or stored energy to the impinging energy, one might derive efficiency factors, and then cross-sections, for Raman scattering and for fluorescence, or even for photosynthesis.

These properties, defined at the single-particle level can be related to the absorption and scattering coefficients for a suspension, a and b, respectively. They are simply expressed as the product of the absorption or scattering cross-section with the number of particles per unit volume of suspension, N/V. The units are m^{-1}. That is,

$$\begin{aligned} a &= (N/V)Q_a s \\ b &= (N/V)Q_b s \end{aligned} \tag{5.1}$$

Within the suspension (or in seawater) for the concentration of a given substance, denoted C (C is often the chlorophyll concentration when dealing with algae, but could be carbon concentration for a more general use), the "specific" coefficient (starred symbol) is defined as the ratio of the absorption or scattering coefficient to this concentration; thus

$$\begin{aligned} a^* &= a/C \\ b^* &= b/C \end{aligned} \tag{5.2}$$

with

$$C = (N/V)c_i v$$

or

$$a^*, b^* = Q_{a,b}(c_i d)^{-1} g$$

where g (3/2 for a sphere) is a geometrical factor defined as $g = (s \bullet d)\ v^{-1}$, where v is the volume of an individual particle, d is the characteristic size (e.g., the diameter if particles can be assumed spherical), and c_i is the internal (cellular) concentration of the substance of interest. If the size distribution of particles is polydisperse, the formulations are somewhat more complex and become

$$a,b = \frac{1}{V}\int_0^\infty F(d)Q_{a,b}(d)s(d)\,\partial d$$
$$C = \frac{c_i}{V}\int_0^\infty F(d)v(d)\,\partial d \tag{5.3}$$

where $F(d)$ is the size distribution function, with sizes from 0 to ∞ (or other more realistic limits), and $s(d)$ and $v(d)$ are, respectively, the geometrical cross-section and the volume of the particle expressed as a function of its characteristic size.

For particles sufficiently large compared to the wavelength, the laws of geometrical optics and diffraction can be applied. For the simplest case, consider a totally absorbing particle for which, by definition, $Q_a = 1$. For such a particle the theorem of complementary screens (Babinet's principle) states that the diffraction pattern of the particle is the same as the diffraction pattern due to a pinhole having the same cross-section. This means that an amount of energy equal to that impinging on the geometrical cross section is diffracted (i.e., scattered). Therefore, $Q_b = 1$ also. Consequently, the attenuation efficiency factor, $Q_c = 2$. This entails that such a particle is able to remove twice as much as energy it can geometrically intercept. This result is generally referred to as the "extinction paradox." Another extreme case is that of a totally transparent particle for which, by definition, $Q_a = 0$. The diffraction pattern is unchanged from the previous example, but now all the light entering the particle, which cannot be absorbed, actually is diverted by refraction and reflection, or in other words is scattered. This leads to $Q_b = 2$ (1 for the diffraction and 1 for refraction plus reflection) with also $Q_c = Q_b = 2$. In the intermediate situation of a large particle that is partly absorbing, Q_a is between zero and 1, and Q_b is between 1 and 2, so that Q_c remains equal to 2. This value is only a limiting value for those particles that are large enough with respect to the wavelength.

In general, particles are not necessarily large with respect to the wavelength. In such a case, all the efficiency factors are functions of the size and of the index of refraction of the particles. The important length scale is the term given by the relevant size with respect to the wavelength, denoted α and defined as

$$\alpha = \frac{\pi d}{\lambda} n_w \tag{5.4}$$

where λ is the wavelength of the light in vacuo, and n_w is the index of refraction of the surrounding medium (water in our case, and λ/n_w is the wavelength in

water). The particle refractive index of interest is the relative index with respect to that of water, denoted m. Generally, this index has a complex form, meaning that it describes the absorption by an imaginary term, related to the absorption coefficient of the substance forming the particle:

$$m = \frac{m_{\text{subst}}}{n_w} = n - in' \tag{5.5}$$

with

$$n' = \frac{\lambda}{4\pi n_w} a_{\text{subst}}$$

Note that n_w is also a complex number; in the visible part of the spectrum, however, the imaginary part can safely be neglected. For weakly refractive (or "soft") particles, the anomalous diffraction theory as developed by van de Hulst (1957) can be applied to derive the Q factors. Biological material in suspension in seawater is adaptable to this approximation, which implies that the real part of the relative index is close to 1 and that the imaginary part is very small. Marine phytoplankton (also free-living bacteria and other heterotrophs) have a high water content, and also, the organic substances they contain (carbohydrates, proteins, and lipids) have refractive indices only slightly above that of water (see Aas, 1981). Even silica in diatoms (relative index 1.08) is not very refringent; the exception is calcite with $n = 1.15$, and detached scales from coccolithophorids are no longer soft particles. For the living cells, and likely for most of the organic detritus, n remains well below 1.10 (Zaneveld et al., 1974; Spinrad and Brown, 1986). The imaginary part is never high, even for the most pigmented phototrophic species, and n' does not seem to exceed 0.015. Therefore the van de Hulst approximation can be used.

When using this approach, the dimensionless parameters α and m are conveniently combined according to

$$\rho = 2\alpha(n - 1) \tag{5.6}$$

$$\rho' = 4\alpha n' = a_{\text{subst}} d \tag{5.7}$$

The first term is, physically speaking, the phase lag along the central ray that passes through the particle (along the diameter for a sphere). The second term is the optical thickness of this particle along the same central ray. The two terms can be combined as follows: if

$$\frac{n'}{n - 1} = \tan \xi \tag{5.8}$$

then

$$\rho' = 2\rho \tan \xi$$

The Q factors are functions of these parameters according:

$$Q_c(\rho) = 2 - 4e^{-\rho \tan \xi} \left[\left(\frac{\cos \xi}{\rho} \right) \sin(\rho - \xi) + \left(\frac{\cos \xi}{\rho} \right)^2 \cos(\rho - 2\xi)^2 \right] + 4 \left(\frac{\cos \xi}{\rho} \right) \cos 2\xi \tag{5.9}$$

$$Q_b(\rho) = Q_c(\rho) - Q_a(\rho) \tag{5.10}$$

$$Q_a(\rho) = 1 + \frac{e^{2\rho \tan \xi} (2\rho \tan \xi + 1) - 1}{2\rho^2 \tan^2 \xi} \tag{5.11}$$

There is a simplification of Eq. (5.9) if the particle is nonabsorbing (with $\xi = 0$ and $Q_a = 0$); in that case Q_b becomes simply equal to Q_c, with

$$Q_c = 2 - \frac{4}{\rho} \sin \rho + \frac{4}{\rho^2} (1 - \cos \rho) \tag{5.12}$$

It can be verified that for large particles (large ρ values), Q_c tends asymptotically toward the value 2 (Eqs. 5.9 or 5.12), whereas Q_a tends toward 1 (Eq. 5.11). Figure 5-1 shows the behavior of the efficiency factors for different values of the imaginary part of the relative refractive index for increasing ρ values. In the natural environment, or even in a culture experiment, one must take into consideration the fact that the cell sizes (or particle sizes) are not all the same, therefore a particle size distribution function has to be considered. When combining such a function with the above expressions, the result is a reduction in the amplitude of the oscillations in the Q_c (or Q_b) curve by an amount dependent on the width of the size distribution (see Fig. 5-2).

Only the efficiency factors can be derived using the van de Hulst approximation. To obtain information about the volume scattering function, Mie theory must be used (also to compute the exact solution for the Q factors when the particles cannot be considered "soft," for instance, when dealing, with minerals).

There is another physical phenomenon that is important in governing the absorption and scattering properties of a particle. It is the fact that the real part and the imaginary part of the index of refraction are not independent. This phenomenon, called anomalous dispersion, follows the Ketteler–Helmotz theory, which predicts that the real part of the refractive index changes slightly in the vicinity of an absorption band, when n' departs from zero (Fig. 5-3). As a consequence, the absorption affects the scattering in two ways: "directly" because with Q_a differing from zero, Q_b (= $Q_c - Q_a$) is depressed, and "indirectly", because the fluctuations in n induced by the existence of n' act upon

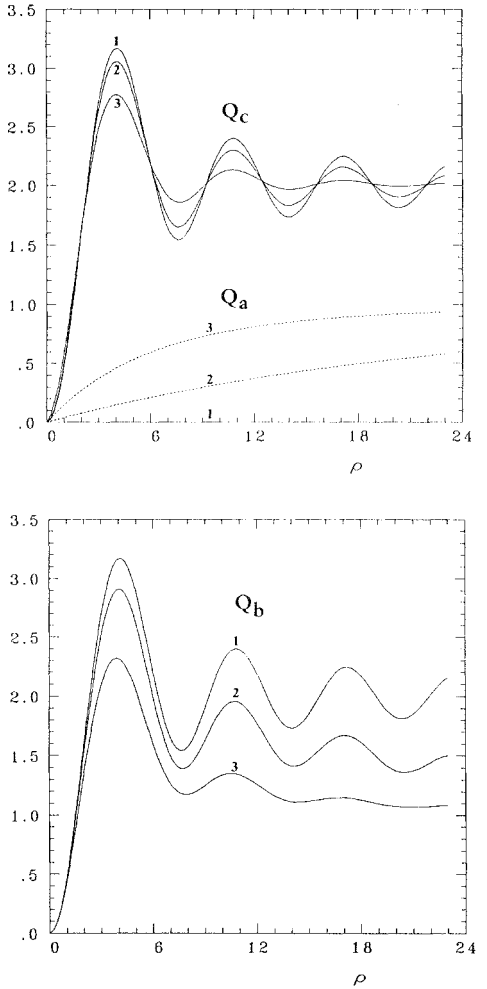

Fig. 5-1. *Upper*: efficiency factor for attenuation, Q_c, and for absorption, Q_a, as a function of ρ (Eqs. 5.6, 5.9, and 5.11) and for three values of $\tan \xi = n'/(n - 1)$, namely 0 (nonabsorbing particle, with $Q_a = 0$), 0.03 and 0.12, curves labelled 1, 2, and 3, respectively. *Lower*: corresponding efficiency factor for scattering, Q_b, obtained as $Q_c - Q_a$. (Adapted from Morel and Bricaud, 1986.)

the Q_c values. This second effect (in reality these effects cannot be simply discoupled) explains the spectral shift between the absorption maximum and the scattering minimum. These effects are systematically observed in measurements of naturally occurring species such as *Synechococcus* as shown in Fig. 5-3.

With the above relationships it is also possible to develop a model of the optical properties of an algal cell (Bricaud and Morel, 1986). The input parameters for the model are the absorption spectrum, and the size distribution function in absolute number of cells per unit of volume and per size increment.

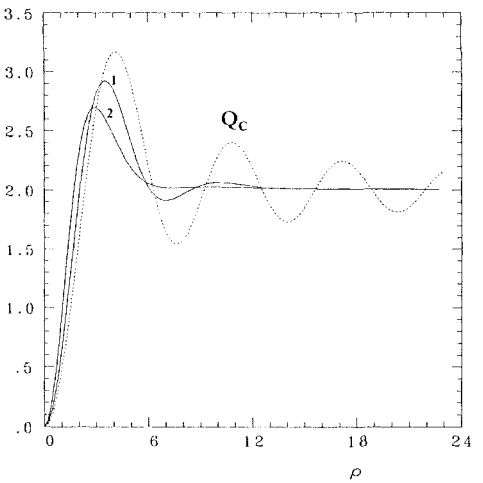

Fig. 5-2 . Mean efficiency factor for attenuation Q_c for a "mean" particle representative of a population of nonabsorbing particles for which the size distribution is a log-normal function. The dotted curve is for monosized particles (curve 1 from Fig. 5-1, upper panel); the solid curves 1 and 2 are for size distribution with increasing widths. (Adapted from Morel and Bricaud, 1986.)

From these one can derive the $Q_a'(\lambda)$ spectrum (the prime means that $Q_a(\lambda)$ is obtained for a "mean cell" representative of the population and accounts for the actual size distribution). From these $Q_a'(\lambda)$ values the corresponding imaginary part of the refractive index can be computed as a function of the wavelength. To do that, Eq. (5.11) is solved for ρ' at each wavelength and thus provides the $n'(\lambda)$ spectrum (Eq. 5.7). This spectrum is then decomposed into several oscillators of varying amplitude and damping constant (see Fig. 5-3) and the corresponding fluctuations in the real part, n, are computed (Ketteler–Helmotz theory) and summed. The fluctuations in the $n(\lambda)$ spectrum are around a "central" value (denoted $1 + \varepsilon$ in Figure 5-3) that is not yet determined. Using Eq. (5.6), the computed $Q_c'(\lambda)$ spectrum is put into coincidence with the experimental $Q_c'(\lambda)$ spectrum by changing the ε value. If this coincidence can be achieved (only when measurements are reliable) the real part of the index, $n(\lambda)$, is obtained. The assumption of sphericity (included in Eqs. 5.9 and 5.11) may be a source of error in this scheme. It could be abandoned and other shapes considered (see Aas, 1984). Conversely if this assumption is satisfied a priori (for specific spherical cells) the above scheme can reduce to an iterative and simultaneous use of Eqs. (5.9) and (5.11), by demanding that the computed $Q_a'(\lambda)$ and $Q_c'(\lambda)$ spectra be coincident with the experimental ones (Stramski et al., 1988). No resort to oscillators is needed and the $n(\lambda)$ and $n'(\lambda)$ are obtained directly.

Another consideration is evolution of the efficiency factor for absorption, Q_a, as a function of the ρ' parameter (Fig. 5-4). The curvature and the saturation portion of this curve have an important consequence. This implies that doubling the internal concentration of intracellular pigments, and thus doubling ρ', does

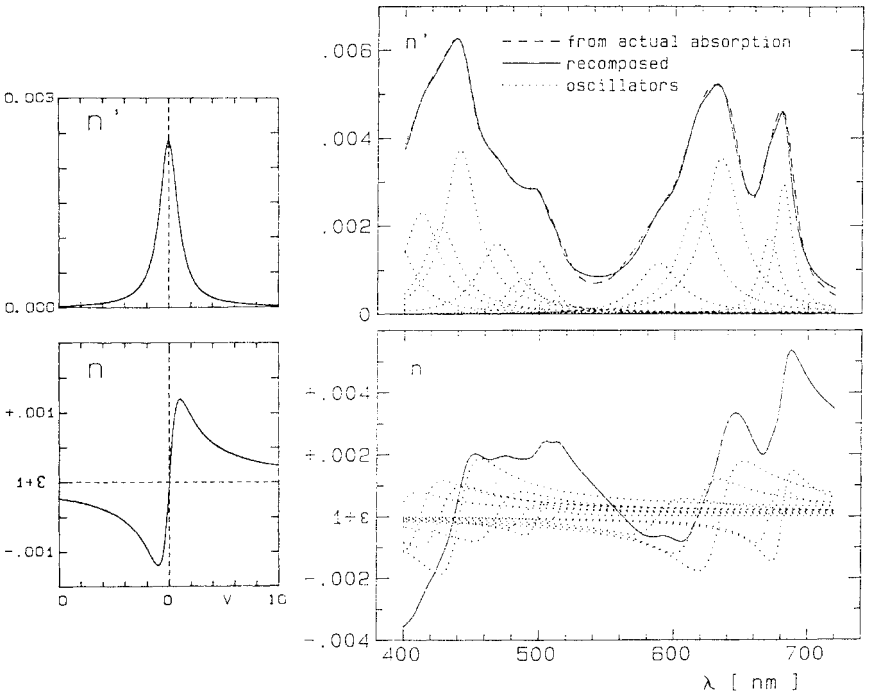

Fig. 5-3. *Left*: concomitant variations of the real and imaginary parts of the index of refraction, n and n', around an absorption band, as predicted by Ketteler–Helmotz theory. The abscissa, ν, represents the quantity $\nu = 2\ (\nu - \nu_0)/\gamma$, where ν is the wavenumber, ν_0 the wavenumber at the resonance peak (maximum in absorption and in n') and γ is the damping constant. *Right*: "experimental" $n'(\lambda)$ spectrum (computed from actual $Q_a(\lambda)$ values and solving Eq. 5.11) shown as a dashed curve; the dotted curves represent the oscillators with the corresponding n and n' variations (as in the left panel). The addition of their effect provides the "recomposed" $n'(\lambda)$ spectrum and the corresponding variations of $n(\lambda)$, shown as solid curves. (Adapted from Stramski et al., 1988; experiment with *Synechocystis* sp. grown under 20 $\mu E\, m^{-2}\, s^{-1}$.)

not necessarily double the capacity of the cell to capture light (this capacity is expressed by Q_a). This is the so-called "packaging" effect or "discreteness" effect (Kirk, 1975; Morel and Bricaud, 1981), now recognized as being characteristic of most of phytoplanktonic species, apart from the very tiny ones (having ρ' small enough that the Q_a curve is practically confounded with its initial tangent). Coming back to Eq. (5.2), the chlorophyll-specific coefficient, a^*, cannot be a constant because of the nonlinear behavior of Q_a with respect to the inner concentration in chlorophyll (in c_i). This reasoning assumes that chlorophyll is the only absorbing pigment (an assumption roughly verified in the red absorption band). In addition, with accessory pigments in changing proportions according to the species, it is conceivable that the $a^*(\lambda)$ spectra, by virtue of normalization to the sole pigment, chlorophyll, are necessarily variable for various phytoplantkers. Associated with the packaging effect there is also a

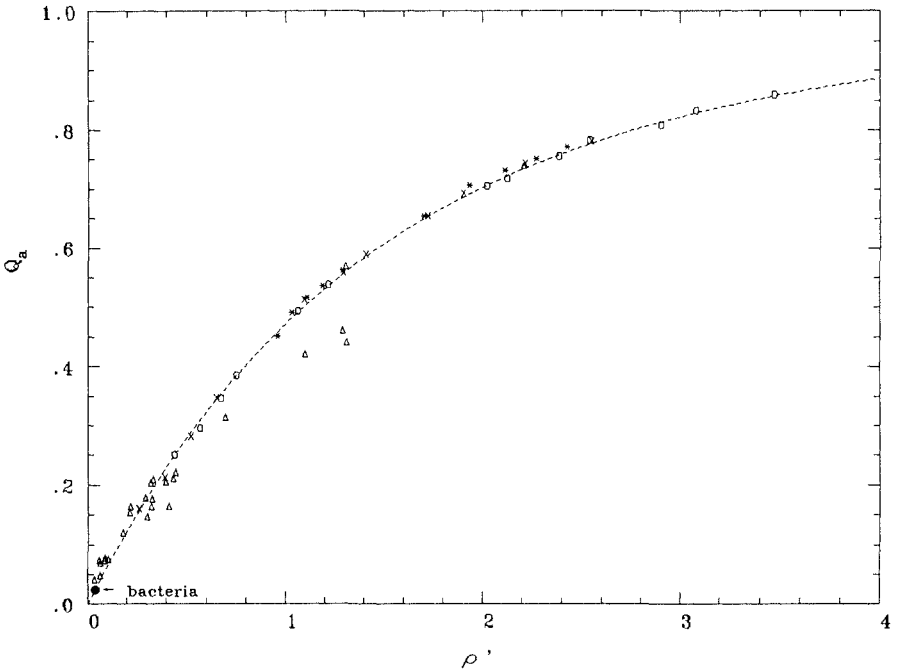

Fig. 5-4. Theoretical variations of the efficiency factor for absorption Q_a (dashed line) as a function of the parameter ρ' (Eqs. 5.7 and 5.11). Experimental determinations of Q_a, at 675 nm, for various algae are also shown [triangles and circles are for algal species studied by Ahn (1990) and Morel and Bricaud (1986); crosses are values for three algal species grown under various irradiances and studied by Sosik (1988)].

flattening effect on the absorption spectrum with increasing cell size (Duysens, 1956). These effects of the variability of Q_a with ρ', or of a*(λ), have been seen for a wide variety of naturally occuring algae (see, e.g., Bricaud et al., 1988). They have been detected at the level of single cells using the micro-spectrophotometric method (Iturriaga et al., 1988) and indirectly via fluorescence to the extent that the packaging effect modulates the excitation radiation (Mitchell and Kiefer, 1988b, Perry and Porter, 1989; Sosik et al., 1989; see also Chapter 6).

Variations in the chlorophyll-specific scattering coefficient of algae, b^*, are also expected, even if the packaging effect does not affect the scattering process. With sizes spanning at least two orders of magnitude (0.5–50 μm), algal cells may exhibit all kinds of Q_b values. The cellular chlorophyll concentration (c_i in Eq. 5.2) is also highly variable from below 1 to more than $10\,\mathrm{kg\,m^{-3}}$, and therefore interspecific variations of b^* are wide ($0.1–1\,\mathrm{m^2\,mg\,Chl^{-1}}$). It seems that there is a trend for very small (≤1 μm) or large species (>10 μm) to exhibit low b^* values, whereas the high values would be typical of intermediate

(2–5 μm) sizes (see figure 5-2 in Morel, 1987). This trend, however, remains to be confirmed.

Free-living bacteria recently studied (Morel and Ahn, 1990; Stramski and Kiefer, 1990) are also relevant of the van de Hulst approximation. Apart from a peak around 415 nm (cytochrome absorption), these cells are almost transparent. Because of their small sizes (0.5–0.9 μm), leading to small ρ values, the expansion of Eq. (5.12) can be reduced to its first term

$$Q_b \approx \tfrac{1}{2}\rho^2 = 2\pi^2 n_w^2 (n-1)^2 d^2 \lambda^2 \tag{5.13}$$

with interesting and simple consequences (experimentally verified), such as the λ^{-2} wavelength dependence of the scattering or the fact that the scattering coefficient (proportional to sQ_b) varies as the fourth power of the mean size, d. Experiment shows and theory predicts the backscattering efficiency Q_{bb}, to be independent of the wavelength.

Optical properties of oceanic waters

Taking these concepts to the realm of the mesoscale oceanic environment involves an understanding of its basic nature. What are referred to as Case 1 waters form a special (simplified) environment, which, however, is prevalent in the world ocean (perhaps 95% or 97% of its total area). These Case 1 waters ideally form a two-component system comprising the water itself and the biological component, i.e., the phytoplankton with covarying organisms and associated by-products. This water is amenable to simple modeling because, to first order, the only variable is the pigment concentration. In fact the problem is more complicated because inside the biological component the ratio between the chlorophyll-bearing cells and the other materials is not constant. These materials are not only the organic debris and dissolved organic matter resulting from grazing and natural decay, but also other living heterotrophic organisms: among them, bacteria, at least, could form a sizable part of the particulate matter (Ducklow, 1986; Cho and Azam, 1988). The fact that the ratio between the algal and the nonalgal compartments is not constant would form an obstacle to any prediction if its variations were completely random. The variations in this ratio, fortunately, seem rather organized (see below) leading to nonlinear relationships between chlorophyll and optical properties, as first pointed out by Smith and Baker (1978a). A second problem already examined is that living algae themselves are highly variable in their optical properties, such as chlorophyll-specific absorption and scattering coefficients. Accordingly, even for "simple" Case 1 waters, there exists natural variability, which manifests itself as inevitable noise in any algorithm relating pigment concentration to ocean optical properties (including the ocean "color").

The nonlinear relationship between the living algae component and their associated particulate matter is evident in a plot of the scattering coefficient (at the wavelength 550 nm) as a function of the pigment concentration for discrete

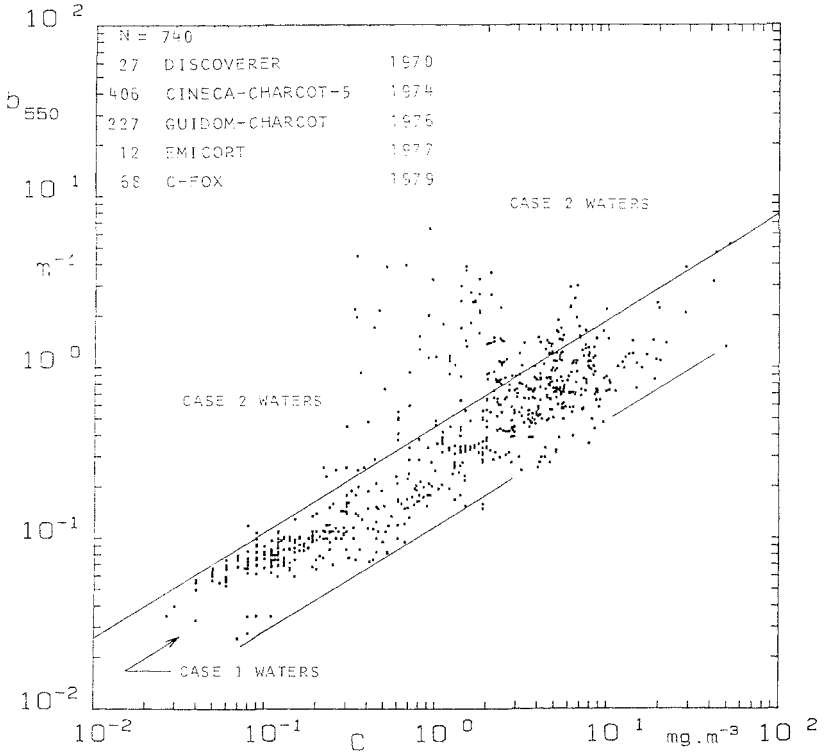

Fig. 5-5. Scattering coefficient b at 550 nm plotted as a function of C, the pigment (chlorophyll + pheophytin) concentration determined at the same depth within the upper layer in various parts of the ocean. The two lines delimit a band corresponding to Case 1 waters; the empirical relationship for these waters is $b = 0.30\ (\pm\ 0.15)\ C^{0.62}$. (Adapted from Gordon and Morel, 1983.)

samples within the upper layer (Fig. 5-5). In these Case 1 waters, scattering is proportional to pigment concentration raised to the 0.6 power, therefore the ratio of scattering to pigment concentration (the "specific" scattering) is proportional to the concentration raised to the −0.4 power. Hence the specific scattering is higher, relatively, when the pigment concentration is low. This suggests that the ratio of nonalgal to algal materials increases more or less regularly from eutrophic to mesotrophic and finally oligotrophic situations.

A plot of the measured diffuse attenuation coefficient for downwelling irradiance, $K_d(\lambda)$, (an analog of the absorption coefficient) as a function of the pigment concentration is shown in Fig. 5-6. Again, the exponent is not unity, but more like 0.7 meaning that the nonlinearities in the absorption-to-chlorophyll and scattering-to-chlorophyll relationships are similar. Empirical relationships such as that shown in Fig. 5-6 have been established for all wavelengths in the visible domain. They can be used to develop a spectral bio-optical model to reconstruct

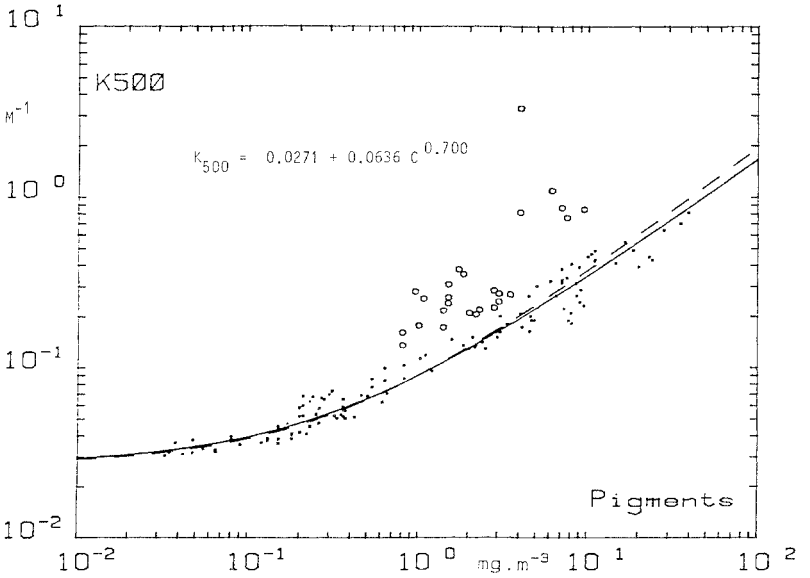

Fig. 5-6. Diffuse attenuation coefficient for downwelling irradiance K_d (at 500 nm) plotted as a function of the pigment concentration (mg m^{-3}). The circles are for turbid Case 2 waters, excluded from the regression analysis; the points are for Case 1 waters. The solid curve (and the equation inset) result from the regression analysis performed on the log-transform data. The value 0.0271 is that of pure seawater [other examples are in Gordon and Morel (1983) or in Morel (1988)].

the $K_d(\lambda)$ spectrum for a given pigment concentration and from that to predict the daylight penetration or the reflectance of the ocean (Morel, 1988). Other parametrizations accounting for the nonlinearities have been adopted (Gordon et al., 1988) with similar results, allowing the upwelled radiances at the sea surface to be predicted as a function of the phytoplankton pigment concentration for Case 1 waters.

If a rather satisfactory description and prediction (at the mesoscale) of the optical properties of these Case 1 waters is now possible, the formation of the optical coefficients is far from being understood from the knowledge of the optical properties at the single cell or particle level, and then from their addition.

A useful application of the spectral model lies in the possibility of predicting the euphotic zone depth as a function of the pigment content. The empirical relationships, directly established through regression analysis using field data (Morel, 1988), namely,

$$Z_e = 38C^{-0.43} \tag{5.14}$$

$$\langle C \rangle_{\text{tot}} = 38C^{0.57} \tag{5.15}$$

have been corroborated via the model; Z_e is the euphotic depth (in meters), C is the mean pigment (Chl + Pheo) concentration (mg m^{-3}) within the column and $\langle C \rangle_{tot}$ is the vertically integrated pigment content (mg m^{-2}).

For mean pigment concentration ranging in Oceanic Case 1 waters between, say, 0.03 and 30 mg m^{-3}, Z_e would vary between 170 and 9 m according to Eq. (5.14), whereas the spectral model gives the more realistic values 130 m (and again 9 m). When the pigment concentration increases, the integration leading to $\langle C \rangle_{tot}$ is effected over a diminishing Z_e thickness, with the result expressed by Eq. (5.15), showing that $\langle C \rangle_{tot}$ varies approximately as the square root of C. Interestingly, with the above values of C that span three orders of magnitude, the algal biomass varies by only 1.5 order of magnitude (from 5 to 265 mg m^{-2}). This is ecologically significant when compared to the terrestrial phytosphere, able to experience much wider variations between, for instance, the Sahara Desert and the Equatorial rain forest.

The model can also be operated using actual pigment profiles allowing the depth Z_e to be derived (when it has not been measured), and also $\langle C \rangle_{tot}$. About 4000 vertical profiles of pigment have been analyzed using this approach. A statistical analysis of the characteristics and shapes of all profiles is possible once they are scaled in a dimensionless way. This is obtained by dividing the actual depth by Z_e and the local concentration by the mean concentration within the euphotic layer. A highly significant relationship is found between the integrated content $\langle C \rangle_{tot}$ and the concentration in the upper layer, C_{sat}, for stratified waters, expressed as (Morel and Berthon, 1989)

$$\langle C \rangle_{tot} = 40.6\ C_{sat}^{0.46} \tag{5.16}$$

For well-mixed waters (as in high latitudes), a slightly different expression is obtained (because in such waters, there is no deep pigment maximum). Such relationships can prove to be useful in transforming the remotely sensed pigment concentration (by ocean color sensor) into maps of the integrated algal biomass. The shape of the vertical profile can also be (statistically) related to the upper layer concentration. This information, when introduced into the spectral light–photosynthesis model, allows the primary production within the entire euphotic layer to be computed. For global application and use of satellite imagery, the model is operated to produce a "climatology" of the Ψ^* parameter, which represents the cross section for photosynthesis per unit of areal chlorophyll and is expressed as m^2(gChl)$^{-1}$ (Morel, 1991). With this cross-section, the photosynthetically stored radiant energy per day, $\overline{PSR}$, is related to the available incident energy, $\overline{PAR}$, and the column integrated chlorophyll content $\langle Chl \rangle_{tot}$ through

$$\overline{PSR} = \overline{PAR}\ \langle Chl \rangle_{tot} \Psi^* \tag{5.17}$$

The cross section Ψ^* is not an independent parameter in this expression. It depends on $\overline{PAR}$ itself and its time evolution (i.e., on date, latitude, and

cloudiness); it depends on the actual biomass $\langle \mathrm{Chl} \rangle_{\mathrm{tot}}$ and its vertical distribution. In addition it is also governed by physiological parameters on which the model is built, such as the capacity of algae to capture and use radiative energy, the response of algae to varying illumination, and so forth. Thus, for an application dealing with mesoscale or even global scale, optical and physiological research at the microscopic scale is a prerequisite.

6

MEASUREMENTS OF PHYTOPLANKTON ABSORPTION OTHER THAN PER UNIT OF CHLOROPHYLL *a*

Mary Jane Perry
University of Washington

Introduction

Phytoplankton plays a critical role in determining light fields of the world's oceans, primarily through absorption of light by photosynthetic pigments (see Chapters 1 to 5). Consequently there has been considerable interest from optical researchers in determining phytoplankton absorption. Conversely, from the biological point of view, this absorption assumes paramount importance because it is the sole source of energy for photosynthesis and thus should be central to direct estimates of primary production. There are two logical parts in determining this effect of phytoplankton and in estimating primary production. One is the estimation of abundance, and the other is estimation of specific effect or specific production rate.

The earliest estimates of phytoplankton abundance were based on cell counts. From the time of Francis A. Richards' Ph.D. dissertation, however, measurement of chlorophyll *a* concentration per unit of water volume, because of its relative ease, has assumed a central role in abundance estimation. Physiological studies and technological advances in optical instrumentation over the last decade lead me to question whether the continued use of chlorophyll *a* concentration to estimate phytoplankton abundance was wise either from the viewpoint of narrowing confidence intervals on estimates of absorption and production or from the viewpoint of mechanistic understanding of the processes involved. The measurement of chlorophyll *a* has become such a routine tool of biological oceanography, however, that the reasons for my heresy require elaboration.

Some of the reasons are not too subtle. Chlorophyll *a* exists with other photosynthetic pigments in organized arrays associated with photosynthetic membranes. The function of these arrays is to harvest photons and transfer their energy to the specialized reaction center complexes that mediate photochemistry (see Chapter 9). The size of the arrays or packages and the ratio of chlorophyll *a* molecules to other light-harvesting pigments within the packages vary with phytoplankton cell size, total irradiance and its spectral distribution, as well as

with other environmental parameters. It is well known that dark-adapted (= light-limited) cells increase their complements of photopigments. This plasticity in pigment packaging is evidenced in the variability of chlorophyll *a*-specific absorption coefficients. Simple optical models based only on chlorophyll *a* concentrations cannot be accurate or precise unless the effects of pigment packaging are considered. The substance of my heresy is to suggest direct estimation of absorption by phytoplankton—from the scale of individual cells to the scale of satellite images—in place of the intermediate step of chlorophyll *a* measurement, as a more robust approach in modeling and measuring phytoplankton as determinants of ocean optics.

Photosynthetic efficiency and physiology

My own interest in bio-optics and pigment packaging began with measurements of photosynthetic efficiency normalized to the abundance of photosynthetic reaction center complexes rather than to chlorophyll *a* concentration alone. One important lesson from this work is that not all chlorophyll *a* is created equally. Most of the chlorophyll *a* molecules act as light-harvesting pigments, but only a very small number of molecules are capable of photochemical transformation of energy or charge separation. The specialized chlorophyll *a* molecules that constitute the heart of the reaction centers are P700, which exists as a chlorophyll *a* dimer in reaction center I, and P680, which exists as a chlorophyll *a*–pheophytin *a* dimer in reaction center II. To study photosynthetic efficiency, we (Perry et al., 1981) grew cultures of a number of phytoplankton species under high and low irradiances. The phytoplankton grown under low light exhibited the classical photoadaptive response of greatly increased cellular chlorophyll *a* concentration. The novel finding was the great difference in photosynthetic unit size (simply defined as the ratio of the number of light-harvesting chlorophyll *a* to P700 molecules) between the low- and high-light grown cells. Photosynthetic unit size varied as a function of species and growth irradiance, but the range was from a low of 200 chlorophyll *a* to P700 molecules for some high-irradiance grown cultures to a high of 1400 for some low-irradiance cultures, quite a dramatic variation in pigment packaging (Falkowski and Owens, 1980; Perry et al., 1981). In spite of this gross change in some species, others responded by proliferating the number of reaction centers rather than changing their photosynthetic unit size. Both strategies yield enhanced rates of photon encounter at low light levels and improve the overall rates of photosynthesis per cell but give wildly different rates of photosynthesis per unit of chlorophyll *a*. This fact reminds one that the fundamental unit of adaptation is the individual, not the chlorophyll *a* molecule or the reaction center.

We found that these alterations of sizes and numbers of pigment packages have a very direct benefit in photosynthetic efficiency of cells grown under low light. Short-term photosynthetic rates were measured as ^{14}C fixation over a wide range of irradiances. Photosynthetic efficiency, defined here as the efficiency of photon utilization at low photon flux, was calculated as carbon fixed per unit of

chlorophyll *a* or per P700. When photosynthetic efficiency was normalized to chlorophyll *a* concentration, a clear trend emerged: individual chlorophyll *a* molecules in large photosynthetic units were much less efficient than their counterparts in small photosynthetic units. The converse was true, however, when photosynthetic efficiency was normalized to P700. As the number of light-harvesting chlorophyll *a* molecules capable of transferring photon energy to the reaction centers increased, the photosynthetic efficiency of the reaction centers increased. These experiments demonstrated that physiologically induced changes in pigment packaging are an important mechanism for enhancing photosynthetic rate at low irradiances.

More recently we addressed the issue of pigment packaging and photosynthetic physiology in context of the photosynthetic quantum yield, which can be determined quite simply for cultures grown in the laboratory (Cleveland and Perry, 1987). Photosynthetic rate versus irradiance (*P* vs. *I*) was measured as ^{14}C incorporation; quantum yield was calculated as the slope of the *P* vs. *I* curve divided by the phytoplankton absorption coefficient. For our application, the units were moles carbon reduced per mole of photons absorbed. Although the theoretical maximal quantum yield at very low irradiances is a constant, the physiology of the phytoplankton can affect the actual maximal quantum yield. The measurement of maximal quantum yield can, therefore, provide important information about the photosynthetic physiology of phytoplankton in the sea. My colleagues and I attempted to measure maximal quantum yield during the spring 1985 BIOWATT program in the Sargasso Sea (Cleveland et al., 1989; see Chapter 10 for more details on the BIOWATT program). We measured *P* vs. *I* and the total particulate absorption coefficient (Mitchell and Kiefer, 1984) for seawater samples taken from a number of depths. Maximal quantum yield of photosynthesis was then calculated as for the laboratory cultures, but the resulting quantum yields were extremely low. When we looked at spectra of total particulate absorption coefficients from samples from the BIOWATT cruise and compared them to those from healthy phytoplankton cultures, we observed a profound discrepancy between the shapes of the field vs. the culture spectra. When the spectra were normalized in the red region where only chlorophyll and pheopigments absorb, the major effect of detrital material on absorption at blue wavelengths could be seen clearly. Using an end-member reconstruction technique, Cleveland (1988) was able to derive the phytoplankton component of absorption from the total particulate absorption coefficient. I should note that this work was performed before Kishino et al. (1985) published a methanol extraction method for chemically separating all solvent-extractable pigment from detrital material (see Chapter 4).

Using the corrected phytoplankton absorption coefficients to calculate maximal quantum yields, we were able to evaluate photosynthetic physiology as a function of nitrogen availability. Photosynthesis and nitrogen use are closely coupled. Protein nitrogen is essential in the light-harvesting step because pigment-binding proteins provide the essential physical structure for pigment arrays in photosynthetic membranes. Nitrogen is also essential in the reduction of

carbon as ribulose-1,5-bisphosphate carboxylase and the other Calvin cycle enzymes. If nitrate is abundant and serves as the main source of nitrogen to phytoplankton, maximal quantum yield is limited because of the direct competition between nitrate reduction and carbon reduction for NADPH (nicotinamide adenine dinucleotide phosphate-reduced form) and ATP (adenosine triphosphate). If nitrogen is limiting, maximal quantum yield is also depressed. If ammonium serves as the primary nitrogen source and ammonium flux is sufficient to sustain the phytoplankton nitrogen requirement, measured quantum yield will be closer to the theoretical maximum (Cleveland et al., 1989).

There are three important implications of this work. The first is that chlorophyll *a* concentration is inadequate to describe phytoplankton absorption because of physiologically induced variability in pigment packaging. The second is that the efficiency with which the absorbed photons are used in photosynthesis depends on environmental variables, primarily nitrogen availability and its redox state. The third is that phytoplankton is a variable component of total particulate absorption in the upper ocean. If we are ever going to mechanistically understand the variability from one water mass to another either in primary production or relative contribution of phytoplankton to the total absorption, we must learn how to better parametrize phytoplankton. If chlorophyll *a* per cell and absorption and photosynthesis per unit of chlorophyll *a* vary so much with environment, then why not circumvent this source of measurement error and instead estimate absorption per cell directly? Although measurement of the total phytoplankton absorption of "bulk" seawater samples is becoming more common (cf. Roesler et al., 1989), my conclusion is that mechanistic understanding of absorption can come only from evaluation of that process at the level of individual cells and other marine particles.

Single cell analysis

Flow cytometry is a powerful tool for enumerating and studying individual phytoplankton cells and nonliving particles (see Chapter 8); it can also be used to ask how different groups of organisms vary in abundance as a function of environmental conditions such as stratification versus mixing. During the 1987 BIOWATT cruises, I took a flow cytometer to sea to analyze fresh samples. It was possible to classify the phytoplankton into three groups based on their forward scattering and fluorescence properties and to enumerate cells within these three groups. Cyanobacteria were clearly distinguished by their phycoerythrin fluorescence and low scatter at forward angles. *Prochlorococcus* (Chisholm et al., 1988 and 1992) were identified on the basis of their very dim chlorophyll *a* fluorescence and very small forward scatter. The remaining phytoplankton were classified very broadly as eukaryotes. Improved classification, based on forward angle light scatter (cell size) or some other optical signal, would be a better way of further decomposing the eukaryotes. Cryptomonads, for example, have a phycoerythrin fluorescence similar to that of cyanobacteria, but

are easily distinguished from them on the basis of the much larger size and forward scattering signal of the cryptomonads. Olson et al. (1991) have used polarization of the forward scatter signal by the calcite crystals of coccoliths to identify coccolithophorids. Cell-surface antibodies show future promise for identifying species or genera (Ward and Perry, 1980; Campbell et al., 1983; Shapiro et al., 1989a), with flow cytometry automating the process.

Phytoplankton ensembles are composed of many individual cells representing diverse taxa, cell geometries, and chemical compositions. Answers to many questions, such as the contribution of phytoplankton to absorption and scattering or the magnitude of primary production, lie in the analysis of the individuals constituting the phytoplankton ensemble. A key technical question is whether flow cytometry can provide any of these answers. I think the answer is yes. A simple example of the power of individual cell analysis is given in Fig. 6-1, which shows how a specific group of phytoplankton can be identified, enumerated and analyzed with regard to the physiology of adaptation to low irradiance. Cyanobacterial phycoerythrin fluorescence was analyzed as a

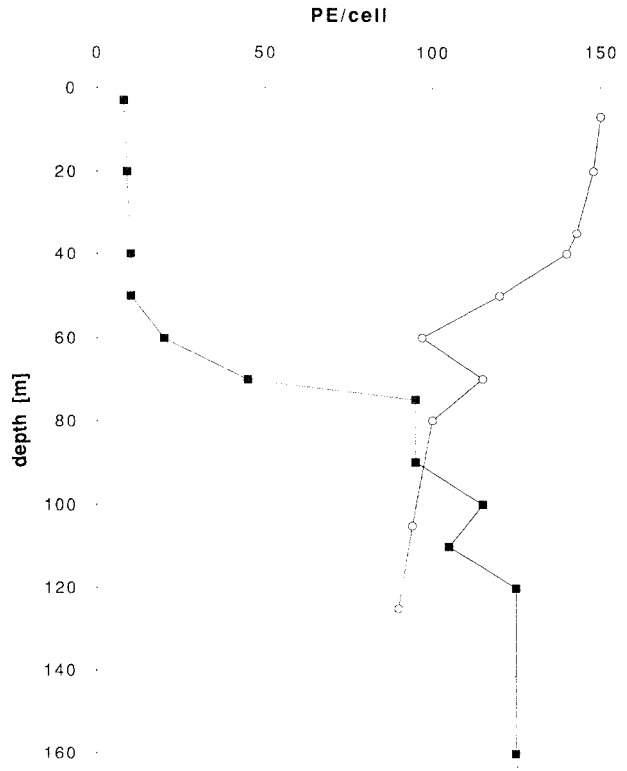

Fig. 6-1. Flow cytometric analysis of phycoerythrin fluorescence (PE) per cell as a function of depth from May (filled squares) and December (open circles) cruises to the Sargasso Sea during the 1987 BIOWATT experiment.

function of depth during three BIOWATT cruises to the northwestern Sargasso Sea in 1987. Individual phytoplankton cells were irradiated in a flow cytometer with a 20-mW, 488-nm, argon-ion laser. During May and August, when the upper water column was highly stratified, a distinct pattern in phycoerythrin fluorescence per cell was observed as a function of depth. Phytoplankton in the shallow upper mixed layer were exposed to high irradiances and had very low phycoerythrin fluorescence per cell (N.B.: May and August profiles were very similar). Below the upper mixed layer, light was consistently low and phycoerythrin fluorescence per cell increased. In December, day length was at the annual minimum and incident irradiation was low at the surface. A strong winter storm eroded the upper mixed layer to a depth of at least 80 m, resulting in the exposure of all cyanobacteria to very low irradiances. Cyanobacteria sampled from all depths had uniformly high phycoerythrin fluorescence per cell. Under controlled excitation irradiances in the flow cytometer, the magnitude of fluorescence is proportional to the absorption coefficient and, to a lesser degree, the concentration of pigment. The effect of low-light adaptation can be seen in the magnitude of cellular phycoerythrin fluorescence throughout the entire profile in December and at depth in the May profile (Fig. 6-1).

A natural progression from this study is to ask what is the actual absorption coefficient of these individual phytoplankton cells is and whether single-cell absorption coefficients can be determined from the flow cytometer fluorescence measurements. To address this issue, 17 species of phytoplankton were grown in the laboratory under a variety of light conditions. Chlorophyll *a* fluorescence per

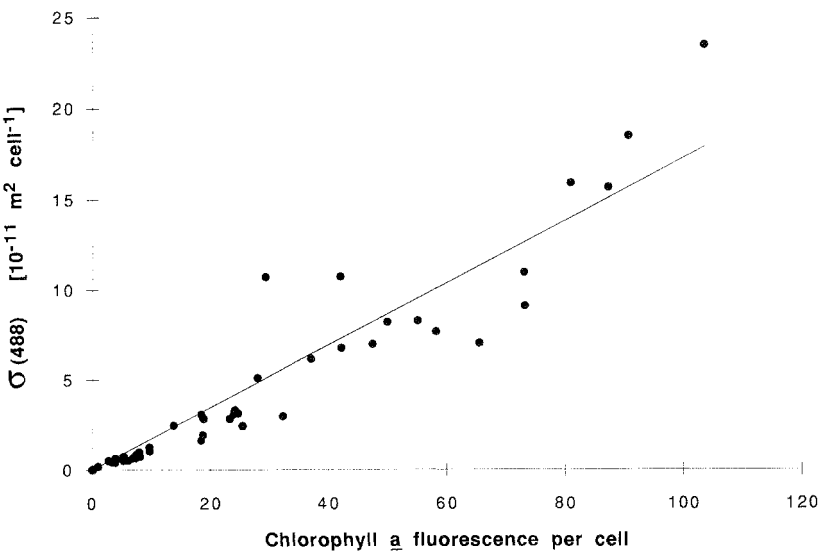

Fig. 6-2. Regression of absorption cross-section (σ) at 488 nm vs. flow cytometric chlorophyll *a* fluorescence for individual cells from cultures of 17 algal species; $\sigma(488) = 0.173 \times 10^{-11} \times$ chlorophyll *a* fluorescence per cell; $r^2 = 0.93$. (From Perry and Porter, 1989.)

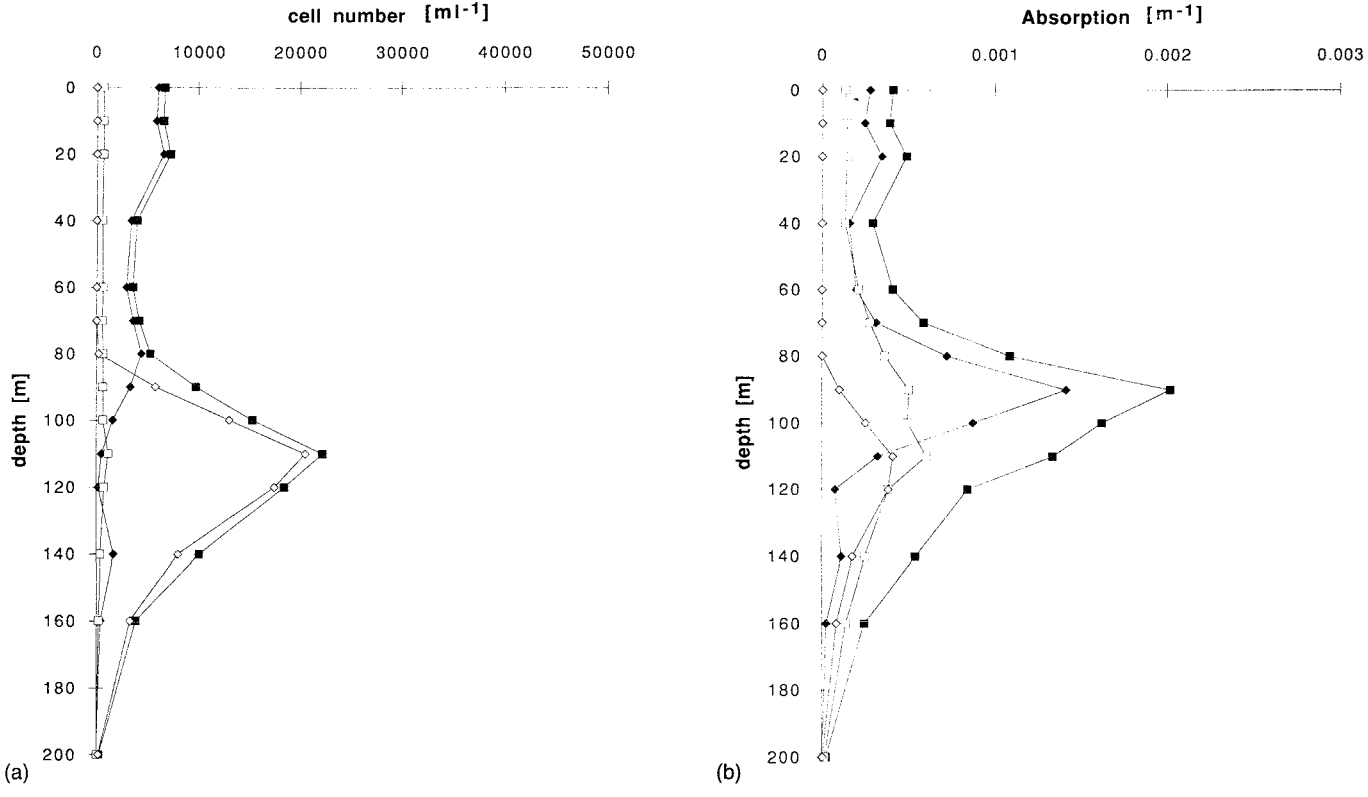

Fig. 6-3. (a) Numbers of eukaryotes (open squares), cyanobacteria (filled diamonds), *Prochlorococcus* (open diamonds), and total phytoplankton (filled squares) in August 1987 in the Sargasso Sea. (b) Total absorption coefficients were obtained by summing $\sigma(488)$ for all cells in each category in Fig. 6-3a.

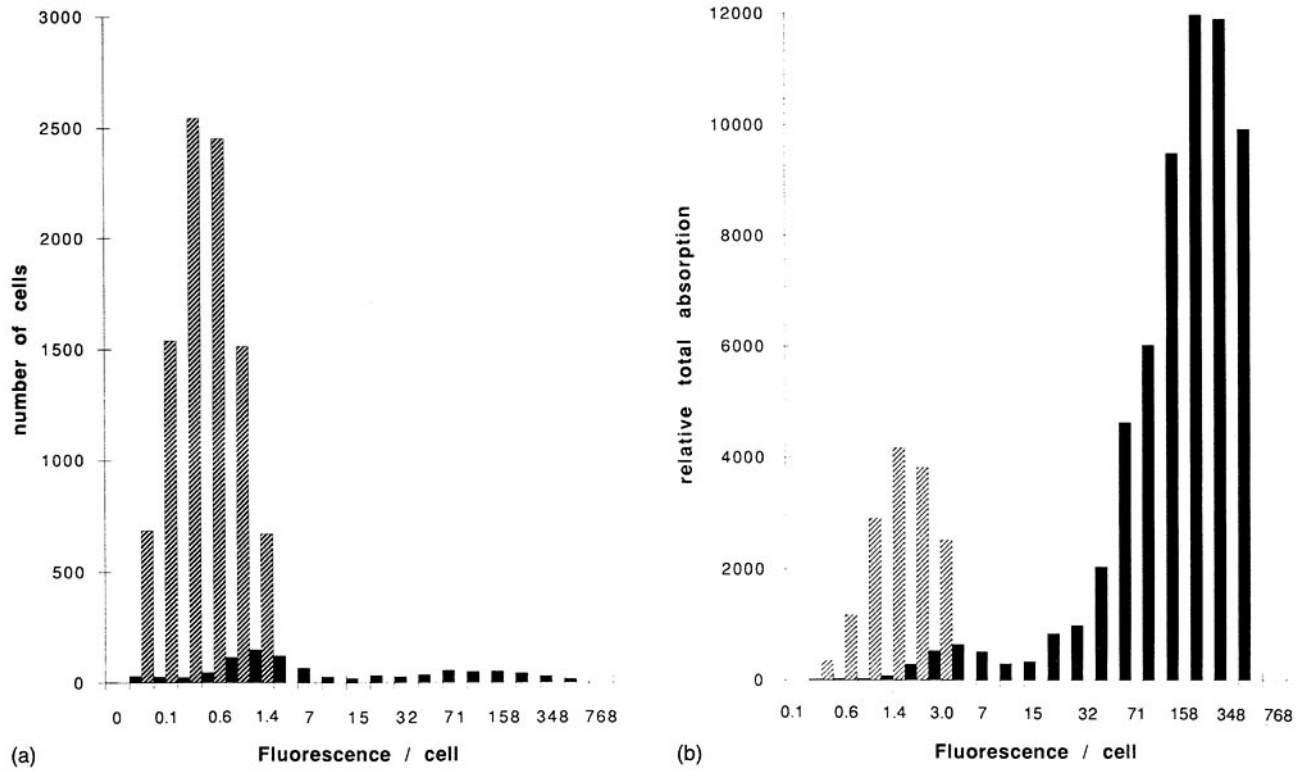

Fig. 6-4. (a) Histogram of numbers of cells with a given cellular chlorophyll *a* fluorescence for a water sample from the Gulf of Maine in July 1990; hatched bars are cyanobacteria and solid bars are eukaryotes. (b) Histogram of the relative absorption coefficients for each category of cyanobacteria and eukaryote shown in Fig. 6-4a.

cell was measured in the flow cytometer at an excitation wavelength of 488 nm. The cellular absorption cross-section at 488 nm σ, in units of $m^2 cell^{-1}$ was calculated from the absorption of a suspension of cells measured in a scanning spectrophotometer and normalized to the cell number. An empirical relationship with a relatively high correlation coefficient ($r^2 = 0.93$; Perry and Porter, 1989) suggested that the cellular absorption coefficient at 488 nm could be inferred from flow cytometric fluorescence (Fig. 6-2).

With this relationship, one can begin to ask about the contribution of specific groups as well as individuals to absorption and about the relationship between cell size, cell number, and absorption. The optical answers to these questions are also important for irradiance-based models of primary production. In the Sargasso Sea in August, *Prochlorococcus* were numerically most abundant at depth by at least an order of magnitude in comparison to the eukaryotes and cyanobacteria (Fig. 6-3a). The regression equation from Fig. 6-2 was applied to convert single-cell fluorescence measurements to absorption cross sections, which were then summed for all cells within each of the three categories (*Prochlorococcus* , eukaryotes, and cyanobacteria). Figure 6-3b shows the results as the total absorption coefficient of each group for 488-nm light. Cyanobacteria dominate the absorption signal at depth, not because of their abundance but primarily because of their increased pigmentation per cell as a photoadaptive response. The prochlorococcal cells, while abundant, were so small and had such low absorption per individual cell that they were less important than the cyanobacteria in terms of the total phytoplankton absorption.

The important contribution of a relatively few individuals to total phytoplankton absorption can be seen in data from the Gulf of Maine in July 1990. The interaction of cell size, physiology, and total numbers of cells determines the total absorption coefficient from a given group of phytoplankton. Although cyanobacteria were numerically dominant in this water sample (Fig. 6-4a), a few large and brightly fluorescent eukaryotic phytoplankton cells contributed disproportionately to the absorption signal (Fig. 6-4b). The importance of large, relatively rare cells needs to be incorporated into models of optical variability as well as into models of primary production (Goldman, 1988).

Modeling absorption and primary production

Is it possible to construct models of primary production and its variability based on the individual cells that constitute the total phytoplankton ensemble? In theory the answer is yes, that it should be possible to apply general bio-optical photosynthetic models to individual cells. Bio-optical models of primary production are generally based on *in situ* irradiance, phytoplankton absorption coefficient, and a coefficient for photosynthetic quantum yield. Spectral irradiance as a function of depth is now routinely measured at sea. From Fig. 6-2, the absorption cross-section of an individual phytoplankton cell can be determined at one wavelength, 488 nm. The absorption cross-section at other wavelengths can be approximated on the basis of the data in Fig. 6-5, although

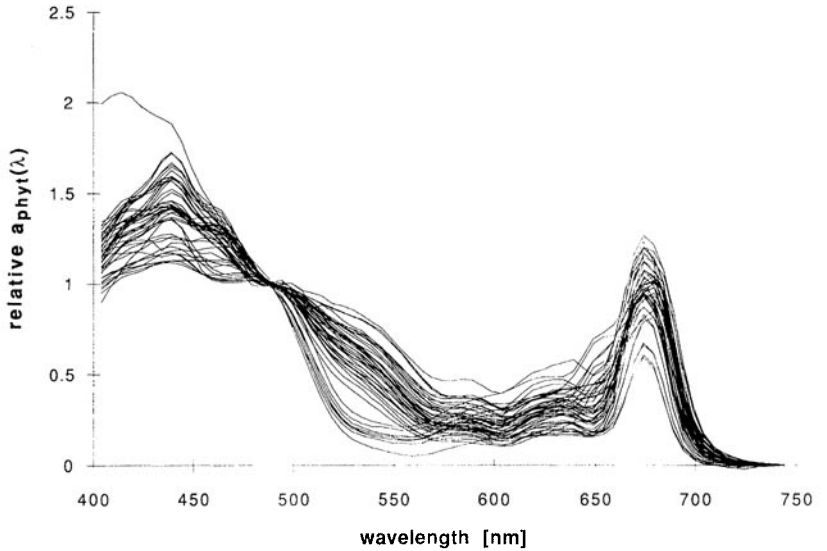

Fig. 6-5. Variation in spectral absorption, normalized at 488 nm, for 16 species of eukaryotic algae grown under a range of irradiances. (From Perry and Porter, 1989.)

it should be noted that these estimates are less constrained and that the errors are larger at wavelengths farther from the 488-nm tie point. Given the mean and the standard deviation for Fig. 6-5 and the spectral quality of light in different submarine water types, e.g., green coastal waters versus blue oceanic waters, one can establish confidence limits for estimating spectral photon absorption based on the 488-nm tie point. The estimate can be greatly improved by using the single-cell microspectrophotometric approach of Iturriaga et al. (1988) to reduce the error in spectral shapes for a given water sample. Information about the nitrogen availability and redox state allows further improvements by narrowing the estimate of light-limited photosynthetic quantum yield (Cleveland et al, 1989; Kolber et al., 1990).

Estimation of light-saturated photosynthetic rates based on absorption cross section is much more problematic. One approach is to measure the concentration of Rubisco (ribulose-1,5-bisphosphate carboxylase), a key enzyme in the photosynthetic Calvin cycle, in individual phytoplankton cells. An antibody labeled with a fluorescent probe and specific to Rubisco can bind stoichiometrically with the enzyme. The concentration of Rubisco is proportional to the fluorescence of the bound antibody and, hence, its concentration can be quantified flow cytometrically in individual cells. Initial tests of this technique show that, for a laboratory culture, the maximal light-saturated photosynthetic rates, P_{max}, as measured with ^{14}C fixation and normalized per cell, were well correlated with antibody concentration (Orellana and Perry, 1992). If we can constrain P_{max} with singe-cell immunological methods and light-limited photosynthetic rates with bio-optical models based on absorption cross-section,

I think that we can start to produce realistic estimates of primary production for individual cells.

Conclusions

The goal of getting at absorption rates for individual cells thus appears to be within reach. It allows for the first time rigorous statistical evaluation of the effects of averaging across taxa and states of physiological adaptation and thus is sure to be a boon to analyses of the propagation of errors in bio-optical models. The need for measurement or estimation of chlorophyll *a* concentration becomes less clear at the cellular level as well as beyond. We know that phytoplankters use chlorophyll *a* to absorb light, but we also know that both chlorophyll *a* per cell and chlorophyll *a* per reaction center vary widely. The final step in developing my heresy is to suggest that absorption, the proximate optical step in primary production, has been measured with greater accuracy and precision on large scales than one might suspect. The Coastal Zone Color Scanner and its descendants use backscattered light to detect something about phytoplankton. What color scanners measure is the leftovers from absorption. I would like to suggest that color scanners thus potentially provide a better estimate of absorption and, hence, production than they do of standing stocks. The work presented here shows why chlorophyll *a* concentration is a poor estimator of phytoplankton abundance and photosynthetic efficiency. I therefore assert that it should be possible to estimate production from space with greater precision than we have been able to estimate standing stocks. It is time to ask critically when, where, and why we should continue to measure and estimate the abundance of chlorophyll *a*.

7

A HISTORY OF EARLY OPTICAL OCEANOGRAPHIC INSTRUMENT DESIGN IN SCANDINAVIA

Niels K. Højerslev
University of Copenhagen

Brief history of optical oceanography in Europe

Interest in the optical characteristics and variability of the sea has grown for nearly two centuries. Most of the early work in this area was performed by European investigators. Perhaps the earliest reference to an optical oceanographic research cruise can be found in the book by Otto Krümmel (1886), in which the author refers to the Rurik circumnavigational cruise of 1817 made by Otto von Kotzebue. In these studies von Kotzebue made measurements using optical instrumentation comprised of a piece of red cloth tethered to a line and lowered into the sea. With this technique, von Kotzebue was able to crudely measure the depth of penetration of light. This technique was refined by using a white plate, and the first measurements in the Pacific (at 10°N 152°W) yielded measurements of 49 meters. It is worth noting that this work was done several decades before the famous efforts of Secchi (1866).

Efforts to incorporate photographic techniques to characterize the underwater light field were also developing in the late 1800's. In March, 1885 some experiments were made in the waters off Nice, France, in which a photographic plate was submerged to depths of several hundred meters. Additional historical information can be found in the classical textbook by Sauberer and Ruttner (1941).

Theoretical treatments of optical oceanography developed somewhat later. Ludvig Valentin Lorenz published the first works on the theoretical aspects of marine light scattering. This work, originally published in Danish (Lorenz, 1890), was subsequently translated into French in 1915. Martin Knudsen (founder of International Council for the Exploration of the Sea, and developer of some of the fundamental concepts for making hydrographic calculations) also had concerns about marine optics as reflected in correspondence he sent to Professor Otto Pettersson (father of Hans Pettersson) in Sweden:

> In studying those provinces of water and particularly of sea water, which are of importance to the organisms living therein, the study of the light contents of the water must occupy the prominent place. Light contents play in many respects a similar part to that of oxygen content but have not been so strongly investigated as the latter. This is presumably due to the fact that while reliable and accurate measures are available for determining the quantity of oxygen absorbed, we still lack scientifically worked out methods for measuring the absorption of light in the sea.
>
> (Knudsen, 1922)

The first Scandinavian textbook on oceanography was published by Hans Pettersson (chief scientist on the circumnavigational cruise of the Albatross) in 1939. The volume includes an extensive chapter dealing with marine optics. A subsequent textbook by Sverdrup (1952) includes some scant information on underwater optics (including a provocative figure suggesting that in the Sargasso Sea one could read a newspaper at a depth of 170 meters using only ambient light). The two books by Jerlov (1968, 1976) are perhaps the best-known texts on marine optics.

Theoretical considerations for inherent optical properties

Any optical quantity describing the changes in the underwater daylight field can serve two main purposes. If daylight energy heat inputs to the oceans are to be studied, the pertinent input parameters to the problem will be, say, the light absorption coefficient, the volume scattering function, the vertical attenuation coefficient for the downward irradiance, and so forth. For ocean heating models it is unnecessary to know about the different water constituents like plankton, detritus, and organic dissolved matter (see Chapter 6). If, however, parameters like biomass concentrations, sediment loads, etc., are sought, a different set of optical measurements are suitable because they can give continuous and near-synoptic information about the quantity in question.

Generally there exists a relationship between, say, the light beam attenuation coefficient, c, and parameters, P, of biological, physical, chemical, or geological significance. Such relationships are typically determined in the laboratory on known suspensions or dilutions and the relationship obtained is the calibration curve for that optical parameter for a specific mixture of components. The key question is how the inversion of physical parameters, like c, into quantities like P, such as biomass concentration, affects the accuracy in determining P.

Fundamentally, the optical properties (in this case, c, the beam attenuation coefficient), may be expressed as a function of P (where P is one of the other parameters described above):

$$c = f(P)$$

or, inversely (7.1)

$$P = g(C)$$

By proper combination of the above two functional relations it is found that

$$\frac{dP}{P} = \phi(c)\frac{dc}{c} \tag{7.2}$$

in which

$$\phi(c) = \frac{g'(c)}{g(c)}c \tag{7.3}$$

and

$$\frac{dc}{c} \approx \frac{e^{cr}}{cr}dT \tag{7.4}$$

The expression in Eq. (7.2) is, in fact, an estimate for the relative accuracy for a given system of measurement. Equation (7.4) expresses the relative uncertainty of a light transmission measurement performed over the pathlength r and presented in terms of c. The term dT is interpreted as signal fluctuations in the light output as well as electronic noise in the instrument. Consider now two different examples. The most straightforward case is that of a correlation between P and c:

$$P \propto c^n$$

so

$$\frac{dP}{P} = n\frac{dc}{c} = n\frac{e^{cr}}{cr}dT \tag{7.5}$$

where

$$T = e^{-cr} \quad \text{and} \quad \phi(c) = n$$

The implication, therefore, is that the function (i.e., the accuracy of the measurement) has a minimum when the optical path length, cr, equals 1. This is the design criterion used in developing optical oceanographic equipment for this application. For example, when measuring beam attenuation in the blue part of the spectrum in the Sargasso Sea ($c = 0.05\,\mathrm{m}^{-1}$) the path length of the meter should be 20 m. For the cases where n is numerically smaller than 1, it should be noted that the beam transmissometer is most suitable for measuring a quantity that can be obtained directly from Eq. (7.5).

One might also consider the following relationship between P and c, which expresses that P is proportional to the absorbance, A ($= 1 - T$, where T is the transmittance):

$$P \propto 1 - e^{-kc}$$

so (7.6)

$$\phi(c) = \frac{e^{-kc}}{1 - e^{-kc}}kc$$

and consequently,

$$c \to \infty \Rightarrow \frac{dP}{P} \to 0$$

and (7.7)

$$c \to 0 \Rightarrow \phi(c) \to 1$$

which is the linear case previously described (where Beer's law is valid).

Implementation of design considerations for inherent optical properties

An early application of some of these concepts was the Tyndall meter used by Jerlov (1951a) on the Albatross expedition (Fig. 7-1). With this device an observer's eye was the detector by which light passing through a seawater sample was compared with the source illumination (compare with Fig. 7-2). Jerlov and

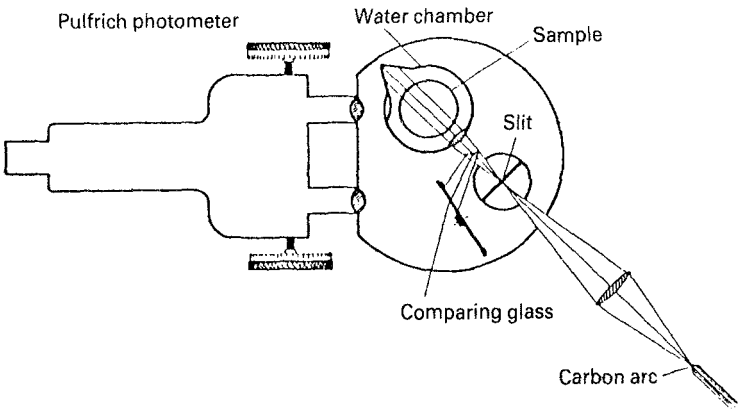

Fig. 7-1. The first Tyndall meter for in vitro oceanographic purposes (Jerlov, 1951a,b).

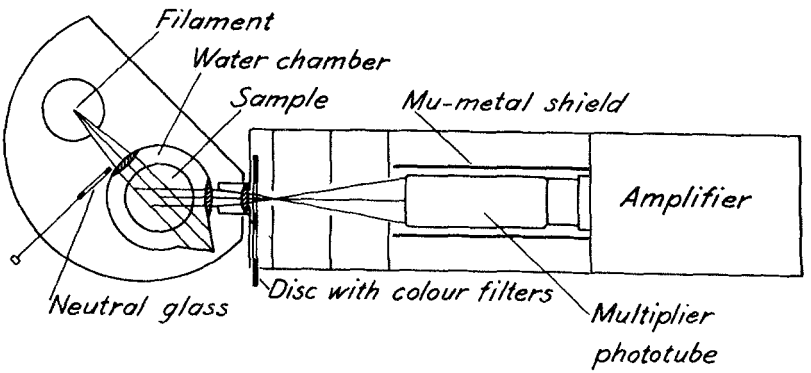

Fig. 7-2. An improved version of the Tyndall meter (Jerlov, 1957b).

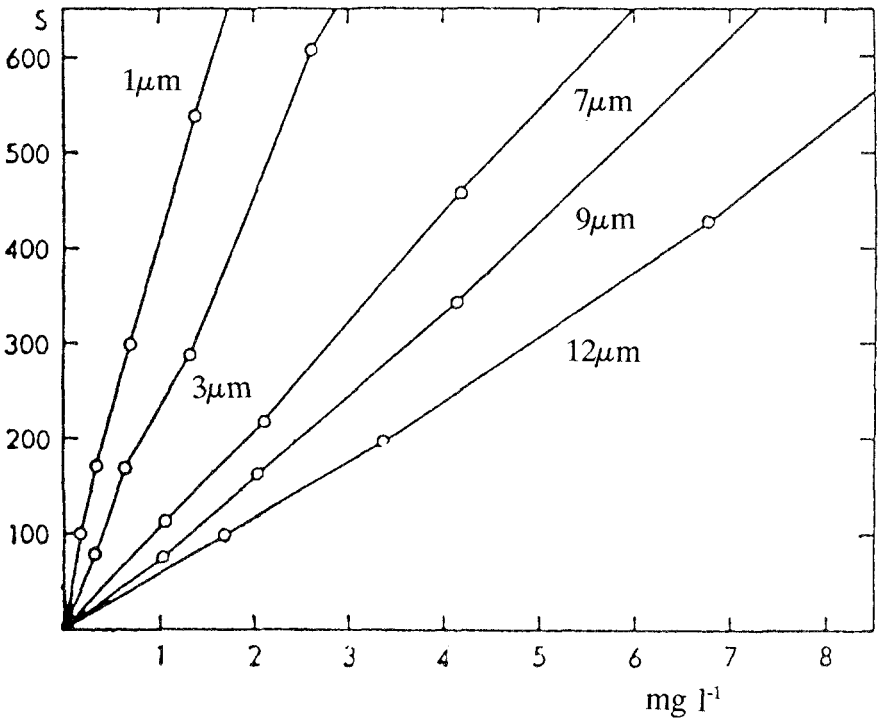

Fig. 7-3. The Tyndall effect. *S* is the light scattering at 45°, for various concentrations of different size-fractions of quartz or feldspar. The Tyndall effect is most pronounced for the finest grain sizes (Jerlov and Kullenberg, 1953).

Kullenberg (1953) made measurements with this instrument of size-fractionated mineral suspensions (quartz and feldspar) (Fig. 7-3). They demonstrated that for the same concentrations of different-sized particles, the light scattering was significantly different (the Tyndall effect). Jerlov (1953) went on to use this instrument to characterize the optical variability in the region of the Göta Älv (Fig. 7-4), including the absolute concentration of suspended particles.

Early measurements of backscattering were addressed with a large-volume in situ scattering meter developed by Pettersson (1934) (Fig. 7-5). Much later, Jerlov (1961) developed a light scattering meter capable of measuring the volume scattering function (Figs. 7-6 and 7-7).

The Pettersson and Jerlov scattering meters were both produced in Gothenburg. Pettersson also developed a folded-path transparency meter (Fig. 7-8), the philosophy of which was to increase the pathlength in order to decrease the inaccuracies. Pettersson used the two instruments separately in a Swedish fjord to study the stratification of particulate layers, and their apparent correlation with hydrographic features (Fig. 7-9). Subsequently, Pettersson (1939) put the two

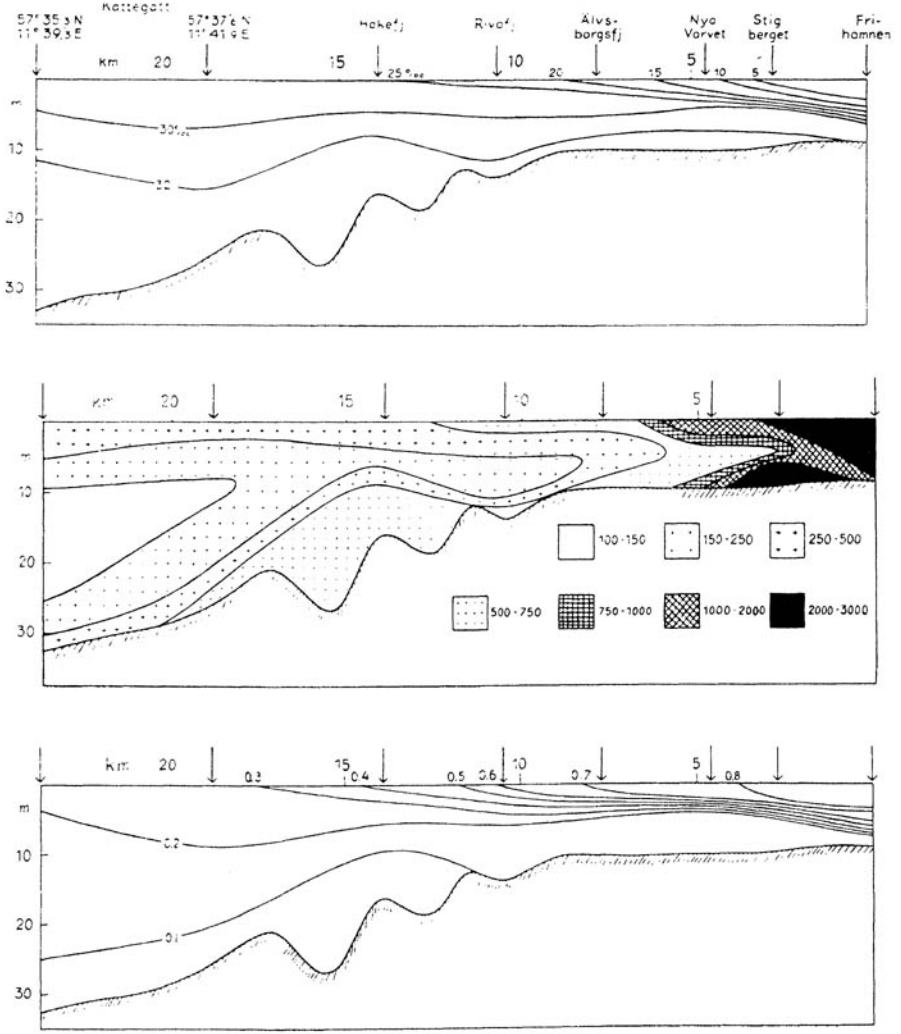

Fig. 7-4. The vertical distribution of salinity (top panel: parts per thousand), particles (middle: per ml), and yellow substance (lower: mg per liter) for a section of the Gota Alv in the Gothenburg region.

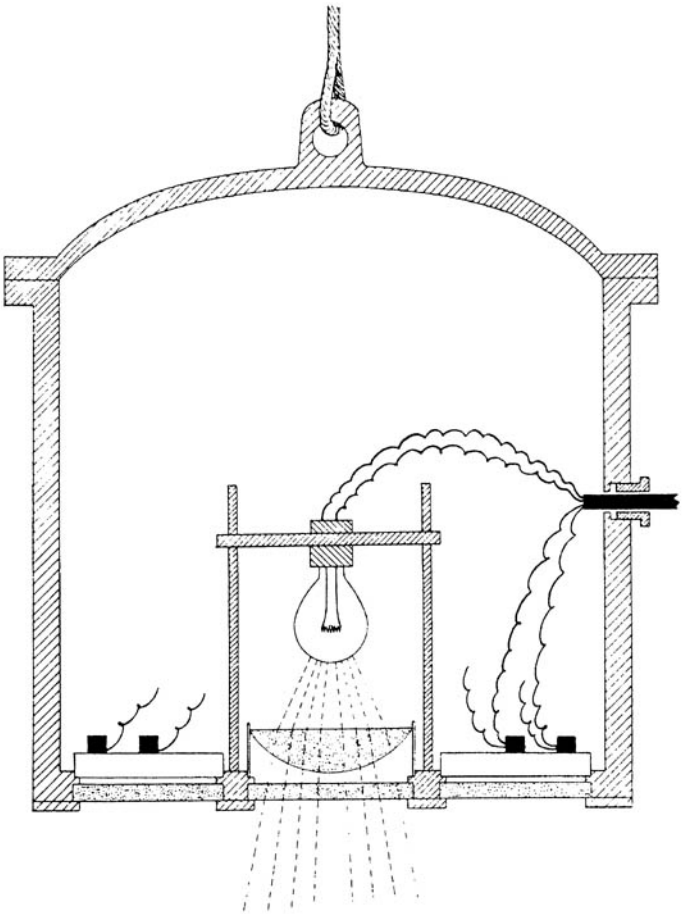

Fig. 7-5. The first in situ backscatttering meter (Petersson, 1934).

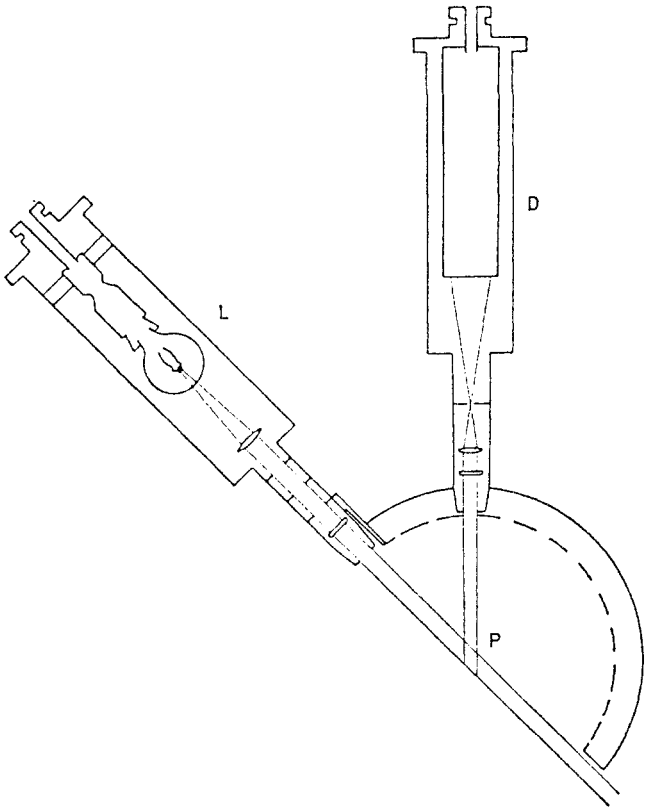

Fig. 7-6. Plan of an in situ light scattering meter covering the angular range of 10–165°. *L* = source lamp; P = sample; D = detector (Jerlov, 1961).

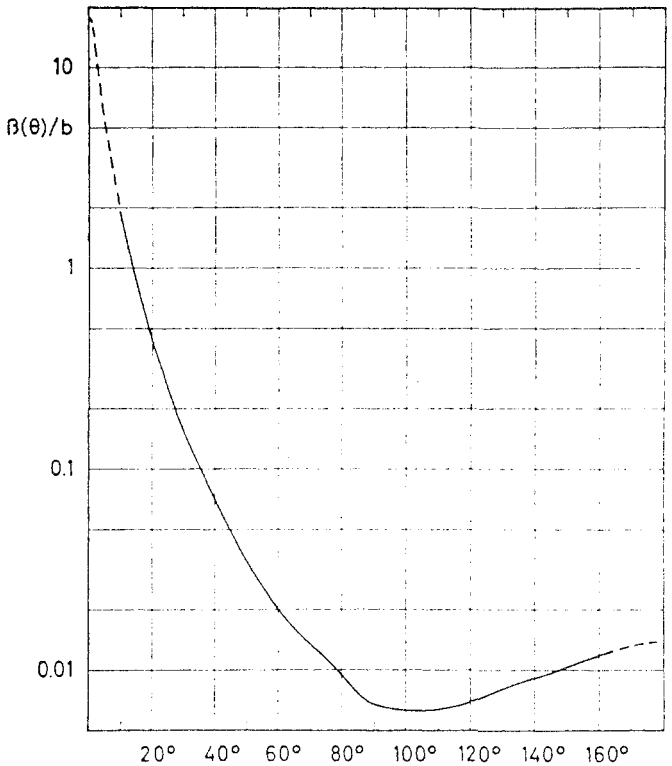

Fig. 7-7. The ratio between the volume scattering function, $\beta(\theta)$, and the total scattering coefficient, b, as a function of scattering angle (Jerlov, 1961).

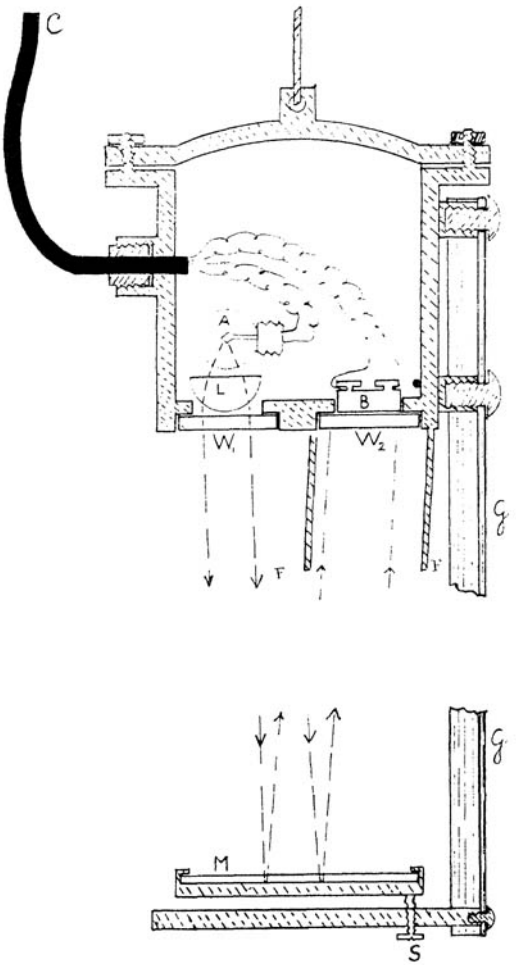

Fig. 7-8. The first in situ attenuation meter. Note that the mirror arrangement doubles the optical pathlength to 1 m (Petersson, 1934).

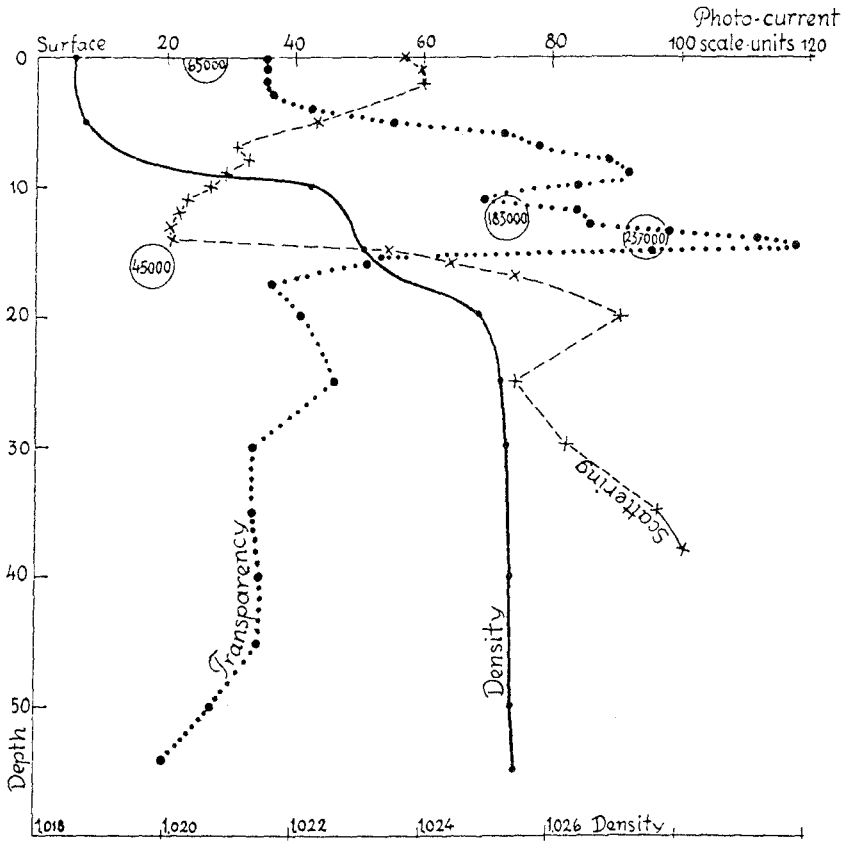

Fig. 7-9. A vertical profile of backscattering and light transmission (arbitrary units) and seawater density ($g\,cm^{-3}$). Depth is in meters and the numbers in circles are particle counts (Petersson, 1936).

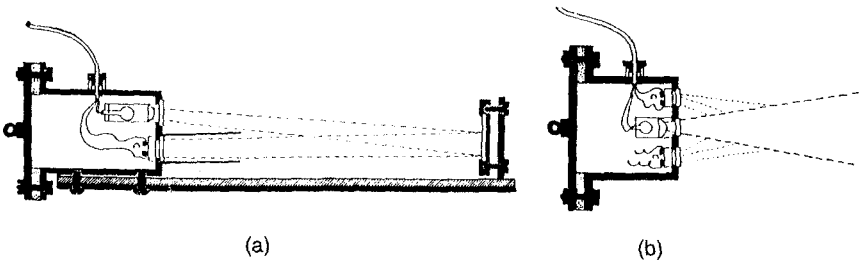

Fig. 7-10. A combined light scattering and light attenuation meter for in situ measurements (Petersson, 1939).

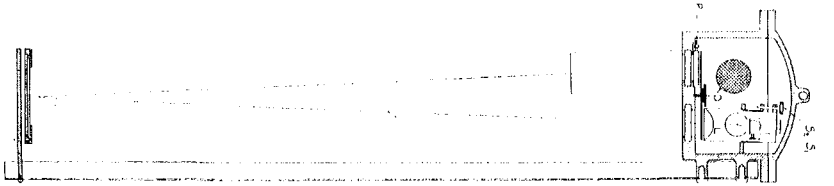

Fig. 7-11. An in situ light attenuation meter with a total optical pathlength of 2 m, for use in clear waters (Johnson [Jerlov], 1944).

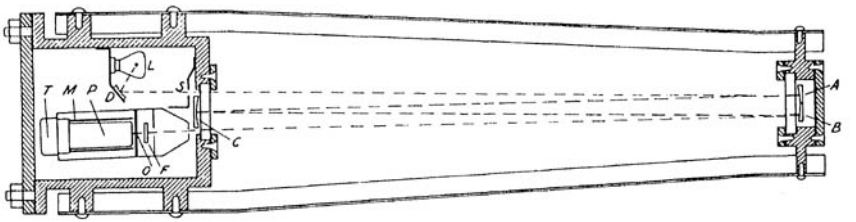

Fig. 7-12. Transparency meter in which mirrors produce a pathlength of 10 m, making the instrument suitable for use in the clearest ocean waters (Jerlov, 1957a).

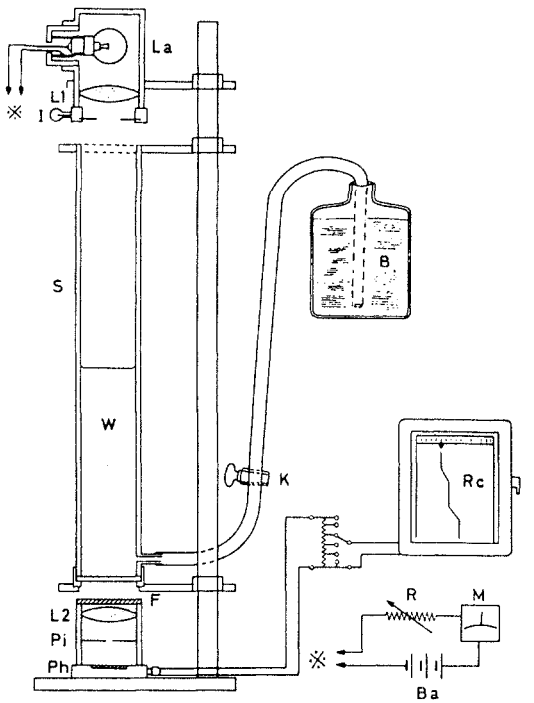

Fig. 7-13. Transmittance meter for laboratory bio-optical measurements. B, sample bottle; Ba, battery; F, filter; I, iris; K, stopcock; L1 and L2, lenses; La, lamp; M, ammeter; Ph, photovoltaic cell; Pi, pinhole; R, resistor; Rc, recorder; S, cylinder; W, sample (Fukuda, 1960).

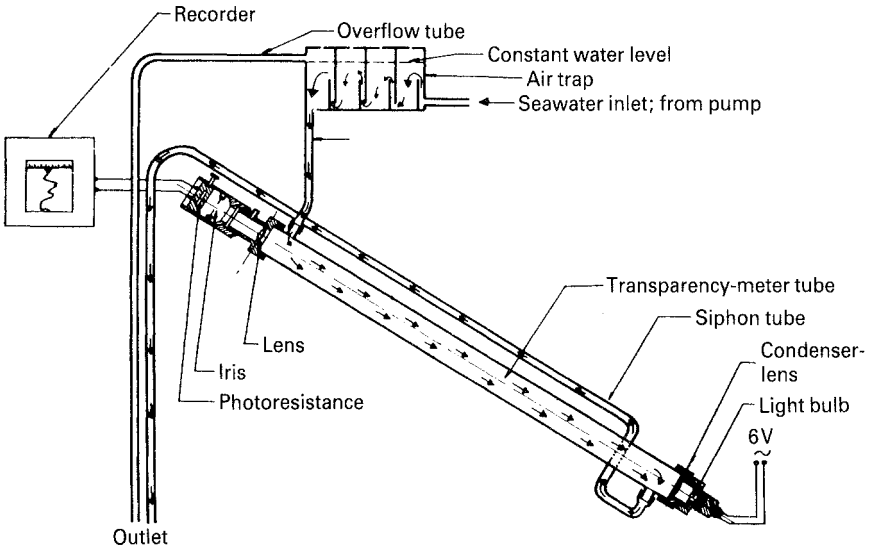

Fig. 7-14. Sea-going laboratory transparency meter for measuring light transmission of surface waters while underway (Berge, 1961).

instruments together into a single package to allow for simultaneous measurement of light transmission and backscattering (Fig. 7-10).

Johnson[1] (1944) developed a similar folded-path transmissometer, but with some modifications (Fig. 7-11). The total pathlength was increased (again, to increase the accuracy) and the detector was shielded (a primitive sort of cylindrical limitation) to avoid influences of the ambient light field and allow operation at any depth during the day or night. Since the light sources used in this instrument were inherently unstable, it was beneficial to lengthen the pathlength as much as possible. In 1957, Jerlov designed a transmissometer with a multiply folded path (Fig. 7-12).

In the 1970s the development of stable light-emitting diodes allowed the pathlength of the transmissometers to be greatly shortened with no sacrifice of accuracy (e.g., Bartz et al., 1978). Prior to that development, however, Fukuda (1960) and Berge (1961) developed some of the first pumped systems for measuring transparency on board a ship. These could be used while underway (Figs. 7-13 and 7-14).

Theoretical considerations for apparent optical properties

The nature of the radiative transfer equation and its behavior in the ocean environment must be considered in the design of optical oceanographic equipment.

[1] Johnson was the name under which Nils Jerlov published early in his career

For a light beam incident on a volume of water, some of the light is absorbed, representing a true loss of radiant energy. Some other part of the light is scattered from the incident direction with no loss of radiant energy. There are also some gains of radiant energy within the volume. For example, the path structure defines light that might be scattered from another volume into the volume in question. There might also be production of light, such as that due to inelastic scattering, fluorescence, or bioluminescence (for the case described here polarization considerations are ignored). It is also worth noting that for radiative transfer there are different time dependencies in the open ocean. Scales might range from long-term changes in solar input to the rapid changes induced by effects of clouds and waves. For the purposes of this exercise one might consider the variability observed on a clear day with a flat sea so that conditions are steady state, because the variation of the light input is much shorter-term than the duration of the measuring period. This leads to the radiative transfer equation written as

$$\cos\theta \frac{\partial L}{\partial z} = -cL + L_* + F_*$$

where (7.8)

$$F_* = F_*(\lambda_1 \rightarrow \lambda_2)$$

and $F_* = 0$ for the monochromatic case. L_* is the gain in radiance described by Gordon in chapter 1 (Eq. 1.22). In nature the source, the sun, is of a wide bandwidth, so the F term must be well known or accommodated with appropriate spectral filtering (see Chapter 12). For this example let $F_* = 0$.

From the resulting radiative transfer equation

$$\cos\theta \frac{\partial L}{\partial z} = -cL + L_* \tag{7.9}$$

and if L is known, one can calculate scalar radiance, downward irradiance, upwelling irradiance, the total attenuation and all the K functions (see chapters 1 and 2). One can also determine the remaining inherent optical properties from the radiance distribution and therefore

$$L_*(\theta,\phi,z) = \int_{4\pi} L(\theta',\phi',z')\beta(\alpha)\,\partial\omega' = \cos\theta \frac{\partial L}{\partial z} + cL$$

$$= (-\cos\theta K_L + a)L + L\int_{4\pi} \beta\,\partial\omega \tag{7.10}$$

which implies that

$$\int_{4\pi} \beta(\alpha) \left(\frac{L(\theta',\phi',z)}{L(\theta,\phi,z)} - 1 \right) \sin\theta' \, \partial\theta' \, \partial\phi' = a - K_L(\theta,\phi,z) \cos\theta \qquad (7.11)$$

indicating that for a known L one can actually derive the scattering function. The most ambitious intention then is to be able to measure the complete spectral radiance distribution.

Implementation of design considerations for apparent optical properties

Figure 7-15 shows the first radiance meter as recorded in a classical publication (Johnson and Liljequist, 1938). The device is an irradiance meter with a movable

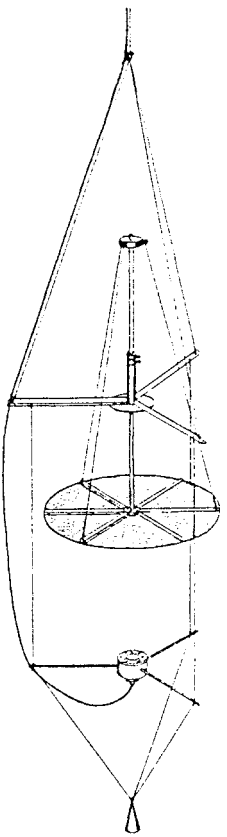

Fig. 7-15. Screened photometer (in situ radiance meter) for measuring azimuthally integrated radiances. The screen is moved vertically and through subtraction the radiances for different zenith angles can be determined (Johnson [Jerlov] and Liljequist, 1938).

black plate. The sensor integrates the radiance in the integral volumes not shaded by the black plate. As the plate is moved vertically, the sensor yields a sum of azimuthally averaged radiances. With appropriate mathematical manipulation (i.e., by subtracting the different signals), one obtains the radiance distribution at different depths. This device was later modified to allow for measurement over the azimuthal angles as well (Fig. 7-16). Figures 7-17 and 7-18 show the type of data that could be obtained from these measurements. Near the surface, the radiance distribution is skewed strongly toward the sun angle, but at deeper depths the distribution becomes more nearly vertical, as one would expect from the predictions of the asymptotic radiance distribution (Jerlov and Fukuda, 1960; Fig. 7-18).

Early on, Sir John Murray and Dr. Johan Hjort conducted an optical oceanographic cruise (Murray and Hjort, 1912). They made measurements of

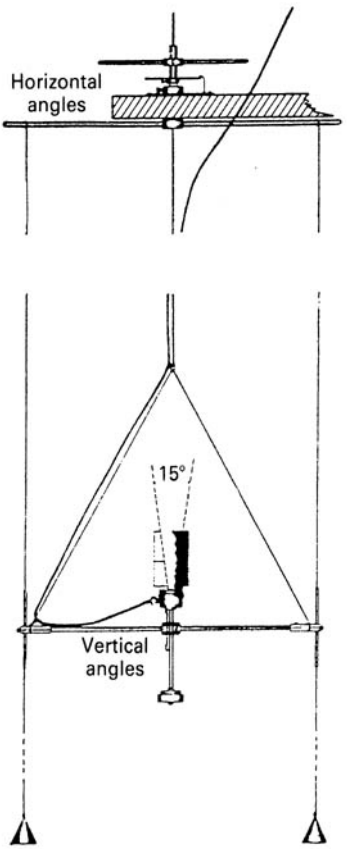

Fig. 7-16. Directional photometer for measuring radiances at selected azimuth and zenith angles. The Gershun tube can be set mechanically at fixed zenith angles and rotated about the azimuth (Johnson [Jerlov] and Liljequist, 1938).

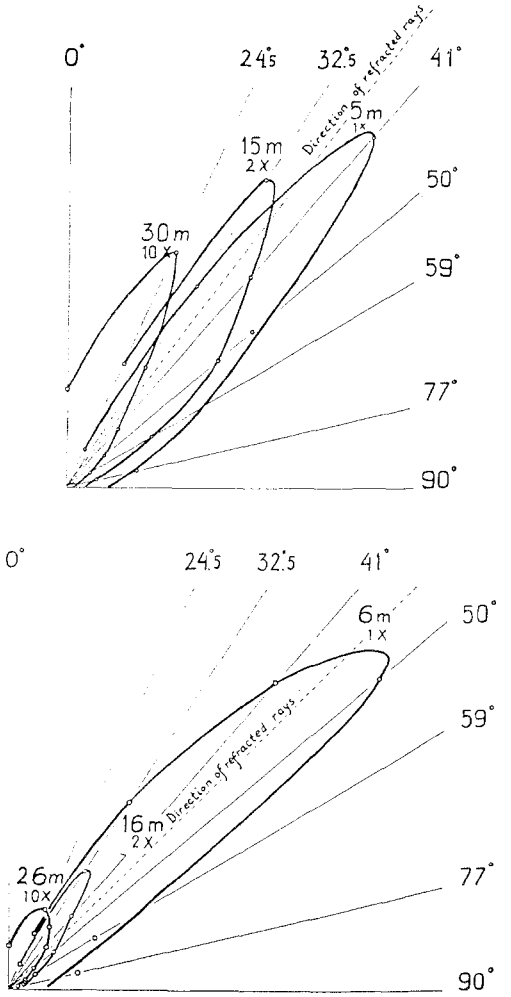

Fig. 7-17. In situ radiance measurements in the sea, performed with the directional photometer. Angular distributions are shown for measurements made at three depths in each case (Johnson [Jerlov] and Liljequist, 1938).

underwater irradiance using a modified submersible camera. The device operated at depth upon being triggered by a messenger weight sent down the wire (Fig. 7-19). At that time, even a qualitative understanding of vertical variability in the underwater light field was being sought.

Knudsen (1922) developed one of the earliest devices for measurement of spectral variability underwater. The instrument is shown in Fig. 7-20. Photographic measurements of spectral radiance, not irradiance, were made with this instrument. Knudsen was clearly aware of expected vertical spectral

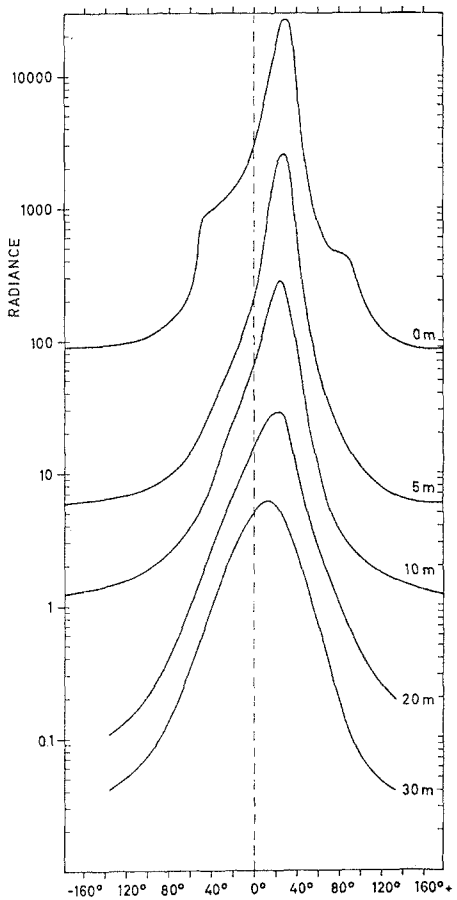

Fig. 7-18. Angular distribution of observed radiance (535 nm) at several depths (arbitrary units of radiance). Measurements were made with a single Gershun tube placed at different orientations (Jerlov and Fukuda, 1960).

variability, as he stated that "It must possible to investigate separately every single water layer of arbitrary chosen thickness since we already know that the conditions of light absorption can vary with depths." As with the Murray and Hjort instrument, Knudsen's sensor was operated with triggering messenger weights. Exposures were controlled by the time between the release of consecutive messengers (one to open the shutter, the next to close it). Careful calibration afforded him the ability to make what are now recognized as reasonably accurate estimates of diffuse attenuation.

In 1934, Ålvik also developed a spectral irradiance meter, shown in Fig. 7-21. Figures 7-22, 7-23, and 7-24 also show some representative data from this instrument from which quantitative values of the spectral diffuse attenuation

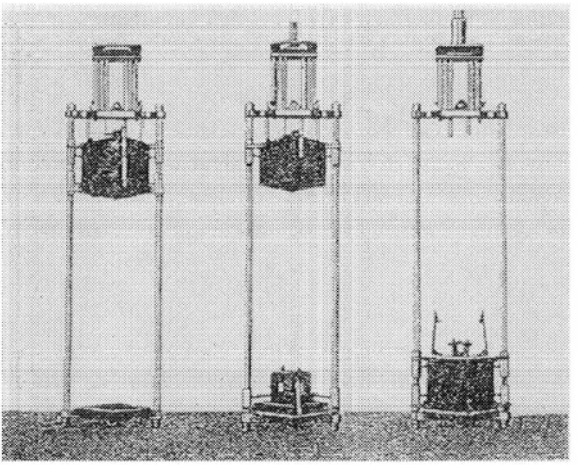

Fig. 7-19. The Helland–Hansen photometer. *Left*: instrument as lowered into the water. *Center*: instrument in the measuring position so that light could impinge on a photographic plate at the bottom before closing *(right)* (Murray and Hjort, 1912).

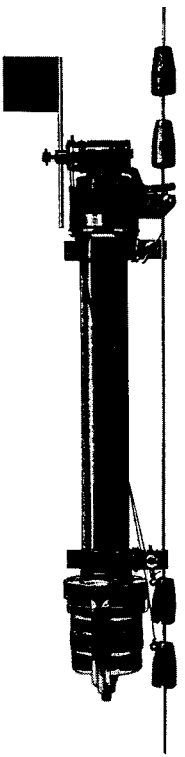

Fig. 7-20. Spectral zenith radiance meter. The instrument package consisted of two units at different depths so that the vertical attenuation coefficient could be measured accurately even during changing daylight conditions (Knudsen, 1922).

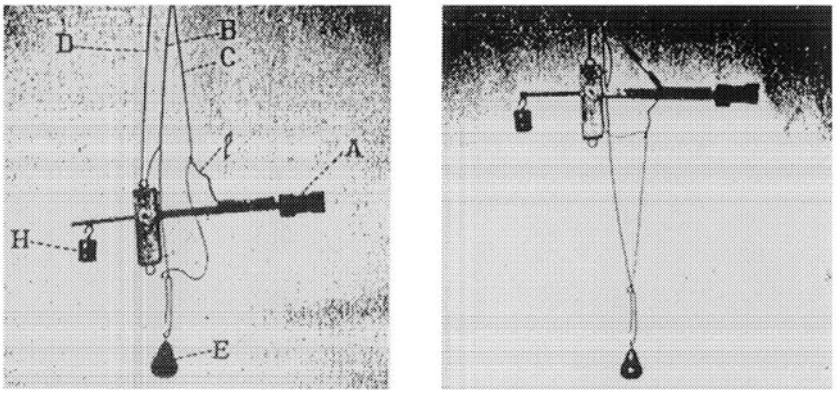

Fig. 7-21. Second version of the Helland–Hansen photometer, including the capability to measure spectral irradiance, using a filter difference technique. Instrument is closed on the left, open on the right (Ålvik, 1934).

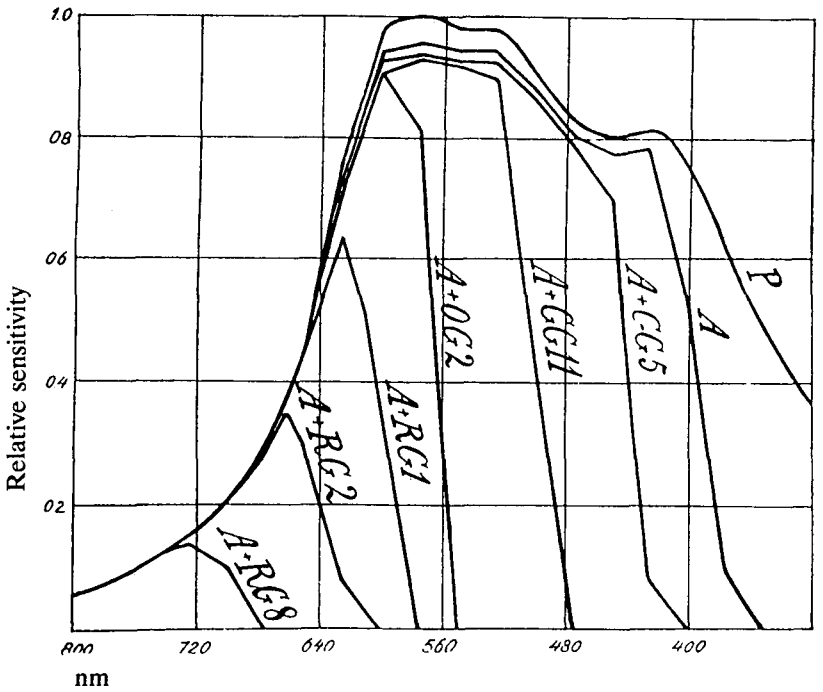

Fig. 7-22. Filter combinations used in the Ålvik photometer (Fig. 7-21). Note the inverted wavelength axis (blue to right) (Ålvik, 1937).

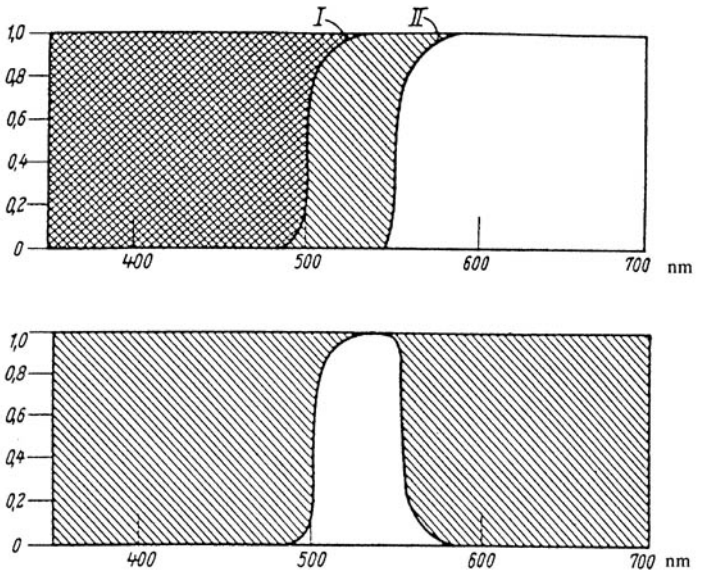

Fig. 7-23. Filter difference technique. Downward irradiance is first measured with the long-pass filter II. Measurement is repeated with filter I. By subtraction the spectral irradiance centered on 530 nm is determined (Sauberer and Ruttner, 1941).

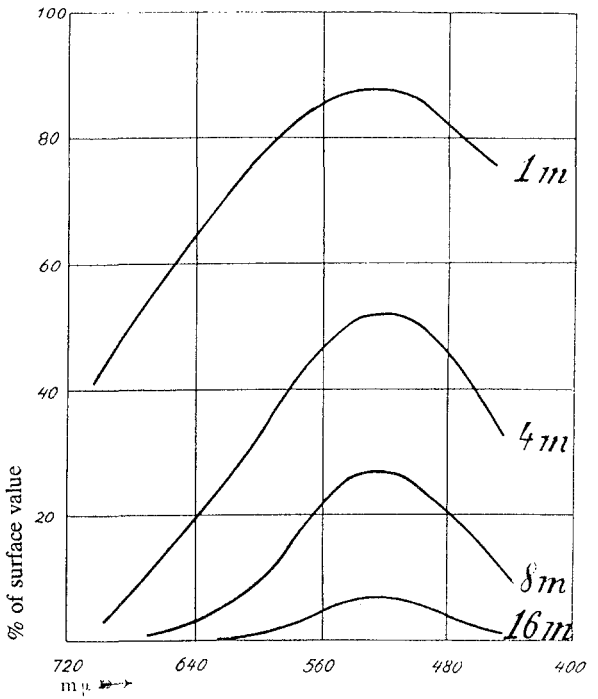

Fig. 7-24. The spectral distribution of downward irradiance at different depths in a typical Norwegian fjord (Ålvik, 1937).

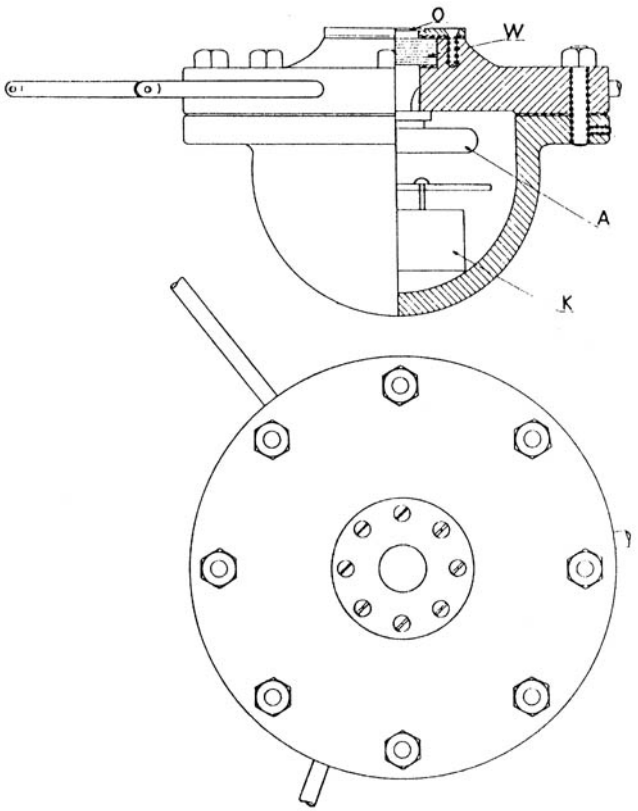

Fig. 7-25. Spectral underwater camera with remote filter control and light exposure control. This camera was used on the Swedish Albatross circumnavigation in 1949 (Jerlov and Koczy, 1951).

coefficient can be extracted. These data show similar characteristics for a Norwegian fjord to those seen nowadays with modern measurement techniques. Underwater irradiance meters based on camera techniques disappeared around 1951. One such late version is depicted in Fig. 7-25.

Electronic irradiance meters

One of the first electronic irradiance meters was developed by Pettersson and Landberg (1934) and is shown in Fig. 7-26. This type of instrument and contemporary versions (Figs. 7-27 and 7-28) were used extensively by many limnologists. The careful selection of glass absorption filters allowed for some of the first attempts at measuring the spectral variability in the in situ irradiance. The instrument was used to profile the water column with progressively narrower bandwidth filters (see Figs. 7-22 and 7-23). In this way a subtractive technique could be used to determine the high resolution spectral variability.

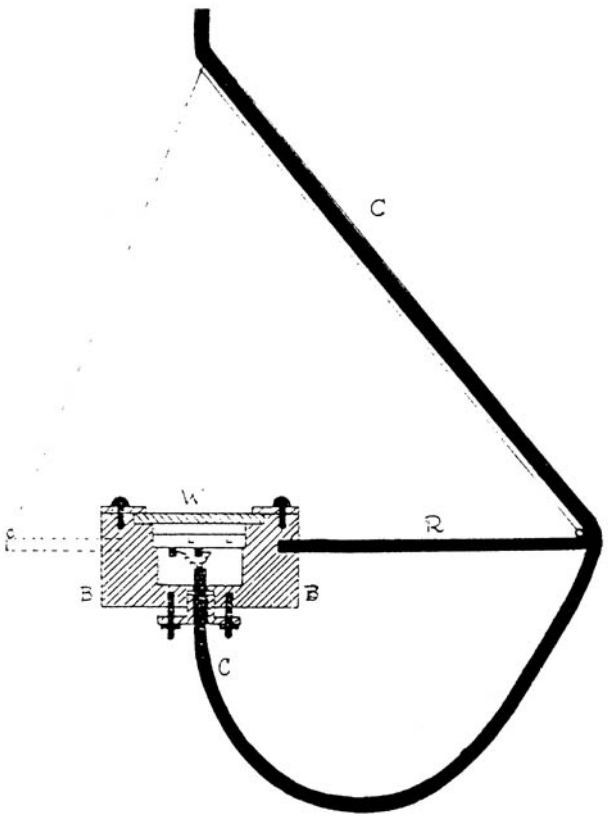

Fig. 7-26. Submarine actinometer; a downward irradiance meter utilizing a photovoltaic Lange cell instead of photographic plates (Petersson and Landberg, 1934).

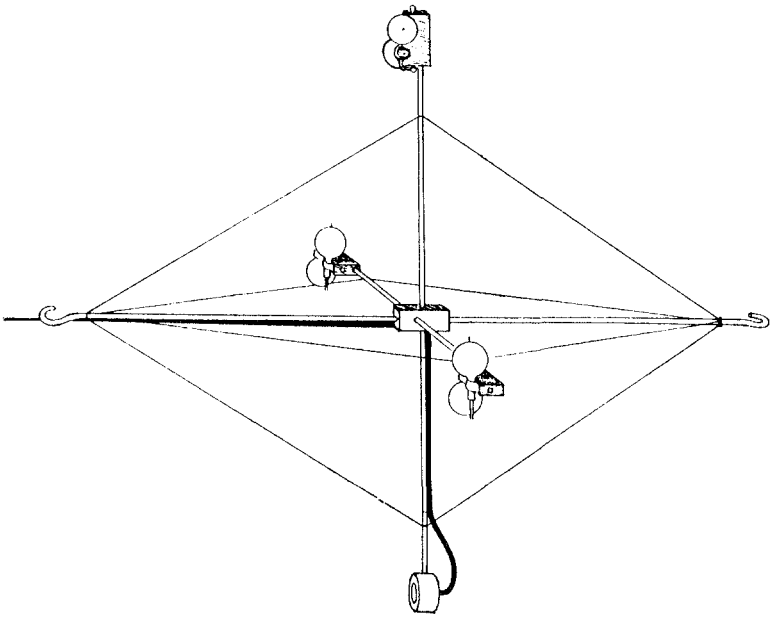

Fig. 7-27. In situ device for measuring primary production in the sea. Changes in oxygen contained in dark and transparent bottles provided the measure of production (Petersson et al., 1934).

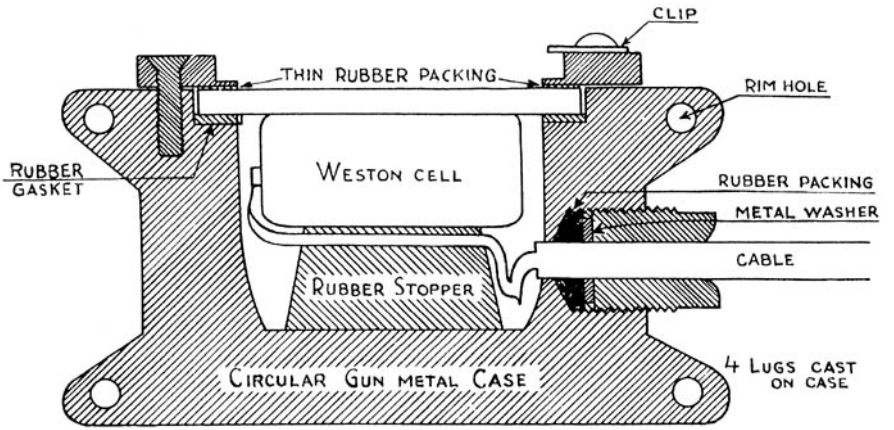

Fig. 7-28. Section through improved irradiance meter, which incorporates shock-protection (Petersson and Poole, 1937).

In 1937 Petterson and Poole developed a combined transmissometer and irradiance meter (Fig. 7-29). As shown in Fig. 7-29, the concept was to use simultaneous measurements of the downwelling solar irradiance and the transmission of an artificial light source, a concept that was later employed by Austin and Ensminger (1978).

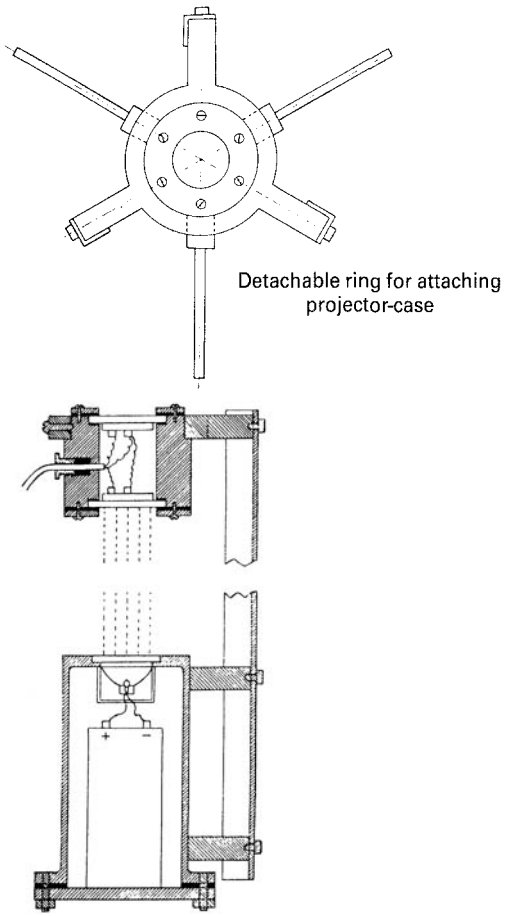

Fig. 7-29. Combined daylight and transparency meter (Petersson and Poole, 1937).

During World War II Scandinavian marine optical research was modest, judging from publications. Immediately after the termination of the war Swedish scientific activity became noteworthy again. The first start was given by the first attempt to establish an optical classification of seawaters (Johnson and Kullenberg, 1946; see Fig. 7-30).

One of the first underwater ultraviolet radiometers was developed by Johnson (1946; Fig. 7-31). This device incorporated clear quartz hemispheres to measure downward irradiance. Ultraviolet filtration was performed by filling the "intrasphere" regions with various chemical solutions having fixed and well-known spectral absorption characteristics. The water classifications of Jerlov in which values of K(310) are listed included measurements made with this sensor.

The next generation of irradiance meters was described by Jerlov (1951a) (Figs. 7-32 and 7-33). This instrument represents the type of thinking and design

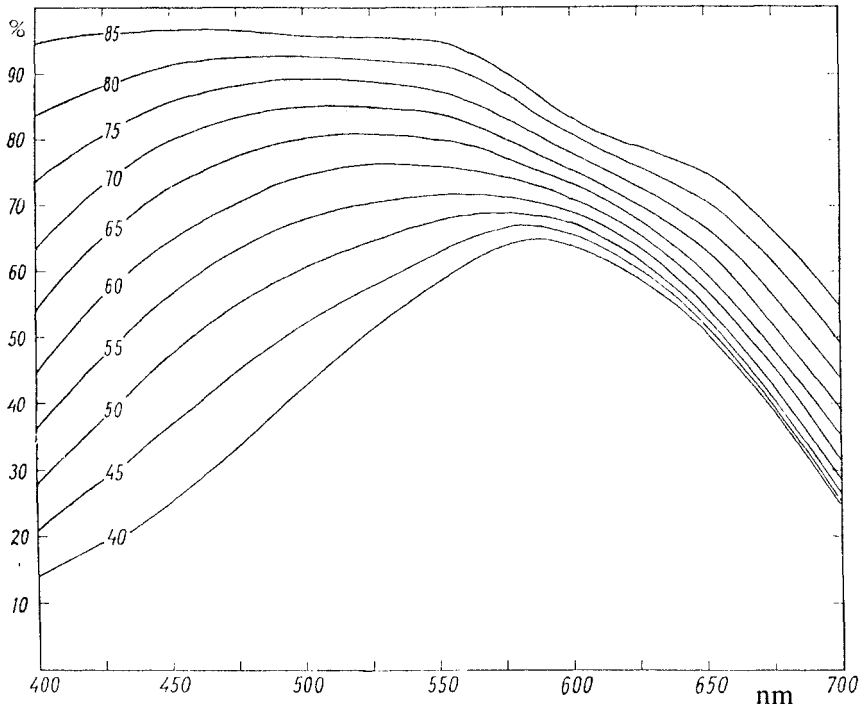

Fig. 7-30. First attempts to establish an optical classification of water masses by means of spectral light transmission (ordinate), in part obtained with the Petersson and Poole unit (Johnson [Jerlov] and Kullenberg, 1946).

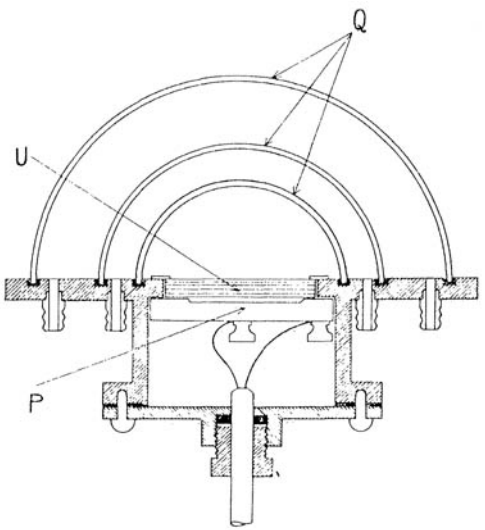

Fig. 7-31. Plan of the UVB meter for measuring downward irradiance around 310 nm. The meter was constructed for measuring the production of vitamin D and the amounts of yellow substance in the sea (Johnson [Jerlov], 1946).

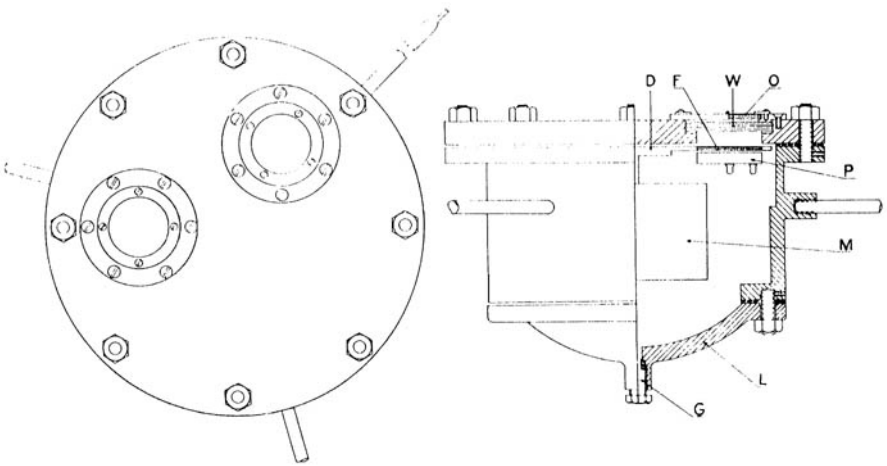

Fig. 7-32. Plan of the spectral irradiance meter used for developing the Jerlov optical classification of seawaters. One of the two cosine collectors uses a neutral-density filter for near-surface measurements (Jerlov, 1951a).

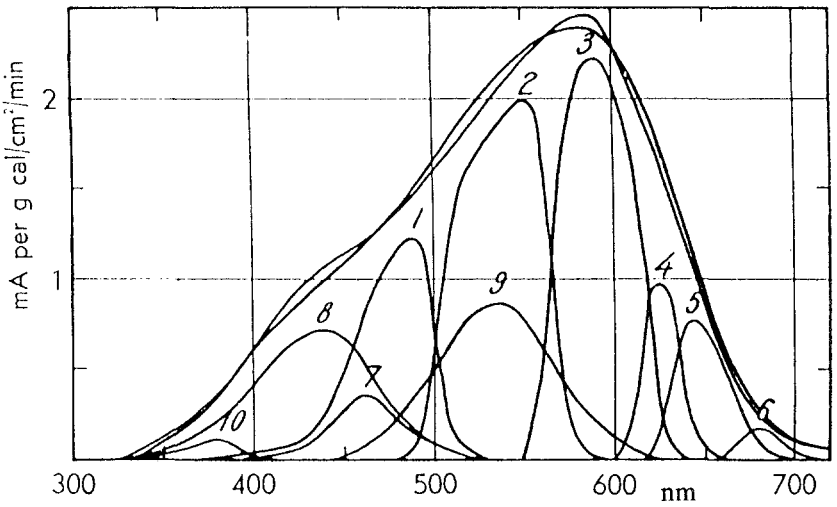

Fig. 7-33. Filters used in the Jerlov irradiance meter of Fig. 7-32 (Jerlov, 1951a).

characteristics found in modern irradiance meters. The sensor is an irradiance meter containing a filter disk enabling measurement of the irradiance at ten different wavelengths. A shipboard controller is used to move a filter wheel in front of the detector, thus scanning the spectrum from ultraviolet through the visible wavelengths. Neutral-density filters are used at the surface and removed at depth to extend the depth capabilities of the instrument.

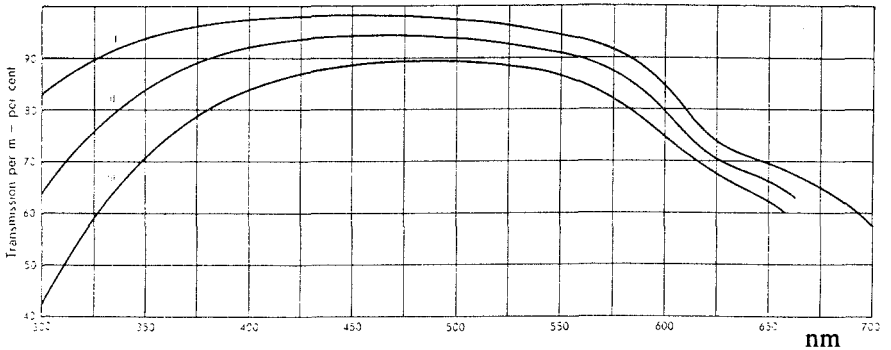

Fig. 7-34. Normal transmission curves for different ocean water types, with zenith sun. This is the first example of the Jerlov optical classification of ocean waters (Jerlov, 1951a, 1968, 1976).

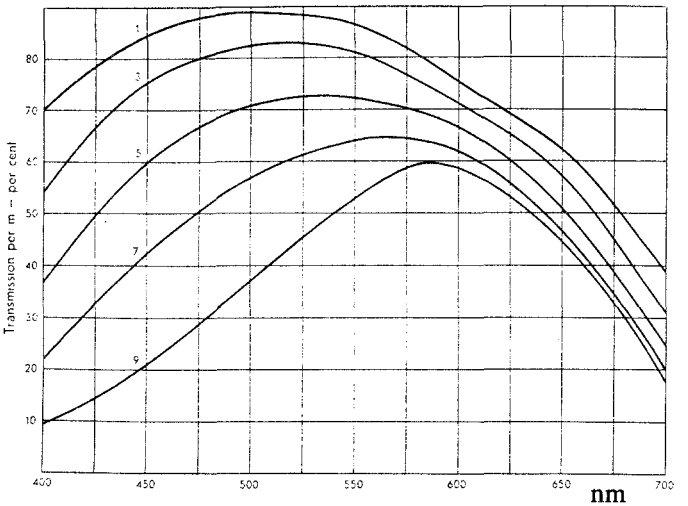

Fig. 7-35. Normal transmission curves for different coastal water types, with solar altitude of 45° (Jerlov, 1951a, 1968, 1976; see also Johnson [Jerlov] and Kullenberg, 1946).

The instrument shown in Fig. 7-32 was used to establish the Jerlov optical water mass classification depicted in Figs. 7-34 and 7-35. The original motivation for the measurements was to understand the role of spectral light transmission in the ocean with respect to the heating of the ocean. Specifically, one was interested in being able to extrapolate the attenuation at one wavelength to the complete spectrum, in order to simplify the measurement of total radiation entering the sea and the total absorption of that radiation (i.e., can a single measurement of irradiance be used to calculate the heat budget?). It is known now that such an extrapolation and calculation is not straightforward. At the time

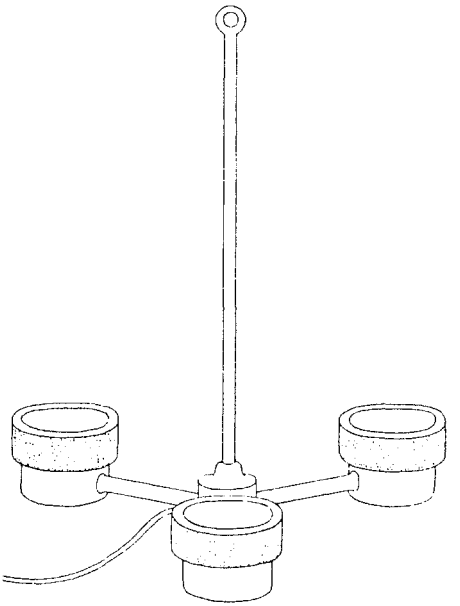

Fig. 7-36. A three-channel submarine photometer designed for primary production studies in the marine environment (Steemann-Nielsen, 1951).

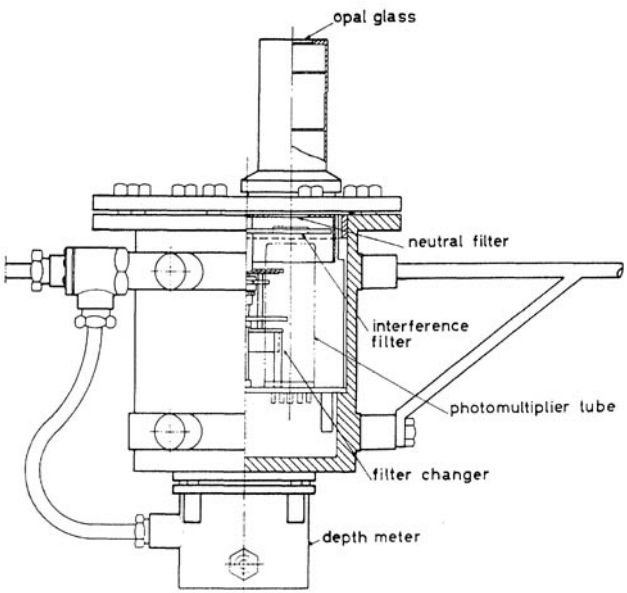

Fig. 7-37. Irradiance meter with interference filters, neutral density filter combinations, and a photomultiplier. Cosine collector is surrounded by air and water so that the immersion coefficient is 1.0.

of this work, however, this spectral approach represented a major step forward in optical oceanography.

Steemann-Nielsen (1951) developed a multispectral irradiance meter that allowed simultaneous measurements of downwelling irradiance at three different wavelengths (Fig. 7-36). The sensors were fitted with red, green, and blue filters, respectively. In combination, the spectral profiles with depth were used to define the wavelength-dependent photic depths. The meter was purposely made as simple as possible to insure that it would replace the white Secchi disk in Danish marine biological circles (until then without much success).

The last instrument to be mentioned in this chapter represents an end of one epoch with respect to spectral irradiance measurements. Twenty-five years ago the irradiance meter shown in Fig. 7-37 stood for some of the best available (Jerlov, 1965), and was used in that configuration for 20 years. Those were the days. . .

8

WHY IS THE MEASUREMENT OF FLUORESCENCE IMPORTANT TO THE STUDY OF BIOLOGICAL OCEANOGRAPHY?

Charles S. Yentsch
Bigelow Laboratory for Ocean Sciences

Introduction

What follows are my impressions of why the measurement of fluorescence has been and will continue to be important in biological oceanography. I will present some of the early history behind the introduction of fluorescence techniques to biological oceanography. What you will read is my impression of how the use of fluorescence advanced our studies, the history of why it was needed, and where it can take us. The text may read as elementary to some, but hopefully has the potential of generating interest in others. Let us begin by trying to answer the question posed by the title. The best short answer is: "Measurements of fluorescence are important for the study of primary production in the oceans." Figure 8-1 shows a block diagram of major areas of interest that used fluorescence techniques and the approximate dates of appearance. These blocks will serve to outline the major points of my discussion.

The search for a standard method for the measurement of chlorophyll

At the time I started my career in oceanography (1950), the quantitative measurement of chlorophyll was becoming an important objective for studies of primary production. Two important methods helped to advance this research: (1) the trichromatic spectrophotometric method of Richards with Thompson (1952), and (2) the introduction of membrane filtration by Creitz and Richards (1955). Neither of these may seem to be very important today; however, their importance concerns what was going on before these methods were introduced. The first advance introduced the Beckman DU spectrophotometer to the subject of quantitative analysis of ocean chemistry. Some of the best chlorophyll methods available in the 1950s used filter colorimeters; others used visual standards. The Richards with Thompson method called for optical measurements better than filter colorimetry could provide. The ability to characterize mixtures of pigments

I. Prior to Fluorometric Techniques

Richards with Thompson(1952)

1) spectrophotometric measurement of extracts

2) simultaneous equations for accessory chlorophylls

Creitz and Richards (1955)

1) membrane filtration

II. Sequence of Development of the use of Fluorometric Techniques and Areas of Continuing Research

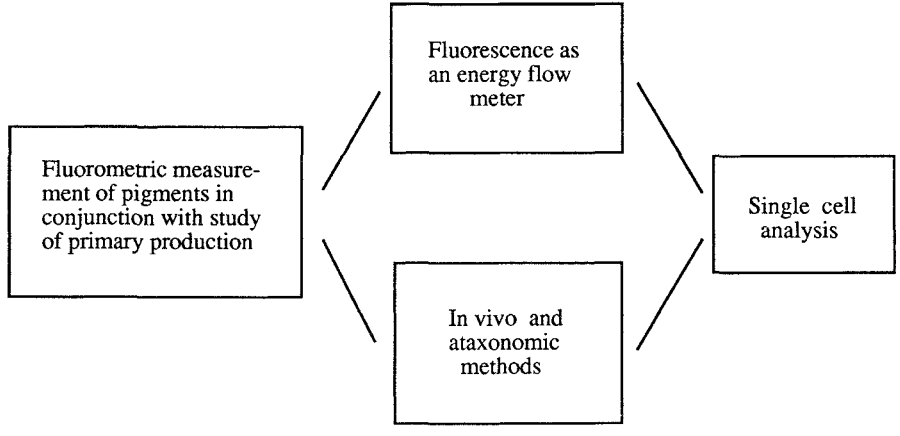

Figure 8-1. Block diagram and approximate timeline of major advancements in fluorescence techniques for biological oceanography.

in vitro required 10-nm spectral resolution and photometric accuracy that would insure that Beer's law was obeyed. The Beckman DU spectrophotometer met those requirements. The second advance introduced the use of membrane filters for microfiltration of particles from seawater. Prior to the use of membrane filters, one had to resort to fine mesh netting or centrifugation. I spent many hours on the end of a rubber policemen attempting to recover the algae from a Forest Centrifuge Cup. J.H. Ryther called my attention to a paper in which the author had resorted to a felt hat to filter out the phytoplankton.

One other issue was also important in the promotion of fluorescence techniques. During the 1960s, there was major interest in the assessment of open ocean productivity and determining why different regions were more or less productive. With the introduction of the radiocarbon method for the measurement of carbon fixation by primary producers, there arose a need for a standard method of measuring phytoplankton chlorophyll as a biomass estimate. It became apparent that spectrophotometry did not have enough sensitivity to measure the low concentrations of open ocean chlorophyll, unless one was willing to filter 5–10 liters of seawater. When analysts attempted to increase sensitivity by increasing the light pathlength through the cuvette, they encountered problems with light scattering from minute particles and changes in the refractive index of the extract solution. The major difference in sensitivity between light absorption and fluorescence is explained as follows. In the spectrophotometer, some of the parallel light is absorbed by the solution and can be related to the concentration (c) of the absorbing molecules by Beer's law:

$$\log \frac{I_0}{I} = \varepsilon c l \tag{8.1}$$

where $\log (I_0/I)$ is the optical density of the sample, I_0 is the incident light intensity, I is the transmitted light intensity, ε is the molar extinction coefficient, and l the light pathlength. At dilute concentrations of chlorophyll the spectrophotometer must distinguish the ratio of large numbers for I_0 and I that constitutes the optical density. Hence, the only means to increase this difference (assuming instrument noise is constant) is to increase the pathlength (see, for example, Chapter 4).

This is not the case for the fluorometric measurement of chlorophyll. The concentration of chlorophyll (c) is related to fluorescence (F) by

$$F = I_0 k c \cdot \phi \tag{8.2}$$

where k is an instrument factor, and ϕ is the fluorescence quantum efficiency of chlorophyll. Fluorescence intensity is directly proportional to the amount of incident light (I_0) and sensitivity can be improved by detecting low levels of light. The Turner fluorometer exhibited high sensitivity at low light levels due to a sensitive photomultiplier tube detector within a stable optical bridge. To the biological oceanographer this increase meant that less than 1 liter of open ocean

water needed to be filtered for the estimate of chlorophyll (Yentsch and Menzel, 1963).

The main problem with the measurement of chlorophyll by fluorescence concerned instrument calibration. The conventional method of standardization generally compared the fluorescence signal to the optical density of chlorophyll *a* extracts subject to specific instrumental conditions such as excitation intensity, broadband colored glass filters for excitation and emission wavelength selection, and the spectral response of the photodetector. For example, if one compares fluorescence to the optical density of pure solutions of chlorophyll *a*, the linearity and precision are excellent. However, when crude extracts of natural phytoplankton are used, the relationship becomes noisy because the extract also contains some of the accessory pigments chlorophyll *b* and chlorophyll *c*. The contribution to the fluorescence signal by these accessory chlorophylls is not totally removed by the broadband colored glass filters.

There is also a related but separate problem due to the presence of chlorophyll *b*. Dave Menzel and I had added the step of extract acidification to the fluorometric technique to measure the effect of pigment degradation. Acidification of chlorophyll *a* causes the fluorescence intensity to decrease about 50% due to changes in the quantum efficiency of pheophytin, the primary degradation product of chlorophyll. If the extract contains all pheophytin, there is little change in fluorescence after acidification. Pathways of degradation are

1. chlorophyll *a* – magnesium → pheophytin
2. chlorophyll *a* – phytol → chlorophyllide
3. chlorophyllide – magnesium → pheophorbide

It was recognized that the presence of chlorophyll *b* would interfere because fluorescence from pheophytin *b* after acidification was greater than that for the undegraded pigment before acidification.

Pursuit of the so called "acid ratio" technique was justified on the basis that it was believed that chlorophyll *b* was not a dominant pigment of marine phytoplankton. This impression has changed with the discovery of smaller microalgae in natural populations which, on a cellular basis, have a high proportion of chlorophyll *b* to chlorophyll *a*. The presence of chlorophyll *b* causes an overestimate of pheopigment concentration. How much error is attributed to chlorophyll *b* is presently unknown and probably can be resolved by comparative measurements with high-performance liquid chromatography (HPLC). Thin-layer techniques and solvent separation yield the same picture of the vertical distribution of chlorophyll and degraded products: chlorophyll *a* is most abundant in the upper layer of the euphotic zone with the percentage of pheopigments increasing with depth (Fig. 8-2). It is useful for bio-optical students to recognize that. A considerable fraction of the total pigment often called chlorophyll is degraded pigment. This knowledge is important to those interested in optical budgets in water masses and remote sensing of primary production.

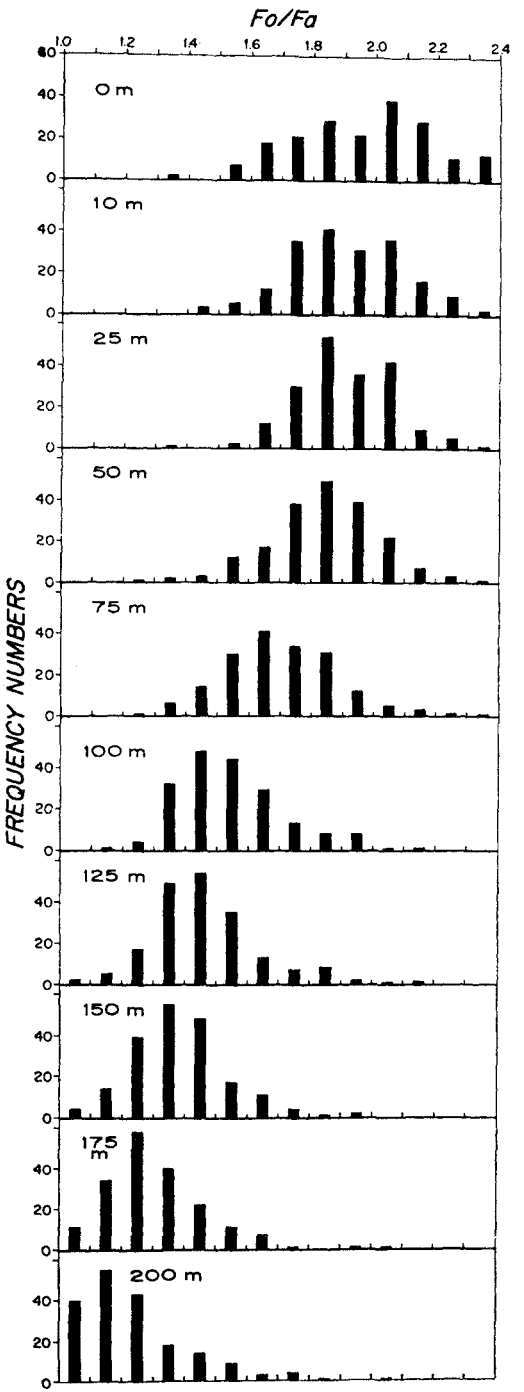

Fig. 8-2. Pheopigment concentration as fluorescence acid ratio versus depth at an Indian Ocean Station. $F_0/F_a > 2$ indicates undegraded chlorophyll *a*, $F_0/F_a = 1$ indicates 100% pheopigment. (Reproduced from McGill and Lawson, 1966.)

In the end, fluorescence replaced spectrophotometry as a rapid, sensitive, and precise standard method for the measurement of phytoplankton chlorophyll in vitro. Many variations of the method exist and the major problems of calibration and interference by accessory chlorophylls persist. However, fluorescence continues to be important as researchers strive to replace the standard methods with new technologies, such as HPLC.

Chlorophyll fluorescence as an energy flow meter

In 1965, Carl Lorenzen used a Turner fluorometer equipped with a flow-through door to establish that phytoplankton biomass could be measured by fluorescence in a continuous mode. This method, like its in vitro counterpart, suffered problems of calibration; yet it was these problems that were soon to become of research interest. In identical fashion to plant physiologists, who pioneered measurements of fluorescence, biological oceanographers recognized that variation in fluorescence yield was telling something about the kinetics of photosynthesis. Thus, kinetics could be measured remotely, and continuously.

The interest stimulated by these techniques is voluminous—a review of it alone is warranted, but not here. I call the attention of interested students to the important papers of Kiefer (1973) and Blasco (1973). These researchers have dealt with the influence of environmental variables on cellular fluorescence. The crux of the research was to determine what environmental factors influenced photosynthesis and growth. Variations in fluorescence yields were observed and interpreted as an index of energy flow in photosynthesis.

The concepts behind this research are that fluorescence and photosynthesis both increase with increasing light intensity. But with regard to photosynthesis, a portion of the curve is linear at low light levels, and flattens at high light intensities. Fluorescence, however, increases almost linearly with light. Close analysis of the F vs. I curve (Fig. 8-3) showed that it is composed of three slopes. The first slope occurs at low light intensity at or near the compensation intensity for photosynthesis. Another slope occurs in the region where photosynthesis appears to be a linear function of incident light. The third slope change, where F vs. I steepens, occurs near the onset of light saturation of photosynthesis (P_{max}). Franck and co-workers (see Clayton, 1965) interpreted these changes in slope to mean that when photons are not being actively used in photosynthesis, they are fluoresced. For example, below compensation practically all the photons are needed for photochemistry. With increasing light and photosynthesis, the curve gradually steepens then sharply increases at light saturation. The explanation is that when the amount of incident light satisfies photochemistry, more fluorescence (the yield) increases. Therefore, one concludes that anything that blocks light energy transfer to carbon fixation will increase cellular photosynthesis.

Needless to say, it is important to know in the ocean environment when, where, and why carbon fixation is uncoupled from light. Figure 8-4 outlines the thrust of much of this research. Pathway 1–2 is the photon pathway leading to

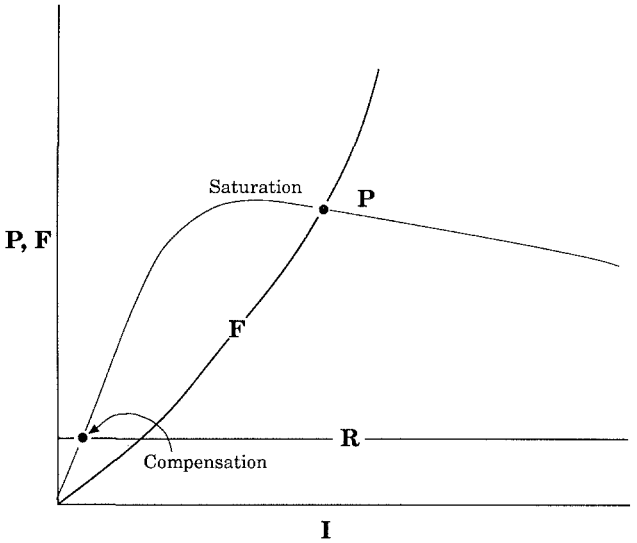

Fig. 8-3. Photosynthesis (P) and fluorescence (F) as a function of light intensity (I) for phytoplankton. Respiration (R) is a constant, unaffected by light intensity. Compensation point is where photosynthesis equals respiration, while saturation is the maximum for photosynthesis (P_{max}) whereby light intensity causes photoinhibition and a decrease in photosynthesis. Within the different regimes fluorescence yield increases with increasing light intensity until photosynthesis is light-saturated and absorbed photons are shunted off as fluorescence.

fluorescence from chlorophyll; pathway 1–3 is the pathway for reducing energy-rich substances needed to facilitate carbon fixation. The dark enzymatic reactions of carbon fixation are sensitive to temperature and the lack of carbon dioxide and nutrients, such as nitrogen and phosphorus. The plant herbicide DCMU introduced by plant physiologists is also used by ocean biologists to isolate the light from the dark reactions and to estimate the influence of the limiting parameters of carbon fixation.

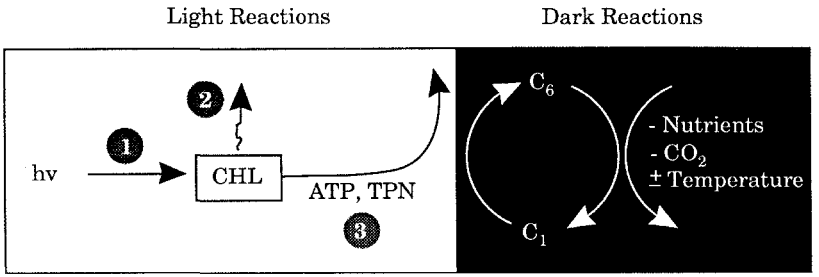

Fig. 8-4. Light and dark reactions of photosynthesis. Pathway 1–2 represents fluorescence, with pathway 1–3 representing carbon fixation. Respiration (in black) is affected by nutrients, substrate (CO_2) concentration, and temperature.

The reason these ideas are so attractive to those interested in phytoplankton photosynthesis concerns the possibility of arguing that the amount of in vivo fluorescence per unit of extracted pigment is in reality an energy flow meter and offers the possibility of assessing the efficiency of phytoplankton photosynthesis and what factors are affecting this efficiency. Exciting new results are appearing from Kiefer's and Falkowski's laboratories that suggest that in vivo fluorescence can be used for direct estimates of carbon fixation in natural populations of marine phytoplankton.

Ataxonomic methods

Those measuring primary production have yet to come to grips with the diversity of species in natural populations and the possibility of exploring kinetic diversity. There are those who do not see this as a research problem. Others wish to know why there are so many species, and why they change in time and space. Unfortunately, conventional taxonomy, when vigorously practiced, does not provide a feasible approach when extended over the dimensions of the oceans.

By measuring chlorophyll *a* fluorescence as excited by accessory pigments, it is possible to measure the contribution of different algal "color groups" within

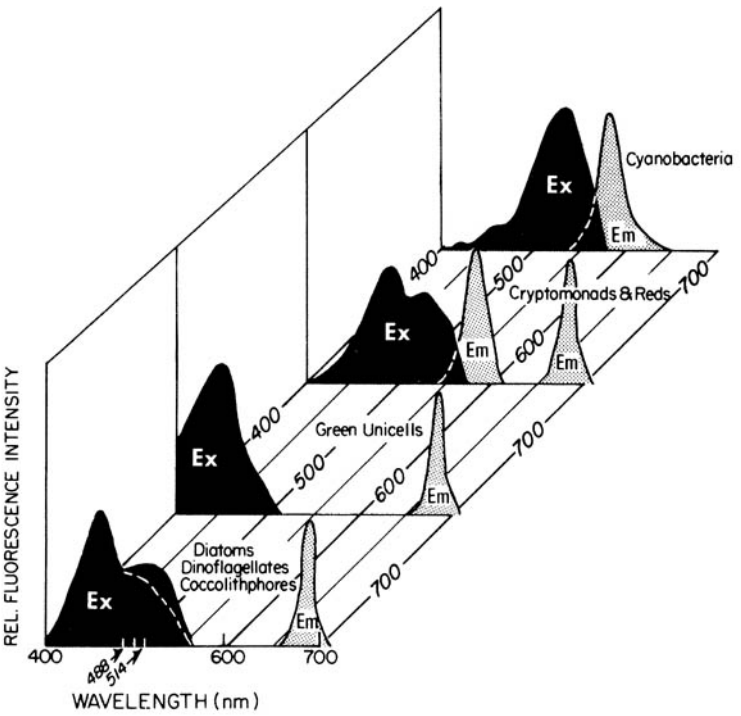

Fig. 8-5. Action spectra for fluorescence of major color groups of phytoplankton. Black curves are excitation spectra and open curves are emission spectra. (Reproduced from Yentsch and Phinney, 1985b.)

phytoplankton populations (Yentsch and Yentsch, 1979). Using this ataxonomic technique, many feel that continuous or remotely sensed measurements of these broad color groupings could be useful to obtain oceanic biogeographic data. Ideally, such a grouping should include diatoms, dinoflagellates, coccolithophores, chlorophytes, cryptomonads, and cyanobacteria. The crux of this ataxonomic approach lies in measuring the differences between the action spectra for light absorption of these groups (Fig. 8-5). The reality of this approach is that the principal differences in action spectra are between organisms without accessory pigments, namely, the green algae, and those containing accessory carotenoids such as fucoxanthin (mainly diatoms and dinoflagellates) or accessory phycobiliproteins (cyanobacteria and cryptomonads). How useful is a method with these restrictions? It has been recognized that some groups can be distinguished by measuring the excitation ratio (E_{530}:E_{450}) for chlorophyll *a* fluorescence (Yentsch and Phinney, 1985a; Mitchell and Kiefer, 1988a). Table 8-1 summarizes the ranges in the excitation ratio for various groups of organisms. For the most part organisms having carotenoids similar to fucoxanthin have higher ratios. But the phycoerythrin of cryptomonads absorbs in almost the same region, giving a high excitation ratio that causes confusion with diatoms and dinoflagellates. In any case, there are large biogeographical differences in the excitation spectra of different populations. For example, at the mouth of the Mississippi River one can encounter patches of water of markedly different ocean color over extremely short distances (Fig. 8-6). These signatures are designated as green and blue waters. The chlorophyll concentration was about 10 times greater in the green water than in the blue. The major difference in the spectral signatures was how effectively light at 530 nm excited chlorophyll *a* fluorescence. Presumably diatoms and other high-ratio groups were present in the green water. From other studies, we know that oligotrophic blue waters are dominated by other

Table 8-1.

Components	Principal accessory pigments	530:450	685^{a}_{EM}	$570–580_{EM}$
Diatoms	Chl C, fucoxanthin	0.8–0.9	Yes	No
Dinoflagellates	Chl C, peridinin	0.7–0.8	Yes	No
Coccolithophores	Chl C, UC-P[b]	0.3–0.4	Yes	No
Gold-brown unicells[c]	Chl C, UC-P	0.3–0.4	Yes	No
Green unicells[d]	Chl B, –	0.1–0.2	Yes	No
Cryptomonads	Chl C, PE, PC[e]	0.7–0.8	Yes	No
Cyanobacteria	–, PE, PC	–	No[f]	Yes

[a] Chlorophyll fluorescence at 685 nm when excited by light at 450 and 530 nm independently.
[b] Unidentified carotenoid protein complex.
[c] Examples are prymnesiophytes, chrysophytes.
[d] Examples are chlorophytes, prasinophytes.
[e] PE = phycoerythrin, PC = phycocyanin.
[f] Chlorophyll fluorescence at 685 nm appears to be undetectable in young marine cultures: the same emission at this wavelength can be detected in old cultures.

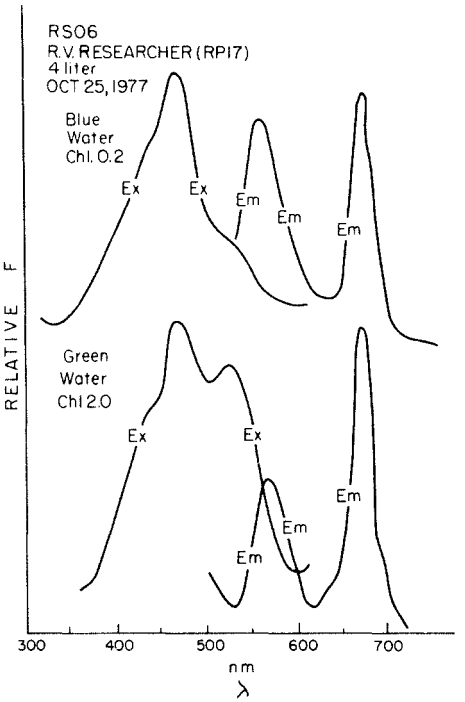

Fig. 8-6. Fluorescence spectra of natural phytoplankton populations occurring at a color front in the Mississippi River plume, October 25, 1977. Blue water population has low E_{530}:E_{450} ratio and high phycoerythrin content, presumably from cyanobacteria. Green water has higher color ratio and less phycoerythrin. (Reproduced from Yentsch and Phinney, 1985a.)

organisms less than 5.0 μm in diameter that have low ratios. The ability to sense differences in the action spectra of oligotrophic versus eutrophic populations and to relate these differences to average cell size places color ataxonomy as a valuable parameter for understanding the meaning of diversity.

To test this idea we (Yentsch and Phinney, 1985a) serially sieved and filtered phytoplankton populations using plankton netting and membrane filters and measured the excitation and emission spectra for various size fractions. Figure 8-7 shows spectra for three sizes. Note that for organisms 10 μm or larger, there exists a conspicuous shoulder in the excitation spectra at 530 nm. The excitation ratio (E_{530}:E_{450}) is greater than 0.50. Those organisms retained by the 1.0-μm filter exhibited no appreciable shoulder at 530 nm and the excitation ratio is less than 0.50. For those organisms that pass through the 1.0-μm filter and are retained on the 0.45-μm membrane, the fluorescence emission by phycoerythrin is markedly apparent and the excitation ratio is less than 0.40. By size fractionating a large number of samples of oceanic populations we can compare E_{530}:E_{450} over the size range 0.45–58 μm (Fig. 8-8). Highest ratios occur when cell diameter is greater than 10 μm. At sizes below 10 μm, the ratios are lower. There exists considerable spread around the data and we do not know whether this is due to experimental error and/

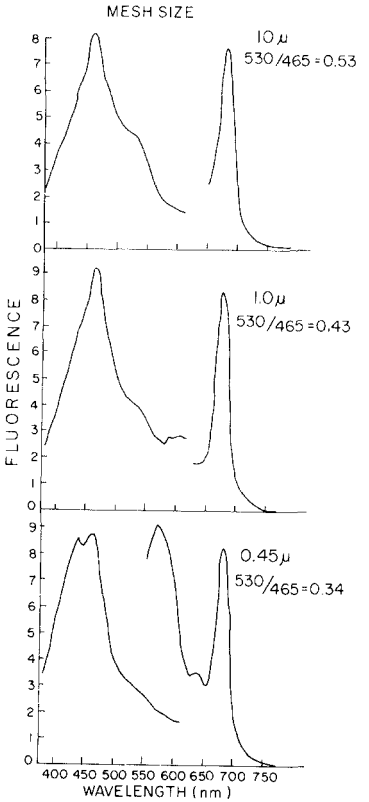

Fig. 8-7. Fluorescence spectra of size-fractionated natural phytoplankton population. Color ratio increases with increasing size and phycoerythrin is present only in the smallest size fraction, presumably the cyanobacteria. (Reproduced from Yentsch and Phinney, 1985a.)

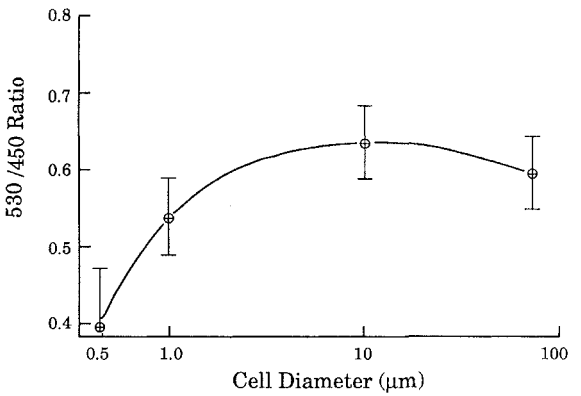

Fig. 8-8. Color ratio as a function of size for entire data set as in Fig. 8-7. High ratio for cell sizes >10 μm, low ratio for smaller cells. (Reproduced from Yentsch and Phinney, 1985a.)

or variance among species. The ecological significance of the data concerns the relationship between phytoplankton growth and mean cell size: Size is directly proportional to nutrient assimilation, photosynthesis, respiration, and growth.

We can summarize our findings to date by illustrating some of the major points:

1. The excitation ratio E_{530}:E_{450} is correlated with the chlorophyll biomass of the ocean.
2. Chlorophyll *a* excitation ratio E_{530}:E_{450} is higher in coastal than offshore populations.
3. With the exception of filamentous cyanobacteria, fluorescence from phycobiliproteins is not observed in samples taken by fine plankton nets.

It is clear that excitation and emission characteristics contain information about individual phytoplankton particles in natural populations.

Fluorescence studies in single-cell flow cytometry

A recent advance in particle analysis is a technique called flow cytometry (Fig. 8-9; see also Chapter 6). Advantages of flow cytometric analysis include the

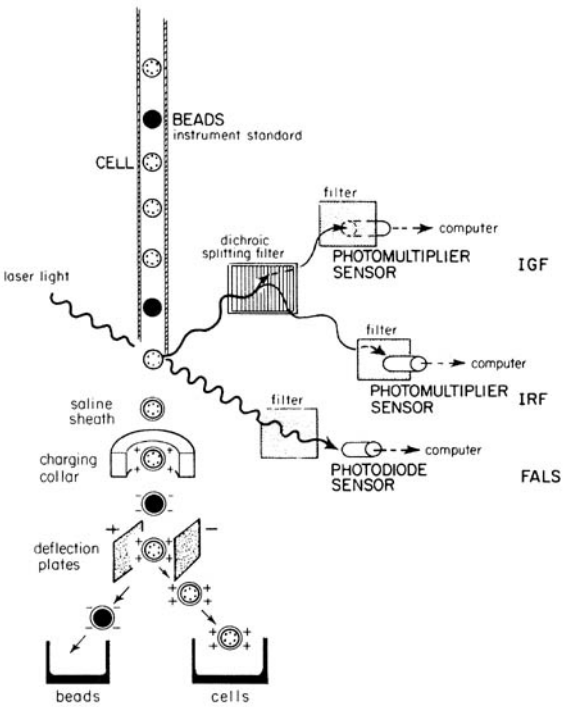

Fig. 8-9. Schematic diagram of a laser-based flow cytometer with sorting capabilities. Cells and beads in a laminar flow stream intersect the laser beam one at a time. Signals of green or red fluorescence (IGF or IRF) and forward angle light scatter (FALS) are used by the instrument computer to make sort decisions. (Reproduced from Yentsch and Spinrad, 1987.)

speed of analysis (in excess of 10 000 particles per second), the multiparametric measurements for the same particle, extremely high precision and sensitivity, and the ability to physically sort out from the flow stream particles that meet specific size and/or fluorescence criteria. This technique provides state-of-the-art technology for the sizing (0.3–150 μm range) and simultaneous measurement of optical properties of individual particles. Specific measurements include particle size measured as equivalent spherical volume, particle size measured as forward angle light scatter, 90° light scatter, and up to three colors of fluorescence (Phinney and Cucci, 1989).

Fluorescence is a highly sensitive method of detection utilizing not only autofluorescent pigments and many useful stains but also fluorescent labels that can be linked to numerous antibody probes (Ward, 1990). Figure 8-10 depicts

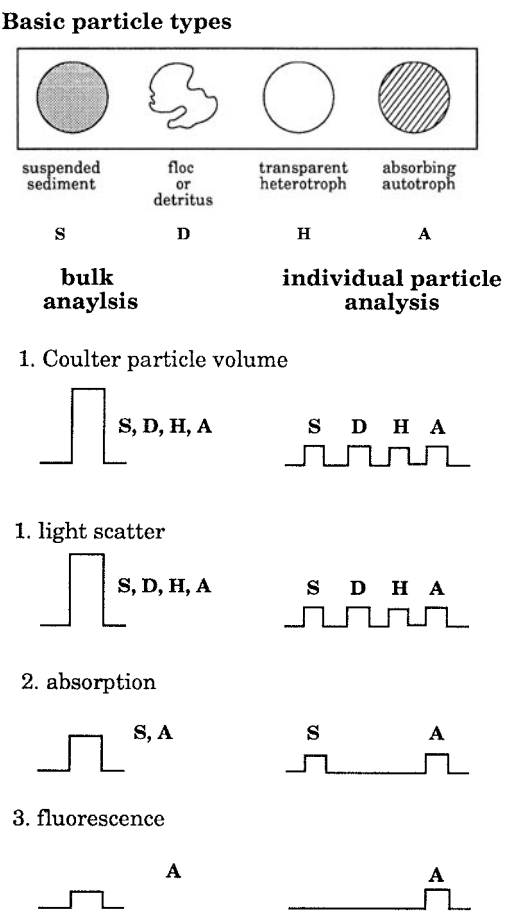

Fig. 8-10. Upper panel, Particles of near-equal "size" but vastly differing optical properties. The suspended sediment particle (S) absorbs and scatters light. Floc or detritus (D) is amorphous but does scatter light. Transparent heterotrophs (H) scatter light. Autotrophs (A) absorb, scatter, and fluoresce light.

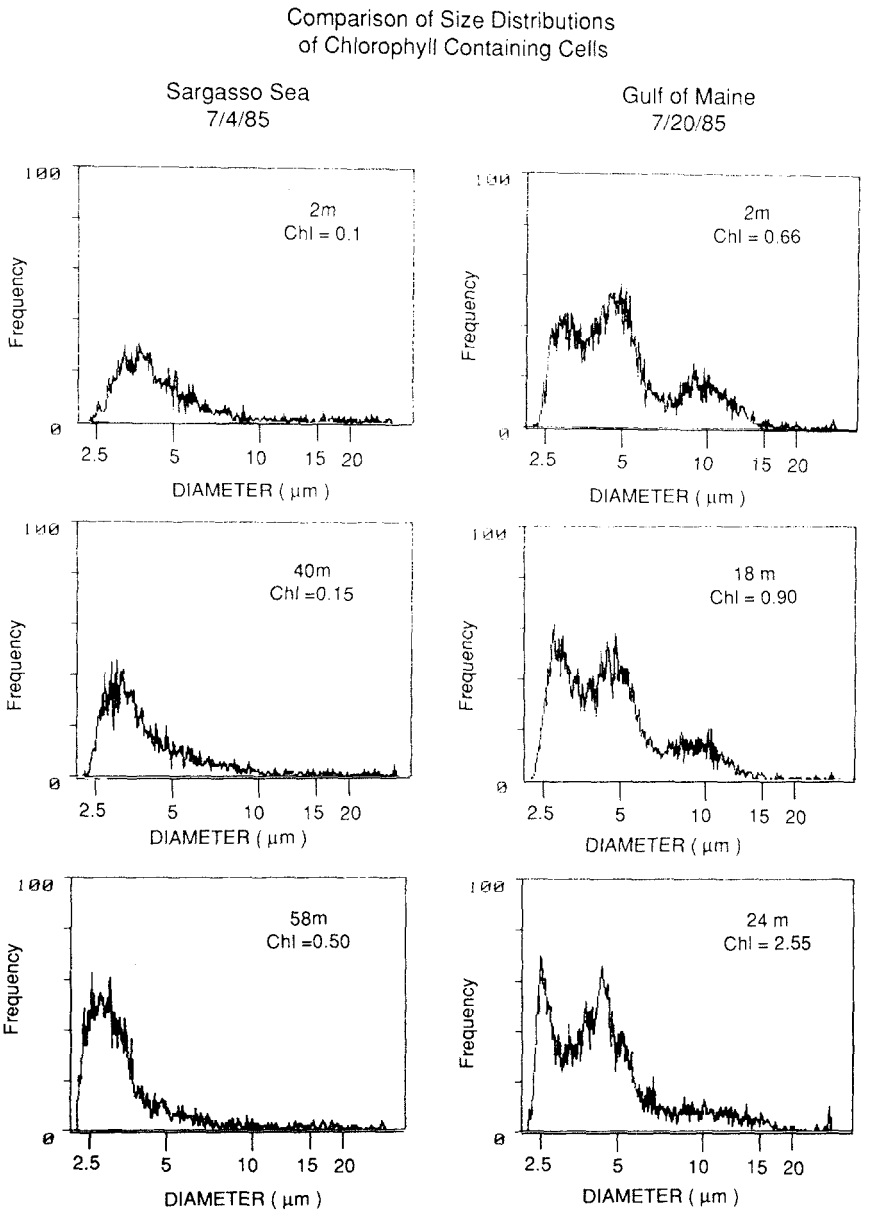

Fig. 8-11. Size spectra of fluorescent phytoplankton for the Sargasso Sea (left) July 4, 1985 and the Gulf of Maine (right) July 20, 1985 obtained by flow cytometry. (Reproduced from Yentsch and Phinney, 1989.)

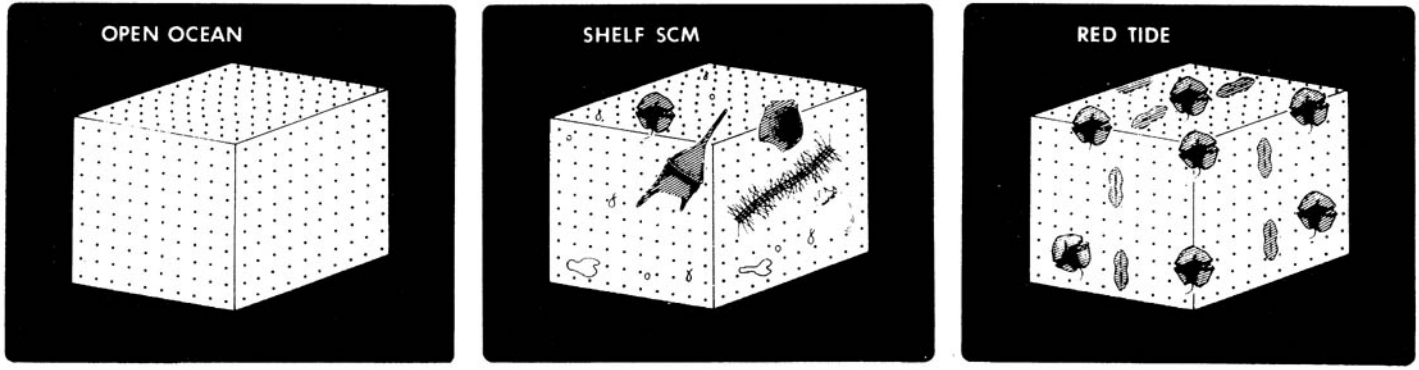

Fig. 8-12. Schematic diagrams scaled to size representing 0.01 ml samples. *Left*: open-ocean sample dominated by <3 μm cells at 10^5 ml^{-1}. *Center*: shelf-water subsurface chlorophyll maximum (SCM) sample has equal concentration of <3 μm cells as open-ocean but also has 10^3 ml^{-1} concentration of 3–8 μm, 10^2 ml^{-1} of 8–30 μm and 10^1 ml^{-1} of 30–100 μm cells. Detrital particles are indicated by lack of shading. *Right*: red tide sample is similar to SCM with the exception that one or two species tend to dominate. A pennate diatom is shown with the red tide dinoflagellate *Protogonyaulax tamarensis* var. *excavata*. (Reproduced from Yentsch and Spinrad, 1987.)

particle detection capabilities: equivalent spherical volume and light scatter detectors count and measure each type of particle (S = suspended sediment; D = detritus or floc; H = heterotroph; A = autotroph or microalgae). Fluorescence detection eliminates the measurement of nonfluorescing particles, or particles that fluoresce at wavelengths shorter or longer than the target wavelengths. This serves as a useful characterization of oceanic biogenic particles.

Figure 8-11 presents two extremes in the size spectra (from light scattering data) of cells of chlorophyll-containing organisms. At one extreme are the populations observed in the oligotrophic Sargasso Sea. At the other extreme are populations observed in the waters of the continental shelf off New England. In both cases, there is a subsurface chlorophyll maximum: at 58 m in the Sargasso Sea and at 24 m in the Gulf of Maine. The mean spherical diameter for the Sargasso Sea population is centered at about 3.0 μm. In contrast, the Gulf of Maine population exhibits three prominent maxima in cells size: 3.0, 5.0, and, in the case of the surface, 10.0 μm. The comparison of the two regions demonstrates that with increasing nutrient availability in coastal regions the cell size spectrum confirms the appearance of large cell sizes. It is important to recognize that this is not because of removal of small cells but rather the addition of large cells. Yentsch and Spinrad (1987) suggested that the larger cells associated with rich coastal waters are present in reduced number, but that their cell volume contributes significantly to the biomass, again demonstrating that size spectra change not because of the elimination of certain small sizes but because of the addition of large sizes (Fig. 8-12). The large particles shown in this illustration

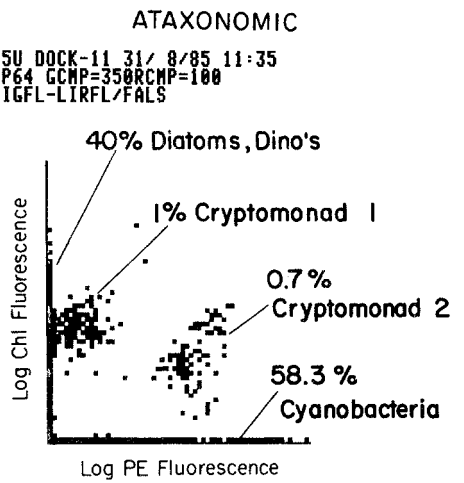

Fig. 8-13. Ataxonomic flow cytometry analysis of <5 μm size fraction of a natural phytoplankton population based on two colors of fluorescence. Cyanobacteria exhibiting only phycoerythrin (PE) fluorescence lie along the abscissa, diatoms and dinoflagellates that exhibit only chlorophyll (Chl)fluorescence lie along the ordinate, while two populations of cryptomonads exhibiting both Chl and PE fluorescence can be distinguished. Argon-ion laser excitation at 514 nm, 500 nm. PE emission = 540–590 nm; Chl emission >670 nm. (Reproduced from Phinney and Cucci, 1989.)

are phytoplankton species characteristic of eutrophic coastal waters; red tide dinoflagellates and diatoms. The important message of this illustration concerns the sparsity of large particles in the open sea and the universal background abundance of small particles. Figure 8-13 demonstrates the diversity of the smaller particles measured by flow cytometry.

Conclusions

In presenting the early history of the use of fluorescence in oceanography, I found it rather easy to trace early developments, but more difficult as time progressed to the present. The use of fluorescence in biological oceanography is rapidly growing; it is being pushed by studies of single cell analysis, bulk and particle optics, and remote sensing.

There is little doubt in my mind that the early in vitro methods tended to direct our attention to the analysis of extracts. Our attention now has shifted to quantification and characterization of individual particles. The diversity of particles in the sea now touches every aspect of biological oceanography.

9

LIGHT ABSORPTION, FLUORESCENCE, AND PHOTOSYNTHESIS: *SKELETONEMA COSTATUM* AND FIELD MEASUREMENTS

Dale A. Kiefer
University of Southern California

Introduction

In this chapter we will consider the fate of photons that are absorbed by phytoplankton. While such interaction will involve both the scattering and absorption of photons, we will be concerned with absorption and the subsequent processes of photosynthesis and the fluorescence of chlorophyll *a*. In particular and as the title of this chapter indicates, I wish to consider the environmental factors that cause variations in the cellular rates of light absorption, fluorescence, and photosynthesis. This consideration will focus on how environmental factors such as temperature, nutrient concentration, light intensity, and photoperiod effect changes in these three processes.

Our approach to examining the relationship between light absorption, fluorescence, and photosynthesis is based upon phenomenological formulations between these three processes. The rate of chlorophyll *a* fluorescence from a suspension of cell of cells, F_f, is by definition the product of the rate of light absorption by the suspension, $F_a(\lambda)$, and the quantum yield of fluorescence, $\phi_f(\lambda)$:

$$F_f = \int_{400}^{700} \phi_f(\lambda)\, F_a(\lambda)\, d\lambda \tag{9.1}$$

Similarly, the instantaneous rate of photosynthesis, F_c, is the product of the rate of light absorption, $F_a(\lambda)$ and the quantum yield of photosynthesis, $\phi_c(\lambda)$:

$$F_c = \int_{400}^{700} \phi_c(\lambda)\, F_a(\lambda)\, d\lambda \tag{9.2}$$

The rate of light absorption by the cell suspension will of course vary with both the concentration of cells, the cellular concentration and types of pigments,

and the spectral distribution of the irradiance. Thus, it is often convenient to represent the rate of light absorption by the cell suspension as the product of the concentration of chlorophyll, chl, the chlorophyll-specific rate of light absorption cross section, a_{chl}, and irradiance:

$$F_a = \text{chl} \int_{400}^{700} a_{chl}(\lambda) E_0(\lambda) d\lambda \tag{9.3}$$

We will examine variations in quantum yields and cellular concentrations of chlorophyll, which will be indexed by the cellular concentration of carbon (see definition of θ below). The relationship between light absorption and photosynthesis will be analyzed in the continuous cultures of the marine diatom *Skeletonema costatum*. We will then consider field measurements that confirm the relationships found in *Skeletonema* . Finally, drawing largely on field studies, we will examine the relationship between natural fluorescence, the concentration of chlorophyll, and photosynthesis. We will address the question of how well we can estimate rates of photosynthesis from measurements of the rates of fluorescence. Unfortunately, there is little information available to us to assess whether there are large differences in the response between different species.

Light absorption and growth in continuous culture

The relationship between cellular light absorption and photosynthesis is well illustrated by the steady state growth of *Skeletonema costatum*. One study by Yoder (1979) examined the cellular concentration of chlorophyll *a* and growth rate of cells limited by light intensity and temperature. Yoder grew *Skeletonema costatum* in a turbidostat at five temperatures, 0, 5, 10, 16, 22°C and at five light intensities ranging between 9 and 240 mmol m^{-2} day^{-1}. Although cultures were also grown under a number of different photoperiods, values for the ratio of cellular carbon to chlorophyll *a* were reported only for a 15-h light and 9-h dark cycle.

The other study by Sakshaug et al. (1988) examined cellular concentration of chlorophyll *a* and growth rate of cells grown at 15°C and limited by either light intensity, daylength, or rate of nutrient supply. *Skeletonema costatum* was grown continuously by daily dilution with a medium with an elemental composition that insured nitrogen limitation. The cultures were maintained at 20°C, at six light intensities, ranging from 12 to 1200 mmol m^{-2} day^{-1}, three photoperiods, 6-h light, 14-h light, and 24-h light, and between four and six rates of dilution. The matrix of light intensities, dilution rates, and photoperiods was not complete.

We will explore the results of these two studies by examining the terms in a phenomenological equation that is somewhat more detailed than those presented in the introduction:

$$g = \frac{D}{\theta} \int_{400}^{700} \phi_c(\lambda) a_{chl}(\lambda) E_0(\lambda) d(\lambda) \tag{9.4}$$

where g is the carbon specific photosynthetic rate in units of day^{-1}, ϕ_c is the quantum yield of steady-state carbon fixation in units of g-atom carbon/mole photons, a_{chl} is the chlorophyll specific absorption coefficient in units of m^2 per mg chlorophyll a, E_0 is the scalar irradiance in units of mol photons $m^{-2}\,day^{-1}$, D is the photoperiod in units of the fraction of a 24-h day, and θ is the ratio of cellular carbon to cellular chlorophyll a in units of g-atom carbon per g chlorophyll a.

In fact the studies of Yoder and Sakshaug et al. consisted of measurements of E_0, D, θ, and specific growth rate, μ. In order to calculate the quantum yield, ϕ_c, from Eq. (9.4) we assumed that a_{chl} had a constant value of $16\,m^2$ per g chlorophyll a and that the specific respiration rate was an insignificant fraction of the carbon specific photosynthetic rate. To a limited extent both assumptions can be questioned.

Adaptation to temperature

Figures 9-1 through 9-3 summarize the adaptive response of *Skeletonema* to variations in temperature at a fixed photoperiod of about 14-h and a rate of supply of nutrients that is saturating to growth. Figure 9-1 indicates that at 0°C maximal growth is about $0.3\,day^{-1}$, at 5°C it is $0.6\,day^{-1}$, at 10°C it is $1.1\,day^{-1}$, and at 16°C and 22°C it is $1.8\,day^{-1}$. We also note from the data that the irradiance sufficient to saturate growth decreases with temperature. At 0°C $1.5\,mol\,m^{-2}\,day^{-1}$ is sufficient to saturate growth. At 5°C saturation is $2\,mol\,m^{-2}\,day^{-1}$, and at 10, 16, and 22°C it is about $6\,mol\,m^{-2}\,day^{-1}$.

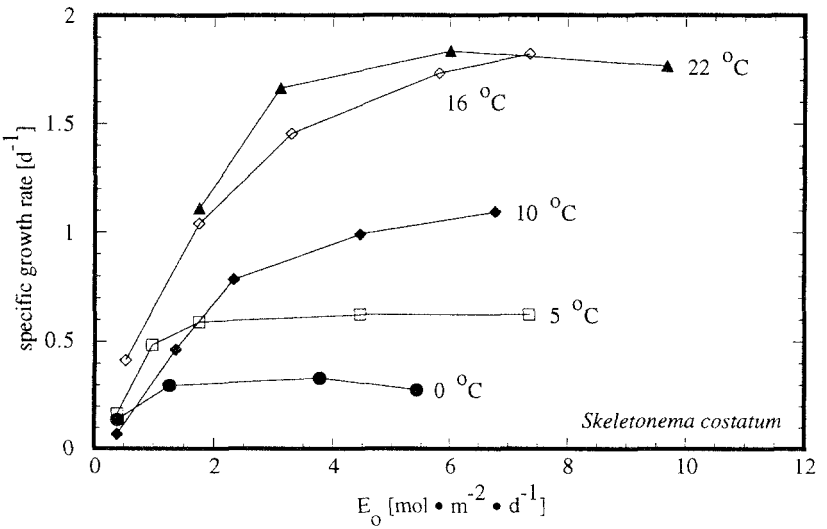

Fig. 9-1. The specific growth rate of *Skeletonema costatum* versus irradiance. As indicated the lines connect measured values for cultures grown at a given temperature. Nutrient concentrations were saturating to growth, and the photoperiod was about 14 h.

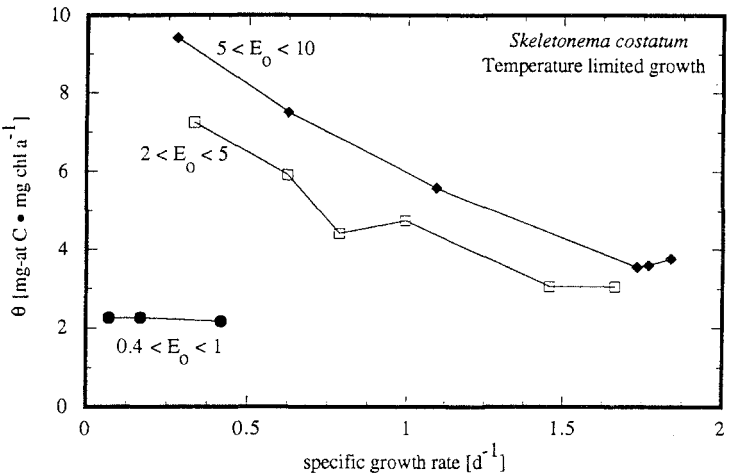

Fig. 9-2. The ratio, θ, of cellular carbon to chlorophyll *a*, versus specific growth rate. The lines connect measured values for cultures grown at a given irradiance but varying temperatures. Nutrient concentrations were saturating to growth and the photoperiod was about 14 h.

In Figure 9-2 the carbon to chlorophyll *a* ratio, θ, for a given irradiance is plotted as a function of the temperature-limited specific growth rate, $\mu(T)$. Since the photoperiod is 15 h for all the data, the growth rate for a given irradiance is uniquely determined by temperature. Thus, for example, the coordinates for $\mu(T)$ and θ for the line connecting light intensities between 5 and 10 mol m^{-2} day^{-1} are values for increasing temperature as one looks from left to right. Two features of

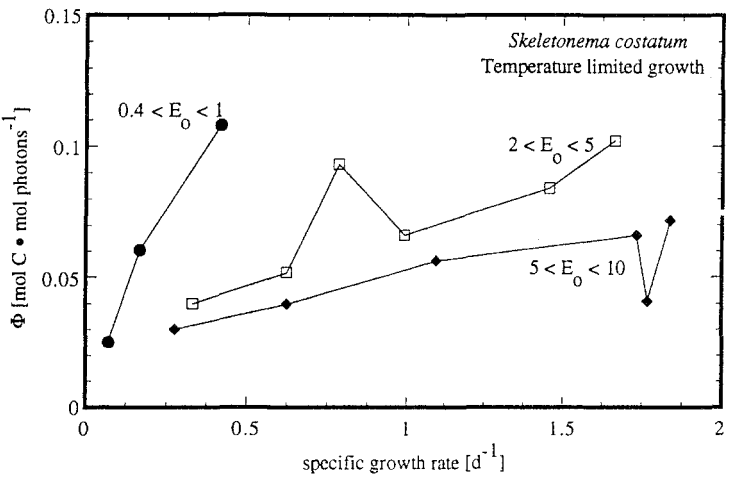

Fig. 9-3. The photosynthetic quantum yield, ϕ_c, versus specific growth rate. The lines connect measured values for cultures grown at a given irradiance but varying temperature. Nutrient concentrations were saturating to growth and the photoperiod was about 14 h.

this figure are noteworthy. First, the larger the values of E_0, the larger are the values of θ. Second, the response to change in temperature differs with irradiance. At low values of E_0 ($0.4 < E_0 < 1$), θ changes little with temperature-limited growth rate, but at high values of E_0 (e.g., $5 < E_0 < 10$), θ decreases with increases in temperature-limited growth rate.

In Figure 9-3 the quantum yield calculated from Eq. (9.4), ϕ_c, for a given irradiance is plotted as a function of $\mu(T)$. We note that ϕ_c decreases with increases in E_0. In addition we note that the response to temperature-limitation differs with irradiance. At low values of E_0, ϕ_c increases sharply with increases in $\mu(T)$ ($0.4 < E_0 < 1$), but at high values of E_0 (e.g. $5 < E_0 < 10$), ϕ_c shows only a small increase with $\mu(T)$. Thus, a comparison of Figs. 9-2 and 9-3 indicates a dichotomy in the adaptation of *Skeletonema*: At high light levels temperature limitation causes increases in the cellular ratio of carbon to chlorophyll *a* but little change in quantum yield. At low light levels temperature limitation causes little change in the cellular ratio of carbon to chlorophyll *a* but sharp decreases in the quantum yield. We will see that this dichotomy also exists for nutrient limitation.

Adaptation to nutrient supply

Figures 9-4 through 9-7 summarize the adaptive response of *Skeletonema* to variations in nutrient supply at differing light levels (Figs. 9-4 and 9-5) and at differing photoperiods (Figs. 9-6 and 9-7). In Figure 9-4 the carbon to chlorophyll *a* ratio, θ, for a given irradiance and a photoperiod of 24 h is plotted

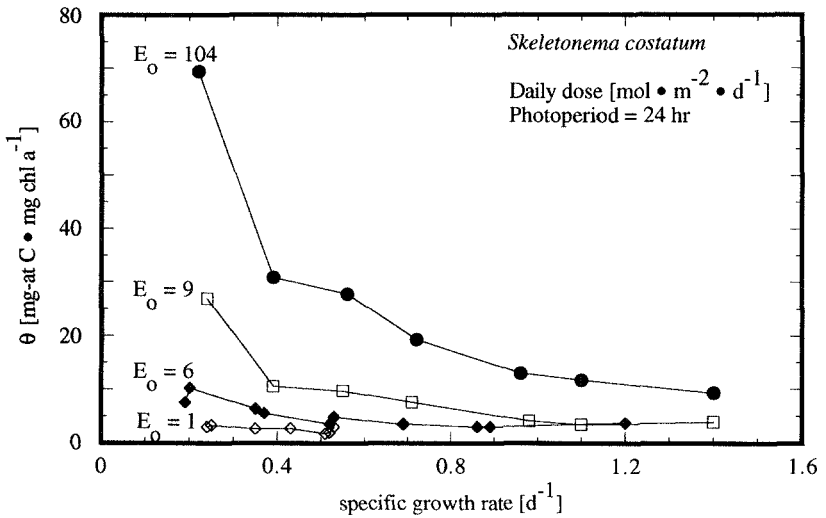

Fig. 9-4. The ratio, θ, of cellular carbon to chlorophyll *a*, versus specific growth rate. The lines connect measured values for cultures grown at a given irradiance but varying rate of supply of nitrate. The photoperiod was 24 h and the temperature was 18°C.

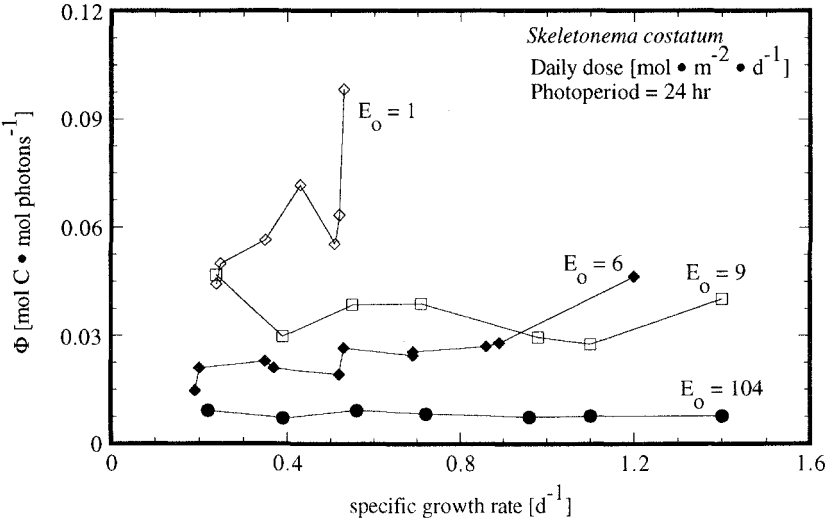

Fig. 9-5. The photosynthetic quantum yield, ϕ_c, versus specific growth rate. The lines connect measured values for cultures grown at a given irradiance but varying rate of supply of nitrate. The photoperiod was 24 h and the temperature was 18°C.

as a function of the nutrient-limited specific growth rate, $\mu(N)$. As was the case for temperature-limited adaptation two features of this figure are noteworthy. θ increases with E_0. In addition the response to changes in nutrient supply differs with irradiance. At low values of E_0 (e.g. $E_0 = 1$), θ changes little with nutrient-limited growth rate, but at high values of E_0 (e.g. $E_0 = 104$) θ increases sharply with decreases in $\mu(N)$. In Figure 9-6, where θ at a given photoperiod and an irradiance of 8.6 moles/(m^2 d) is plotted as a function of nutrient-limited growth rate, a similar pattern is observed. The values for θ are larger the longer the photoperiod, D. In addition the response to changes in nutrient supply differ with photoperiod. At low values of D (e.g. D = 6 hr), θ changes little with $\mu(N)$, but at high values of D (e.g. D = 24), θ increases sharply with decreases in $\mu(N)$.

In Figure 9-5 the quantum yield for a given irradiance and a photoperiod is plotted as a function of the nutrient-limited specific growth rate. We note that the values for ϕ_c are generally larger, the smaller the values of E_0, and that the response to nutrient-limitation differs with irradiance. At low values of E_0, ϕ_c decreases sharply with decreases in $\mu(N)$ ($E_0 = 1$), but at high values of E_0 (e.g. $E_0 = 104$), ϕ_c shows only a small increase with $\mu(N)$. In Fig. 9-7, ϕ_c at a given photoperiod and an irradiance of 8.6 mol m^{-2} day^{-1}) is plotted as a function of nutrient-limited growth rate. Here we see that differences in photoperiod have little effect upon quantum yield. Thus, a comparison of Figures 9-5 and 9-7 indicates that in terms of quantum yield, adaptation to photoperiod is distinctly different from adaptation to light level. On the other hand, as is the case for light level, changes in ϕ_c caused by changes in nutrient supply differ with photoperiod. At large values of D (e.g., $D = 24$ h), ϕ_c changes little with $\mu(N)$,

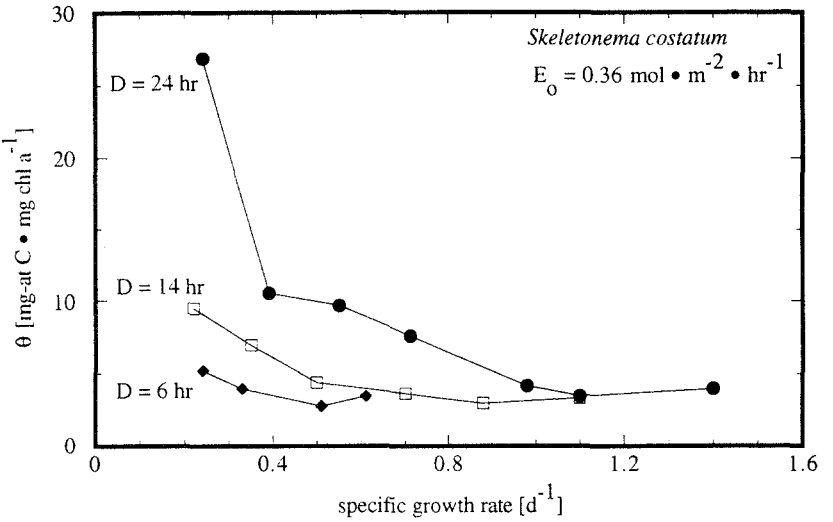

Fig. 9-6. The ratio, θ, of cellular carbon to chlorophyll *a*, versus specific growth rate. The lines connect measured values for cultures grown at a given photoperiod but varying rates of supply of nitrate. The irradiance was 8.6 mol m^{-2} day^{-1} and the temperature was 18°C.

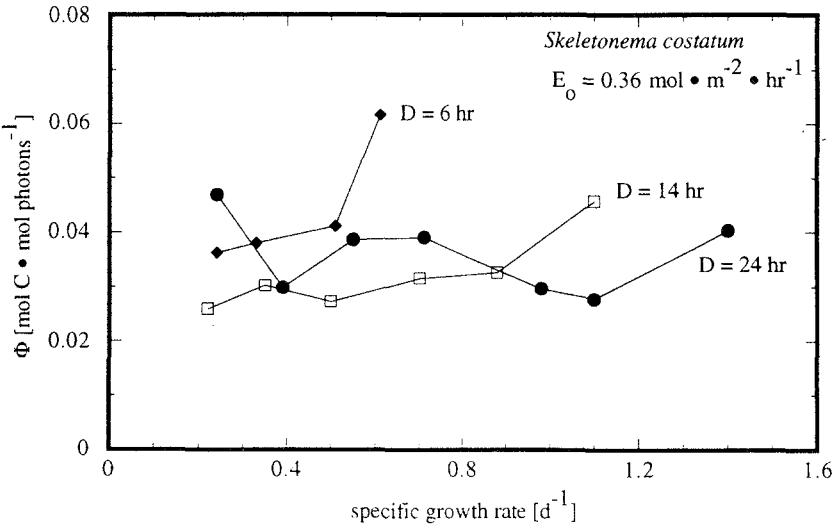

Fig. 9-7. The photosynthetic quantum yield, ϕ_c, versus specific growth rate. The lines connect measured values for cultures grown at a given photoperiod but varying rates of supply of nitrate. The irradiance was 8.6 mol m^{-2} day^{-1} and the temperature was 18°C.

but at small values of D (e.g., $D = 6$ h), ϕ_c appears to decrease with decreases in $\mu(N)$. The dichotomy mentioned earlier appears to hold not only for temperature limitation but also for nutrient limitation: When light levels are sufficiently low and photoperiods sufficiently short to limit growth rate, θ is near its minimum value and varies little with nutrient supply; on the other hand, ϕ_c decreases with decreases in nutrient supply. When light levels are high and photoperiods sufficiently long to maintain high growth rates, θ increases, and ϕ_c remains constant with decreases in nutrient supply.

Adaptation to photoperiod

In Fig. 9-8 the specific growth rate of *Skeletonema* is plotted as a function of irradiance for the three photoperiods indicated and a temperature of 18°C. Since the data were obtained by picking from Sakshaug's study the maximum specific growth rates for the given light and photoperiod shown in the figure, the response is considered to be that of nutrient-saturated growth. We see from this figure that for a photoperiod of 24-h irradiance of about 9 mol m^{-2} day^{-1} is sufficient to saturate growth. For a photoperiod of 14-h, irradiance of less than 52 but more than 9 moles/(m^2 d) is sufficient to saturate growth; and for a photoperiod of 6 h, growth is far from saturated at an irradiance of 52 mol m^{-2} day^{-1}.

In Fig. 9-9 the carbon to chlorophyll *a* ratio, θ, for a given irradiance is plotted as a function of the photoperiod-limited specific growth rate, $\mu(D)$, and in Fig. 9-10 the quantum yield for a given radiance is plotted as a function of $\mu(D)$. Unfortunately, because of the limitations in number and range of measurements it is difficult to draw conclusions. Figure 9-9 indicates that at these three irradiances θ is unchanged by changes in photoperiod. Figure 9-10 indicates once

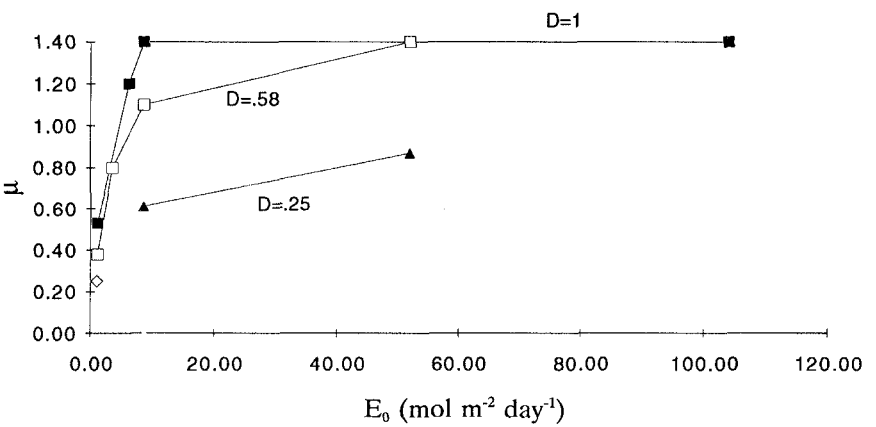

Fig. 9-8. The specific growth rate versus irradiance. The lines connect measured values for cultures grown at a given photoperiod and near-saturating rates of supply of nitrate. The temperature was 18°C.

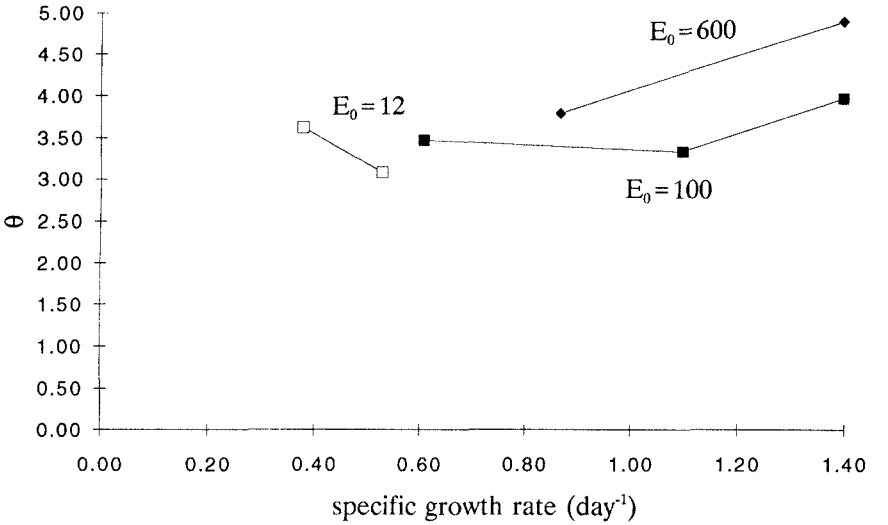

Fig. 9-9. The ratio, θ, of cellular carbon to chlorophyll *a*, versus specific growth rate. The lines connect measured values for cultures grown at a given irradiance but varying photoperiod. The temperature was 18°C and the rate of supply of nitrate was near saturating to growth.

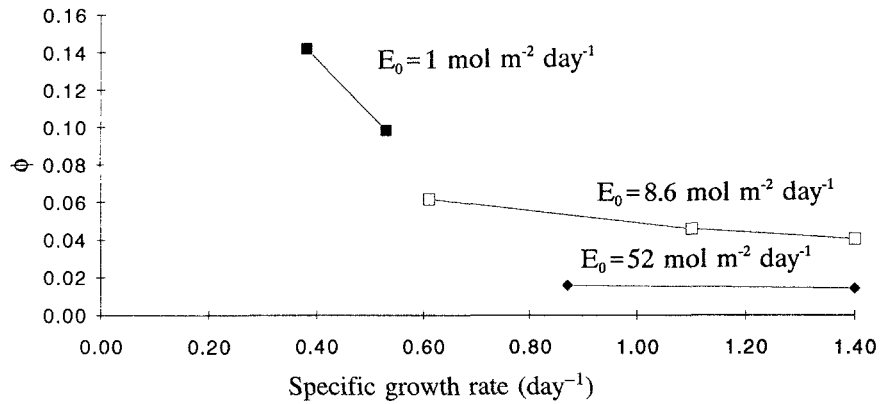

Fig. 9-10. The photosynthetic quantum yield, ϕ_c, versus specific growth rate. The lines connect measured values for cultures grown at a given irradiance, but varying photoperiod. The temperature was 18°C and the rate of supply of nitrate was near saturating to growth.

again that the value of ϕ_c is smaller the larger the value of E_0. We also note that ϕ_c changes little with photoperiod-limited growth rate, a response that is different from that for temperature- and nutrient-limited growth.

Interpretation

Unfortunately, a complete quantitative understanding of the adaptation discussed above has not been achieved. Although a number of mathematical models of

steady state growth have been proposed (Bannister, 1979; Laws and Bannister, 1980; Kiefer and Mitchell, 1983; Sakshaug et al., 1988, 1990; Cullen, 1990), none of them provides a complete description of the interaction of temperature, irradiance, photoperiod, and nutrient supply. One can draw several general conclusions from the adaptations of *Skeletonema*. Although each of the four environmental variables – temperature, irradiance, photoperiod, and nutrient supply – can determine specific growth rate, their effects upon quantum yields, ϕ_c, and cellular chlorophyll, q, are distinctive. Increases in E_0 cause increases in θ and decreases in ϕ_c. The magnitude of the response increases with decreases in temperature and nutrient supply.

Nutrient limitation and temperature limitation effect similar responses that may be considered second-order to those of irradiance. When irradiances are large, decreases in temperature and nutrient supply have little effect upon ϕ_c and large effects upon q. When irradiances are small, decreases in temperature and nutrient supply have little effect upon θ and large effects upon ϕ_c. Although the database is inadequate to be conclusive, I suggest that photoperiod has little effect upon ϕ_c and can have large effects on q. Despite our limitations in a quantitative understanding of such behavior, the adaptation of *Skeletonema* has implications for understanding the growth of phytoplankton in the sea as well as of optical variability.

Light absorption and growth rate

In order to explore our ability to predict rates of carbon fixation from bio-optical measurements, we have applied three models of varying sophistication to the *Skeletonema* database. In the first model we simply plot μ as a function of $D E_0/\theta$, a factor that is proportional to the daily rate of light absorption by the cells (Fig. 9-11). One sees that some of the variability in μ is associated with variability in the rate of light absorption, but a large amount still remains.

In the second model we apply Eq. (9.4) to a prediction of μ (Fig. 9-12). The complexity of the model has been increased by formulating a relationship between quantum yield, ϕ_c, and irradiance, E_0:

$$\phi_c = \int_{400}^{700} \frac{\phi_{c\max}(\lambda)\, k\phi(\lambda)}{a_{\text{chl}}(\lambda)\, E_0(\lambda) + k\phi(\lambda)}\, d\lambda \tag{9.5}$$

$\phi_{c\max}$, a constant, is the maximum quantum yield, and $k\phi$, another constant, is the chlorophyll-specific rate of light absorption at which $\phi_c = \phi_{c\max}/2$ (Kiefer and Mitchell, 1983; see also Tyler, 1975). In practice the spectral integration is not done and mean PAR values for the terms within the integrand are used instead. This formulation is consistent with a steady-state Poisson distribution based upon the rate at which the photosynthetic unit can process photons and the mean rate of supply of photons to the unit. $k\phi$ is proportional to the processing time, and E_0 is proportional to the rate of supply of photons to the unit (e.g.,

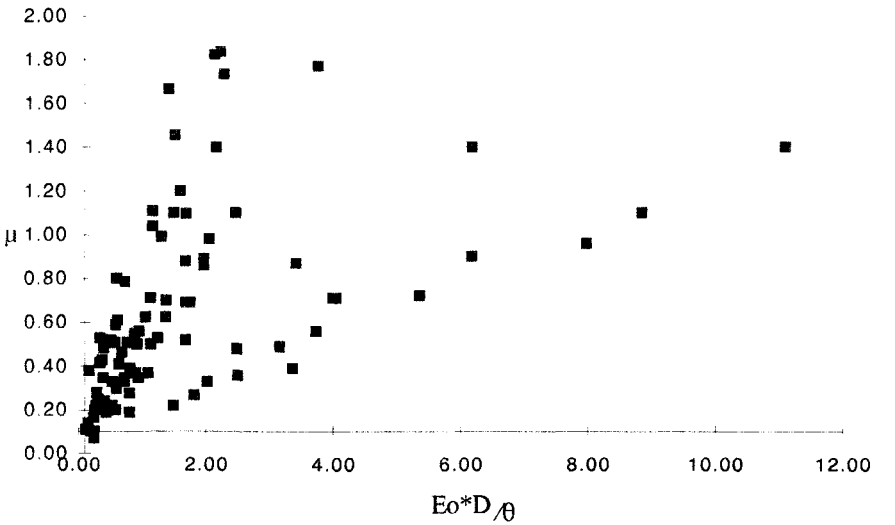

Fig. 9-11. The specific growth rate versus an index of the daily rate of cellular light absorption, E_0D/θ. The data include all combinations of irradiance, photoperiod, temperature, and nutrient supply rate reported in the Yoder and Sakshaug studies.

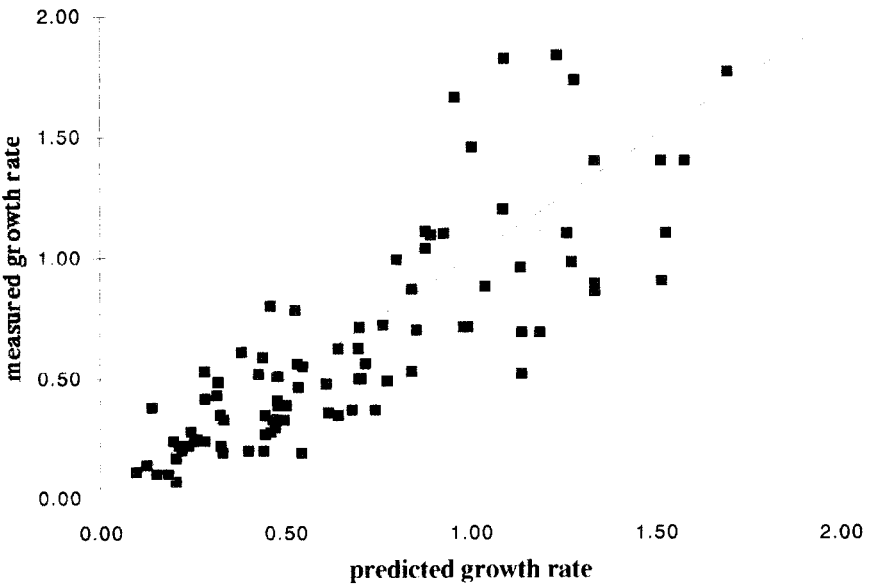

Fig. 9-12. The measured specific growth rate versus the predicted growth rate. As described in the text, the predicted growth rate is based upon a formulation in which the photosynthetic quantum yield is a function solely of irradiance.

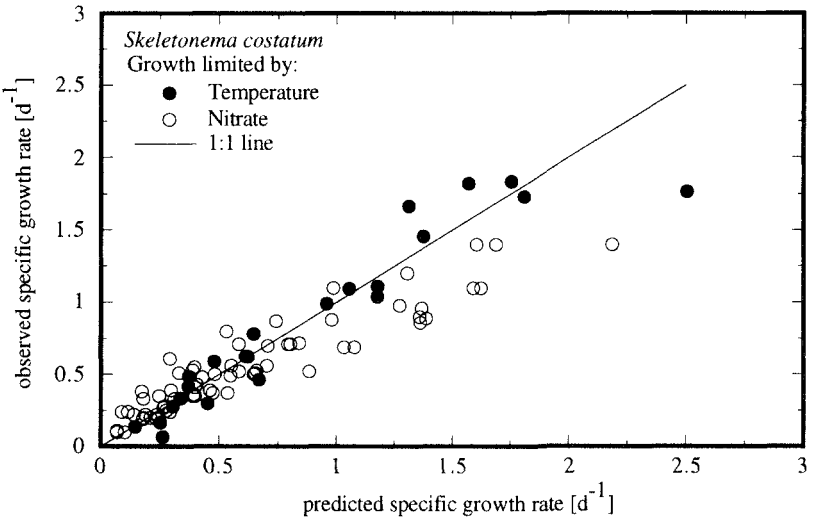

Fig. 9-13. Measured specific growth rate versus the predicted growth rate. As described in the text, the predicted growth rate is based upon a formulation in which the photosynthetic quantum yield is a function of irradiance, nutrient supply rate, and temperature.

Dubinsky et al., 1986). In this context ϕ_{cmax} is the stoichiometric coefficient for the conversion of photons into organic carbon atoms under conditions of steady-state growth. We see from Fig. 9-12 that the addition of a formulation for light-dependent variations in quantum yield increases the amount of variance in μ that can be predicted by the phenomenological equation (Eq. 9.4). Although models of this type have been subjected to a limited number of tests in the field, predicted photosynthetic rates have compared well with measured rates (Marra et al., 1993).

It is obvious from Figs. 9-3, 9-5, and 9-7 that temperature and nutrient supply as well as irradiance contribute to variations in the quantum yield. On the other hand, photoperiod does not appear to affect quantum yield. We have developed a still more complicated model that includes formulations describing differences in the value of $k\phi$ of Eq. (9.5) caused by differences in temperature and nutrient supply. The measured growth rates are plotted as a function of the rates predicted by this model in Fig. 9-13. The errors in prediction are further diminished, but not greatly.

Cellular chlorophyll and optical properties

The large changes in the cellular ratio of carbon to chlorophyll seen in *Skeletonema* occur in the sea. At the sea surface over the world's oceans the temperatures vary from 0 to 30°C, photoperiods vary from 0 to 24 h, mid-day

irradiances vary from 0 to 2000 $\mu mol\, m^{-2}\, s^{-1}$, and nitrogenous nutrient concentrations vary from tens of nanomoles per liter to 35 $\mu mol\, l^{-1}$. Within the euphotic zone water at a given location, mid-day irradiance may vary with depth by 100-fold, and nutrient concentrations and temperatures may also vary severalfold. Furthermore, the phytoplankton within the surface mixed layer will adapt to modifications of the light regime effected by vertical turbulent transport.

Increases with depth in the cellular concentration of chlorophyll have been directly measured with a microphotometer (Morrow, 1988). In addition, flow cytometric measurements of the fluorescence of chlorophyll *a* in prochlorophytes and the fluorescence of phycoerthyrin in *Synechococcus* document large changes in the cellular concentration of photosynthetic pigment. Olson et al. (1990) found in the Sargasso Sea that the cellular concentration of photosynthetic pigments in both groups of prokaryotic cells sampled at the sea surface varied seasonally. In the winter when the mixed layer was deeper, surface irradiance was lower, daylength was shorter, and surface nutrient concentrations were higher, the cellular concentrations of pigments were as much as 10 times greater than in the summer. Moreover, in the summer when the water column was well stratified, the cellular concentration of the two pigments was about 10 times greater for cells found near the bottom of the euphotic zone than for cells found within the surface mixed layer (see also Fig. 6-1).

Indirect evidence of differences in the cellular concentration of chlorophyll *a* has also been obtained from simultaneous measurements in the field of the beam attenuation coefficient and the fluorescence of chlorophyll *a* (Kiefer, 1986; Kitchen and Zaneveld, 1990). If one assumes that the concentration of carbon in phytoplankton covaries with the beam attenuation coefficient, and that the fluorescence of chlorophyll *a* covaries with pigment concentration, then the ratio of the two parameters is a measure of q. Figure 9-14 is a plot of the ratio as a function of the optical depth at which the measurement was made. The data were obtained during the 1984 ODEX Cruise for a transect of stations extending seaward off Monterey California and into the north central Pacific Gyre. Similar patterns have been measured in the north Atlantic and in a meridional transect of the central North Pacific (Pak et al., 1988).

One notices from these analyses that the ratio of beam attenuation to fluorescence generally decreases with optical depth. The ratio is largest and is relatively constant within the mixed layer and then decreases until about four optical depths, which is about the bottom of the euphotic zone. The ratio varies little below this depth. One also notes in these patterns that the value of the ratio within the surface mixed layer is smaller the larger the optical depth at the bottom of the layer. In the case of a very deep mixed layer, the ratio has a value that approaches the value found at the bottom of the mixed layer in stratified waters. These patterns are most easily explained in terms of systematic variations in the cellular concentration of chlorophyll *a*. Phytoplankton cells found at low irradiances, short photoperiods, or in waters of high nutrient concentration will be characterized by small scattering cross-sections relative to fluorescence

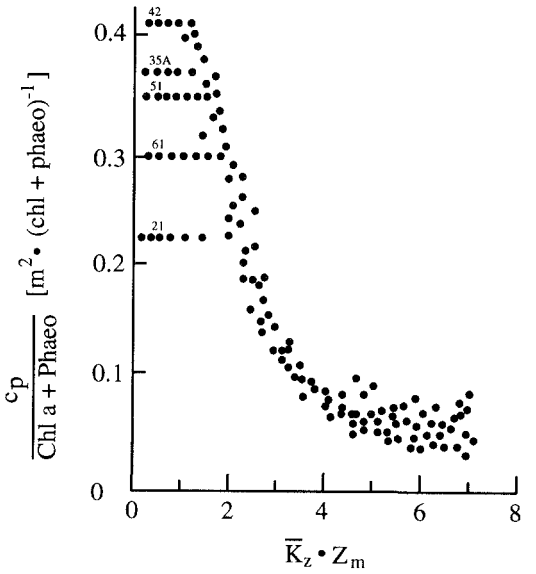

Fig. 9-14. The ratio of the beam attenuation coefficient for suspended and dissolved materials (650 nm) to the sum of the concentrations of chlorophyll *a* and pheophytin *a* versus the optical depth at which the measurement was made. *Z* is the depth at which the measurement was made and $\overline{K}_z$ is the average value of the diffuse attenuation coefficient at 488 nm in the waters above this depth. The data were obtained during the 1984 ODEX Cruise for a transect of stations extending seaward off Monterey, California and into the north central Pacific Gyre.

cross-sections. Cells found in cold waters, high irradiances, long photoperiods, or in waters of low nutrient concentration will be characterized by a large scattering cross sections relative to fluorescence cross-sections.

Natural fluorescence, chlorophyll a, and photosynthesis

Measurements of the spectrum of upwelled light indicate that, throughout most of the euphotic zone, far red light comes predominantly from the fluorescence of chlorophyll *a* (Gordon, 1979). The emission from this pigment is centered at 683 nm, and its bandwidth is about 15 nm on each side of this maximum. This fluorescence, which comes largely from photosystem II, is like photosynthesis excited by the cellular absorption of blue-green light.

Figures 9-15a and 9-15b show the depth distribution of nadir radiance at 683 nm, $L_u(683)$, scalar irradiance for PAR, E_0(PAR), and temperature at an oligotrophic station (23°53'S, 161°37'W) and a mesotrophic station (36°15'S, 171°9'W) in the south Pacific Ocean. One notes in both profiles of $L_u(683)$ that its value drops rapidly in the upper 6 m of the water column and then decreases more slowly and regularly with depth. The rapid decrease near the surface is primarily caused by the attenuation of scattered sunlight at 683 nm. Below 6 m

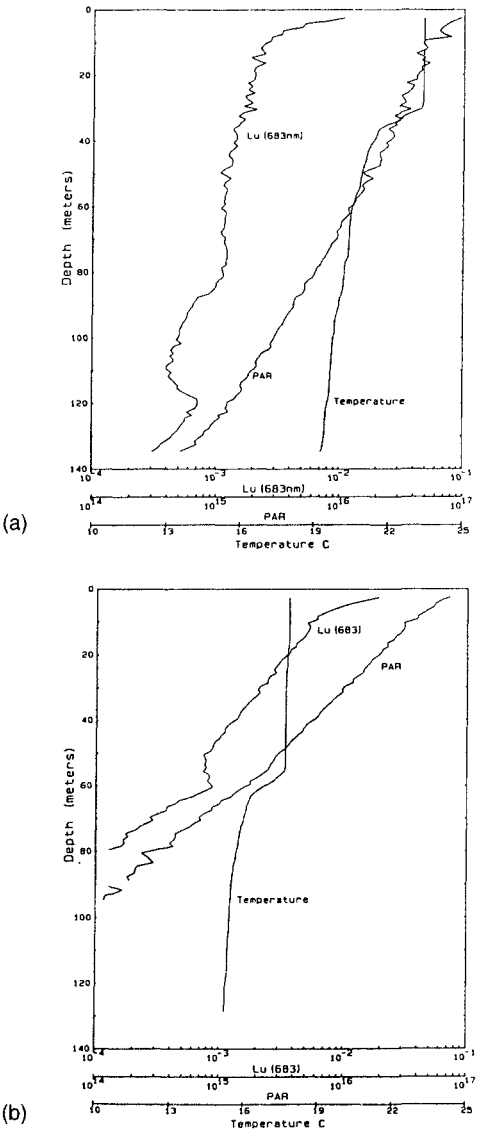

Fig. 9-15. Vertical profiles of nadir radiance at 683 nm, $L_u(683)$, scalar irradiance for PAR, E_0(PAR), and temperature at: (a) an oligotrophic station (23°53'S, 161°37'W); (b) a mesotrophic station (36°15'S, 171°9'W) in the south Pacific Ocean.

the strong absorption of red light by water has effectively removed most solar path radiance, and the signal is dominated by the fluorescence of chlorophyll *a*. Below 6 m the attenuation of $L_u(683)$ with depth roughly parallels the attenuation of E_0(PAR), a feature to be expected since E_0(PAR) is a measure of the intensity of fluorescence excitation.

A comparison of the two stations indicates that $L_u(683)$ and $E_0(\text{PAR})$ decrease much less rapidly with depth at the oligotrophic station than at the mesotrophic station. At the oligotrophic station natural fluorescence is still measurable at 130 m, which is near the bottom of the euphotic zone. At the mesotrophic station, $L_u(683)$ is measurable only to a depth of 60 m. Note that for comparable intensities of PAR, the value of $L_u(683)$ is about 5 times higher at the

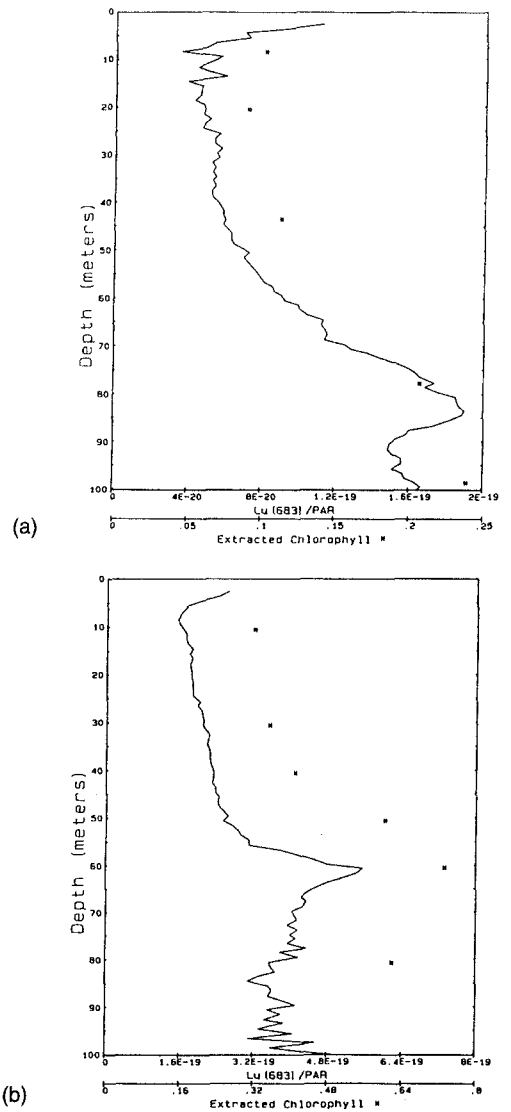

Fig. 9-16. Vertical distribution of the concentration of chlorophyll *a* obtained from water samples, and the ratio of nadir radiance to scalar irradiance, $L_u(683)/E_0(\text{PAR})$ at same stations as in Fig. 9-15.

mesotrophic station, and thus roughly proportional to the increased concentration of chlorophyll *a*.

Figures 9-16a and 9-16b, which contain additional information about the depth distribution of $L_u(683)$ at the two stations, show the vertical distribution of the concentration of chlorophyll *a*, and the ratio of nadir radiance to scalar irradiance, $L_u(683)/E_0(\text{PAR})$. The vertical distribution of chlorophyll *a* at the two stations is characterized by a subsurface chlorophyll maximum, 85 m at the oligotrophic station, and 60 m at the mesotrophic station. Above the chlorophyll maximum, increases in chlorophyll concentration with depth are most likely caused by changes in the cellular chlorophyll concentration. Clearly, the vertical distribution of the ratio $L_u(683)/E_0(\text{PAR})$ is similar to that of chlorophyll *a*.

Figure 9-17 is a detailed temporal record of $L_u(683)$ and $E_0(\text{PAR})$ at 10 m and 50 m at the mesotrophic station. It is obvious, in these waters where the concentration of chlorophyll *a* at a given depth did not change significantly during the sampling period, that changes in $L_u(683)$ with time are largely determined by changes in the intensity of exciting light, $E_0(\text{PAR})$. The flatter shape for $L_u(683)$ at 10 m relative to the shape at 50 m suggests that the quantum yield for fluorescence may be lower at higher light intensities.

Measurements of natural fluorescence like the examples above have been applied to calculations of both the concentration of chlorophyll *a* (Kishino et al., 1984a,b) and photosynthetic rate (Kiefer et al., 1989; Chamberlin et al., 1990). These calculations are best considered by referring to our phenomenological equations. Recalling Eq. (9.1), we let F_f represent natural fluorescence, defined as the flux of photons emitted from cells in a unit volume of water. F_a is the flux

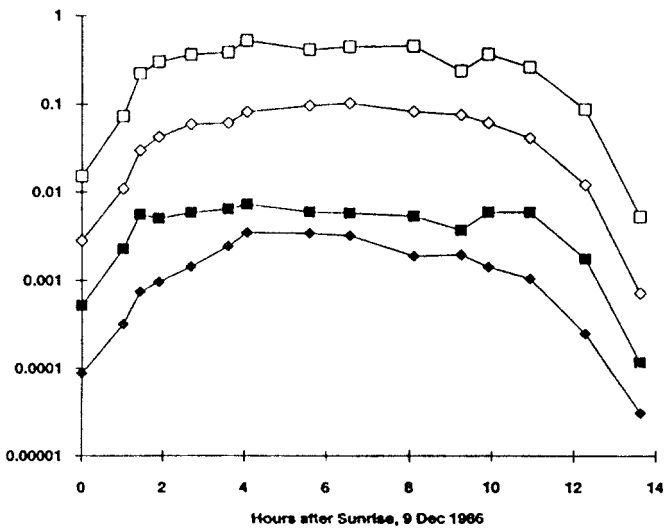

Fig. 9-17. Detailed temporal record from sunrise to sunset at depths of 10 m (open squares) and 50 m (open diamonds) of $L_u(683)$ and $E_0(\text{PAR})$ at 10 m (filled squares) and 50 m (filled diamonds) at the mesotrophic station (36°15'S, 171°9'W).

of photons absorbed by these cells. One can obtain a relationship between natural fluorescence and chlorophyll a by substituting the right-hand side of Eq. (9.3) for F_a in Eq. (9.1):

$$\text{chl} = \frac{F_f}{\int_{400}^{700} \phi_f(\lambda)\, a_{\text{chl}}(\lambda)\, E_0(\lambda)\, d(\lambda)} \tag{9.6}$$

We see from this equation that the accuracy with which one can calculate the concentration of chlorophyll a from measurements of natural fluorescence will depend upon the accuracy with which one can predict the values for the product of the spectral-averaged absorption coefficient, a_{chl}, and the quantum yield of fluorescence, ϕ_f:

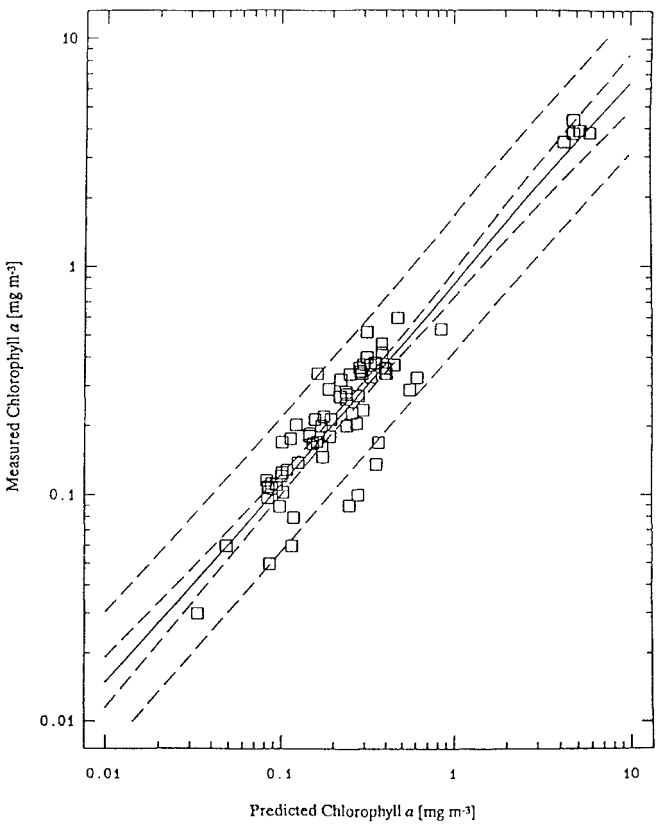

Fig. 9-18. Log–log plot of measured concentration of chlorophyll versus the concentration calculated from the measurement of natural fluorescence and scalar irradiance. The measurements were made throughout the water column in distant waters.

$$\text{chl} = \frac{F_f}{\phi_f a_{\text{chl}} E_0(\text{PAR})} \tag{9.7}$$

In Fig. 9-18 the measured value of the concentration of chlorophyll *a* is plotted as a function of the value calculated from measurements of natural fluorescence. The samples come from throughout the euphotic zone and distributed geographic waters (Chamberlin et al., 1990).

The relationship between natural fluorescence and photosynthesis is simply derived by recalling both Eqs. (9.1) and (9.2). If we accept the approximation that the values of ϕ_f and ϕ_c are independent of wavelength, then the integrand of Eqs. (9.1) and (9.2) can be replaced by the product of the spectral-mean rate of light absorption, F_a, and the respective quantum yield. Elimination of F_a from these two equations yields a description of the relationship between the rates of photosynthesis and natural fluorescence:

$$F_c = (\phi_c/\phi_f)F_f \tag{9.8}$$

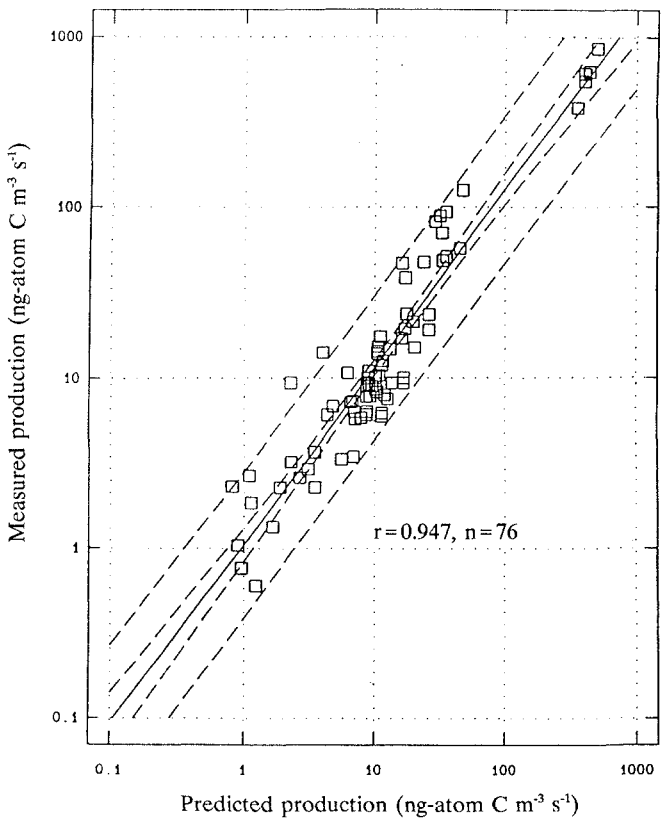

Fig. 9-19. Log–log plot of measured photosynthetic rate versus the rate calculated from the measurement of natural fluorescence and scalar irradiance. The measurements were made throughout the water column in distant waters.

According to Eq. (9.8), the accuracy with which one can calculate photosynthetic rate from measurements of natural fluorescence depends upon the accuracy with which one can predict the ratios of the two quantum yields. In Fig. 9-19 the measured photosynthetic rate is plotted as a function of the rate calculated from measurements of natural fluorescence. The calculated rate of photosynthesis was obtained by introducing an empirical formulation of the dependence of ϕ_c/ϕ_f upon irradiance:

$$\frac{\phi_c}{\phi_f} = \int_{400}^{700} \frac{\left(\dfrac{\phi_{c\max}(\lambda)}{\phi_{f\max}(\lambda)}\right) k\phi(\lambda)}{a_{\text{chl}}(\lambda)\, E_0(\lambda) + k\phi(\lambda)}\, d\lambda \tag{9.9}$$

Both $\phi_{c\max}/\phi_{f\max}$ and $k\phi$ are empirical constants. As is the case for the comparison in Fig. 9-18, the samples come from throughout the euphotic zone and distributed geographic waters (Chamberlin et al., 1990). The causes of error in the estimates of both chlorophyll *a* and photosynthetic rate will be discussed below.

Sources of variability

We have seen that the physiological adaptation of *Skeletonema* involves changes in the cellular concentration of chlorophyll *a*, in *q*, and in the photosynthetic quantum yield, ϕ_c. Since F_a drops out of the relationship between fluorescence and photosynthesis, variations in θ will have no direct effect upon the accuracy of prediction. The remaining four terms in Eqs. (9.1), (9.2), and (9.3) are $\phi_f(\lambda)$, $\phi_c(\lambda)$, $a_{\text{chl}}(\lambda)$, and $E_0(\lambda)$. Since this chapter concerns only the transformations of light that has been absorbed by the cell, only the first three of these terms will be considered.

Unfortunately, although ϕ_f, ϕ_c, and a_{chl} are known to vary, knowledge of the range and causes of variability in the sea is poor. The studies of *Skeletonema* discussed above provide rough information on the variability of ϕ_c for cells in fully adapted, steady-state growth. The data clearly show that ϕ_c will vary with irradiance, and to a lesser degree with temperature and nutrient supply. The studies provide no information on changes in ϕ_c caused by rapid changes in irradiance over the course of a day or via vertical mixing.

Variations in ϕ_f and ϕ_c caused by differences in irradiance have been categorized in terms of two processes. Photochemical quenching, which occurs at irradiances that are less than saturating to photosynthesis, is caused by the opening of the reaction centers of photosystem II. Such opening will cause corresponding increases in the quantum yield of photosynthesis. Butler (1978) has proposed a most successful model of energy transformation within the photosystem that provides a quantitative description of changes in ϕ_f and ϕ_c induced by changes in the fraction of open/closed reaction centers. According to this model, which consists of reaction centers and associated antennae, the

quantum yields for the two competing processes of fluorescence and photochemistry are functions of the "single-pass" probabilities for fluorescence from the antenna, Ψ_f, energy transfer from the antenna to the reaction center, Ψ_T, and reciprocally from the reaction center to the antenna, Ψ_t, to the reaction center, the photochemistry within the reaction center, Ψ_p, and the fraction of open reaction centers, A:

$$\phi_c = \phi_{c\max} \Psi_T \Psi_p A \tag{9.10}$$

$$\phi_f = \Psi_f \left(1 - \Psi_T \Psi_t \frac{1 - A}{1 - \Psi_T \Psi_t} \right) \tag{9.11}$$

If all reaction centers are closed, A equals 0, ϕ_c equals 0, and ϕ_f is maximal. If all are open, A equals 1, ϕ_c is close to $\phi_{c\max}$ since Ψ_T and Ψ_p are both close to 1, and ϕ_f is minimal. In fact the value of ϕ_f is about 2 to 2.5 times greater when all centers are closed than when all are open.

Nonphotochemical quenching, which occurs at irradiances that are saturating to photosynthesis, is caused by the production of photochemical traps in the antenna of the photosynthetic unit. The fluorescences measured with traditional strobe or continuous-source instruments indicate that in the ocean nonphotochemical quenching is a more noticeable feature than photochemical quenching. At times nonphotochemical quenching can account for three- to fourfold variations in fluorescence at the sea surface (e.g., Kiefer, 1973). Its effect decreases rapidly with depth and roughly parallels downwelling irradiance. There is now considerable evidence that much of nonphotochemical quenching is caused by isomerization of xanthophyll in the antenna (Deming-Adams, 1990).

Recently, pump-probe fluorometers, which can monitor differences in fluorescence excited by flashes of variable intensity, have exploited equations like those of Butler's model to measure the state of reaction centers and rates of photosynthesis (Kolber and Falkowski, 1991; Kolber et al., 1990). Figure 9-20 is an example of such measurements on the marine diatom *Chaetoceros gracilis*. In this figure the fluorescence from cells that have had all reaction centers closed by an intense actinic flash, F_s, and the fluorescence for cells that have had a variable fraction of reaction centers closed by ambient irradiance, F_p, are plotted as a function of the ambient irradiance. Values for variable fluorescence, $(F_s - F_p)/F_s$, which is an index of A, are also shown.

One should note in this figure that at low irradiances the closing of reaction centers causes a two-fold increase in fluorescence yield, F_s/F_p. At high irradiance the increase is much less, presumably because a large fraction of the reactions centers are closed by the ambient irradiance. One should also note that the fluorescence under ambient light, F_p, does not increase with irradiance as would be expected because of increases in A. F_p, which is in fact an index of the quantum yield of natural fluorescence, ϕ_f, remains relatively constant despite large changes in ambient irradiance. Moreover, the fluorescence from cells

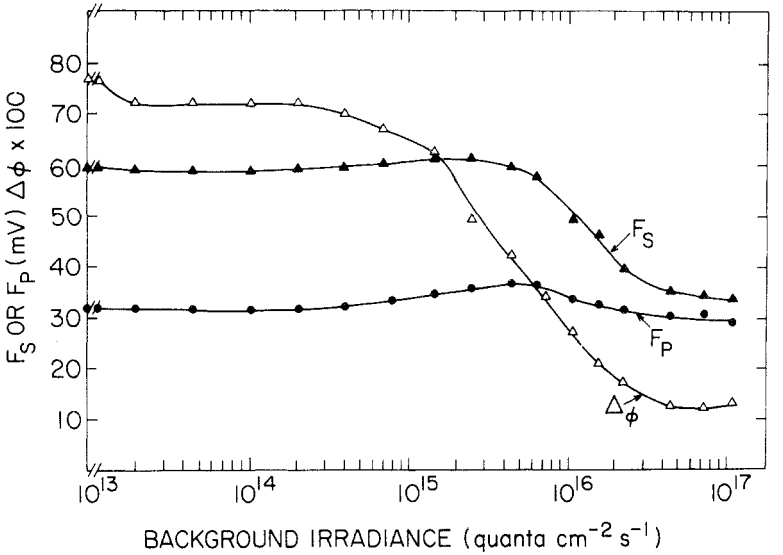

Fig. 9-20. Photosynthetic rate and pump-probe fluorescence measurements for a culture of *Chaetoceros gracilis* under continuous background irradiance. Fluorescence was measured with a weak probe flash before (F_p) and following (F_s) a saturating pump flash. $\Delta\phi$ is the varable fluorescence normalized to F_p.

whose reaction centers are closed, F_s, does not remain constant over the range in irradiances, as would be expected if the fraction of open/closed reaction centers were the only process affecting quantum yield. F_s decreases at higher intensities. These features result from a second process, called nonphotochemical quenching, which will be discussed below.

Figure 9-21 is an example of similar measurements made at sea. The left panel presents the vertical distributions of irradiance, E_0(PAR), the concentration of chlorophyll *a*, chl, and the chlorophyll-specific photosynthetic rate, P^B. The right panel presents the vertical distributions of strobe-induced fluorescence, F_s, for cells that have had all reaction centers closed by an intense actinic flash, and the fluorescence, F, for cells that have a variable fraction of reaction centers closed by ambient irradiance. The panel also includes calculated values of the fraction of reaction centers that are open, and an index of the quantum yield of natural fluorescence. The index of quantum yield was calculated by dividing F by the product of E_0(PAR), chl, and ϕ_f.

The major sources of change in F with depth are differences in the concentration of chlorophyll *a* as well as differences in photochemical and nonphotochemical quenching. The distribution of A indicates that the fraction of open reaction centers is about 0.25 at the sea surface and increases to over 0.9 at about 45 m. According to Eq. (9.10), such an increase indicates that the opening of reaction centers has caused an increase in the quantum yield of photosynthesis,

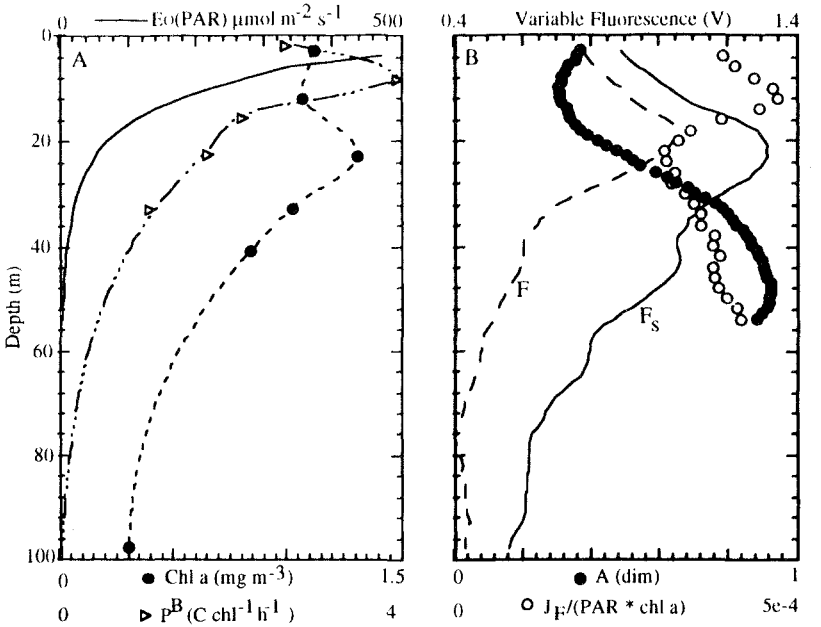

Fig. 9-21. Vertical profiles from station EN89312 on 18 March, 1989 at 37°41.37'N, 74°20.55'W, 19:45 local time. *Left*: the distribution of scalar irradiance (E_0(PAR)), chlorophyll *a* concentration, and photosynthetic assimilation number, P^B. *Right*: relative in situ fluorescence yield excited by a weak probe flash before (F) and following (F_s) a saturating pump flash, fraction of open reaction centers (A), calculated from measurements of F_s, F, and F_0, the fluorescence of dark adapted cells. The ratio proportional to quantum yield of natural fluorescence, J_F/(PAR × chl *a*) is shown by open circles.

increased by a factor of about 3.5-fold (0.9/0.25). The rapid increase in F_p (F, in the figure) between the surface and 20 m indicates that there is considerable nonphotochemical quenching within the upper water column. If the principal cause of increased nonphotochemical quenching is an increase in the rate constant for heat production in the antenna and all other rate constants remain the same, then according to Butler's model, Ψ_T will vary proportionally with F_s (Kiefer and Reynolds, 1992). Thus, a 2-fold decrease in F_s will cause a two-fold decrease in both Ψ_T and the photosynthetic quantum yield for open reaction centers (Eq. 9.11). The total change in ϕ_c within the water column is therefore about 7-fold (0.9/(0.5 × 0.25)). This is about the range in ϕ_c calculated for the continuous culture of *Skeletonema* (Fig. 9-5).

The counteractive effects upon fluorescence of photochemical and non-photochemical quenching cause the quantum yield of natural fluorescence, ϕ_f, to remain relatively constant with depth (open circles in the right hand panel). Thus, at this station, which is typical of others, variations with depth in the ratio of photosynthetic quantum yield to the fluorescence quantum yield, ϕ_c/ϕ_f, are predominantly caused by variations in ϕ_c rather than ϕ_f. The similarity between

Eq. (9.5), which describes the dependence of ϕ_c upon E_0, and Eq. (9.9), which describes the dependence of the ratio ϕ_c/ϕ_f upon E_0, is consistent with this behavior. While models like Butler's provide information on the short-term dynamics of ϕ_f and ϕ_c, little is known about their variability in cells fully adapted to temperature, photoperiod, nutrient supply, and irradiance. The few studies that have begun to address this problem suggest that ϕ_f as well as ϕ_c varies with temperature and nutrient supply (Kolber et al., 1988; Cleveland and Perry, 1987; Chamberlin and Marra, 1992).

Additional sources of error in the predictions based upon fluorescence measurements may be caused by species-specific variations in the spectral shape of ϕ_f and ϕ_c, and contamination of the fluorescence signal by detrital pigments. Finally, the spectral, chlorophyll-specific absorption coefficient, $a_{\text{chl}}(\lambda)$, may also vary. Its value will of course vary with differences in the contribution of photosynthetic accessory pigments and nonphotosynthetic pigments to absorption. Such differences may occur because of changes in the taxonomic composition of the crop or by physiological adaptation within a species. While increases in the cellular concentration of nonphotosynthetic pigments will cause increases in a_{chl}, they will also cause proportional decreases in ϕ_f; thus, according to Eq. (9.6), estimates of the concentration of chlorophyll *a* will be insensitive to such variations. On the other hand, increases in the concentration of photosynthetic accessory pigments in photosystem II will cause increases in both a_{chl} and ϕ_f, and thus the estimate of concentration will be biased. In addition, variations in the size of the phytoplankton cell and the cellular concentration of pigments may cause variations in the efficiency of light absorption (see Chapter 8). A large cell with a large cellular concentration of pigment will absorb less efficiently and have a smaller absorption coefficient than a small cell with smaller cellular concentration of pigments.

10

CAPABILITIES AND MERITS OF LONG-TERM BIO-OPTICAL MOORINGS

John Marra
Lamont-Doherty Earth Observatory of Columbia University

Introduction

There are primarily three ways in which the ocean can be sampled. First, depth profiles of water properties can be collected. The sampling resolution for depth profiles can be very high (<1 m), and time resolution can be good under some circumstances. But since relatively few stations can be completed, geographic coverage is generally poor. Variability in space can be optimized if data can be collected while the ship is underway. In this second sampling mode, water is pumped aboard for sampling, or else sensing instruments are towed behind the ship. This method vastly improves sampling horizontal variability; however, depth resolution is compromised, and measurements cannot be ordered in time.

The third method is to place instruments in the ocean, either tethered to moorings or on drifters. While depth resolution is only moderately good (typically, tens of meters), and spatial data nonexistent, this method has the advantage, unobtainable with the other modes, of high resolution in time. While moorings and drifters have been in the repertoire of physical oceanographic sampling for some time, it is only recently that they have been used to sample biological and optical properties of the sea. In this chapter, I discuss the capabilities of this kind of sampling from the point of view of a recent program, the BIOWATT Mooring Experiment in 1987. One of the express purposes of this experiment was to expand the range of variables that can be measured from moored instrumentation. Here, I will show how the time resolution made possible with moored sensors allows the measurement of parameters of phytoplankton production on diurnal time scales, as well as allowing a look at seasonal variability.

The BIOWATT Mooring Experiment was a collaboration among a large number of people, all of whom contributed to its success. It was the first deployment of a mooring with a variety of sensors and whose goal was to record the optical, biological, and physical variability over a seasonal cycle. The idea for

this type of experiment for BIOWATT originated with Tom Dickey and his (then) graduate student, Dave Siegel. In concluding ODEX (Optical Dynamics Experiment), which was designed around a time series of bio-optical variables observed from the Research Platform FLIP (e.g., Siegel and Dickey, 1987), they came to realize that bio-optical sensors may have evolved to the point where it was possible to moor them like current meters (Dickey et al., 1990).

There was a precedent for mooring sensors of this type. Scientists at Scripps Institution of Oceanography had, for a time, maintained a semi-permanent moored installation in near-shore waters (Warner et al., 1983). In the deep ocean, transmissometers had been attached to Anderaa current meters, as well as being moored by themselves (e.g., Gardner, 1989). The group at Brookhaven National Laboratories developed a fluorometer for use in moorings in coastal waters (Whitledge and Wirick, 1986; Falkowski et al., 1988). The BIOWATT experiment benefited greatly from these, and also from three instrument developments. First was a new dissolved oxygen sensor that was sensitive and stable enough for use on oceanic moorings (Langdon, 1986). Second was a new in situ fluorometer, developed by SeaTech for the estimation of chlorophyll *a*, that was more compact, calibration-stable, and less power-hungry than its predecessors (see Marra and Langdon, 1993). Third were two new kinds of moored optical sensors, the bio-optical moored sensor (Booth and Smith, 1988) and the bioluminescence moored sensor (Swift and Booth, 1988).

There are two fundamental time scales in biological oceanography, the diurnal and the seasonal (Marra and Hartwig, 1984). The general belief is that diurnal signals are mostly accessible from shipboard observations. However, evaluation of seasonal cycles requires observations for a long period of time, but with sufficiently high sampling density to account for shorter period phenomena such as weather and diurnal changes (Marra and Hartwig, 1984; Dickey et al., 1986). These shorter-period changes are particularly important to biological and optical sampling because so much of the dynamics is driven by the day–night cycles and the synoptic weather (e.g,. Marra et al, 1990). When planning a seasonal sampling program in the open ocean, it becomes clear that moored observations are favored. The BIOWATT Mooring Experiment was carried out as 3 mooring deployments of about three months each. With the exception of the current meter, and to some extent the transmissometer, these sensors had never been deployed in such a manner before. The experiment was successful, with an overall data recovery of 75%.

Instrumentation

The usual problems associated with moored observations become magnified with the addition of more sensors, and the use of bio-optical sensors in the sensor suite. For example, the problem of bio-fouling becomes especially acute. In addition to the usual surfaces for microbial growth, such as current meter rotor blades, etc., there are optical windows to be considered. Also, biological and optical properties have strong gradients in the upper water column.

Fouling has been seen on transmissometers moored near the bottom (Gardner, 1989), and was a problem in the Scripps Canyon Mooring (C.R. Booth, personal communication). Most pioneering efforts in mooring bio-optical sensors have been in coastal environments, where the relatively heavy particle load causes substantial fouling of sensors. The investigators at Brookhaven, in designing a fluorometer for coastal mooring devised a mechanical system to wash or scrape the optical windows periodically (Whitledge and Wirick, 1986). This option consumes power, and thus may cause other compromises in an experiment, such as the reduction in the number of sensors, or redesign of the mooring. Deployment in an oceanic regime reduces the fouling problem drastically. Details of the solution to this problem for BIOWATT can be found in a recent data report (Bitte et al., 1989).

Another consideration is that the larger number of sensors located at a particular moored depth means that data acquisition schemes have to be revamped, because the current meters that have been used in the past were never meant to function as data loggers for a large number of accessory sensors. For example, the vector measuring current meter (VMCM) designed by Weller and Davis (1980) is generally considered to be the instrument of choice for upper water column work, but requires modifications if it is to be used as a data-logging device for the other sensors. Another problem in interfacing several sensors is that the time constants of the sensors should be matched to each other and the variability in the ocean (Maccio and Langdon, 1988).

An example of a moored bio-optical package is shown in Fig. 10-1, the Multi-Variable Moored Sensor used in BIOWATT. For the experiment in 1987, these instruments were placed on a taut-wire mooring similar to that used in the LOTUS program (Briscoe and Weller, 1984). A surface buoy contained meteorological instrumentation (Deser et al., 1983), a tensiometer for measuring mooring tensions, and an ARGOS transmitter for relaying, via satellite, the position of the mooring and the tension it experienced. We deployed eight MVMSs in the upper water column, (nominal depths: 10, 20, 40, 60, 80, 100, 120, and 160 m) along with two Bio-Optical Moored Sensors (BOMS; 30 and 50 m) and a Bioluminescence Moored Sensor (BLMS; 50 m). Descriptions of these latter devices are given in Booth and Smith (1988) and Swift and Booth (1988).

Diurnal variability

The enhanced time resolution in moored observations allows a better look at short-term variability. In BIOWATT large diurnal changes in fluorescence, beam attenuation coefficient (''beam-*c*''), and dissolved oxygen were observed in large portions of the record. Changes in dissolved oxygen from the daily cycles of photosynthesis and respiration were expected because the new electrodes were sensitive enough (Langdon, 1986). Siegel et al. (1989) have interpreted the diurnal changes in beam-*c* they observed during ODEX as a result of particle

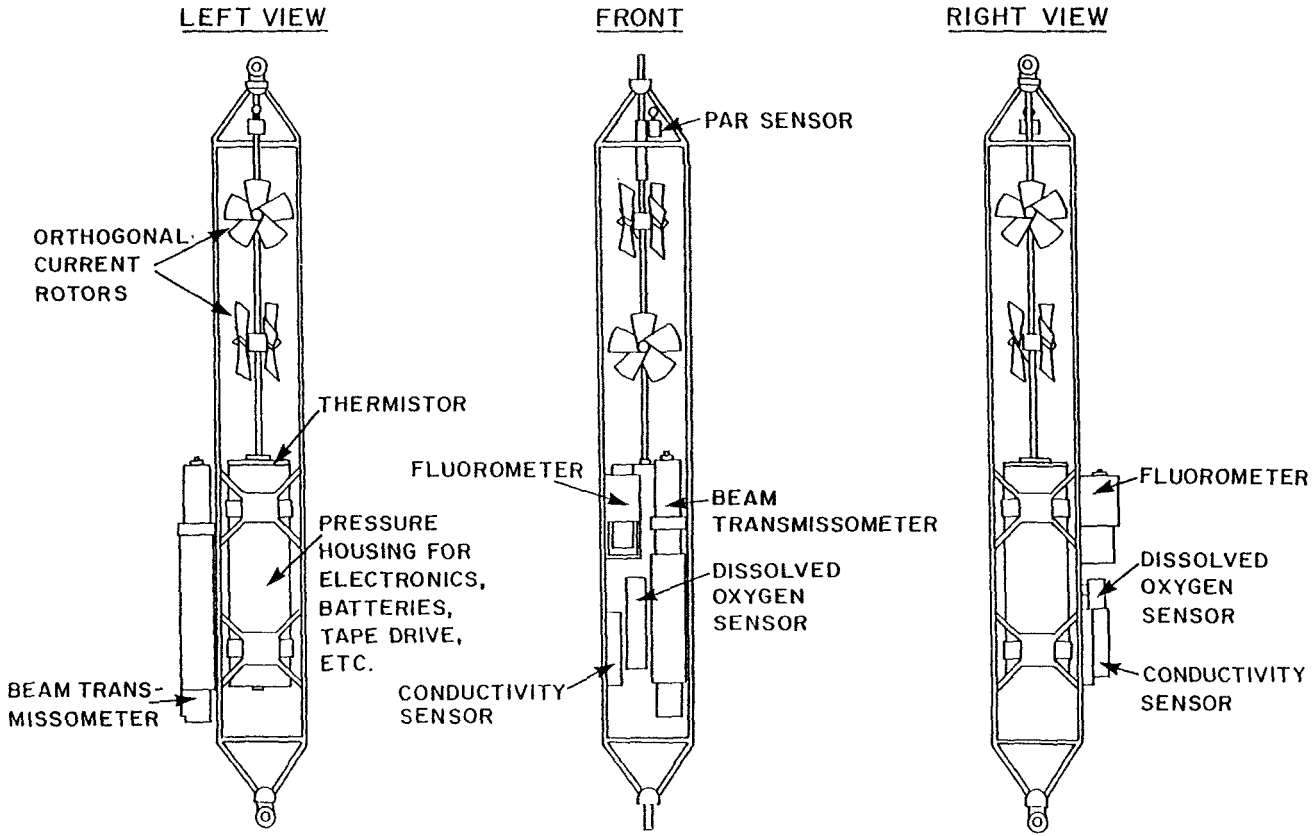

Fig. 10-1. Schematic view of the Multi-Variable Moored Sensor (MVMS), showing the component sensors. The bio-optical sensors were largely mounted on a polyvinyl chloride plate attached to the lower third of the stainless-steel frame used for the Vector Measuring Current Meter (VMCM).

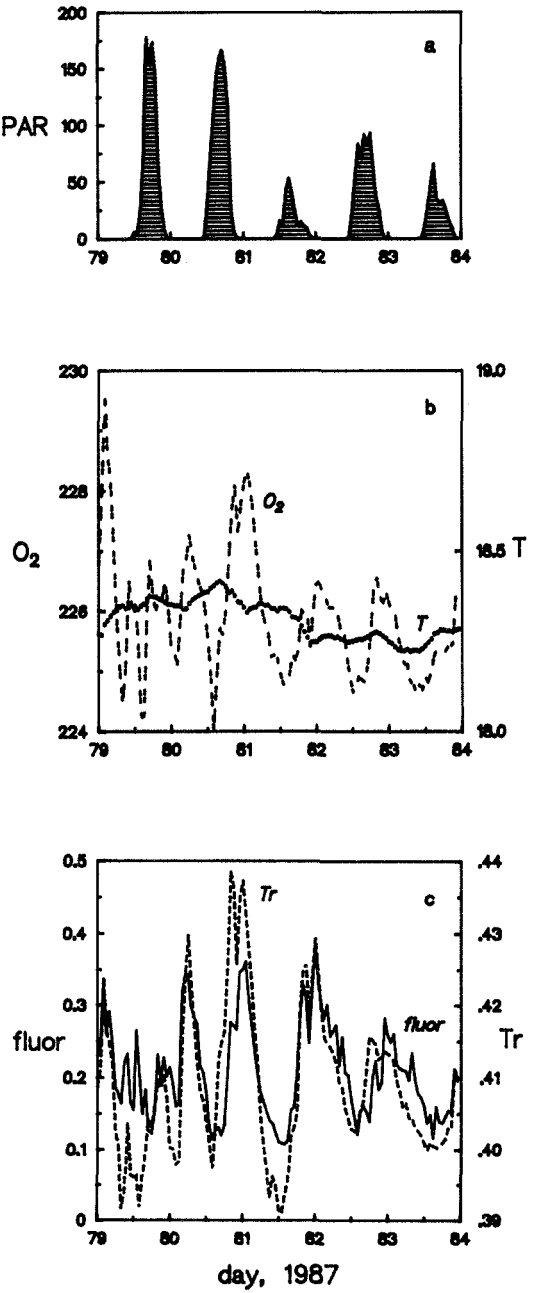

Fig. 10-2. MVMS data for the period 20–25 March, 1987 (days 79–84) for the MVMS unit at 23 m. These are hourly averages of (a) photosynthetic active radiation (PAR) in μEinstein $m^{-2} s^{-1}$; (b) dissolved oxygen (μmol l^{-1}) and temperature (°C); (c) beam attenuation coefficient (Tr in m^{-1}) and fluorescence of chlorophyll *a* ('fluor' but represented as μg chl l^{-1}).

growth. Variability in fluorescence also was not unexpected but could have arisen from a number of sources. A diurnal signal could come about from changes in chlorophyll itself (i.e., growth), changes in fluorescence yield per unit chlorophyll, or changes in chlorophyll with respect to phytoplankton carbon (see Chapters 8 and 9). If there were a mid-day depression in fluorescence yield, any changes in chlorophyll biomass might be masked.

Figure 10-2 shows an example of the diurnal variability observed in the mooring during a 5-day period in the spring, in mid-March, at a depth of 23 m. The raw unfiltered data have been averaged over 1 hour (i.e., an average of 12 records per hour). Clear diurnal signals can be discerned in dissolved oxygen (Fig. 10-2b) and in chlorophyll, and beam attenuation (Fig. 10-2c). The diurnal signals for all of deployment 1, of which Fig. 10-2 is only a part, and at a single depth, have been presented in Hamilton et al. (1990).

The origin of these signals is biological, and not due to advection of water masses with different biological properties past the mooring. These diurnal signals are a common feature throughout the 9-month experiment, and occur at the various depths at which mooring data were obtained. For this time period at

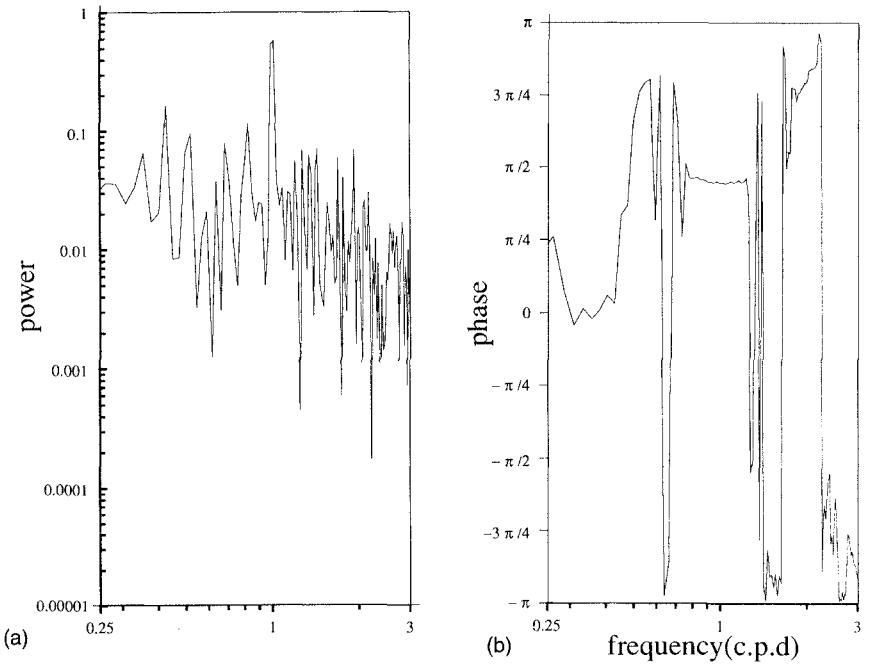

Fig. 10-3. (a) Power spectrum of chlorophyll fluorescence for the MVMS at 23 m depth for the period 28 February–10 May 1987. Note the peak in power (variance) at 1 c.p.d. (b) Phase spectrum for chlorophyll fluorescence and irradiance (PAR) for the same depth and time period as in (a). The steady-phase value around 1 c.p.d. indicates a positive phase lag in fluorescence to PAR at $\pi/2$ radians or 90°. (A phase lag of zero means that the signals are coincident in time. A phase lag of π radians or 180° means that the signals behave oppositely to each other in time.)

least, the signals do not correlate with inertial currents. Variance spectra for chlorophyll *a* show a peak at the daily frequency (Fig. 10-3a) . The phase spectrum of chlorophyll and irradiance (PAR) shows a steady value around the daily frequency of $\pi/2$ radians (Fig. 10-3b). This is a positive phase lag of 90°, that is, chlorophyll peaking later than solar irradiance. In other words, the diurnal maxima occur at sunset, which is to be expected if the diurnal signals represent photosynthetic growth. Interestingly, there are large decreases in the signal overnight (losses due to respiration or grazing?), suggesting a close coupling between growth and loss processes on the diurnal time scale.

Siegel et al. (1989) have analyzed a diurnal signal in beam attenuation from R/P FLIP. There is a similar signal in beam attenuation (and chlorophyll: Fig. 10-3a) here, and by fitting the logistic equation to the data, particle growth rates are calculated to be 0.1–0.5 day^{-1}. For these data, the chlorophyll fluorescence signal tracks the turbidity change and not the solar cycle. Thus the chlorophyll fluorescence appears to give a good indication of biomass change. Langdon (personal communication) has derived daily net production rates for these diurnal signals, and where the data co-occur they are reasonably correlated with respect to production rates from ^{14}C experiments. Thus, it is possible to obtain realistic estimates of net production from the mooring at the daily time scale.

The raw data shown in Fig. 10-2 are internally consistent, as indicated by comparing the rate of net primary production calculated from the oxygen signal with the changes in chlorophyll fluorescence. The average amplitude in the oxygen signal is about 1.4 $\mu mol\, l^{-1}$. Assuming a photosynthetic quotient (the ratio of oxygen evolved to carbon fixed) of 1.5, because nitrate was the most probable nitrogen source at this time of year, the carbon assimilation rate is computed to be about 0.9 $\mu mol\, C\, l^{-1}$. The amplitude of the fluorescence signal was 0.15 V. The fluorescence was converted to a chlorophyll concentration by the factor of 1.25 (Marra and Langdon, 1991). Assuming a carbon-to-chlorophyll ratio of 50, the resulting rate of carbon production is 0.8 $\mu mol\, C\, l^{-1}$ and compares well with oxygen-based estimates.

Figure 10-4 shows another part of the data record that also indicated diurnal variability; this record is from a sequence of days during the second deployment later in the spring (May). For this sequence it was not possible to rule out the effects of local currents and temperature. In Fig. 10-4b, for example, there is a large signal in temperature and in fluorescence that exhibits a roughly diurnal pattern. That is, during certain periods the chlorophyll fluorescence signal exhibits the aforementioned phase relationship with irradiance (PAR), while at other times it does not. Chlorophyll fluorescence, however, also appears to be out of phase with temperature; when temperatures are high, chlorophyll fluorescence is low. Temperature can be influenced by diurnal heating, but passing internal gravity waves will also change the temperature measured at a single depth. These data are from 62 m, a depth zone of high stratification, thus the presence of a large internal wave signal should not be unusual.

This region is part of the subsurface chlorophyll maximum (actually near the top of it). Thus, chlorophyll fluorescence will be affected not only by the diurnal

cycle, as we have shown in Fig. 10-2, but also by the vertical movement of the water caused by the internal waves. As a wave passes a sensor at a particular (fixed) depth, the chlorophyll maximum will move vertically with the wave and the time record will show a variation. Since, at the depth we are examining, chlorophyll increases with depth but temperature decreases, the variation of each of these parameters will vary in the opposing sense, and this is what is observed in Fig. 10-4b. The crest of the passing wave moves deeper, colder water past the thermistor on the MVMS, and water with a greater amount of chlorophyll; the trough is warmer water with less fluorescence. The beam attenuation signal is coherent with the chlorophyll fluorescence signal for this time period.

The fluorescence variability appears to be a mixture of the diurnal signal noted above and the variability caused by the internal wave field. The goal is therefore

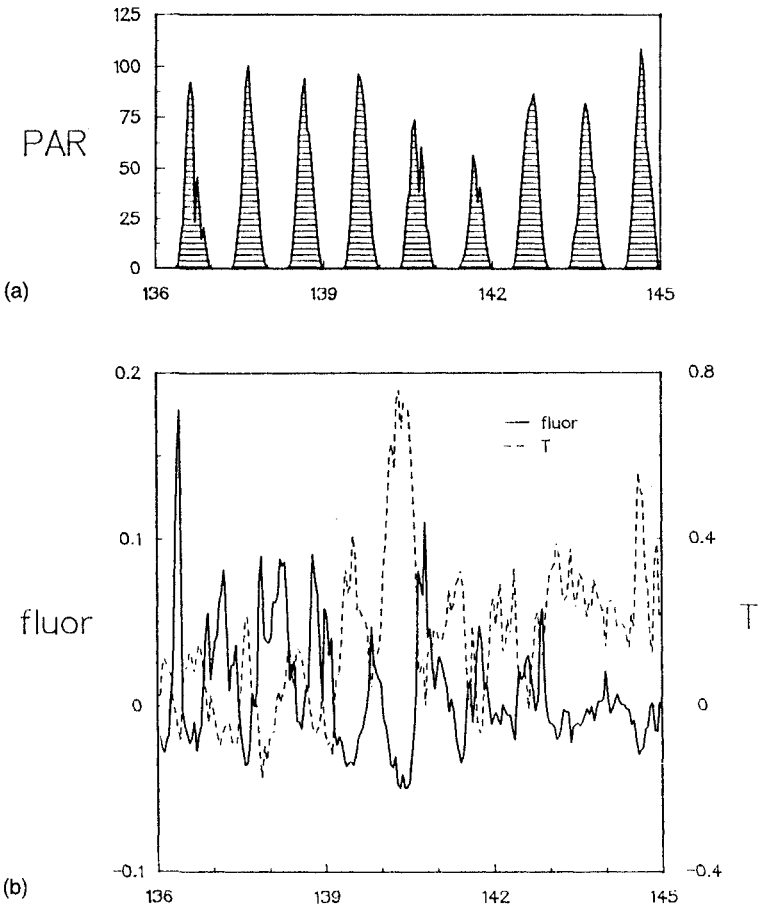

Fig. 10.4a, b

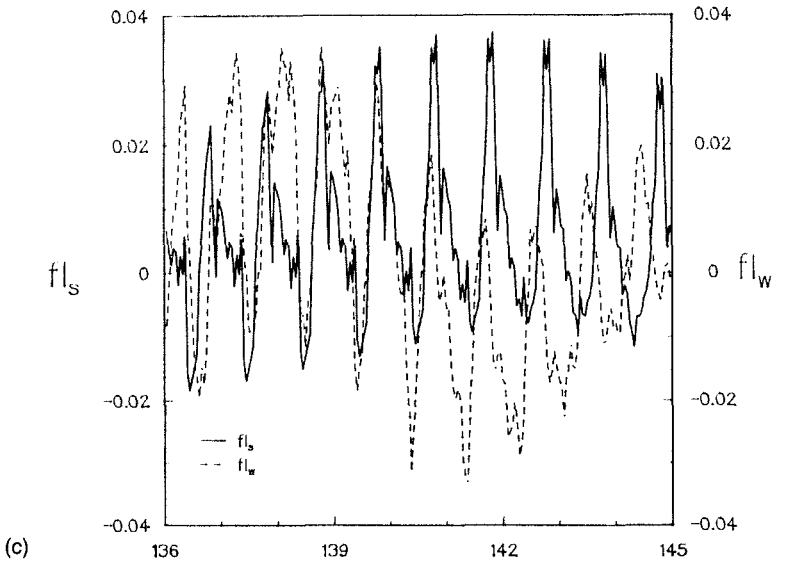

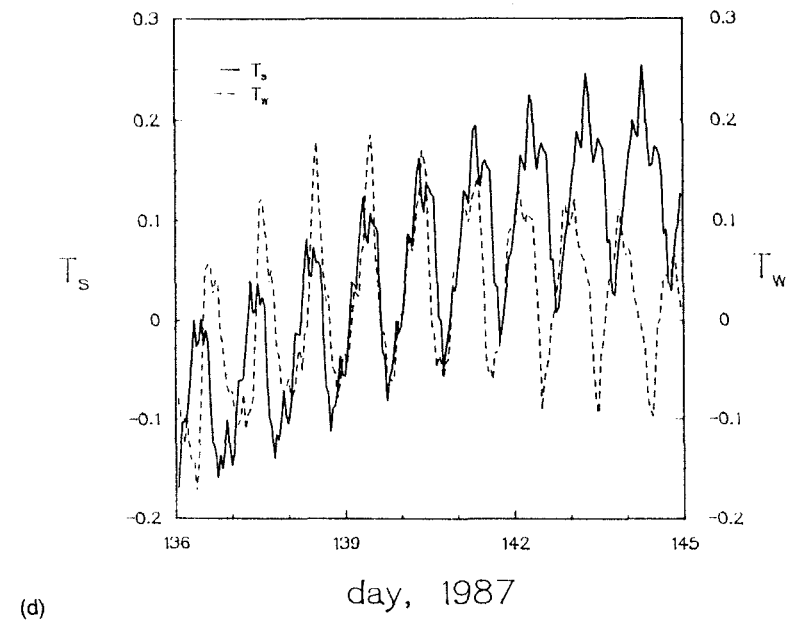

Fig. 10-4. MVMS data for the period 16–25 May, 1987 (days 136–145) for the MVMS unit at 62 m. These are de-trended hourly averages of (a) PAR; (b) chlorophyll fluorescence and temperature; (c) the decomposed fluorescence signal; and (d) the decomposed temperature signal. Units are the same as for Fig. 10-2. These are portions of a longer de-trended time series (days 134–154) needed for the statistical analysis described in the text, and that is why the de-trended series are not symmetrical about zero in (b). The decomposed signals (c) and (d) are reconstructions of selected frequency bands, as described in the text.

to separate the temperature and fluorescence signals into two parts: one influenced by diurnal irradiance (including, by supposition, diurnal heating and photosynthetic growth), and the other by the internal wave field.

Initially, data from a 10-day period during the time period in question were subjected to Fourier analysis. The data set consisted of hourly averages with 240 data points, which translates into a 12 cycle-per-day (c.p.d.) cutoff frequency and 0.1 c.p.d. resolution in the frequency domain. This resolution in frequency turned out to be insufficient, so to separate the frequencies more effectively, a 20-day sequence was used, giving the cutoff frequency of 12 c.p.d., and a 0.05 c.p.d. resolution.

All data were de-trended to reduce the long-term changes that were not of interest for this specific question of diurnal patterns. The Fourier coefficients corresponding to $1, 2, \ldots 12$ c.p.d. were collected and used to compute the influence of the diurnal signal on temperature or fluorescence. The diurnal signal is easily parametrized by the PAR sensor. Numerically, these exact Fourier coefficients are not easy to obtain. In actuality, the frequencies used are $n \pm 5\%$ c.p.d., where $1 \leq n \leq 12$. Some of these coefficients are clearly related to the PAR signal. Other coefficients are influenced by internal waves and other sources of variability. Variance spectra of the data show peaks at the diurnal frequency and also at about 1.1 c.p.d. which we attribute to internal gravity waves.

Figures 10-4c and 10-4d show reconstructions of the chlorophyll fluorescence and temperature caused by the diurnal change (fl_s and T_s, respectively) and the chlorophyll fluorescence and temperature signals caused by the internal waves (fl_w, T_w respectively). It should be noted that these sources of variability together represent only about 20–30% of the total signal. Other sources of variability (i.e., other water movements, changes in fluorescence yield, etc.) in these data are not resolved by our techniques. The changing phase relationship between fl_s and fl_w, and between T_s and T_w, explains why at times the chlorophyll fluorescence is in phase with the diurnal irradiance and at other times it is out of phase (compare with Fig. 10-2). This may be because the deeper population at 62 m does not receive irradiances sufficient for growth until later in the day than nearer the surface. More importantly, there are certainly errors in extracting frequencies from the original data, which are further complicated by our use of a simple low-pass filter, the hourly average.

The BIOWATT program was originally conceived to study diurnal variability from shipboard and seasonal data from a mooring. It is perhaps ironic that such a good set of diurnal data was obtained from the mooring, while it otherwise seems impossible to collect diurnal data from any but the most stable platform (such as R/P FLIP; see Siegel et al., 1989). The diurnal signals, as exemplified in Figs. 10-2 and 10-3, are interesting in several respects. First, the evidence suggests that reasonable growth rates can be obtained from the mooring data. This requires assumptions about what the transmissometer is measuring as particles, but those can be addressed by scaling and abundance arguments. The fluorometer gives additional important information on the nature of the particles—that they are autotrophs. Thus the only type of particles that appear to

be in sufficent abundance and have a fluorescent signal are the phytoplankters. The calculated growth rates are in the right range. The magnitude of the diurnal amplitude decreases with depth (Hamilton et al., 1990) and appears to respond to changes in irradiance in a realistic way. Biological oceanographers have argued for years about the growth rates of phytoplankton in the ocean (see Chapter 9). The mooring contains data to verify these directly.

Second, loss rates are significant in these data. Because they are difficult to measure, respiration and other loss terms are only simple parametrizations in models for the plankton. The mooring data provides actual community losses, and the startling fact is their apparent extent. As seen in Fig. 10-2 (and probably Fig. 10-4b), the loss is almost always equal to the previous day's production or gain. These results may suggest that blooms in the ocean are likely to be short-lived. To evaluate production, then, it may be just as important to measure heterotrophy as autotrophy, since nearly all the production is transferred to higher trophic levels.

Third, the diurnal signal should also appear in absorption and scattering properties. It would be interesting to know if the optical properties also showed a comparable signal. That is, would the calculation of the attenuation coefficients

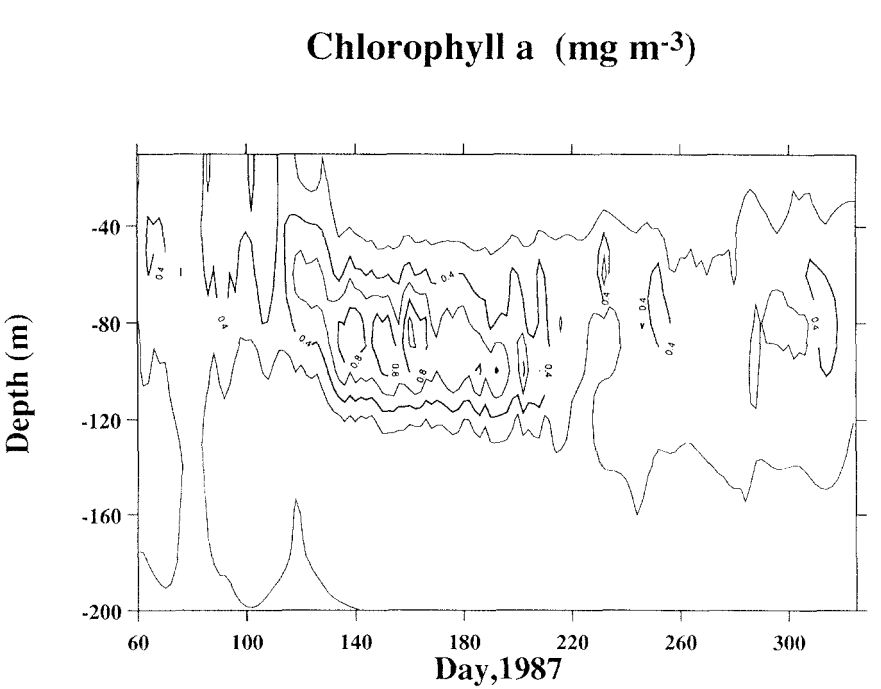

Fig. 10-5. Contours of chlorophyll fluorescence represented as μg chl l^{-1} from all three deployments, that is, from 1 March–20 November, 1987 (days 60–320). These data are daily averages. The contour interval is 0.2 μg chl l^{-1}. The maximum seen in late March and early April is >0.8 μg chl l^{-1}. This is a computer-generated contour plot and is one possible realization of the depth distribution of chlorophyll over the growth season.

from spectroradiometer data agree with the magnitude of change from the transmissometer and fluorometer? Since the diurnal change is in chlorophyll *a*, we can resort to an optical model such as Morel's (1988). Accordingly, a doubling of chlorophyll from, say 0.2 to 0.4 μg chlorophyll *a* per liter, averaged over the euphotic zone, could result in a change in the diffuse attentuation coefficent of from 0.06 to 0.08 m^{-1}, and a shallowing of the euphotic zone of 75 to 55 m.

Seasonal changes

My emphasis has been on short-term variability occurring at a single depth, but data from moored sensors can also be used for long-term studies and to look at variability within the water column at a given time. As stated earlier, the moored data sacrifice depth resolution in favor of highly resolved variability in time.

Figure 10-5 shows a composite realization, contoured by computer, of the chlorophyll data for the entire length of the mooring from March until the end of November. Because of the few sampled depths, we regard this as one possible view. Nevertheless, there are features in this diagram that attest to its veracity. There is a chlorophyll maximum near the surface during the time when a spring bloom can be expected to occur. Observations at this site in previous years agree with this pattern (Marra et al., 1990). Later, this chlorophyll maximum appears to "sink," although in this data it looks as if a different population of phytoplankton appears at this depth range. Still later in the growing season, we can see the formation and maintenance of the deep chlorophyll maximum (with variations in its intensity at 10- 20-day intervals). The subsurface maximum is attenuated late in the summer and early fall, until it becomes $<0.2\ \mu g\ l^{-1}$, the lowest contouring interval used.

Summary

Once, the acquisition of these kinds of data was the province of physical oceanography. Although measurement problems remain to be solved, biological and optical oceanographers now have additional tools at their disposal. And as well as improving the time resolution of planktonic events, it is now possible to delve into aspects of ecology and algal physiology that were not accessible using normal modes of field data collection. One prime example is the capability to measure planktonic production in several different ways and with several independent moored sensors. The change in oxygen concentration measures net production; autotrophic particle production can be assessed from the beam attenuation and fluorescence data; and finally, the irradiance (PAR) and chlorophyll data can be used, by means of a model, to estimate photosynthesis. Studies of the nighttime decline in fluorescence and beam attenuation should be interesting with respect to interactions in the microbial food web.

It is instructive to provide some perspective on moored observations. Moorings give data that are highly resolved in time, and compared to ship

sampling these data can be collected for relatively long periods. Typically, one can expect sampling frequencies of at least several per hour for periods as long as 6 months. This kind of sampling, however, sacrifices resolution in depth (tens of meters), and since the mooring only occupies one point in geographic space, one is forced to assume horizontal homogeneity for some distance around the mooring.

11

POLARIZATION OF LIGHT IN THE OCEAN

George W. Kattawar
Texas A&M University

Introduction

The effects of polarization on our perception of the environment about us have been recognized for at least 1000 years. The earliest reports were in response to the polarization in blue skylight as observed through various polarizing crystals. Since blue skylight is a source of polarized light, and atmospheric observations are a quite natural part of our daily routine, it is not surprising that an extraordinary amount of research on the polarization of skylight has been undertaken. Study of the polarization properties of the ocean and the hydrosols contained therein has, unfortunately been very limited, perhaps because man has not been a natural resident of the sea.

This chapter will introduce a description of the polarized light field beneath the sea by first providing a brief history of polarization. This will familiarize the reader with its rather ubiquitous presence in our environment, even though our visual perception of it is very weak. Finally, a method is presented (Mueller matrices) to fully characterize the polarization properties of the submarine light field and the polarized effects that various hydrosols have on the light field. For a collection of the many diverse applications of polarization, the reader is referred to the excellent book by Gehrels (1974)

Background

About 1000 years ago, the Vikings discovered the dichroic properties of crystals such as cordierite. This property of exhibiting various colors when viewed from different directions is due to the selective absorption of waves oscillating along a particular plane of the crystal. When Vikings viewed the blue skylight through such crystals held in a certain orientation, they located portions of the sky relative to the solar position that seemed to disappear. With this discovery of the polarization of the blue sky, they learned to navigate even in the absence of the sun (e.g., when it was below the horizon). It was another six and one-half centuries before other polarization properties were reported (see Table 11-1 taken from Gehrels, 1974, and Können, 1985).

Table 11-1. A chronology of the discoveries on polarization

~1000 A.D.	The Vikings discovered the dichroic properties of crystals like cordierite. With these crystals they observed the polarization of the blue sky and were thus able to navigate in the absence of the sun.
1669	Erasmus Bartolinus from Denmark discovered the double refraction of calcite crystals (Iceland spar) but was unaware of its polarization properties.
1690	Christiaan Huygens discovered the polarization of the doubly-refracted rays of calcite, but was unable to explain the phenomenon.
1808	E.L. Malus, motivated by a prize offered by the French Academy for a mathematical theory of double refraction, found the polarization of reflected light by using a calcite crystal as a filter. This filter apparently loses its double refraction when the entering light is polarized and the crystal is held in the correct position. Afterwards Malus formulated his law (Malus' law), giving the relationship between the position of a polarizing filter and the quantity of transmitted light, when the entering light is totally (linearly) polarized.
1809	D.F.J. Arago rediscovered the polarization of the blue sky and also noted the maximum at about 90° from the sun. He later found the neutral point (20–25° above the antisolar direction), which was named after him. In 1811 he discovered the optical activity of quartz, and in 1812 he constructed a filter out of a pile of glass sheets. In 1819 he found the polarization of comet tails and in 1825 the (weak) overall polarization of 22° haloes. In 1824 he found the polarization of the glow emitted by hot, incandescent metals. He was also the first to record the fact that on the moon the polarization of the maria was greater than that of the highlands.
1811	J.B. Biot discovered the polarization of the rainbow. In 1815 he established the optical activity of fluids such as turpentine, and in 1818 he studied the optical activity of gaseous turpentine in a gas column that was 15 m in length. Unfortunately, this apparatus exploded before he could finish his measurements. In 1815 Biot also discovered the strong dichroism of tourmaline.
1812	Sir David Brewster discovered the relationship between the index of refraction and the angle of incidence at which light is totally converted by reflection into linearly polarized light (Brewster's law). In 1818 he discovered Brewster's brush in pleochroic (different absorption for fast and slow axes) crystals, and in 1842 the neutral point (20°–25° below and in the direction of the sun) which was named after him.
1816	A. Fresnel gave the first theoretical explanation of Malus' observations. He also derived the formulas (Fresnel's laws) relating the reflection coefficients of dielectric materials to the angle of incidence and the direction of polarization of the incoming wave.
1828	W. Nicol invented his prism, which can be considered to be the first easily usable polarizing filter.
1840	A. Babinet discovered the neutral point (20°–25° above and in the direction of the sun) which was named after him.
1844	W. Haidinger found that the human eye has the ability to distinguish between unpolarized and polarized light, because in the latter case a yellowish figure appears on the retina (the Haidinger's brush). He also discovered circular dichroism in crystals of amethyst quartz.

1845 Michael Faraday discovered the rotation of the polarization plane of linearly polarized light propagating parallel to magnetic field lines.

1848 L. Pasteur described hemihedral crystals that exhibit optical activity.

1852 W.B. Herapath, using iodine and quinine, made a synthetic crystal with very high dichroism, which was the first step on the way to the construction of simple sheet polarizers.

1852 Sir George Stokes described the four parameters that define the properties of a light beam and that now bear his name (Stokes parameters).

1858 E. Liais, a French astronomer, while observing a solar eclipse, discovered that the light from the solar corona was partially linearly polarized.

1860 G. Kirchhoff found that incandescent tourmaline emits polarized light according to the radiation law that he also formulated.

1869 D. Tyndall established the fact that the polarization characteristics of light scattered by particles were strongly dependent on the particles' size.

1871 Lord Rayleigh (born John W. Strutt) began his studies of the polarization of the blue sky.

1872 Lord Rosse discovered some polarization on Venus.

1874 A.W. Wright discovered the polarization of zodiacal light.

1875 John Kerr discovered the birefringence of electrified media (Kerr effect). He also discovered changes in metallic reflection of polarized light in the presence of magnetic fields (Kerr magneto-optic effect).

1884 Kiessling recorded that the glory is polarized.

1889 A. Cornu found that artificial haloes in sodium nitrate crystals are highly polarized.

1896 P. Zeeman discovered the broadening of spectral lines when radiating atoms are in the presence of an intense magnetic field. He later observed the splitting of spectral lines by magnetic fields and their associated polarization (Zeeman effect).

1905 N. Umov described the relationship between the degree of polarization of light reflected from rough surfaces and the albedo of the surface.

1908 G.E. Hale, by using polarization measurements of the Zeeman effect, discovered the existence of strong magnetic fields in sunspots.

1908 G. Mie and P. Debye independently developed the theory of scattering of a plane wave from a sphere of arbitrary size.

1911 A.A. Michelson discovered that certain beetles have a gloss that is circularly polarized.

1928 E.H. Land constructed his first sheet-type dichroic polarizing filter. Further developments of this filter made it possible to study effects of polarization with a simple and efficient sheet filter. Such filters are also used in sunglasses, etc., to reduce the intensity of glare. Compared with the Nicol and other crystal filters used up to that point, the development of this kind of sheet filter meant great progress.

1929	B. Lyot published his thesis containing major discoveries on the linear polarization of light from planets and terrestrial substances.
1935	R.A. Beth posited that circularly polarized light exerts a slight mechanical torque on materials, and thus proved directly the rotating character of this light.
1939	Y. Le Grand and K. Kalle reported that scattered light underwater is polarized.
1940	J. Bricard found that supernumerary fog-bows shift when one looks at them through a linear filter that is then rotated.
1942	Y. Öhman found polarization in the galaxy M31.
1943	H. Mueller developed an approach using a 4×4 matrix (Mueller matrix) to transform the four-component Stokes vector.
1947	H.C. van de Hulst gave the first feasible explanation of the glory and explained its polarization directions.
1947	H.W. Babcock discovered that certain A-type stars have strong magnetic fields.
1949	K. von Frisch discovered that bees are more capable than man of distinguishing polarized from unpolarized light and use this ability to orientate themselves.
1949	J.S. Hall and W.A. Hiltner discovered linear interstellar polarization, and later published catalogs on polarized starlight.
1954	V.A. Dombrovsy discovered the strong polarization of the Crab Nebula, which had been predicted a year earlier with synchrotron radiation by I.S. Shklovsky.
1955	W.A. Shurcliff discovered that the human eye is also capable of distinguishing circularly polarized from unpolarized light.
1956	H.H. Jaffé proved that, when the egg cells of certain algae are irradiated by linearly polarized light, they tend to develop in the direction of vibration of the light.
1957	C.H. Mayer, T.P. McCullough, and R.M. Sloanaker detected radio polarization of the Crab Nebula and were the first to measure the polarization of an extragalactic radio source in 1962.
1962	N.M. Shakhovskoy found a variable polarization in early-type eclipsing binary β Lyrae stars.
1966	K. Serkowski detected strong polarization for Mira stars.
1970	J.C. Kemp discovered circular polarization on a white dwarf star, which led to a large number of findings of circular polarizations on planets, stars, and nebulas.
1972	T.H. Waterman demonstrated polarotaxis in certain marine organisms.

Source: Gehrels (1974); Können (1985).

By the end of the seventeenth century, birefringence (double-refraction) of calcite crystals had been discovered by Erasmus Bartolinus, who observed double images of objects viewed through them. Shortly thereafter the linear polarization properties of these doubly-refracted rays were discovered by Huygens. Following the turn of the nineteenth century, rapid discoveries of the polarization properties of various materials and natural media were made. Malus' law relating the quantity of transmitted light to the relative position of a polarizing filter when viewing polarized light seemed to catalyze a flurry of research activity dealing with polarization (see Table 11-1). Linear polarization of reflected light, the optical activity (polarization rotation) of quartz and various fluids, the neutral points (points with no polarization) of the sky, polarization of comet tails, rainbows, and 22° haloes were either discovered or explained in rapid sequence. Finally, in 1816 Fresnel gave a theoretical explanation of the existence of polarization that also explained reflection, refraction, and Brewster's law. For the next century and one-half more observations of the polarization effects of natural phenomena were observed, and improvements were made in the fabrication of efficient linear polarizers. Furthermore, theoretical explanations of polarization of atmospheric scattering phenomena based upon applications of Maxwell's equations to scattering by small spheres (e.g., Mie, 1908; van de Hulst, 1948, 1957) have helped to explain polarization in the blue sky, rainbows, and the glory (a bright, halolike backscattering pattern observed around the shadow of one's head when viewing a cloudy medium).

Theoretical considerations

In 1864, James Clerk Maxwell formulated an elegant, concise mathematical statement of the observed laws of electricity and magnetism. It unified the concepts behind the relationships posed by Gauss, Faraday, Ampere, and Ohm. Maxwell's equations are (following the treatment in Bohren and Huffman, 1983)

$$\begin{aligned} \nabla \cdot \mathbf{D} &= \rho_F \\ \nabla \times \mathbf{E} + \frac{\partial \mathbf{B}}{\partial t} &= 0 \\ \nabla \cdot \mathbf{B} &= 0 \\ \nabla \times \mathbf{H} &= \mathbf{J}_F + \frac{\partial \mathbf{D}}{\partial t} \end{aligned} \tag{11.1}$$

where $\mathbf{E}$ is the electric field and $\mathbf{B}$ the magnetic induction. Also ρ_F and $\mathbf{J}_F$ are the "free" charge and current densities, respectively. $\mathbf{D}$ (called the electric displacement) and $\mathbf{H}$ (called the magnetic field) are defined by

$$\mathbf{D} = \varepsilon_0 \mathbf{E} + \mathbf{P} \qquad \mathbf{H} = \frac{\mathbf{B}}{\mu_0} - \mathbf{M} \tag{11.2}$$

where $\mathbf{P}$ is the electric polarization vector (average electric dipole moment per unit volume), $\mathbf{M}$ is the magnetization vector (average magnetic dipole moment per unit volume), and ε_0 and μ_0 are the permittivity and permeability respectively, of free space.

The constitutive relations can be expressed as

$$\mathbf{J}_F = \sigma\mathbf{E} \qquad \mathbf{B} = \mu\mathbf{H} \qquad \mathbf{P} = \varepsilon_0\chi\mathbf{E} \tag{11.3}$$

where σ, μ, and χ are the conductivity, permeability, and electric susceptibility respectively, of the medium.

We make the following assumptions about σ, μ, and χ of the medium; (a) they are independent of the fields (linear medium), (b) they are independent of the position in the medium (homogeneous), (c) they are independent of direction in the medium (isotropic).

Now let us consider plane wave propagation where the fields can be described by

$$\mathbf{E}_c = \mathbf{E}_0 \exp(i\mathbf{k}\bullet\mathbf{x} - \mathrm{i}\omega t) \qquad \mathbf{H}_c = \mathbf{H}_0 \exp(i\mathbf{k}\bullet\mathbf{x} - i\omega t) \tag{11.4}$$

where $\mathbf{E}_0$ and $\mathbf{H}_0$ are constant vectors that are compatible with Maxwell's equations. The angular frequency of the wave is ω and the wave vector $\mathbf{k}$ may be complex

$$\mathbf{k} = \mathbf{k}' + i\mathbf{k}'' \tag{11.5}$$

where $\mathbf{k}'$ and $\mathbf{k}''$ are real vectors. Substitution for $\mathbf{k}$ results in

$$\begin{aligned} \mathbf{E}_c &= \mathbf{E}_0 \exp(-\mathbf{k}''\bullet\mathbf{x})\exp(i\mathbf{k}'\bullet\mathbf{x} - i\omega t) \\ \mathbf{H}_c &= \mathbf{H}_0 \exp(-\mathbf{k}''\bullet\mathbf{x})\exp(i\mathbf{k}'\bullet\mathbf{x} - i\omega t) \end{aligned} \tag{11.6}$$

where $\mathbf{E}_0 \exp(-\mathbf{k}''\bullet\mathbf{x})$ and $\mathbf{H}_0 \exp(-\mathbf{k}''\bullet\mathbf{x})$ are the amplitudes of the electric and magnetic fields. Note that $\mathbf{k}''$ produces a damping effect on the propagating wave. The phase of the wave is

$$\phi = \mathbf{k}'\bullet\mathbf{x} - \omega t \tag{11.7}$$

A plane surface, the normal to which is $\mathbf{K}$, is defined by $\mathbf{K}\bullet\mathbf{x}$ = constant, where $\mathbf{K}$ is any real vector. As a result, $\mathbf{k}'$ is perpendicular to the surfaces of constant phase, and $\mathbf{k}''$ is perpendicular to the surfaces of constant amplitude. If $\mathbf{k}'$ is parallel to $\mathbf{k}''$, the wave is said to be *homogeneous*, otherwise it is said to be *inhomogeneous*.

To demonstrate propagation of surfaces with constant phase (see Fig. 11-1), let $\mathbf{k}' = k'\hat{\mathbf{z}}$ then $\phi = k'z - \omega t$ will be the phase at time t. In a time interval Δt, the surface of *constant* phase will have moved a distance Δz, where

$$\phi = k'z - \omega t = k'(z + \Delta z) - \omega(t + \Delta t) \tag{11.8}$$

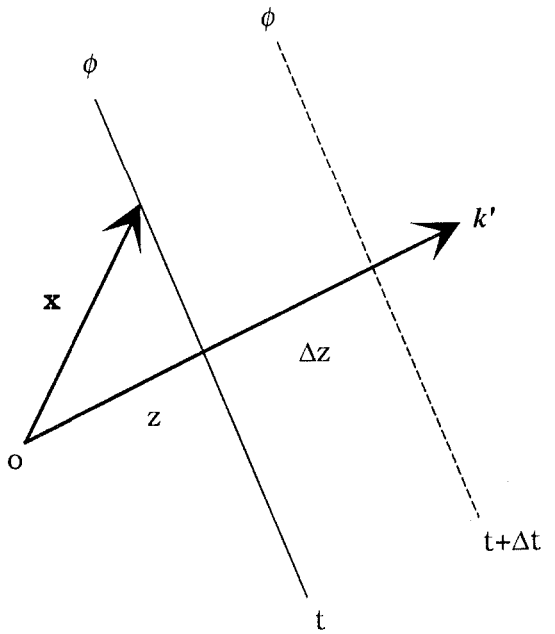

Fig. 11-1. Propagation of surfaces of constant phase.

Therefore the phase velocity v is

$$v = \frac{\Delta z}{\Delta t} = \frac{\omega}{k'} \tag{11.9}$$

and the vector $\mathbf{k}'$ specifies the direction of propagation.

For a plane wave when $\rho_F = 0$ (no free charges), Maxwell's equations simplify to

$$\begin{aligned} \mathbf{k}\bullet\mathbf{E}_0 &= 0 \qquad \mathbf{k}\bullet\mathbf{H}_0 = 0 \\ \mathbf{k} \times \mathbf{E}_0 &= \omega\mu\mathbf{H}_0 \qquad \mathbf{k} \times \mathbf{H}_0 = -\omega\varepsilon\mathbf{E}_0 \end{aligned} \tag{11.10}$$

Taking the vector product with $\mathbf{k}$ of the third equation above we obtain:

$$\mathbf{k} \times (\mathbf{k} \times \mathbf{E}_0) = \omega\mu\mathbf{k} \times \mathbf{H}_0 = -\omega^2\varepsilon\mu\mathbf{E}_0 \tag{11.11}$$

Using the vector identity

$$\mathbf{A} \times (\mathbf{B} \times \mathbf{C}) = \mathbf{B}(\mathbf{A}\bullet\mathbf{C}) - \mathbf{C}(\mathbf{A}\bullet\mathbf{B}) \tag{11.12}$$

we obtain

$$\mathbf{k}\bullet\mathbf{k} = \omega^2\varepsilon\mu \tag{11.13}$$

Compatibility with Maxwell's equations requires the following two conditions:

$$\begin{aligned} \mathbf{k}\cdot\mathbf{E}_0 &= \mathbf{k}\cdot\mathbf{H}_0 = \mathbf{E}_0\cdot\mathbf{H}_0 = 0 \\ (k')^2 - (k'')^2 + 2i\mathbf{k}'\cdot\mathbf{k}'' &= \omega^2\varepsilon\mu \end{aligned} \tag{11.14}$$

Note that ε and μ are properties of the *medium* in which the wave propagates; the vectors $\mathbf{k}'$ and $\mathbf{k}''$ are properties of the wave.

Let us consider a homogeneous wave where

$$\mathbf{k} = (k' + ik'')\hat{\mathbf{e}} \tag{11.15}$$

and $k', k'' \geq 0$ and $\hat{\mathbf{e}}$ is a real unit vector in the direction of propagation. Equation (11.13) implies

$$k = k' + ik'' = \frac{\omega N}{c} \tag{11.16}$$

where c is the speed of light in vacuo and N is the *complex refractive index* defined by

$$N \equiv c\sqrt{\varepsilon\mu} \equiv \sqrt{\frac{\varepsilon\mu}{\varepsilon_0\mu_0}} \tag{11.17}$$

Many authors write $N = n + ik$ or $N = n' + in''$. If the time dependence $\exp(i\omega t)$ had been chosen, then one would have to use the complex conjugate of the above expressions, i.e., $N = n - ik$ or $N = n' - in''$. The free-space wavenumber is $\omega/c = 2\pi/\lambda$ where λ is the wavelength in vacuo. A plane homogeneous wave has the form

$$E_c = E_0 \exp\left(-\frac{2\pi n'' z}{\lambda}\right) \exp\left(\frac{i2\pi n' z}{\lambda} - i\omega t\right) \tag{11.18}$$

where $z = \hat{\mathbf{e}}\cdot\mathbf{x}$. Therefore n'' determines the attenuation of the wave as it propagates and n' determines the phase velocity $v = c/n'$.

The Poynting vector of a plane wave is

$$\mathbf{S} = \frac{1}{2}\Re[\mathbf{E} \times \mathbf{H}^*] = \Re\left[\frac{\mathbf{E} \times (\mathbf{k}^* \times \mathbf{E}^*)}{2\omega\mu^*}\right] \tag{11.19}$$

where

$$\mathbf{E} \times (\mathbf{k}^* \times \mathbf{E}^*) = \mathbf{k}^*(\mathbf{E}\cdot\mathbf{E}^*) - \mathbf{E}^*(\mathbf{k}^*\cdot\mathbf{E}) \tag{11.20}$$

and $\Re$ denotes taking the real part of the expression in brackets and the asterisk (*) denotes complex conjugation. If the wave is homogeneous,

$\mathbf{k}\bullet\mathbf{E} = 0$ implies that $\mathbf{k}^*\bullet\mathbf{E} = 0$. For a wave of this nature propagating in the $\hat{\mathbf{e}}$ direction we get

$$\mathbf{S} = \frac{1}{2}\Re\left[\sqrt{\frac{\varepsilon}{\mu}}\right]|\mathbf{E}_0|^2\exp\left(-\frac{4\pi n'' z}{\lambda}\right)\hat{\mathbf{e}} \tag{11.21}$$

Note that $\mathbf{S}$ is in the direction of propagation. It has the units of *irradiance* (energy per unit area per unit time). To see how $\mathbf{S}$ is related to the radiance, the reader is referred to Preisendorfer (1965, page 392). As the wave traverses the medium, the attenuation is given by

$$I = I_0\exp(-az) \tag{11.22}$$

where the absorption coefficient a is

$$a = \frac{4\pi n''}{\lambda} \tag{11.23}$$

It should be noted that the above expression for the attenuation is not strictly valid even in homogeneous media, due to the scattering that is usually always present, and unless special techniques are used one can only measure the *combined* effects of absorption and scattering (see Chapter 5).

Polarization

If we write the electric field vector, $\mathbf{E}$ of a wave traveling in the z direction as the real part of a complex electric field, we have

$$\mathbf{E} = \Re[(\mathbf{A} + i\mathbf{B})\exp(ikz - i\omega t)] = \mathbf{A}\cos(kz - \omega t) - \mathbf{B}\sin(kz - \omega t) \tag{11.24}$$

where the real vectors $\mathbf{A}$ and $\mathbf{B}$ are independent of position. The tip of the electric vector traces out a curve:

$$\mathbf{E}(z = 0) = \mathbf{A}\cos(\omega t) + \mathbf{B}\sin(\omega t) \tag{11.25}$$

This equation describes the *vibration ellipse* (see Fig. 11-2). If $\mathbf{A} = 0$ or $\mathbf{B} = 0$ the vibration ellipse is just a straight line and the wave is said to be linearly polarized. If $|\mathbf{A}| = |\mathbf{B}|$ and $\mathbf{A}\bullet\mathbf{B} = 0$, the vibration ellipse is a circle and the wave is said to be *circularly* polarized.

For a wave propagating in the z direction, its vibrational plane at $z = 0$ is aligned with $\mathbf{A}$. At the same instant in time at position $z = \pi/(2k)$, or a quarter of a wavelength in the z direction (Fig. 11-3), suppose its plane of vibration has rotated into alignment with $-\mathbf{B}$. If one considers that in this plane as time progresses the electric vector rotates *clockwise* as viewed *toward* the direction of propagation, this rotation is called *right-handed.*

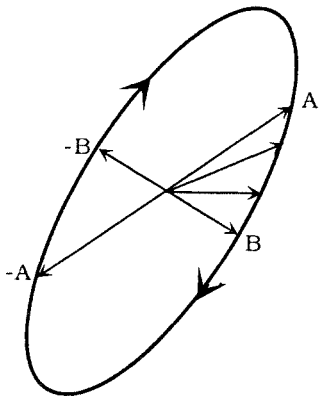

Fig. 11-2. Schematic of the vibration ellipse.

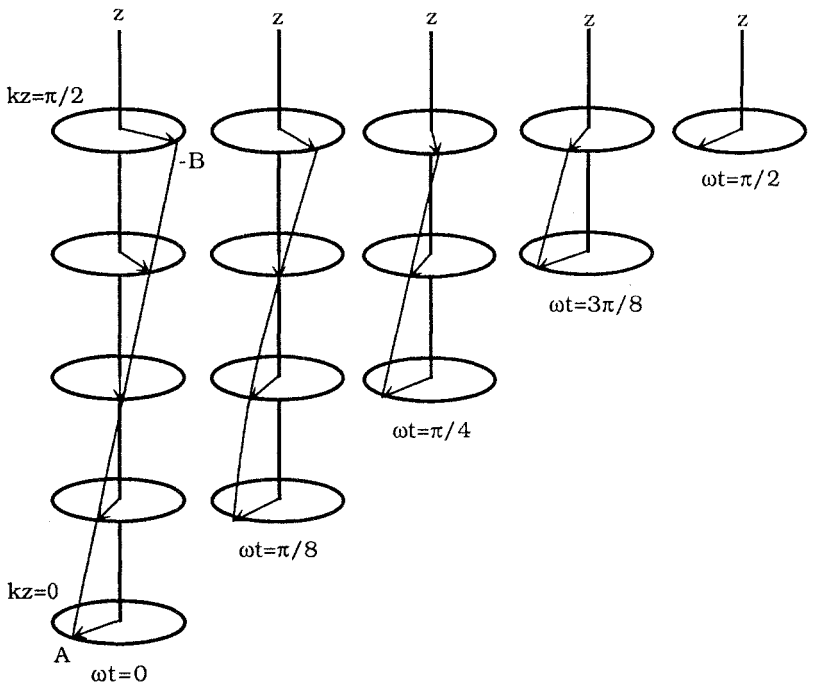

Fig. 11-3. Position of the electric field vector at different instants in time.

When the refractive index of a medium depends on the state of polarization of the wave, the medium can be classified as follows:

1. *Linearly birefringent*: real part of refractive index depends on the linear polarization state
2. *Linearly dichroic*: imaginary part of refractive index depends on the linear polarization state
3. *Circularly birefringent*: real part of refractive index depends on handedness
4. *Circularly dichroic*: imaginary part of refractive index depends on handedness

Stokes parameters

Proper treatment of the Stokes vector formulation requires very careful consideration of reference frames. Referring to Fig. 11-4, the incident beam is denoted by I_i and it along with the $\hat{\mathbf{z}}$ axis defines a plane called the meridian plane in which the radiance can be resolved into two orthogonal components denoted by I_l and I_r where the subscripts l and r refer to vibrations of the electric field parallel and perpendicular to the meridian plane respectively. If we let $\mathbf{l}$ and $\mathbf{r}$ denote unit vectors in the meridian plane and perpendicular to it, respectively, and the sense is chosen so that $\mathbf{r} \times \mathbf{l}$ is in the direction of propagation, then the electric field can be resolved into components as follows:

$$\mathbf{E} = E_l\mathbf{l} + E_r\mathbf{r} \tag{11.26}$$

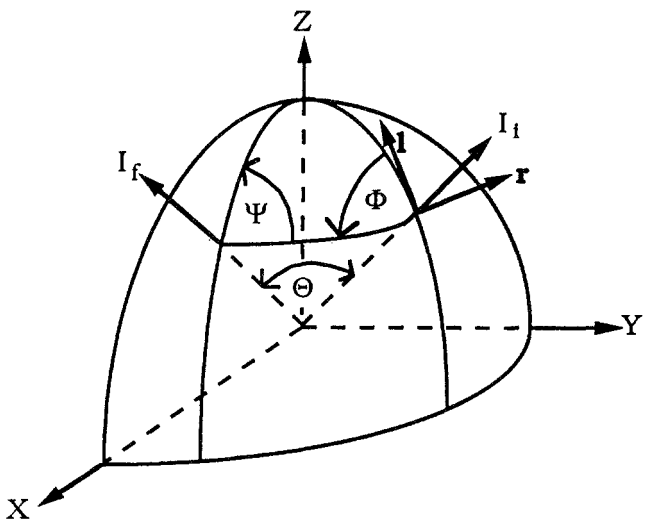

Fig. 11-4. Planes of reference used for describing Stokes vector transformation when scattering occurs.

where E_l and E_r are complex oscillatory functions. The four-component Stokes vector can now be defined as follows:

$$\begin{aligned} I &= E_l E_l^* + E_r E_r^* = I_l + I_r \\ Q &= E_l E_l^* - E_r E_r^* = I_l - I_r \\ U &= E_l E_r^* + E_r E_l^* \\ V &= i(E_l E_r^* - E_r E_l^* \end{aligned} \tag{11.27}$$

where the asterisk denotes complex conjugation. It is clear that the four components are all real numbers and satisfy the relation

$$I^2 = Q^2 + U^2 + V^2 \tag{11.28}$$

The first component I is usually referred to as the radiance and all other parameters have the same units. The most general simple wave can be represented as

$$\begin{aligned} E_l &= a_l \exp(-i(\varepsilon_1 + kz - \omega t)) \\ E_r &= a_r \exp(-i(\varepsilon_2 + kz - \omega t) \end{aligned} \tag{11.29}$$

which gives

$$\begin{aligned} I &= a_l^2 + a_r^2 \\ Q &= a_l^2 - a_r^2 \\ U &= 2a_l a_r \cos\delta \\ V &= 2a_l a_r \sin\delta \end{aligned} \tag{11.30}$$

and $\delta = \varepsilon_1 - \varepsilon_2$. The geometric description of this simple wave with the most general state of elliptical polarization can be written as

$$\mathbf{E} = a\mathbf{p}\cos\beta\sin(\omega t - kz + \alpha) + a\mathbf{q}\sin\beta\cos(\omega t - kz + \alpha) \tag{11.31}$$

Here $\mathbf{p}$ and $\mathbf{q}$ are unit vectors that lie along the semi-major and semi-minor axes of the polarization ellipse, respectively (see Fig. 11-5). It is not too difficult to show that the two descriptions are related as follows:

$$\begin{aligned} a_l^2 &= a^2(\cos^2\beta\cos^2\chi + \sin^2\beta\sin^2\chi) \\ a_r^2 &= a^2(\cos^2\beta\sin^2\chi + \sin^2\beta\cos^2\chi) \\ \tan(\alpha + \varepsilon_1) &= -\cot\chi\cot\beta \\ \tan(\alpha + \varepsilon_2) &= \tan\chi\cot\beta \end{aligned} \tag{11.32}$$

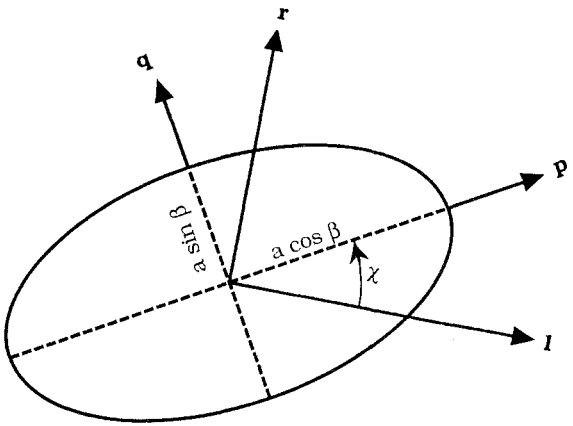

Fig. 11-5. Relationship of the geometric description of an elliptical wave to the (**r**,**l**) representation.

Therefore

$$\tan\delta = \frac{\tan 2\beta}{\sin 2\chi} \tag{11.33}$$

It can be shown (van de Hulst,1981) that the Stokes parameters in the geometric notation become

$$\begin{aligned} I &= a^2 \\ Q &= a^2 \cos 2\beta \cos 2\chi \\ U &= a^2 \cos 2\beta \sin 2\chi \\ V &= a^2 \cos 2\beta \end{aligned} \tag{11.34}$$

One of the very important transformations that must be handled in Monte Carlo emulations is the placing of the Stokes vector in the proper frame of reference for both scattering and Fresnel reflection from the stochastic interface. Referring now to Fig. 11-6, if we rotate the **l** axis *clockwise* by an angle ϕ and now refer the Stokes vector to the **l'** system, the transformation to do this is easily derived to be

$$\begin{bmatrix} I' \\ Q' \\ U' \\ V \end{bmatrix} = \begin{bmatrix} 1 & 0 & 0 & 0 \\ 0 & \cos 2\phi & \sin 2\phi & 0 \\ 0 & -\sin 2\phi & \cos 2\phi & 0 \\ 0 & 0 & 0 & 1 \end{bmatrix} \begin{bmatrix} I \\ Q \\ U \\ V \end{bmatrix} \tag{11.35}$$

The rotation matrix leaves I, $Q^2 + U^2$ and V invariant.

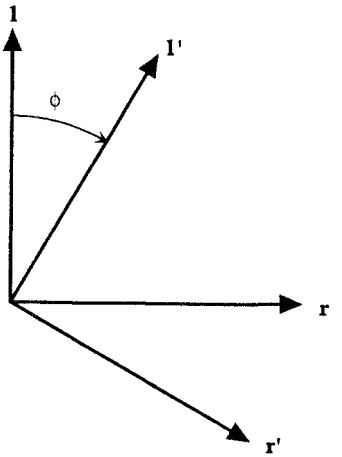

Fig. 11-6. Two sets of axes for Stokes vector representation rotated by an angle ϕ with respect to one another.

The rotation matrix $\mathbf{R}(\phi)$ has some other interesting properties, namely:

$$\begin{aligned} \mathbf{R}(-\phi) &= \mathbf{R}(\pi - \phi) \\ \mathbf{R}(\phi_1)\mathbf{R}(\phi_2) &= \mathbf{R}(\phi_1 + \phi_2) \\ \mathbf{R}^{-1}(\phi) &= \mathbf{R}(-\phi) \end{aligned} \tag{11.36}$$

Several quantities that are of particular importance are the *degree of polarization*, $(Q^2 + U^2 + V^2)^{1/2}/I$; the *degree of linear polarization*, $(Q^2 + U^2)^{1/2}/I$; the *degree of circular polarization*, V/I; the *orientation* of the polarization ellipse, $\tan 2\chi = U/Q$; and the *ellipticity*, $\tan 2\beta = V/(Q^2 + U^2)^{1/2}$.

The Stokes parameters for polarized light can perhaps be best illustrated by use of diagrams, and some examples are given below:

Linear polarization:

0°	90°	+45°	−45°	γ
↔	↕	↘	↙	
$\begin{pmatrix} 1 \\ 1 \\ 0 \\ 0 \end{pmatrix}$	$\begin{pmatrix} 1 \\ -1 \\ 0 \\ 0 \end{pmatrix}$	$\begin{pmatrix} 1 \\ 0 \\ 1 \\ 0 \end{pmatrix}$	$\begin{pmatrix} 1 \\ 0 \\ -1 \\ 0 \end{pmatrix}$	$\begin{pmatrix} 1 \\ \cos 2\gamma \\ \sin 2\gamma \\ 0 \end{pmatrix}$

Circular polarization:

Right	*Left*
$\begin{pmatrix} 1 \\ 0 \\ 0 \\ 1 \end{pmatrix}$	$\begin{pmatrix} 1 \\ 0 \\ 0 \\ -1 \end{pmatrix}$

Unpolarized:

$$\begin{pmatrix} 1 \\ 0 \\ 0 \\ 0 \end{pmatrix}$$

Note that the sum of the squares of the last three elements in each matrix equals unity for polarized light. The fourth component defines right-handed (+) and left-handed (–) circular polarization. For unpolarized light, such as that from the sun, the last three elements are zero.

Measuring the Stokes parameters of a light field is quite easy, and we will now give the prescription for performing the measurements as schematically shown in Fig. 11-7.

I. No polarizer. This measurement will yield the first component, I, or the total radiance

$$I = E_l E_l^* + E_r E_r^* = |E_l|^2 + |E_r|^2 \tag{11.37}$$

It is this component that the human eye perceives

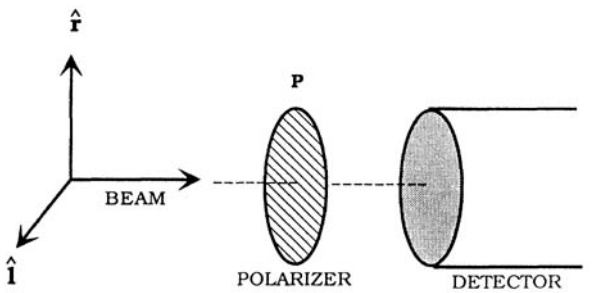

Fig. 11-7. Schematic of arrangement for measuring the Stokes vector of a light beam.

II. Horizontal and vertical polarizers.

1. Let P be a horizontal polarizer; then it will record

$$I_l = E_l E_l^* = |E_l|^2 \tag{11.38}$$

2. Let P be a vertical polarizer then it will record

$$I_l = E_r E_r^* = |E_r|^2 \tag{11.39}$$

Therefore the second component can be obtained as follows:

$$Q = I_l - I_r = E_l E_l^* - E_r E_r^* = |E_l|^2 - |E_r|^2 \tag{11.40}$$

III. +45° and -45° polarizers. To understand this measurement it is advantageous to introduce another set of orthonormal basis vectors; namely,

$$\hat{\mathbf{e}}_+ = \frac{1}{\sqrt{2}}(\hat{\mathbf{l}} + \hat{\mathbf{r}}) \qquad \hat{\mathbf{e}}_- = \frac{1}{\sqrt{2}}(\hat{\mathbf{l}} - \hat{\mathbf{r}}) \tag{11.41}$$

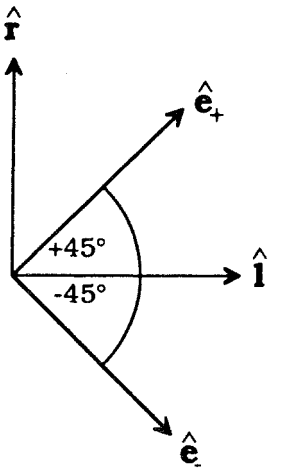

The electric field can be written as $\mathbf{E}_0 = \mathrm{E}_+\hat{\mathbf{e}}_+ + \mathrm{E}_-\hat{\mathbf{e}}_-$ where

$$E_+ = \frac{1}{\sqrt{2}}(E_l + E_r) \qquad E_- = \frac{1}{\sqrt{2}}(E_l - E_r) \tag{11.42}$$

1. Let P be a +45° polarizer.

$$I_+ = |E_+|^2 = \left|\frac{E_l + E_r}{\sqrt{2}}\right|^2 = \frac{(E_l E_l^* + E_l E_r^* + E_r E_l^* + E_r E_r^*)}{2} \tag{11.43}$$

2. Let P be a $-45°$ polarizer.

$$I_- = |E_-|^2 = \left|\frac{E_l - E_r}{\sqrt{2}}\right|^2 = \frac{(E_l E_l^* - E_l E_r^* - E_r E_l^* + E_r E_r^*)}{2} \tag{11.44}$$

then

$$I_+ - I_- = E_l E_r^* + E_r E_l^* \tag{11.45}$$

which gives the third Stokes parameter.

IV. Circular Polarizers. This measurement can best be described by the introduction of a set of complex basis vectors, namely:

$$\hat{\mathbf{e}}_R = \frac{1}{\sqrt{2}}(\hat{\mathbf{l}} + i\hat{\mathbf{r}}) \qquad \hat{\mathbf{e}}_L = \frac{1}{\sqrt{2}}(\hat{\mathbf{l}} - i\hat{\mathbf{r}}) \tag{11.46}$$

These basis vectors represent *right circularly* and *left circularly* polarized waves and are orthonormal in the sense that

$$\hat{\mathbf{e}}_R \cdot \hat{\mathbf{e}}_R^* = 1, \qquad \hat{\mathbf{e}}_L \cdot \hat{\mathbf{e}}_L^* = 1, \qquad \hat{\mathbf{e}}_L \cdot \hat{\mathbf{e}}_R^* = 0 \tag{11.47}$$

The incident field may be written as $\mathbf{E}_0 = \mathrm{E_R}\hat{\mathbf{e}}_R + \mathrm{E_L}\hat{\mathbf{e}}_L$ where

$$E_R = \frac{1}{\sqrt{2}}(E_l - iE_r) \qquad E_L = \frac{1}{\sqrt{2}}(E_l + iE_r) \tag{11.48}$$

1. Let P be a right-handed polarizer; then

$$I_R = |E_R|^2 = \frac{(E_l E_l^* + iE_l E_r^* - iE_r E_l^* + E_r E_r^*)}{2} \tag{11.49}$$

2. Let P be a left-handed polarizer; then

$$I_L = |E_L|^2 = \frac{(E_l E_l^* - iE_l E_r^* + iE_r E_l^* + E_r E_r^*)}{2} \tag{11.50}$$

Therefore

$$I_R - I_L = i(E_l E_r^* - E_r E_l^*) \tag{11.51}$$

which gives the fourth Stokes parameter. We now see that the measurements just described can, in principle, yield the four Stokes parameters.

Mueller Matrices

Now that we have the means to calculate the complete Stokes vector, we need next to ask about the nature of the 4 × 4 matrix that takes an incident Stokes vector that interacts with some optical element and gets transformed into another Stokes vector. This matrix is called the Mueller matrix (Mueller, 1948). It gives essentially *all* the optical information possible about a system where an *elastic* interaction has occurred. We will not go into the theory of Mueller matrices but will refer the reader to the book by Shurcliff (1962).

We will give some examples of Mueller matrices for some typical optical elements.

Ideal Linear Polarizer.

$$\begin{bmatrix} I_t \\ Q_t \\ U_t \\ V_t \end{bmatrix} = \begin{bmatrix} 1 & \cos 2\xi & \sin 2\xi & 0 \\ \cos 2\xi & \cos^2 2\xi & \cos 2\xi \sin 2\xi & 0 \\ \sin 2\xi & \cos 2\xi \sin 2\xi & \sin^2 2\xi & 0 \\ 0 & 0 & 0 & 0 \end{bmatrix} \begin{bmatrix} I_i \\ Q_i \\ U_i \\ V_i \end{bmatrix} \tag{11.52}$$

Where ξ is the smallest angle between $\hat{\mathbf{l}}$ and the transmission axis. The irradiance transmitted by the linear polarizer is

$$I_t = \frac{1}{2}(I_i + Q_i \cos 2\xi + U_i \sin 2\xi) \tag{11.53}$$

The maximum and minimum values of I_t occur for $\xi = \gamma$ and $\xi = \gamma + \pi/2$, where $\tan 2\gamma = U_i/Q_i$; therefore

$$\begin{aligned} I_{max} &= \frac{1}{2}(I_i + Q_i \cos 2\gamma + U_i \sin 2\gamma) \\ I_{min} &= \frac{1}{2}(I_i - Q_i \cos 2\gamma - U_i \sin 2\gamma) \end{aligned} \tag{11.54}$$

$$\frac{I_{max} - I_{min}}{I_{max} + I_{min}} = \frac{\sqrt{Q_i^2 + U_i^2}}{I_i}$$

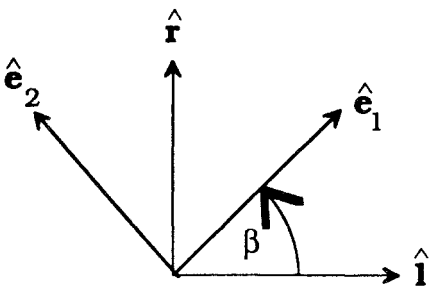

Ideal linear retarder

Ideal linear retarder. An ideal linear retarder divides a given incident electric vector into two linearly polarized components e_1 and e_2, which are mutually orthogonal, and introduces a phase difference (or retardance) $\delta = \delta_1 - \delta_2$:

$$\begin{bmatrix} 1 & 0 & 0 & 0 \\ 0 & C^2 + S^2 \cos\delta & SC(1 - \cos\delta) & -S \sin\delta \\ 0 & SC(1 - \cos\delta) & S^2 + C^2 \cos\delta & C \sin\delta \\ 0 & S \sin\delta & -C \sin\delta & \cos\delta \end{bmatrix} \tag{11.55}$$

where $C = \cos 2\beta$ and $S = \sin 2\beta$.

Now let us consider how we might create a *circular* polarized beam from an *unpolarized* beam. If we place a linear polarizer with horizontal transmission axis ($\xi = 0°$), and a quarter-wave retarder ($\delta = 90°$) in that order in the path of the unpolarized light beam, we can calculate the combined effect of the combination by multiplying their respective Mueller matrices in the correct order. First the Mueller matrix for the linear polarizer can be written as

$$\frac{1}{2}\begin{bmatrix} 1 & 1 & 0 & 0 \\ 1 & 1 & 0 & 0 \\ 0 & 0 & 0 & 0 \\ 0 & 0 & 0 & 0 \end{bmatrix} \tag{11.56}$$

The transmitted beam is then incident on a retarder with $\delta = 90°$ and $\beta = 45°$, which gives the Mueller matrix:

$$\begin{bmatrix} 1 & 0 & 0 & 0 \\ 0 & 0 & 0 & -1 \\ 0 & 0 & 1 & 0 \\ 0 & 1 & 0 & 0 \end{bmatrix} \tag{11.57}$$

The combined effect of polarizer and retarder is obtained by matrix multiplication:

$$\frac{1}{2}\begin{bmatrix} 1 & 0 & 0 & 0 \\ 0 & 0 & 0 & -1 \\ 0 & 0 & 1 & 0 \\ 0 & 1 & 0 & 0 \end{bmatrix}\begin{bmatrix} 1 & 1 & 0 & 0 \\ 1 & 1 & 0 & 0 \\ 0 & 0 & 0 & 0 \\ 0 & 0 & 0 & 0 \end{bmatrix} = \frac{1}{2}\begin{bmatrix} 1 & 1 & 0 & 0 \\ 0 & 0 & 0 & 0 \\ 0 & 0 & 0 & 0 \\ 1 & 1 & 0 & 0 \end{bmatrix} \tag{11.58}$$

Thus if *unpolarized* light is incident on the system we get

$$\begin{bmatrix} 1 & 1 & 0 & 0 \\ 0 & 0 & 0 & 0 \\ 0 & 0 & 0 & 0 \\ 1 & 1 & 0 & 0 \end{bmatrix} \begin{bmatrix} 1 \\ 0 \\ 0 \\ 0 \end{bmatrix} = \begin{bmatrix} 1 \\ 0 \\ 0 \\ 1 \end{bmatrix} = \text{right circular polarization} \quad (11.59)$$

Since the Mueller matrix is always specified with respect to a particular frame of reference, we must be able to transform from the meridian plane to the frame for which the Mueller matrix is referenced. To see how this is done let us again refer to Fig. 11-4, The incident Stokes vector $\mathbf{I}_i$ and the z axis determine the initial meridian plane where the $\mathbf{l}$ and $\mathbf{r}$ directions are shown and the direction of propagation is given by $\mathbf{r} \times \mathbf{l}$. The initial Stokes vector first has to be rotated *counterclockwise* by the angle Φ, which will reference it to the scattering plane, and then it can be be acted upon by the Mueller matrix $\mathbf{L}(\Theta,\Phi)$. To put it back into the final meridian plane we must rotate it *counterclockwise* by the angle Ψ which will place the final Stokes vector in the proper reference frame for the next interaction. Symbolically this sequence is represented as

$$\mathbf{I}_f = \mathbf{R}(-\Psi)\mathbf{L}(\Theta,\Phi)\mathbf{R}(-\Phi)\mathbf{I}_i \quad (11.60)$$

We will now consider the various Mueller matrices that enter the scattering process. If one is doing either atmospheric or oceanic radiative transfer then one is certain to encounter the Mueller matrix associated with Rayleigh scattering. We will only present it and defer the Mie theory Mueller matrix to a later study. The Mueller matrix for Rayleigh scattering is

$$\mathbf{L}(\Theta,\Phi) = \begin{bmatrix} \frac{1+\mu^2}{2} & \frac{\mu^2-1}{2} & 0 & 0 \\ \frac{\mu^2-1}{2} & \frac{1+\mu^2}{2} & 0 & 0 \\ 0 & 0 & \mu & 0 \\ 0 & 0 & 0 & \mu \end{bmatrix} \quad (11.61)$$

where $\mu = \cos\Theta$ and Θ is the scattering angle. There are several interesting features of this matrix. First we see that it possesses the well-known phenomenon of complete linear polarization at 90° scattering angle. Secondly, there can be *no* ellipticity in the multiply scattered radiation if the source is unpolarized. Therefore, any ellipticity appearing in the results can only be due to the dielectric interface, which we will prove shortly.

The reflection (R_{AM}) and transmission (T_{AM}) Mueller matrices for radiation going from *air* into a *medium* have been derived from first principles and are as follows (Kattawar and Adams, 1989):

$$R_{AM} = \begin{bmatrix} \alpha + \eta & \alpha - \eta & 0 & 0 \\ \alpha - \eta & \alpha + \eta & 0 & 0 \\ 0 & 0 & \gamma_{Re} & 0 \\ 0 & 0 & 0 & \gamma_{Re} \end{bmatrix} \quad T_{AM} = \begin{bmatrix} \alpha' + \eta' & \alpha' - \eta' & 0 & 0 \\ \alpha' - \eta' & \alpha' + \eta' & 0 & 0 \\ 0 & 0 & \gamma'_{Re} & 0 \\ 0 & 0 & 0 & \gamma'_{Re} \end{bmatrix} \tag{11.62}$$

where

$$\alpha = \frac{1}{2}\left[\frac{\tan(\theta_i - \theta_t)}{\tan(\theta_i + \theta_t)}\right]^2 \quad \eta = \frac{1}{2}\left[\frac{\sin(\theta_i - \theta_t)}{\sin(\theta_i + \theta_t)}\right]^2$$

$$\gamma_{Re} = \frac{\tan(\theta_i - \theta_t)\sin(\theta_i - \theta_t)}{\tan(\theta_i + \theta_t)\sin(\theta_i + \theta_t)} \tag{11.63}$$

and

$$\alpha' = \frac{1}{2}\left[\frac{2\sin\theta_t \cos\theta_i}{\sin(\theta_i + \theta_t)\cos(\theta_i - \theta_t)}\right]^2 \quad \eta' = \frac{1}{2}\left[\frac{2\sin\theta_t \cos\theta_i}{\sin(\theta_i + \theta_t)}\right]^2$$

$$\gamma'_{Re} = \frac{4\sin^2\theta_t \cos^2\theta_i}{\sin^2(\theta_i + \theta_t)\cos(\theta_i - \theta_t)} \tag{11.64}$$

where θ_i and θ_t refer to the incident and transmitted angles, respectively, and are related by Snell's law; namely, $\sin\theta_i = n\sin\theta_t$ where n is the refractive index of the *medium* relative to *air*. The Brewster angle, defined by $\theta_B^{AM} = \tan^{-1} n$, is the angle at which incoming unpolarized radiation will become *completely linearly* polarized upon reflection.

In going from a medium into air, as long as $\theta < \theta_{crit}$, (θ_{crit} is the critical angle or $\theta_{crit} = \sin^{-1}\bar{n}$ where $\bar{n}$ is the refractive index of air relative to the medium, i.e., $\bar{n} = 1/n$) we can still use Eqs. (11.62), (11.63), and (11.64) to compute both R_{MA} and T_{MA}; namely,

$$R_{MA} = \begin{bmatrix} \alpha + \eta & \alpha - \eta & 0 & 0 \\ \alpha - \eta & \alpha + \eta & 0 & 0 \\ 0 & 0 & \gamma_{Re} & -\gamma_{im} \\ 0 & 0 & \gamma_{im} & \gamma_{Re} \end{bmatrix} \quad T_{MA} = \begin{bmatrix} \alpha' + \eta' & \alpha' - \eta' & 0 & 0 \\ \alpha' - \eta' & \alpha' + \eta' & 0 & 0 \\ 0 & 0 & \gamma'_{Re} & -\gamma'_{Im} \\ 0 & 0 & \gamma'_{im} & \gamma'_{Re} \end{bmatrix} \tag{11.65}$$

where for this region $\gamma_{im} = \gamma_{im}' = 0$. However, for the region where $\theta > \theta_{crit}$ which is the region where total internal reflection takes place, θ_t becomes complex, T_{MA} becomes the null matrix and the following equations must be used to compute R_{MA}.

$$\alpha = \frac{1}{2}\left|\frac{\bar{n}^2\cos\theta_i - i\sqrt{\sin^2\theta_i - \bar{n}^2}}{\bar{n}^2\cos\theta_i + i\sqrt{\sin^2\theta_i - \bar{n}^2}}\right|^2$$

$$\eta = \frac{1}{2}\left|\frac{\cos\theta_i - i\sqrt{\sin^2\theta_i - \bar{n}^2}}{\cos\theta_i + i\sqrt{\sin^2\theta_i - \bar{n}^2}}\right|^2 \tag{11.66}$$

$$\gamma_{im} = \mathrm{Im}\left(\left[\frac{\bar{n}^2\cos\theta_i + i\sqrt{\sin^2\theta_i - \bar{n}^2}}{\bar{n}^2\cos\theta_i - i\sqrt{\sin^2\theta_i - \bar{n}^2}}\right]\left[\frac{\cos\theta_i - i\sqrt{\sin^2\theta_i - \bar{n}^2}}{\cos\theta_i + i\sqrt{\sin^2\theta_i - \bar{n}^2}}\right]\right) \tag{11.67}$$

$$\gamma_{Re} = \mathrm{Re}\left(\left[\frac{\bar{n}^2\cos\theta_i + i\sqrt{\sin^2\theta_i - \bar{n}^2}}{\bar{n}^2\cos\theta_i - i\sqrt{\sin^2\theta_i - \bar{n}^2}}\right]\left[\frac{\cos\theta_i - i\sqrt{\sin^2\theta_i - \bar{n}^2}}{\cos\theta_i + i\sqrt{\sin^2\theta_i - \bar{n}^2}}\right]\right) \tag{11.68}$$

where now $\theta_i > \theta_{crit}$. The corresponding Brewster angle in going from *medium* into *air* is defined by $\theta_B^{MA} = \tan^{-1}\bar{n}$.

Before one can theoretically calculate the polarization of the submarine radiance fields (see Kattawar, et al., 1973, 1988; Kattawar and Adams, 1989), the Mueller matrix for ocean water must be obtained. The first measurement of the Mueller matrix for ocean water samples was performed by Beardsley (1968). He found a great deal of symmetry in the matrices he measured from disparate sources, and the normalized matrix element values were similar to those for a normalized matrix derived for Rayleigh scattering (which we presented earlier). Subsequent measurements made by Soviet scientists (Kadyshevich, 1977; Kadyshevich et al., 1971, 1976) suggested much larger variations in the Mueller matrix as a function of depth and location.

To elucidate this apparent discrepancy, Voss and Fry (1984) made Mueller matrix measurements in the Atlantic, Pacific, and Gulf of Mexico. Their results varied little from site-to-site and confirmed Beardsley's Rayleigh functionality for the matrices. In this depiction (Fig. 11-8), each of the Mueller matrix elements is shown for angles from 10° to 160°. Note the similarity of the elements for the average of the ocean values to those for a Rayleigh scattering simulation.

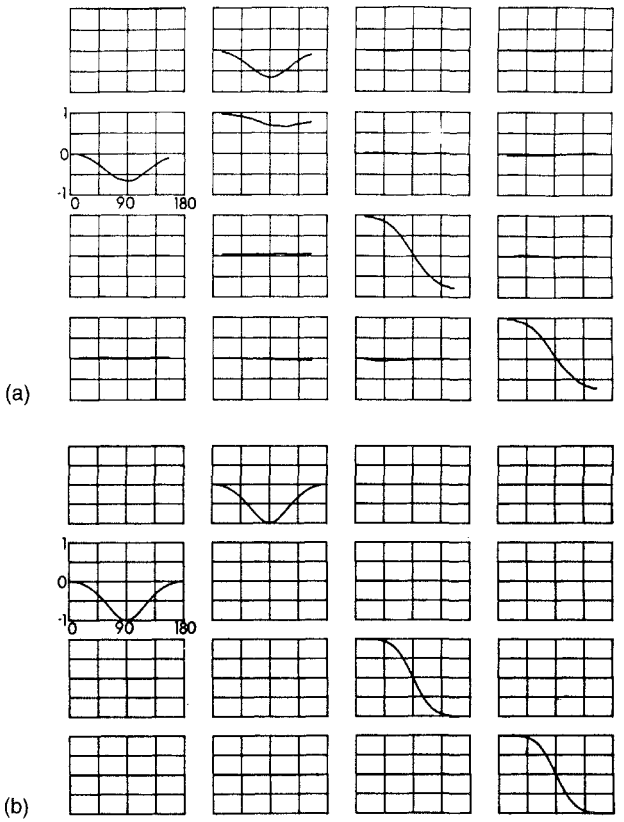

Fig. 11-8. (a) The average 4 × 4 Mueller matrix of the Pacific and Atlantic Oceans. Each graph corresponds to a matrix element labeled in regular matrix order. The abscissa of each graph corresponds to the scattering angle in degrees and the ordinate corresponds to the normalized matrix element value. (b) Calculated Mueller matrix for Rayleigh scattering. (From Voss and Fry, 1984)

From comparisons between modeled and measured matrix values it became immediately evident that the particulates could not be spherical. The reason for this is that the *normalized* Mueller matrix element S_{22} was *not* unity, and for *any* spherical polydispersion it is *always* unity. Using a set of inequalities for the Mueller matrix derived by Fry and Kattawar (1981), Voss was able to obtain a fairly good fit using a polydispersion of spheres with a single refractive index while keeping the S_{22} element in agreement with the measurements.

The zero values in the upper and lower 2 × 2 submatrices indicate little if any optical activity in the samples; however, this is not to suggest that highly concentrated phytoplankton samples would not demonstrate optical activity. Certainly amino acids and sugars have a "handedness," or chirality, and therefore when they are associated with the pigments in the cells they will induce a certain degree of optical activity (Houssier and Sauer, 1970) Also, Pospergelis (1969)

has measured the ratio of *V/I* for the Stokes vector of light reflected from green leaves and found it to be of the order of a few percent. In the low concentrations observed in the open oceans, however, measurement accuracies of one part in 10^4 are required for these effects to be observed.

For modeling polarization in the oceans, Voss' polarimetry measurements can be used to correct volume scattering functions for polarization effects. For concentrated plankton samples, optical activity may yet play a role in quickly assessing the variation of productivity, storage products, and/or total amino acids as a function of species, time of day, and nutrient availability. The task is to measure the Mueller matrix with more accuracy and on a wider variety of ocean particulates.

12

RAMAN SCATTERING AND OPTICAL PROPERTIES OF PURE WATER

Raymond C. Smith and Bruce R. Marshall
University of California at Santa Barbara

Pure water

There are numerous observations of the spectral attenuation, absorption, and scattering of distilled water and seawater. Morel (1974) reviewed the literature with respect to the attenuation coefficient as a function of wavelength and published his seawater and distilled water scattering coefficients. Smith and Baker (1978b) critically reviewed measurements made by many investigators to estimate the relative accuracies in the published values for the total absorption coefficient and the diffuse attenuation coefficient, and found a large range. Early workers frequently did not make a careful distinction between the absorption coefficient, the diffuse attenuation coefficient, and the total beam attenuation coefficient. Preisendorfer (1976) derived a set of inequalities linking the total beam attenuation coefficient, the diffuse attenuation coefficient, the forward scattering coefficient, the average cosine, the backscattering coefficient, and the absorption coefficient. This treatment allows us to define the theoretical bounds for the inherent and apparent optical properties of optically pure water. Morel (1974) defined optically pure water as a medium devoid of dissolved and suspended material. Thus, optically pure water is a medium for which particle backscattering, particle absorption, and the absorption due to dissolved organic material are zero, so the attenuation due to the water is the absorption due to water plus molecular scattering; that is,

$$c_w = a_w + b_m \tag{12.1}$$

Using the relationship (Preisendorfer, 1976)

$$c \approx K + b_b > K = \frac{a}{\bar{\mu}} + b_b > a + b_b > a \tag{12.2}$$

one can derive an inequality for the fresh water diffuse attenuation coefficient, establishing the following limitation (in the absence of transpectral scattering):

$$K_w^{\mathrm{fw}} \geq a_w + \tfrac{1}{2}\, b_m^{\mathrm{fw}} \tag{12.3}$$

where one-half the molecular scattering is included since molecular scattering is isotropic. The diffuse attenuation coefficient given by Eq. (12.3) represents the lowest experimental value one could expect to encounter in natural fresh water based on laboratory measurements of a_w. Conversely, given K_w^{fw} values from clear natural waters, Eq. (12.3) represents an upper bound for the absorption by pure water.

In order to make accurate determinations of the absorption by pure water, the experimental conditions must be optimized. The relative error in the absorption coefficient is related to the photometric error in the measurement of the transmitted beam. It can be shown (Smith and Tyler, 1976) that the optimum pathlength associated with any measurement is essentially the reciprocal of the absorption coefficient (see also Chapter 7). For measurements of clear water (with an absorption coefficient of approximately $0.02\,\mathrm{m}^{-1}$), the optimum path length is roughly 50 meters. Most measurements of the absorption of pure water have historically been made with a centimeter-sized cuvettes, and are therefore three orders of magnitude nonoptimum. An advantage of field observations is that with irradiance meters at depth one can measure the diffuse attenuation coefficient over pathlengths of 50 meters or more. Smith and Baker (1981) used measurements of irradiance in the open ocean and Crater Lake to derive best estimates of pure water absorption and scattering. The estimated relative errors from this approach were approximately +25% to −5% between 380 and 480 nm, and +10% to −15% from 480 to 600 nm. The optical properties of pure water play a central role in hydrological optics and an increase in our knowledge of the absorption and the attenuation of pure water to a much higher accuracy is important, since this is essentially the optical oceanographer's blank.

Raman

Energy transfer associated with light scattering spans a wide range. Chu (1970) has shown that energy transfer can take place over approximately 14 orders of magnitude in the scattering process while there is relatively little momentum exchange. Scattering can produce changes in intensity, direction, polarization, or frequency. Frequency shifts are associated with energy transfer and changes in coherence.

Rayleigh scattering is molecular scattering that is not associated with a significant frequency shift. In the case of Rayleigh scattering the frequency shift is typically less than $10^{-6}\,\mathrm{cm}^{-1}$, and as small as $10^{-11}\,\mathrm{cm}^{-1}$. So, while we tend to think that a Rayleigh-scattered photon comes in and goes out at the same wavelength, there may be an energy transfer characterized by a frequency shift of roughly six orders of magnitude although the amount of energy involved is

very small and produces less than one millionth of a nanometer frequency shift.

A very slight, but more significant frequency shift (of order $0.2\,cm^{-1}$, corresponding to a wavelength shift of about 0.005 nm for blue-green light) is the characteristic feature of Brillouin scattering and a frequency shift of $1000\,cm^{-1}$ (about 25 nm) is characteristic of Raman scattering. Peticolas (1972) has shown that, while we tend to think about these types of scattering as separate processes, they are really a continuum of processes that differ in the energy exchange process. In addition several optical techniques are required to cover the 14 orders of magnitude of energy transfer spanned by these scattering processes. One might measure Rayleigh scattering with frequency mixing or correlation counting techniques to assess diffusion constants or autocorrelation functions. For Brillouin scattering one uses a Fabry–Perot interferometer to measure sound velocities and dispersion, bulk loss, and storage moduli. Raman scattering can be measured with a double monochromator.

The measured cross-section

The value of the Raman scattering cross-section has been highly debated. Table 12-1 shows the range of values obtained by several investigators. Many investigators performed the measurements in an unpolarized context and may have obtained erroneous values as a result. Marshall and Smith (1990) obtained values in agreement with Romanov and Shuklin (1975) and Chang and Young (1972). In the case of Marshall and Smith (1990), the Raman scattering cross-section for water was calibrated against benzene since the Raman scattering cross section for benzene is well established. Corroboration of these values was found when the experimentally derived values were used in the model described below. The high values in Table 12-1, when used in the model, do not reproduce our field observations. There is yet another independent set of evidence for the low value. Petzold (personal communication) did some very careful work in characterizing a field-deployed underwater radiometer. After verifying that light leakage was not an important factor, it was concluded that a spectral energy shift was taking place in the water. The empirically derived transfer function, which

Table 12-I. The Raman scattering cross-section as obtained by several investigators

Cross-section (cm^2 $molecule^{-1}$ sr^{-1})	Reference
8.6×10^{-30}	Chang and Young (1972)
$(8.1 \pm 0.7) \times 10^{-30}$	Romanov and Shuklin (1975)
$(4.5 \pm 0.3) \times 10^{-29}$	Slusher and Derr (1975)
$(9.0 \pm 2) \times 10^{-30}$	Kondilenko et al. (1977)
2×10^{-29}	Sugihara et al. (1984)
$(8.2 \pm 1) \times 10^{-30}$	This study

we now recognize as the Raman cross-section was not unlike the values obtained by Marshall and Smith (1990)

What are the specific mechanisms and processes that define Raman scattering? Peticolas (1972) used a classical theory of light scattering to explain Raman scattering as a quantum phenomenon. Raman scattering is produced by the water molecules and as such it is a volume characteristic of the water. While Rayleigh scattering is recognized as a dipole radiation pattern, Raman scattering is more depolarized and is therefore somewhat more isotropic in terms of its angular distribution.

Much of the work done with Raman scattering has been aimed at understanding the geometrical structure of the water molecule (e.g., Walrafen, 1964). The water molecule may be modeled as a dipole radiator. However, it is not a simple dipole. The molecule has body and structure, with an axis that has some kind of rotational symmetry and modes of vibration that can stretch and oscillate. Consider an induced electric dipole moment, p_i, in the ith direction (where $i = x$, y, or z), with incident light, E, polarized in the jth direction (again x, y, or z), so that there is a nine-component polarizability tensor, α_{ij}, that depends on the geometry of the molecule:

$$p_i = \sum_j \alpha_{ij} E_j \tag{12.4}$$

In Eq. (12.4), elastic and quasi-elastic light scattering occur when the polarization is proportional to the applied field and the induced oscillating dipole acts as a source of secondary radiation with the same frequency as the incident light (i.e., α_{ij} is a simple constant). If that polarization is not strictly a constant but varies periodically, that is,

$$\frac{\partial \alpha_{ij}}{\partial Q_a} \neq 0 \tag{12.5}$$

where ∂Q_a is a displacement of a normal coordinate for the a^{th} vibration, then one can write an equation that shows that the polarizability is

$$\alpha_{ij} = \alpha_{ij}^0 + \left(\frac{\partial \alpha_{ij}}{\partial Q_a} \right)_0 Q_a \tag{12.6}$$

where α_{ij}^0 is the polarizability at equilibrium position $Q_a = 0$, and one can express the incoming radiation, E_j, by

$$E_j = E_j^0 \cos \omega_L t \qquad \omega_L = 2\pi \nu_L \tag{12.7}$$

ω_L is the circular frequency of the incident light and ν_L is the linear frequency of the incident light. We can also write

$$Q_a = Q_a^0 \cos \Omega_a \bullet t \tag{12.8}$$

with Q_a^0 = the maximum amplitude of the displacement of the normal coordinate and Ω_a = the circular frequency of the molecular vibration. These equations include two vibrational frequencies now. Combining the above gives:

$$p_i = \sum_j \alpha_{ij}^0 E_j^0 \cos \omega_L t + \frac{1}{2} \sum_j \left(\frac{\partial \alpha_{ij}}{\partial Q_a} \right)_0 Q_a^0 E_j^0 \{ \cos(\omega_L + \Omega_a)t + \cos(\omega_L - \Omega_a)t \} \tag{12.9}$$

which yields the polarizability again in terms of α_{ij}. The first term on the right-hand side of Eq. (12.9) is the description of elastic scattering. The second term gives rise to scattering at two frequencies. The term includes the sum of the light frequency decreased by the vibrational frequency of the molecule, plus light frequency increased by the frequency of the molecule. These give rise to the Stokes line and the anti-Stokes lines:

$$\begin{aligned} (\omega_L - \Omega_a) &\rightarrow \text{Stokes} \\ (\omega_L + \Omega_a) &\rightarrow \text{anti-Stokes} \end{aligned} \tag{12.10}$$

This defines the mechanism by which the water molecule can rotate and vibrate in such a manner that incoming photons emerge not only at roughly the same frequency but also with a frequency shift on either side. For statistical quantum-mechanical reasons, the anti-Stokes lines are frequently much smaller than the Stokes line. This process serves to define a nine-component tensor called the Raman tensor:

$$\left(\frac{\partial \alpha_{ij}}{\partial Q_a} \right) \tag{12.11}$$

This series of equations describes a conceptual picture of how Raman scattering arises. Basically it occurs because the water molecule has a structure that has rotational and vibrational modes that can be excited by the incoming radiation and can exchange energy with it. This same set of equations can also be used to give a conceptual outline for how Brillouin scattering arises. There are vibrational modes characteristic of the liquid as a whole. These vibrational modes are characteristic of the velocity of sound at the incoming frequency. That velocity of sound defines the oscillation of the liquid as a whole, and an analogous set of equations can be developed for the additive frequency shifts as a result of these oscillations as well.

One can also explore the Raman scattering phenomenon from a quantum-mechanical standpoint. Consider a molecule having a series of energy states, and a photon impinging with an incident frequency. This interaction will raise the molecule to some intermediate state. It can then go through a Raman transition down to a lower state, and a photon is emitted at a frequency representative of the difference between the two energy states. A similar but reverse process

occurs for the anti-Stokes emission. For Rayleigh scattering the incident frequency and the scattered frequency are the same; the wavelength in and the wavelength out remain the same.

In summary, these light scattering processes form a continuum that spans at least 14 orders of magnitude. The regions of interest are dictated by the kinds of instruments that are used for observation. For pure fresh water Rayleigh scattering of 490 nm light has a magnitude of $2.4 \times 10^{-3}\,m^{-1}$ (the value for seawater is slightly higher, $3.1 \times 10^{-3}\,m^{-1}$). The depolarization ratio and the polarization defect term are given, respectively, by

$$\rho_j = 0.047 \qquad \delta = \frac{2\rho_j}{1 + \rho_j} = 0.09 \tag{12.12}$$

Morel (1974) has shown that the total scattering has a $\lambda^{-4.3}$ spectral dependence. Raman scattering is incoherent, but the scattering phase function is similar in shape to that of Rayleigh scattering. For Rayleigh scattering in water the angular distribution is given by

$$\beta(\theta) = \beta(90°)(1 + 0.835\cos^2\theta) \tag{12.13}$$

and for Raman (again, with excitation at 490 nm), the distribution is

$$\beta(\theta) = \beta(90°)(1 + 0.55\cos^2\theta) \tag{12.14}$$

and this distribution is excitation wavelength dependent. The intensity of the Raman scattering is almost an order of magnitude less than the Rayleigh scattering: $2.5 \times 10^{-4}\ m^{-1}$, for fresh water. The Raman depolarization ratio is greater (0.17) and so the polarization defect term is also larger (0.29). The total Raman scattering is proportional to the *emission* wavelength raised to the -4 power, or the excitation wavelength raised to the -4.77 power.

Modeling the ocean environment

Some observers have noted that measurements of ocean optical properties (e.g., diffuse attenuation coefficients) have given anomalous results for years: diffuse attenuation coefficients that are lower than those of pure water, or extremely large values for the diffuse irradiance reflectance. There are a host of instrumentation problems that can give this same kind of an effect: light leakage, for example, wherein an instrument designed to measure red light inadequately blocks all blue light. We now hypothesize that these anomalies can be explained by Raman scattering. The simple picture of Raman scattering by water is that some energy is transferred to a vibrational or rotational state of the molecule, with a resultant frequency shift of $3400\,cm^{-1}$ (corresponding to a wavelength shift from 488 nm to 589 nm).

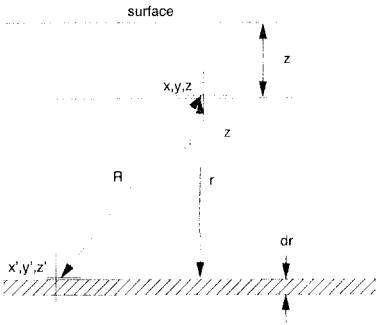

Fig. 12-1. Calculation of the effective absorption coefficient for irradiance produced by a thin layer of Raman scatterers at a distance r in a pure absorbing medium.

A two-flow radiative transfer theory has been developed to include the hypothesis of Raman scattering. From this model attenuation and reflectance values could be predicted for the molecular (i.e., Raman) component and compared with in situ data. A complicating factor in this modeling effort is the role played by inelastic scattering in the form of fluorescence. Fluorescence from organic molecules can produce competing effects. To avoid this, only data from the clearest water was used (as corroborated by near zero values of fluorescence).

An important aspect of the Raman model is the determination of an effective absorption coefficient for irradiance produced by a thin layer of molecular scatterers (this model is independent of particulate absorption and scattering). Consider a layer of scatterers that are absorbing at the excitation wavelength and emitting at the Raman wavelength (Fig. 12-1). By integrating over the entire plane one can determine the Raman irradiance originating in this layer that arrives at a point at depth z. Consider a system having an excitation wavelength at 488 nm (λ'), and an emission wavelength at 589 nm (λ) and Raman radiation from a source at (x', y', z') arrives at (x, y, z), so that the radiance due to Raman scattering is

$$L^{\text{Raman}}(r,\theta) = E_0(\lambda',z + r)\,\beta_r(\theta)\,e^{-aR} \tag{12.15}$$

where $E_0(\lambda',z + r)$ is the scalar irradiance at the excitation wavelength, λ', and depth $(z + r)$, and $\beta_r(\theta) = \beta_r(90°)\,(1 + A\cos^2\theta)$ is the phase function for Raman scattering ($A = 0.55$); a is the absorption coefficient at emission wavelength, λ; $R = r/(\cos\theta)$ is the distance from (x', y', z') to (x, y, z) and $b_r = \int_{4\pi} \beta_r(\theta)\,\partial\omega$ is the total Raman scattering coefficient.

The upward irradiance is then obtained by integrating over the entire plane:

$$E_u^{\text{Raman}}(\lambda,r,z) = \int_{2\pi} E_0(\lambda',z + r)\,\beta_r(\theta)\,e^{-aR}\cos\theta\,\partial\omega \tag{12.16}$$

Further manipulation yields

$$E_u^{\text{Raman}}(\lambda,r,z) \approx E_0(\lambda',z+r)\,\frac{b_r}{2}\,\frac{1}{2}\,e^{-a^*r} \tag{12.17}$$

where the total Raman scattering coefficient is divided by 2, a factor that is effectively the average cosine through the diffuse Raman radiation. In addition, it can be shown that the effective absorption coefficient, a^*, for the Raman vector irradiance, can be approximated by

$$a^* = 1.5a \tag{12.18}$$

The next step in the theory is the creation a two-stream model. This requires that the Raman irradiance be separated from the solar irradiance. For downwelling and upwelling irradiance, respectively, this can be expressed as

$$E_d(\lambda,z) = E_d^{\text{solar}}(\lambda,z) + E_d^{\text{Raman}}(\lambda,z)$$

and (12.19)

$$E_u(\lambda,z) = E_u^{\text{solar}}(\lambda,z) + E_u^{\text{Raman}}(\lambda,z)$$

Additional parameters are defined as: μ_r = the average cosine for Raman scattering process; D = the distribution function for solar irradiance (see Chapter 1); $K(\lambda,z)$ = diffuse attenuation coefficient for the solar irradiance at λ; $K^*(\lambda,z)$ = effective diffuse attenuation coefficient for the Raman irradiance at λ. Optical depths can be derived as follows

$$\tau(z) = \int_0^z K(\lambda,z)\,dz$$

$$\tau^*(z) = \int_0^z K^*(\lambda,z)\,dz \tag{12.20}$$

where $\tau(z)$ is the optical depth from the surface to depth z for solar irradiance and $\tau^*(z)$ is the optical depth from the surface to depth z for Raman irradiance.

From these equations one can develop a set of radiative transfer equations which include Raman scattering:

$$\begin{aligned}\frac{E_d(\lambda,z+dz) - E_d(\lambda,z)}{dz} &= -(aD + b_b)E_d^{\text{solar}}(\lambda,z) + b_bE_u^{\text{solar}}(\lambda,z)\\ &\quad -(a^* + b_b)E_d^{\text{Raman}}(\lambda,z) + b_bE_u^{\text{Raman}}(\lambda,z)\\ &\quad + \frac{\mu_r b_r}{2}E_0(\lambda',z)\end{aligned} \tag{12.21}$$

and, the corresponding equation for E_u is

$$\frac{E_u(\lambda,z+dz)-E_u(\lambda,z)}{dz} = -(aD+b_b)E_u^{\text{solar}}(\lambda,z)+b_bE_d^{\text{solar}}(\lambda,z) -(a^*+b_b)E_u^{\text{Raman}}(\lambda,z)+b_bE_d^{\text{Raman}}(\lambda,z) +\frac{\mu_r b_r}{2}E_0(\lambda',z) \tag{12.22}$$

The total upward irradiance is the sum of the upward Raman and the upward-reflected direct solar light:

$$E_u(\lambda,z) = E_u^{\text{solar}}(\lambda,z)+E_u^{\text{Raman}}(\lambda,z) = E_u^{\text{solar}}(\lambda,0)e^{-Kz}+\frac{b_r}{4}E_0(\lambda',0)\left\{G_+^*\frac{e^{-K'z}}{K^*+K'}+G_-^*\frac{e^{-K'z}-e^{-K^*z}}{K^*-K'}\right\} \tag{12.23}$$

The total downward irradiance is similar:

$$E_d(\lambda,z) = E_d^{\text{solar}}(\lambda,z)+E_d^{\text{Raman}}(\lambda,z) = E_d^{\text{solar}}(\lambda,0)e^{-Kz}+\frac{b_r}{4}E_0(\lambda',0)\left\{G_-^*\frac{e^{-K'z}}{K^*+K'}+G_+^*\frac{e^{-K'z}-e^{-K^*z}}{K^*-K'}\right\} \tag{12.24}$$

where

$$G_-^* = \frac{b_b}{2aD^*} \qquad G_+^* = 1+\frac{b_b}{2aD^*} \approx 1 \tag{12.25}$$

These irradiance values can then be used to compute the reflectance functions. The diffuse reflectance for a homogeneous water column, as a function of depth, is derived as follows. Let

$$R_0 = \frac{E_u^{\text{solar}}(\lambda,z)}{E_d^{\text{solar}}(\lambda,z)} \quad R(\lambda,z) = \frac{E_u(\lambda,z)}{E_d(\lambda,z)} \tag{12.26}$$

then

$$R(\lambda,z) = \frac{E_u^{\text{solar}}(\lambda,0)e^{-Kz} + \frac{b_r}{4}E_0(\lambda',0)\left(G_+^*\frac{e^{-K'z}}{K^* + K'} + G_-^*\frac{e^{-K'z}-e^{-K^*z}}{K^* - K'}\right)}{E_d^{\text{solar}}(\lambda,0)e^{-Kz} + \frac{b_r}{4}E_0(\lambda',0)\left(G_-^*\frac{e^{-K'z}}{K^* + K'} + G_+^*\frac{e^{-K'z}-e^{-K^*z}}{K^* - K'}\right)} \tag{12.27}$$

and, factoring out $e^{-K'z}$ yields

$$R(\lambda,z) = \frac{R_0E_d^{\text{solar}}(\lambda,0)e^{-(K-K')z} + \frac{b_r}{4}E_0(\lambda',0)\left(G_+^*\frac{1}{K^* + K'} + G_-^*\frac{1 - e^{-(K^*-K')z}}{K^* - K'}\right)}{E_d^{\text{solar}}(\lambda,0)e^{-(K-K')z} + \frac{b_r}{4}E_0(\lambda',0)\left(G_-^*\frac{1}{K^* + K'} + G_+^*\frac{1 - e^{-(K^*-K')z}}{K^* - K'}\right)} \tag{12.28}$$

This equation includes a solar term and a Raman term. At depths where z is large the solar term goes to zero and only the Raman light remains. That is, the reflectance is going to approach a value that is dependent on K and K'. Figure 12-2 shows a plot of the irradiance reflectance given by Eq. (12.28). For the orange light at 589 nm there is a surface value that is typical of the solar irradiance component. Then, at some depth it approaches the constant value that is characteristic of the Raman parameters. The further into the blue part of the spectrum, the deeper this occurs. In fact as z approaches infinity, the solar term goes to zero, and only Raman light remains. That is, as

$$z \to \infty, \qquad e^{-(K-K')z} \to 0 \tag{12.29}$$

and only Raman remains.

Further reduction of the equations at depth yields

$$R(\lambda,\infty) \to \frac{1.5K - K'}{1.5K + K'} \tag{12.30}$$

That is, the deep reflectance approaches a constant value.

Similarly, for the irradiance reflectance at the surface, as

$$z \to 0, \qquad R(\lambda,0) \to R_0 + \frac{1}{B(1.5K + K')} \tag{12.31}$$

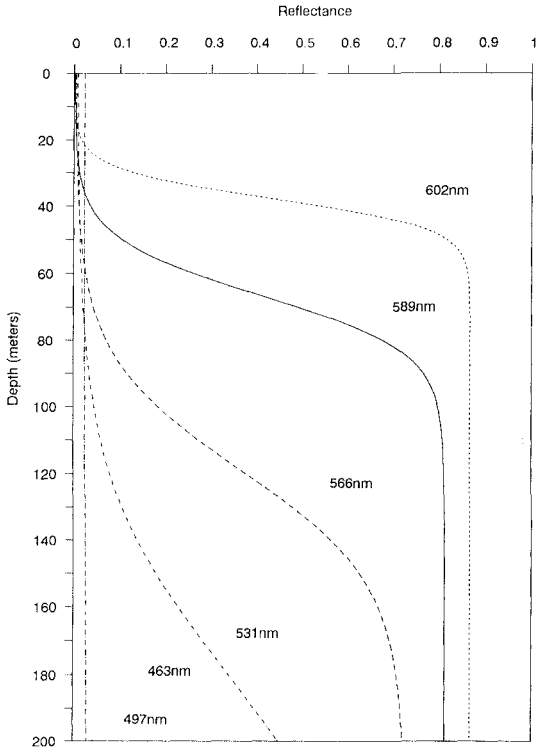

Fig. 12-2. Irradiance reflectance given by Eq. (12.28).

where

$$B = \left(\frac{b_r}{4} \frac{E_0(\lambda',0)}{E_d^{\text{solar}}(\lambda,0)} \right)^{-1}$$

For pure water at 589 nm, B is approximately 1.3×10^4 m, K is approximately $0.15\,\text{m}^{-1}$, and K' is approximately $0.02\,\text{m}^{-1}$. As a result

$$R(589,0) \approx R_0^{589} + 0.0003 \qquad R_0^{589} \approx \frac{b_b}{3a} \approx 0.0012 \tag{12.32}$$

and one can see that even at the surface, for pure water Raman could be a significant fraction (i.e., 20%) of the total reflectance. However, it is important to recognize that the molecular back scattering is a secondary component of total backscattering. Particle scattering is generally significantly larger. Also, at this wavelength, chlorophyll fluorescence becomes a major source of "noise" in the reflectance signal.

The model may also be used to determine the effect of Raman scattering on the diffuse attenuation coefficient. For upwelling and downwelling light the diffuse attenuation coefficients are given respectively, by

$$K_u(\lambda,z) = -\frac{1}{E_u(\lambda,z)}\frac{dE_u(\lambda,z)}{dz}$$
$$K_d(\lambda,z) = -\frac{1}{E_d(\lambda,z)}\frac{dE_d(\lambda,z)}{dz} \tag{12.33}$$

These terms can be expressed as

$$K_u(\lambda,z) = K - (K - K')\left(1 + \frac{\left[B(1.5K - K') - \frac{G_-^*}{R_0}e^{-0.5Kz}\right]e^{-\Delta Kz}}{\frac{G_-^*}{R_0} + \frac{G_+^*(1.5K - K')}{R_0(1.5K + K')}}\right)^{-1}$$

for the upwelled attenuation, and

$$K_d(\lambda,z) = K - (K - K')\left(1 + \frac{[B(1.5K - K') - G_-^* e^{-0.5Kz}]\, e^{-\Delta Kz}}{G_+^* + G_-^*\frac{(1.5K - K')}{(1.5K + K')}}\right)^{-1}$$

for the downwelled attenuation.

Again, consider the limits of these equations: as

$$z \to \infty, \qquad K_u(\lambda,z) \to K' \qquad K_d(\lambda,z) \to K' \tag{12.36}$$

That is, with increasing depth, the diffuse attenuation coefficient of downwelling light at the emission wavelength approaches the attenuation coefficient of the excitation wavelength, since the latter is "feeding" the emission.

At the surface, consider first the upwelling attenuation coefficient as

$$z \to \infty, \qquad K_u(\lambda,0) \to K - (K - K')\left(\frac{1}{1 + BR_0(1.5K + K')}\right) \tag{12.37}$$

at 589 nm.

$$K_u(589,0) \to 0.84K + 0.16K'$$

so a meaningful upwelling diffuse attenuation coefficient cannot be obtained if Raman scattering is ignored.

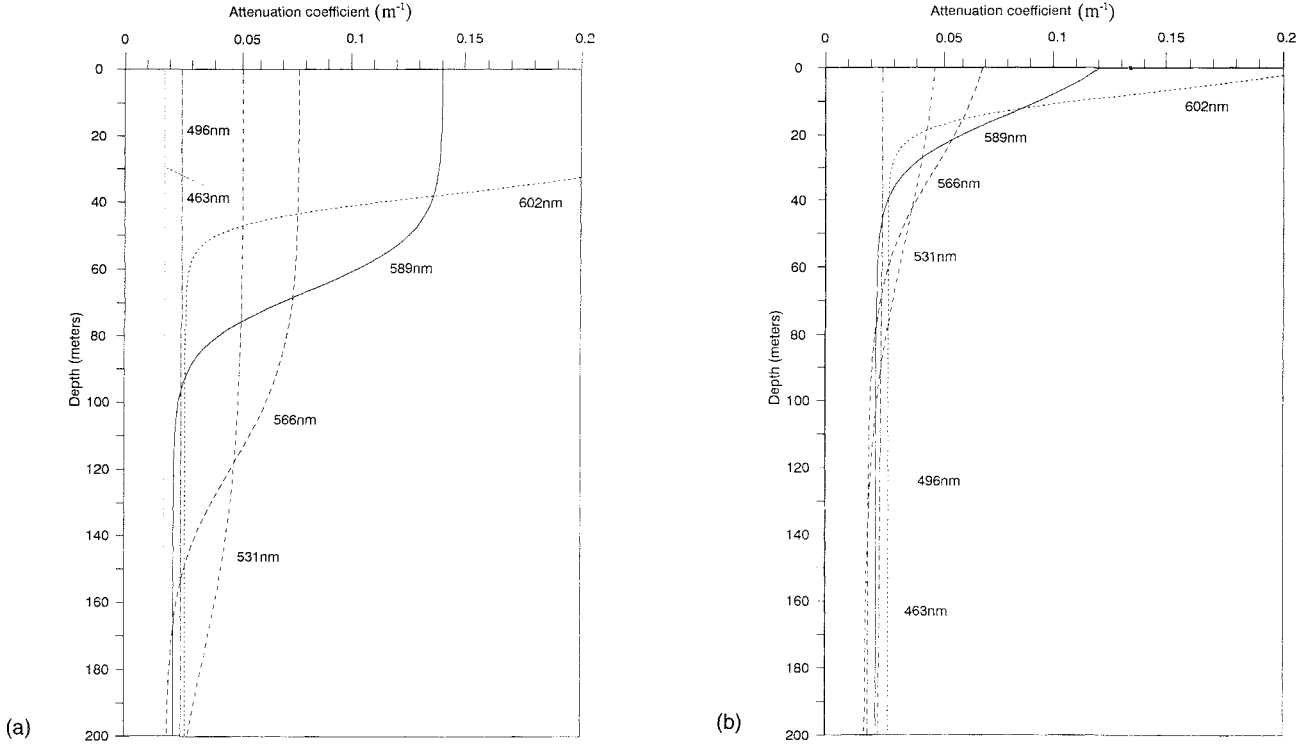

Fig. 12-3. Diffuse attenuation coefficients [(a) downward; (b) upward] as a function of depth, for the pure water model.

For the downwelling attenuation coefficient at the surface,

$$K_d(\lambda,0) \rightarrow K - \frac{2}{B}\left(1 - \frac{K'}{K}\right) \tag{12.38}$$

at 589 nm,

$$\frac{2}{B} \approx 0.00015$$

so,

$$K_d(589,0) \rightarrow K$$

and so the Raman component does not affect the diffuse attenuation coefficient for downwelling light except at depths below the top few attenuation lengths.

Figures 12-3a and 12-3b show the plots of the diffuse attenuation coefficients (downward and upward, respectively) as a function of depth, for the pure water model. As described above, at 589 nm for the downward irradiance line, the coefficient decreases from the surface to a deep water value very close to that of

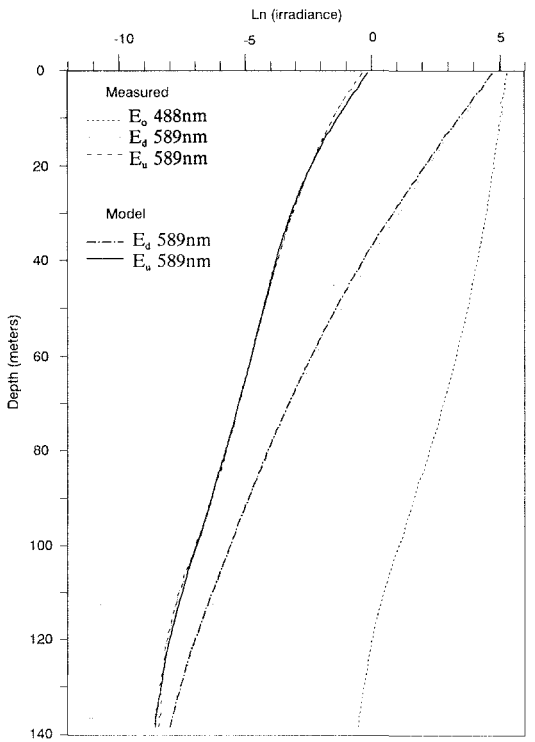

Fig. 12-4. Log measured and calculated irradiance for 488 nm and 589 nm.

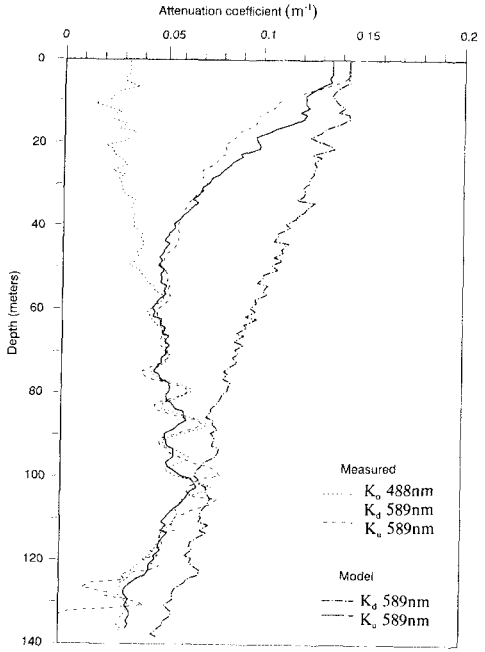

Fig. 12-5. The attenuation coefficients measured with the BOPS (Bio-Optical Profiling System). Shown are the scalar irradiance at 488 nm, and the calculated emissions at 589 nm.

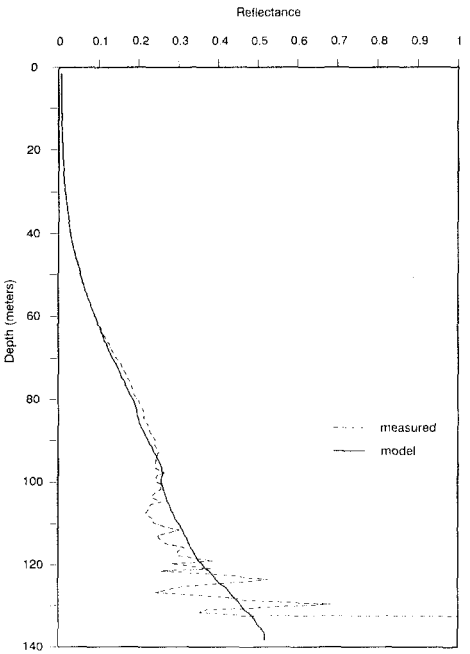

Fig. 12-6. The Raman reflectance function.

the excitation wavelength. The same is true for the other wavelengths. The plot of the attenuation coefficient for the upward irradiance shows that nowhere in the water column is it clear what the true attenuation coefficient is.

Now we can compare the model with measured values from the field. Figure 12-4 shows a plot of log measured and calculated irradiance for 488 nm and 589 nm. Figure 12-5 is a plot of the attenuation coefficients measured with the BOPS (Bio-Optical Profiling System) from a part of the ocean where the top 80–90 meters were essentially uniform, clear water without a lot of structure. Shown are the scalar irradiance at 488 nm, and the calculated emissions at 589 nm. The calculated and the measured values agree down to the noise level of the instrument. In these homogeneously clear waters one would have expected a uniform diffuse attenuation coefficient, but instead there is a diffuse attenuation coefficient that begins to shift toward the excitation wavelength essentially because of the Raman component. Figure 12-6 shows the data for the reflectance function. Again the reflectance at the surface appears to be all "elastic reflectance." At depth the value is more characteristic of the Raman scattering rather than the reflectance of the water column. In fact the additional long wavelength light could not be explained adequately by any local fluorescence from biological material.

A major issue in optical oceanography today is the accurate measurement of the absorption coefficient (see Chapter 3). The use of Gershun's equation is an approach that could be strongly affected by Raman scattering. One must add a Raman term to the Gershun equation in order to balance the energy equation. The inclusion of Raman scattering in Gershun's equation is apt to be less of a problem for extracting the absorption coefficient at short wavelengths.

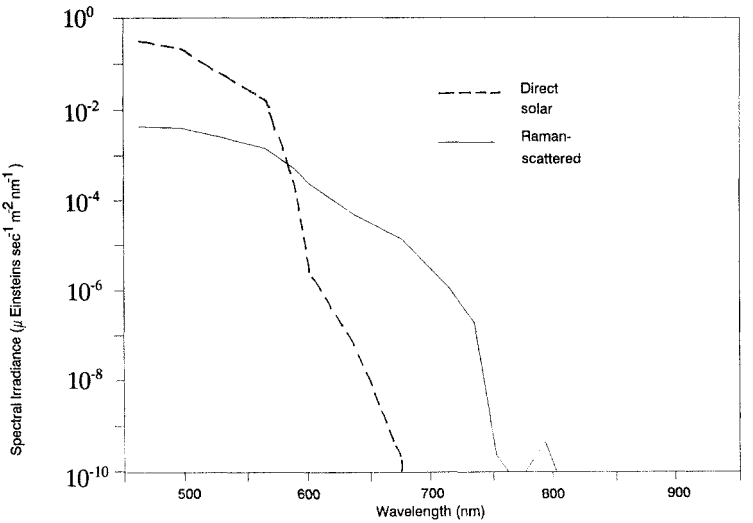

Fig. 12-7. Direct and Raman scattered light at 50 m depth. The total light field is the sum of these two.

For remote sensing the effect of Raman scattering on reflectance is not apt to be a problem, since the values are probably too small.

The implications of Raman scattering on biological oceanography are potentially exciting. Figure 12-7 is a plot of direct and Raman scattered light at 50 m depth in clear water. The total light field is the sum of these two. In the red region of the spectrum there are some six orders of magnitude more light than would be present without Raman scattering. This may be a critical factor in the process of photomorphogenesis: the response of organisms to light signals that regulate changes in structure and form. In this process the red photons act as a switching mechanism. Photomorphogenesis is a switching mechanism based on very small amounts of red light. The Raman light may be playing a role in gametogenesis.

13

OPTICAL EFFECTS OF LARGE PARTICLES

Kendall L. Carder and David K. Costello
University of South Florida

Introduction

Two important problems facing the ocean optics research community in the coming decade concern optical model *closure* and *inversion* (see Chapter 3). We obtain model *closure* if we can describe the measured light environment by combining elementary measurements of the optical properties of the medium with radiative transfer theory. If we can accurately deduce the concentration of various constituents from a combination of measures of the submarine light field and inverse model calculations, we term this process model *inversion.*

The most elementary measurements of the optical properties of the sea are those that are independent of the geometry of the light field, the *inherent* optical properties (Preisendorfer, 1961). Optical properties that are dependent on the geometry of the light field are termed *apparent* optical properties (AOP). Models of the submarine light field typically relate apparent optical properties to inherent optical properties (see Chapter 2). Examples include the relationship between the AOP irradiance reflectance R and a combination of inherent optical properties (backscattering coefficient b_b and absorption coefficient a), and the relationship between the AOP downwelling diffuse attenuation coefficient k_d and a combination of the absorption coefficient, backscattering coefficient, and downwelling average cosine μ_d (e.g., Gordon et al., 1975; Morel and Prieur, 1977; Smith and Baker, 1981; Morel, 1988; Kirk, 1984a).

Under some circumstances these relationships work well enough that the absorption coefficient can be derived indirectly. This is important since measurement of the absorption coefficient by direct means has been difficult. Derived values for the absorption coefficient by model inversion methods are not easily verified by independent measurements, however, because of the difficulty of measuring the absorption coefficient.

Model closure and model inversion both become more tenuous when the following phenomena are present:

1. Transpectral or inelastic scattering such as fluorescence (e.g., Gordon, 1979; Carder and Steward, 1985; Mitchell and Kiefer, 1988a; Spitzer and Dirks, 1985; Hawes and Carder, 1990) or water Raman scattering (Marshall and Smith, 1990; Stavn, 1990; Stavn and Weidemann, 1988a,b; Peacock et al., 1990; Chapter 12 this volume).
2. Particles that are large relative to the measurement volume for inherent optical property meters such as beam transmissometers, light-scattering photometers, fluorometers, and absorption meters.

The effects of these phenomena are not accounted for in most optical models and may be present in measurements when testing for model closure. They will typically be present in AOP data but not always in inherent optical property data. The transspectral phenomena affecting model closure are being actively pursued as a research topic. However, the effects of large particles on model closure and model inversion have been less vigorously studied and are the focus of this study.

Background

A difficulty inherent in addressing the effect of large particles on the light field results from the difference in the scales of measurement typical for apparent optical properties and inherent optical properties. The apparent optical properties derive from measures of the light field associated with water volumes of order one to hundreds of cubic meters, whereas inherent optical properties derive from very local measurements, with sample volumes ranging from of order cubic millimeters to cubic centimeters. This closure problem can be illustrated by using an example case.

A beam-attenuation or c-meter measures the loss of light from a narrow, collimated light beam of length dl. This loss is due to absorption by water, a_w, by particles, a_p, by colored dissolved organic matter, a_{cdom}, and due to scattering by water molecules, b_w, and by particles, b_p (e.g., see Jerlov, 1968; Petzold, 1972; Kirk, 1984a). In order to minimize the error resulting from the collection of near-forward-scattered light by the sensor and thus underestimating the contributions to c due to $b_w + b_p$, c-meters must be well-collimated with beams that are narrow relative to their length. Minimizing the near-forward-scattering acceptance angle does not, however, allow one to quantify this error unless the nature of the scatterers is known. For example, Baker and Lavelle (1984) showed that spheres of 10 μm and 40 μm diameter, both with refractive indices of 1.2 relative to water, would scatter, respectively, 15% and 43% of the incident light into a near-forward cone with half-angle of 1.03°. For much larger particles that approach the size of the beam itself, this effect worsens. Ultimately, the beam may be blocked entirely or the particles may be only partially illuminated, rendering meaningless any interpretation of their effect on c. When present, these large particles are clearly represented in AOP measurements, however, because of the large volumes of water contained in their measurement fields.

Light-scattering photometers, which measure the radiant intensity scattered in various directions by a small, irradiated volume of water, can be saturated by scattering from a particle occupying a significant cross-section of the source beam. An additional problem arises for measurements of the total scattering coefficient and backscattering coefficient. Since most measurements of these variables derive from integrating volume scattering function measurements, $\beta(\theta)$, over 4π or 2π steradians (e.g., see Kullenberg, 1968; Petzold, 1972), and these θ-dependent measurements are typically not synoptic, the optical properties of the sample volume must remain constant during the time required to obtain the entire suite of $\beta(\theta)$ measurements. To obtain data consistency, average values are typically used for each angle after carefully eliminating "aberrant" data points caused at times by "motes," large particles falling or swimming temporarily through the sample volume. These "moteless" volume scattering functions produce "moteless" b_b and b data when integrated over the appropriate solid angles, data no longer consistent with the actual particle size distribution, c value, or the AOPs. The effects of small motes are not problematic for c-meter data and are not removed. As a result, absorption coefficient data derived from the difference, $c-b$, can be too large.

If it were possible to remove mote effects from c-meter data in a way that was consistent with the method used for deriving "moteless" b data, reasonably accurate absorption coefficients could be derived for "moteless" water. These moteless data include all particles statistically represented in the data used in the averaging process, but they ignore the most erratic effects of motes on the inherent optical properties c, $\beta(\theta)$, b, b_b, and "derived" a. It is not expected that closure between model predictions based on "moteless" inherent optical property data will be achieved with AOP measurements that include the optical effects of motes.

When "moteless" inherent optical properties are used to drive model calculations that simulate apparent optical properties and the submarine light field (which do include the effects of motes), closure is not achievable if the motes play a statistically significant optical role. The focus of this chapter is to examine the optical role played by large particles and to present a method for sizing, classifying, and enumerating them in order to assess their effect upon the optical properties of the ocean and the submarine light field.

Approach

The effect of large particles on apparent optical properties is a function of their concentration relative to smaller particles and, therefore, will vary geographically. High concentrations of large particles are generally associated with near-shore or near-bottom environments. However, significant concentrations of optically "large" particles can be found in the open ocean. In the oligotrophic north central Pacific gyre (26°N, 155°W), Betzer et al. (1988) found an influx of optically large (due to size and high relative index of refraction) eolian particles that amounted to some 10 000 particles $m^{-2}\,day^{-1}$. Although the concentrations

from such an influx would likely affect a remotely sensed signal that is dependent on b_b, it is estimated that a typical c-meter with a 1-m pathlength, for example, may measure in these waters a significant perturbation in its background signal due to such eolian particles only 1–2% of the time. A typical scattering meter, because of its small sample volume, would have a probability approaching zero of detecting these particles. Hence, an optically significant portion of the particle population could go essentially undetected.

When particles are present with cross sections that are significant relative to that of the measurement volume, and they are sampled on an infrequent basis or not at all, the inherent optical properties will diverge from those derived from apparent optical properties using inverse models. To estimate the sample volumes required to adequately represent some given particle suite, one must first assume a size distribution function, and also that the particles are evenly dispersed in time and space. A commonly used form for particle size distribution functions is a power-law function of the particle diameter:

$$\frac{dN(D)}{dD} = AD^{-n} \tag{13.1}$$

expressed as particles $\mathrm{cm}^{-3}\,\mu\mathrm{m}^{-1}$ where $N(D)$ is the cumulative number of particles larger than D, $dN(D)$ is the number of particles within size range dD, A is a constant of dimensions particles $\mathrm{cm}^{-3}\,\mu\mathrm{m}^{n-1}$, and D is in μm.

Using an open-ocean example, and assuming a power-law size distribution with $n = 4$ [used by Hunt (1980) for inorganic particles between 2 and 40 μm diameter and by Sheldon et al. (1972) for organic particles from phytoplankton to whales], and considering the size range from 1 μm to 1 cm, one would expect roughly the same amount of particulate volume to be found in the size ranges (diameters) 1-10 μm, 10-100 μm, 100-1000 μm, and 1–10 mm.

Figure 13-1 shows particle frequency as a function of size with this size distribution assumption and the Sheldon et al. (1972) estimate for surface Sargasso Sea particle volume concentration of 0.01 p.p.m. per log-size class. It also illustrates the number of sample volumes for different instruments required in order to reasonably expect to see even a single particle of a given size. Figure 13-1 suggests that for a typical 25-cm pathlength c-meter with a sample volume of about 50 ml, the 1–10 μm diameter size class in this volume would be well represented. There would, however, be only one 100-μm diameter particle present on average. Continuing this analysis, one would have to look at one thousand 25-cm pathlength c-meter sample volumes in order to expect to see even a single 1-mm diameter particle and one million sample volumes in order to see a 1-cm diameter particle.

The question then arises whether these "rare-event" large particles are optically significant enough to attempt to measure since, using the above approach, their numbers diminish by a factor of 10^3 for each larger log-size class. However, even though particle numbers are reduced by a factor of 10^3, individual particle cross-sectional area, a significant optical parameter (van de Hulst, 1957), increases by a factor of 10^2 per log-size class. This results in a reduction of total

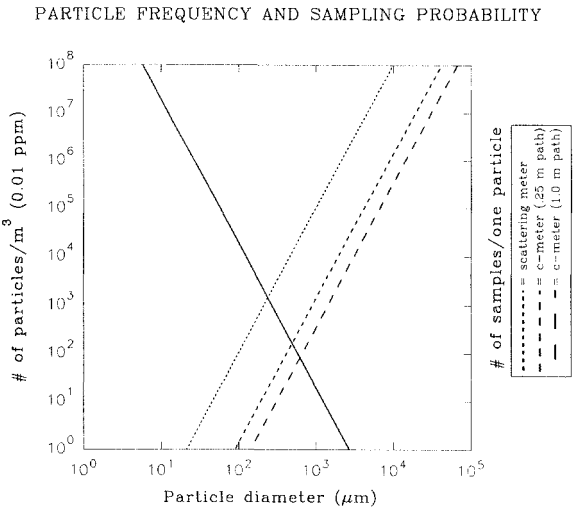

Fig. 13-1. Number of particles m^{-3} (solid line, left ordinate) using Sheldon et al. (1972) estimate for particle volume/water volume ratio (see text). The other three plots show the number of sample volumes required (right ordinate) to expect to capture one particle of a given size: ····, scattering matter; ----, *c*-meter (0.25 m path); ———, *c*-meter (1.0 m path).

particle cross-sectional area per increasing log-size class of only one order of magnitude. One can postulate, then, that at whatever particle size a particular instrument sample volume becomes statistically inadequate (perhaps, 10 μm diameter or less for a scattering meter and 100 μm diameter or less for a *c*-meter), the next largest log-size class could represent an additional 10% of the potential instrument signal that would not be measured.

While this sampling error may not seem great, the larger size-class particles may have optical effects disporportionate to their spherical-equivalent cross-sectional areas. Larger marine particles, especially large aggregates or marine snow (Alldredge and Silver, 1988) tend to be more complex in shape than smaller particles. This greater degree of complexity would tend to increase the ratio of surface area to volume and change the shape of the volume scattering function, $\beta(\theta)$. In microwave analog experiments Greenberg et al. (1971) found that a "roughened" sphere versus a smooth sphere demonstrated enhanced scattering in all orientations. Furthermore, Zerull and Weiss (1974) found, in a comparison of scattering intensities at angles greater than 10°, that "fluffy" particles scattered nearly an order of magnitude more effectively than smooth particles. This would be especially important for backscattering and reflectance measurements. Hence, despite the reduction of particle numbers by a factor of 10^3 in increasing log-size class and the reduction of total cross-sectional area by an order of magnitude, the optical contribution to *c*, through *b*, of the 10–100-μm diameter and the 100-1000 μm diameter size classes could approach the same order of magnitude if "fluffy," marine snow types of aggregates were present in the larger size classes.

Under such circumstances, the optical contribution from neither class would generally be adequately measured by a scattering meter, while the latter class would not be adequately measured by a *c*-meter. Furthermore, because of the nature of these types of instrumentation, there would be zero probability of identifying the large particles, a valuable step when performing model inversions. This would also be the case even for regions having high concentrations of large particles. Hence, even though traditional in situ optical instrumentation may adequately measure the numerically and, generally, optically dominant marine particle classes, the pursuit of model closure and inversion suggests the development of new approaches, especially when considering environments containing large aggregates and animals effecting patchy, schooling types of behavior.

New instrumentation

It is unlikely that existing instrumentation can be simply "scaled up" because of physical limitations, technical considerations, and the critical resultant loss of resolution in measuring the dominant smaller sized particles. This would also not assist in the desired identification of the larger particles. Imaging the large particles, whether it be through photography, holography, video, or some other method, would assist in particle identification and allow the measurement and/or inference of particle optical properties. For example, to first order, the attenuation due to large simple particles can be estimated if the large-particle size distribution is known, since for large particles the attenuation efficiency factor $Q_c \approx 2$ (van de Hulst, 1957). An advantage of continuous, sequential imaging (i.e., video) is that it provides for the behavioral classifications of swimming versus settling and allows the determination of swimming speed for the former and settling speed for the later. For settling particles, if the size and settling speed are known, the dynamic density (which should have some correlation with optical density) can be inferred by inverting the appropriate, shape-dependent, Stokes settling equation (e.g., see Carder et al., 1986; Costello et al., 1989).

Imaging systems

An inherent difficulty in any imaging approach lies in the reduction of massive amounts of information (the images) in order to extract useful data (the particle attributes). A scattering meter or a *c*-meter, for example, will have two discrete "numbers" corresponding to an instantaneous sample volume (the signal and the reference), while a modest two-dimensional video image, digitized in an image processing environment at a typical $512 \times 512 \times 1$ pixels (low resolution compared to photography and very low resolution compared to three-dimensional holography) will have over 250 000 "numbers" corresponding to an instantaneous sample volume. At normal video frame rates (30 frames/second) this generates nearly one-half billion "numbers" per minute. Thus, any attempt to extract a body of statistically meaningful information from an image data base

must necessarily work in an automated image processing/analysis environment. One approach is discussed later.

Many researchers are involved in the acquisition of image-based data at many different scales. For example, Hammer et al. (1987) describe a system for a three-dimensional (time-multiplexed stereo video) study of fish schooling. Carder et al. (1986) and Costello et al. (1989) describe holographic systems for the study of eolian particles. Honjo et al. (1984) and Asper (1987) describe photographic systems for investigating marine snow. Various aspects of these and other efforts are discussed in Alldredge and Silver (1988). To date, the only selective, intelligent in situ particle observation/collection has been performed by humans utilizing equipment ranging from diving gear to remotely operated vehicles (ROVs) and deep-diving manned submersibles. This is simply because autonomous underwater vehicles (AUVs) optimized for particle research do not, as yet, exist.

We are in the process of modifying a small ROV for large-particle observation and selective collection to act as a test bed for a first-generation AUV, tentatively dubbed the Marine Aggregated Particle Profiling and Enumerating Rover (MAPPER). MAPPER will be a "semi-smart" machine (i.e., programmable and able to respond to external stimuli) and a step toward an eventual artificially intelligent AUV.

Figure 13-2 shows a schematic of the envisioned sample volume for MAPPER as a light-sheet configuration (hence, 90° scattering). Elements of materials of

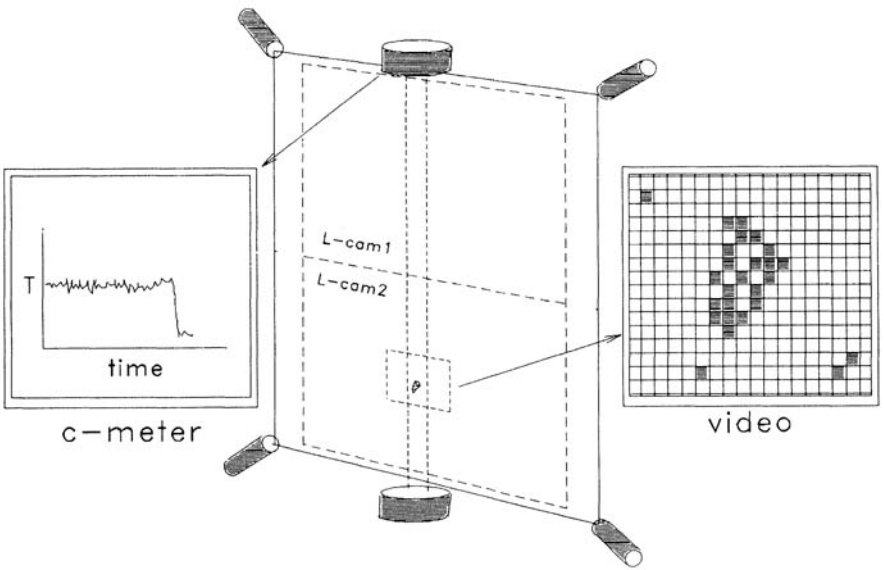

Fig. 13-2. Marine Aggregated Particle Profiling and Enumerating Rover (MAPPER) optical sample volume configuration (see text).

known reflectance (Spectralon, Labsphere Inc., not shown) and a traditional *c*-meter are embedded within the light sheet. The light sheet is at the focal plane in the field-of-view of the two large-field video cameras. A third, higher-spatial-resolution video camera focal plane is embedded within the larger image volume to evaluate particles as small as 50 μm diameter that are observed in the *c*-meter beam within the high resolution field-of-view. In the lower-resolution, large-area camera fields, the pixel resolution is 250 μm.

Depicted in Fig. 13-2 is a large particle in the coincident sample volumes of the *c*-meter and one of the large-field video cameras. In this scenario, the *c*-meter would measure some unknown combination of increased/decreased attenuation relative to the small-particle, background level due to a mix of the following mechanisms: (1) absorption, (2) scattering out of the beam, and (3) enhanced scattering in the near-forward direction within the acceptance angle of the instrument. This scattering would contribute to attenuation if this were an "ideal" *c*-meter. The video image would record the intensity of the 90° side-scatter from the particle (relative to the reference reflector), the size and shape of the particle, and any textural intensity variations caused by particle internal or surface structure. This will enable not only the enumeration of particles by size and shape but also allows an in situ multi-instrument investigation of the optical properties of individual large particles.

MAPPER development is enhanced by utilizing the ROV as a testbed. A light sheet module mounted on the ROV allows experimentation with various lens and camera combinations in different spatial configurations. The ROV is also being utilized in the development of MAPPER control instrumentation (discussed in Costello et. al., 1991) via bidirectional communication multiplexed on the existing ROV video channel. Additionally, the ROV is being used as an independent instrument for the study of large particles. For example, large particles can be actively tracked and stereo views can be acquired using a mirror module and reflected light (near 180° backscatter). This allows an accurate volume determination and an estimate (relative to a standard) of particle reflectivity.

The analysis of the imagery from this or any other large-base imaging system requires an automated image-processing/analysis approach. Furthermore, the inevitable artificially intelligent AUV of the future will require that particle imagery be reduced in near real-time for selective capture to be efficiently implemented. Due to the diversity that marine particles exhibit, the image analysis approach must quickly provide a high degree of information. One method that we have been investigating follows.

Pattern recognition

To describe the distribution of radiance from a particle within an x–y field (i.e., an image), we utilize the method of moment invariants. The two-dimensional $(i + j)$th order moments of a density distribution function $\rho(x, y)$ are defined in terms of Riemann integrals (proper, bounded) as (Hu, 1962)

$$m_{ij} = \int_{-\infty}^{\infty} \int_{-\infty}^{\infty} x^i y^j \rho(x,y)\, dx\, dy \qquad i,j = 1,2,3\ldots \tag{13.2}$$

The low-order ordinary moments are especially useful to the extent that m_{10}/m_{00}, m_{01}/m_{00} locate the (x,y) coordinate position for the centroid of the image intensity distribution. Sequential centroid locations, then, can be used in a first-order classification scheme for particles since inanimate particle centroid trajectories would follow the gravitational vector at a constant velocity (settling) relative to water motion, while animated particles would demonstate non-nadir and/or accelerated velocities (swimming).

For this approach to be useful in pattern recognition strategies, however, the sample-space vectors generated must be invariant with object position and/or orientation within the image field. Translational invariance can be achieved by the determination of object centroid (from the first- and zero-order ordinary moments) and then the ordinary moments can be recalculated with the origin of the coordinate field coincident with the object image centroid. This first step toward both translational and rotational invariance, however, can be achieved (and computational time minimized) by transforming the ordinary moments (m_{ij}) into central moments (μ_{ij}), moments relative to the centroid of the object image. Using the notation of Hu (1962):

$$\mu_{00} = m_{00} = \mu \tag{13.3}$$

$$\mu_{10} = \mu_{01} = 0 \tag{13.4}$$

$$\mu_{20} = m_{20} - \mu\bar{x}^2 \tag{13.5}$$

$$\mu_{11} = m_{11} - \mu\bar{x}\,\bar{y} \tag{13.6}$$

$$\mu_{02} = m_{02} - \mu\bar{y}^2 \tag{13.7}$$

$$\mu_{30} = m_{30} - 3m_{20}\bar{x} + 2\mu\bar{x}^3 \tag{13.8}$$

$$\mu_{21} = m_{21} - m_{20}\bar{y} - 2m_{11}\bar{x} + 2\mu\bar{x}^2\bar{y} \tag{13.9}$$

$$\mu_{12} = m_{12} - m_{02}\bar{x} - 2m_{11}\bar{y} + 2\mu\bar{x}\bar{y}^2 \tag{13.10}$$

$$\mu_{03} = m_{03} - 3m_{02}\bar{y} + 2\mu\bar{y}^3 \tag{13.11}$$

where $\bar{x} = m_{10}/m_{00}$, $\bar{y} = m_{01}/m_{00}$.

It is notable that the first-order central moments μ_{10}, μ_{01} are equal to zero under this transformation. This follows intuitively since the first-order "spread" of an object relative to any axis of a coordinate system drawn through its centroid would center about the origin.

These central moments can then be utilized to produce moment functions that possess the desired invariance with rotation and translation. Seven such functions were first formulated by Hu (1962) and are presented here following the form of Dudani et al. (1977):

$$M_1 = (\mu_{20} + \mu_{02}) \tag{13.12}$$

$$M_2 = (\mu_{20} - \mu_{02})^2 + 4\mu_{11}{}^2 \tag{13.13}$$

$$M_3 = (\mu_{30} - 3\mu_{12})^2 + (3\mu_{21} - \mu_{03})^2 \tag{13.14}$$

$$M_4 = (\mu_{30} + \mu_{12})^2 + (\mu_{21} + \mu_{03})^2 \tag{13.15}$$

$$\begin{aligned} M_5 = {} & (\mu_{30} - 3\mu_{12})(\mu_{30} + \mu_{12})\left[(\mu_{30} + \mu_{12})^2 - 3(\mu_{21} + \mu_{03})^2\right] \\ & + (3\mu_{21} - \mu_{03})(\mu_{21} + \mu_{03})\left[3(\mu_{30} + \mu_{12})^2 - (\mu_{21} + \mu_{03})^2\right] \end{aligned} \tag{13.16}$$

$$\begin{aligned} M_6 = {} & (\mu_{20} - \mu_{02})\left[(\mu_{30} + \mu_{12})^2 - (\mu_{21} + \mu_{03})^2\right] \\ & + 4\mu_{11}(\mu_{30} + \mu_{12})(\mu_{21} + \mu_{03}) \end{aligned} \tag{13.17}$$

$$\begin{aligned} M_7 = {} & (3\mu_{21} - \mu_{03})(\mu_{30} + \mu_{12})\left[(\mu_3 + \mu_{12})^2 - 3(\mu_{21} + \mu_{03})^2\right] \\ & - (\mu_{30} - 3\mu_{12})(\mu_{21} + \mu_{03})\left[3(\mu_{30} - \mu_{12})^2 - (\mu_{21} + \mu_{03})^2\right] \end{aligned} \tag{13.18}$$

It is interesting to note that M_7 is a psuedo-invariant function that undergoes a sign change under reflection and, hence, would be useful for recognition of a mirror-image of a cataloged pattern. M_7 would recognize the "front" or "back" of a cataloged pattern and would also be useful for recognition of spatial features such as a right-hand versus a left-hand spiral structure.

Size invariance is more subtle, however, since for the purposes of estimating particle volume, the knowledge of the discrete size of a target particle is not only desirable but necessary. With discrete size and settling speed information, particle dynamic density can be calculated through the inversion of the appropriate (shape-dependent) Stokes settling equation. Since the sample space will necessarily be three dimensional, however, the apparent size (solid angle) of an object will change with a change in position along the axis between the particle and the sensor (optical axis). What is required is "apparent size" invariance, with retention of discrete size information.

The desired "apparent size" invariance can be effected, however, by normalizing M_1 through M_7 in the manner proposed by Dudani et al. (1977). Here, the radius of gyration of an object is defined as

$$r = (\mu_{20} + \mu_{02})^{1/2} \tag{13.19}$$

and

$$r \cdot B = \text{constant} \tag{13.20}$$

(where μ_{20} and μ_{02} are second order central moments and B is the axial distance of the object from the sensor) since the radius of gyration of an object would be *directly* porportional to the mean image diameter and *inversely* porportional to the distance of the object along the optical axis. Then,

$$M_1' = (\mu_{20} + \mu_{02})^{1/2} \bullet B = r \bullet B \tag{13.21}$$

$$M_2' = M_2/r^4 \tag{13.22}$$

$$M_3' = M_3/r^6 \tag{13.23}$$

$$M_4' = M_4/r^6 \tag{13.24}$$

$$M_5' = M_5/r^{12} \tag{13.25}$$

$$M_6' = M_6/r^8 \tag{13.26}$$

$$M_7' = M_7/r^{12} \tag{13.27}$$

Although M_2' through M_7' are now independent of object distance, this normalization method requires a priori knowledge of B for the utilization of M_1'. In our deployment configuration B will be the focal length of the imaging system where the light sheet is located, and hence it will be known. For stereoscopic and holographic systems, B can be derived from the imagery.

The rotational, translational, and size invariance of the computer code generated to implement Eqs. (13.2–13.27) was tested by the analysis of 15 image fields. An "L"-shaped binary "object" was generated proportionately in four different sizes and placed in fields of four sizes, resulting in eight combinations of image-to-field size. The shapes were translated, rotated, translated and rotated, placed in disporportionately sized fields (which equates to axial displacement), and all of these.

The central moments to third order and functions M_1 through M_7 were first generated for each field without size normalization using the radius of gyration. Results show that the method is invariant for translation, rotation, and reflection but that the algorithm could not identify the same discretely sized object located in fields of differing size. After size normalization was incorporated into the algorithm, the desired size invariance was achieved. Also, function M_7' did change sign for the mirror-image test fields.

It must be noted that this set of tests was conducted on "ideal" image data; that is, with an image field data array that was digitally initialized with discrete values (no error). The tests did show, however, that a digital representation of an object shape can be uniquely described with the software developed, regardless of the position and/or orientation of the object in the image field.

To test the utility of the method for actual marine particles, the images of marine animals and aggregates recorded in situ in a sediment trap in the

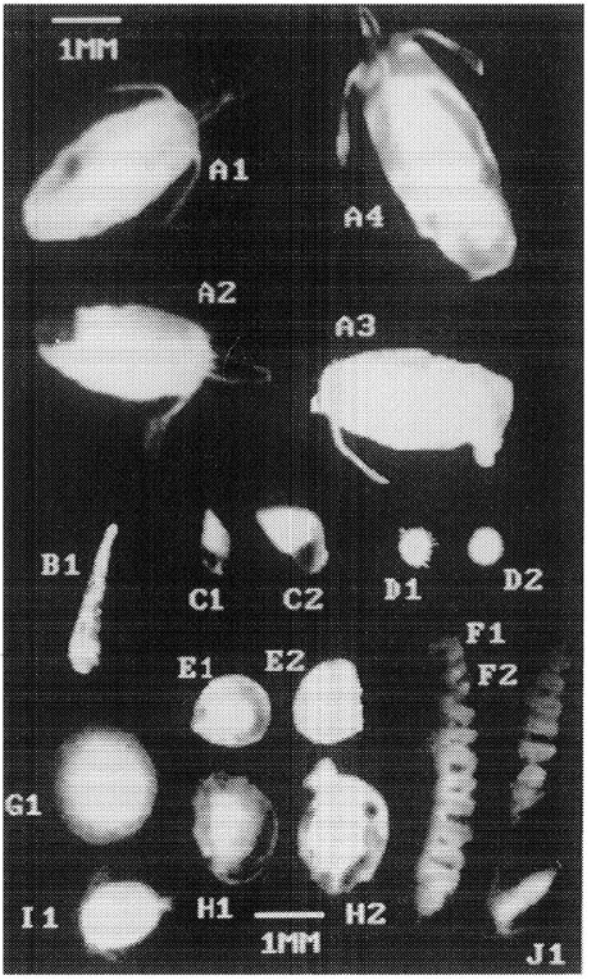

Fig. 13-3. Test images used for verification of pattern recognition strategy.

subtropical North-central Pacific were analyzed. The methodology used in recording the images is discussed in Costello et al. (1989). The pattern recognition (PR) algorithm was applied to the images of 18 marine particles shown in Fig. 13-3 (one group of four, five pairs, and four individuals). To effectively "classify" these images, the PR algorithm must generate classification parameters (feature vectors) that are similar on an intragroup and dissimilar on an intergroup basis. Twelve factors each were generated by operating on the target

silhouette (low-frequency information), target outline (high-frequency information), and the full 8-bit image of the target which includes a contribution from any interior structure. The 12 factors were as follows: the zero-order central moment (image power); the seven normalized invariant moment functions (Eqs. 13.21 through 13.27) as first formulated by Hu (1962) with the size normalization as proposed by Dudani et al. (1977); and the following four moment-generated elliptical classification factors as developed by Teague (1980).

$$\alpha = \left(\frac{2\left\{ \mu_{20} + \mu_{02} + \left[(\mu_{20} - \mu_{02})^2 + 4\mu_{11}^2 \right] \right\}^2}{\mu_{00}} \right)^{1/2} \tag{13.28}$$

$$\zeta = \left(\frac{2\left\{ \mu_{20} + \mu_{02} - \left[(\mu_{20} - \mu_{02})^2 + 4\mu_{11}^2 \right] \right\}^2}{\mu_{00}} \right)^{1/2} \tag{13.29}$$

$$\Gamma = \tfrac{1}{2}\tan^{-1}\left(2\mu_{11}(\mu_{20} - \mu_{02})^{-1}\right) \tag{13.30}$$

$$F = \mu_{00}/\pi\alpha\zeta \tag{13.31}$$

These factors characterize any image as a constant intensity ellipse with intensity F inside and zero outside, defined major axis α, minor axis ζ, and angular orientation Γ within the two-dimensional coordinate field. The method is also computationally attractive since it requires the computation of moments to only second order.

Figure 13-4 depicts three-dimensions of the 36 dimensions available in our classification space and shows how an appropriate classification (separation) of the group, pairs, and individuals is effected in a three-dimensional classification space even though some are not distinguishable in one or both of the two-dimensional classification planes. Two of the classification factors depicted, M_1' and M_2' (Eqs. 13.21 and 13.22) are, in fact, normalized forms of the classification factors (X and Y) originally used by Hu (1962) in his study of automatic alphabetic character recognition. The third factor, α (Eq. 3.28), is a convolved, weighted summation of the other two factors. To our knowledge this approach to the combination of shape recognition factors is unique in that it utilizes highly shape-discriminate factors (the moment invariant functions) as well as factors that emphasize general shape and optical image power (the elliptical factors). Although further work with additional in situ images is required, it appears that the method can adequately address the shape-diverse and the shape-amorphous nature of marine particles. Because of the computationally intensive nature of machine vision and pattern recognition, further work with additional in situ images is also required for the determination of the value and utility of the information content specific to each of the 36 available classification dimensions. However, the method has proven invariant to target translation, rotation, and

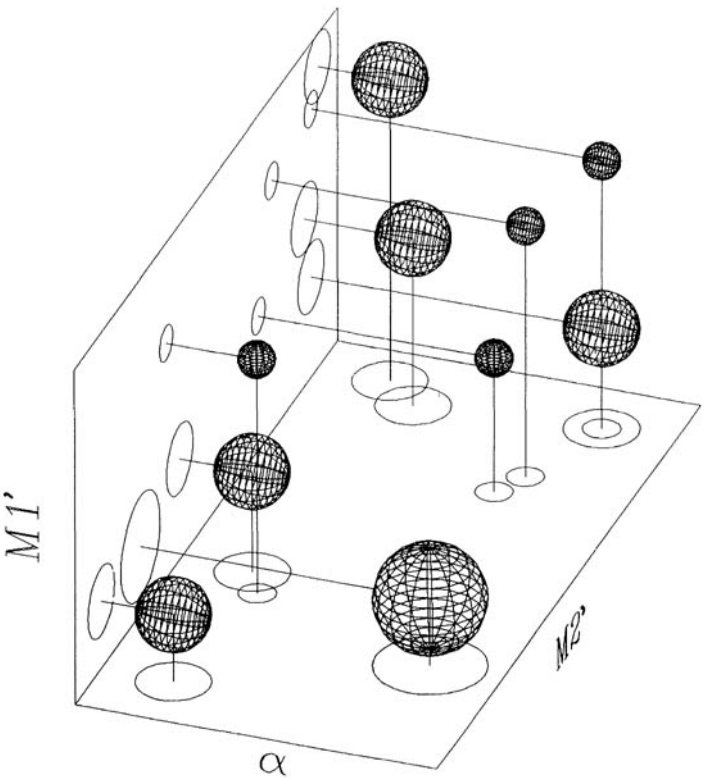

Fig. 13-4. Schematic depicting three dimensions of our 36-dimensional classification strategy. Groups or individuals not resolved in either of the classification planes shown are resolved in the intersection of the planes.

"apparent" size and has successfully classified (separated) computer-generated test patterns, alphanumeric characters, and images of marine particles acquired in situ. Further, image power can be related to $\beta(90°)$, image size can be used to determine the large-particle ends of size distributions, and size and shape can be used to estimate c values for comparison with c-meter perturbations.

Summary

One of the research areas which requires further exploration in the effort toward marine optical model *closure* and *inversion* is the effect of large particles on the underwater light field. The temporally and spatially variable concentration (and, hence, optical effect) of large particles demands an understanding of not only the size and number but also the optical nature of the individual particles. The macroscopic size of the particles allows their study on an individual basis once

they are located and imaged. This requires the development of new, large-volume, in situ instrumentation to augment traditional small-particle methods. The large volume of data required to understand the temporal and spatial distributions of various particle classes demands an automated classification and analysis method.

We are developing a new instrument, MAPPER, to enumerate and image individual particles at rapid sampling rates (on the order of hundreds of liters per minute). To address the large quantity of imagery expected, a classification and analysis scheme based on the method of moment invariants has been developed and presented. Any pattern recognition/classification method is most effective when the particles under analysis exhibit a high degree of intraclass similarity and interclass diversity. However, some types of marine particles (e.g., marine snow and other aggregates) would be generally amorphous to traditional classification schemes. A variation of the method (Teague, 1980) has also been incorporated that will have utility in the study of these generally amorphous types of particles. The utility of this approach for the classification of aggregated particles lies in the retention of the ability to discriminate between the dominant aggregate shapes (chain, comet, elliptical, spherical, etc.) with the quantification of individual particle backscattering or sidescattering (depending on deployment configuration).

Since remote sensing reflectance R_{rs} is highly backscattering-dependent, and the backscattering and sidescattering coefficients are similar (Petzold, 1972), both the MAPPER and the ROV deployment configurations will enhance the interpretation of R_{rs}. This information, when combined with large-particle classification and enumeration constitutes a requisite step toward optical model closure and inversion for a significant part of the world ocean.

REFERENCES

Aas, E., 1981. *The refractive index of phytoplankton.* Institutional Report no. 46, University of Oslo.

Aas, E., 1984. *Influence of shape and structure on light scattering by marine particles.* Institutional Report number 53, University of Oslo.

Aas, E., 1987. Two stream irradiance model for deep waters. *Applied Optics*, **26**, 2095–2101.

Ahn, Y.H., 1990. *Propértés optiques des particules biologiques et minérales présentes dans l'océan.* Thèse, Université Pierre et Marie Curie.

Alldredge, A.L. and M.W. Silver, 1988. Characteristics, dynamics and significance of marine snow. *Progress in Oceanography*, **20**, 41–82.

Ålvik, G., 1934. Plankton-Algen, norwegischer Austernpollen. Licht und Assimilation in verschiedenen Tiefen. *Bergens Museums Årbog 1934. Nat. vid. række*, no. 10., p. 1–90.

Ålvik, G., 1937. Über Lichtabsorption von Wässer und Algen in natürlichen Gewässer, *Bergens Museum Årbog 1937. Nat. vid. række*, no. 2, p. 1–63.

Asper, V.L., 1987. Measuring the flux and sinking speed of marine snow aggregates. *Deep-Sea Research*, **34**, 1–17.

Austin, R.W. and Ensminger, R.L., 1978. *A microprocessor controlled instrument for measuring the transmittance and reflectance of ocean waters.* SIO ref. no. 78-23, Scripps Institution of Oceanography, University of California.

Baker, E.T. and J.W. Lavelle, 1984. The effect of particle size on the light attenuation coefficient of natural suspensions. *Journal of Geophysical Research*, **89**, 8197–8203.

Baker, K.S. and R.C. Smith, 1982. Bio-optical classification and model of natural waters. 2. *Limnology and Oceanography*, **27**, 500–509.

Baker, K.S. and R.C. Smith, 1988. *Bio-optical measurements from the BIOWATT-OC3 and OC4 cruises.* UCMBO Data Report, SIO Ref. no. 89–01, Scripps Institution of Oceanography, University of California.

Bannister, T.T., 1974. Production equations in terms of chlorophyll concentration, quantum yield and upper limit to production. *Limnology and Oceanography*, **19**, 1-12.

Bannister, T.T., 1979. Quantitative description of steady state, nutrient-saturated algal growth, including adaptation. *Limnology and Oceanography*, **24**, 76–96.

Bartz, R., J.R.V. Zaneveld, and H. Pak, 1978. A transmissometer for profiling and moored observations in water. *Ocean Optics V*, Society of Photo-Optical Instrumentation Engineers, **160**, 102–108.

Beardsley, G.F. 1968. Mueller scattering matrix for sea water. *Journal of the Optical Society of America*, **58**, 52–57.

Beardsley, G.F. and J.R.V. Zaneveld, 1969. Theoretical dependence of the near-asymptotic apparent optical properties on the inherent optical properties of sea water. *Journal of the Optical Society of America*, **59**, 373–377.

Berge, G., 1961. Measurements of the primary production and recordings of the water transparency in the Norwegian Sea during May–June 1958. *Rapp. et Proc.-Verb*, vol. 149, 1961. *Cons. Internat. Explor. Mer*, p. 148–157.

Betzer, P.R., K.L. Carder, R.A. Duce, J.T. Merrill, N.W. Tindale, M. Uematsu, D.K. Costello, R.W. Young, R.A. Feely, J.A. Breland, R.E. Bernstein and A.M. Greco, 1988. Long-range transport of giant mineral aerosol particles. *Nature*, **336**, 54–56.

Bitte, I., C. Langdon, J. Marra, and L. Sullivan, 1989. *Improvements to the Multi-Variable Moored Sensor*. Lamont-Doherty Geological Observatory Special Report, Columbia University.

Blasco, D., 1973. A study of the variations in the relation of *in vivo* fluorescence to chlorophyll *a* and its application to oceanography. With reference to limitation by different nutrients, effect of day and night and species dependence. *Investigaciones Pesqueras*. **37**, 532–555.

Bohren, C.F. and D.R. Huffman, 1983. *Absorption and scattering of light by small particles*, Wiley, New York.

Booth, C.R. and R.C. Smith, 1988. Moorable spectro-radiometers in the BIOWATT experiment. *Ocean Optics IX*, Society of Photo-Optical Instrumentation Engineers, **925**, 176–188.

Bricaud, A. and A. Morel, 1986. Light attenuation and scattering by phytoplanktonic cells; a theoretical modeling. *Applied Optics*, **25**, 571–580.

Bricaud, A., A. Morel, and L. Prieur, 1983. Optical efficiency factors of some phytoplankters. *Limnology and Oceanography*, **28**, 816–832.

Bricaud, A., A.L. Bedhomme, and A. Morel, 1988. Optical properties of diverse phytoplanktonic species: Experimental results and theoretical interpretation. *Journal of Plankton Research*, **10**, 851–873.

Briscoe, M.G. and R.A. Weller, 1984. Preliminary results from the long-term upper-ocean study (LOTUS). *Dynamics of Atmospheres and Oceans*, **8**, 243–265.

Butler, W.L., 1978. Energy distribution in the photochemical apparatus of photosynthesis. *Annual Review of Plant Physiology*, **29**, 345–378.

Campbell, L. and R. Iturriaga, 1988. Identification of *Synechococcus* spp. in the Sargasso Sea by immunofluorescence and fluorescence excitation spectroscopy performed on individual cells. *Limnology and Oceanography*, **33**, 1196–1201.

Campbell, L., E.J. Carpenter, and V.J. Iacono, 1983. Identification and enumeration of marine chroococcoid cyanobacteria by immunofluorescence. *Applied and Environmental Microbiology*, **46**, 553–559.

Carder, K.L. and R.G. Steward, 1985. A remote sensing reflectance model of a red tide dinoflagellate off West Florida. *Limnology and Oceanography*, **30**(2), 286–298.

Carder, K.L., R.G. Steward and P.R. Payne, 1984. A solid-state spectral transmissometer and radiometer. *Ocean Optics VII*, Society of Photo-Optical Instrumentation Engineers, **489**, pp. 325–334.

Carder, K.L., D.K. Costello, and R.G. Steward, 1986. State of the art instrumentation for measuring ocean aggregates. *Aggregate dynamics in the sea workshop report*. E. Hartwig and A. Alldredge, eds., Office of Naval Research, pp. 131–181.

Case, K.M., 1957. Transfer problems and the reciprocity principle. *Reviews of Modern Physics*, **29**, 651–663.

Chamberlin, W.S. and J. Marra, 1992. Estimation of photosynthetic rate from measurements of natural fluorescence: analysis of effects of light and temperature. *Deep Sea Research*, **39**, 1695–1706.

Chamberlin, W.S., C.R. Booth, D.A. Kiefer, J.H. Morrow, and R.C. Murphy, 1990. Evidence for a simple relationship between natural fluorescence, photosynthesis, and chlorophyll in the sea. *Deep Sea Research*, **37**(6), 951–973.

Chandrasekhar, S., 1950. *Radiative transfer*, Oxford University Press, London.

Chang, C.H. and L.A. Young, 1972. *Seawater temperature measurement from Raman spectra*. Research Note 920, N62269-72-C-0204, Advanced Research Project Agency, ARPA Order No. 1911.

Chisholm, S.W., R.J. Olson, E.R. Zettler, J. Waterbury, R. Goericke, and N. Welschmeyer, 1988. A novel free-living prochlorophyte abundant in the oceanic euphotic zone. *Nature*, **334**, 340–343.

Chisholm, S.W., S.L. Frankel, R. Goericke, R.J. Olson, B. Palenik, J.B. Waterbury, L. West-Johnsurd, and E.R. Zettler, 1992. *Prochlorococcus marinus* nov. gen. nov. sp.: an oxyphototrophic marine prokaryote containing divinyl chlorophyll *a* and *b*. *Archives of Microbiology*, **157**, 297–300.

Cho, B.C. and F. Azam, 1988. Major role of bacteria in biogeochemical fluxes in the ocean's interior. *Nature*, **332**, 441–443.

Chu, B., 1970. Laser light scattering. *Annual Review of Physical Chemistry*, **24**, 145–174.

Clayton, R.K., 1965. *Molecular physics of photosynthesis*. Blaisdell, New York.

Cleveland, J.S., 1988. *A model of light absorption by phytoplanktonic and detrital particles in the ocean and applications to photosynthetic quantum yield and in vivo fluorescence*. Ph.D. dissertation, University of Washington, Seattle.

Cleveland, J.S., and M.J. Perry, 1987. Quantum yield, relative specific absorption and fluorescence in nitrogen-limited *Chaetoceros gracilis*. *Marine Biology*, **94**, 489–497.

Cleveland, J.S., M.J. Perry, D.A. Kiefer, and M.C. Talbot, 1989. Maximal quantum yield of photosynthesis in the northwestern Sargasso Sea. *Journal of Marine Research*, **47**, 869–886.

Costello, D.K., K.L. Carder, P.R. Betzer, and R.W. Young, 1989. *In situ* holographic imaging of settling particles: Applications for individual particle dynamics and oceanic flux measurements. *Deep Sea Research*, **36**, 1595–1605.

Costello, D.K., K.L. Carder, and R.G. Steward, 1991. Development of the Marine Aggregated Particle Profiling and Enumerating Rover (MAPPER). *Underwater Imaging, Photography, and Visibility*, Proceedings of the Society of Photo-Optical Instrumentation Engineers, **1537**, 161–172. San Diego, Calif.

Cowles, T.J., R.A. Desiderio, and J.N. Moum, 1990. Fluorescence microstructure using a laser/fiber optic profiler. *Ocean Optics X*, Society of Photo Optical Instrumentation Engineers, **1302**, pp. 336–345.

Cox, C. and W. Munk, 1954. Measurements of the roughness of the sea surface from photographs of the sun's glitter. *Journal of the Optical Society of America*, **44**, 838–850.

Creitz, G.I. and F.A. Richards, 1955. The estimation and characterization of plankton populations by pigment analysis. III. A note on the use of 'Millipore' membrane filters in the estimation of plankton pigments. *Journal of Marine Research*, **14**, 211–216.

Cullen, J.J., 1990. On models of growth and photosynthesis in phytoplankton. *Deep Sea Research*, **37**, 667–683.

Deirmendjian, D., 1969. *Electromagnetic scattering on spherical polydispersions.* Elsevier, New York.

Deming-Adams, B., 1990. Carotenoids and photoprotection in plants: a role for the xanthophyll zeaxanthin. *Biochimica et Biophysica Acta*, **849**, 183–193.

Deser, C., R.A. Weller, and M.G. Briscoe, 1983. *Long term upper ocean study (LOTUS) at 34°N, 70°W: meteorological sensors, data, and heat fluxes for May to October 1982 (LOTUS-3 and LOTUS-4).* Woods Hole Oceanographic Institution Technical Report 83–32.

Dickey, T. E.O. Hartwig, and J. Marra, 1986. The BIOWATT bio-optical and physical moored measurement program. *EOS* (Transactions of the American Geophysical Union), **67**, 650–651.

Dickey, T., T. Granata, M. Hamilton, J. Wiggert, D. Manov, D. Siegel, Z. Chai, M. Stramska and J. Scott, 1990. *Final report on the Multi-Variable Moored Sensor System and meteorological data sets taken during the BIOWATT II experiment in the Sargasso Sea in 1987.* University of Southern California Ocean Physics Group Tech, Rept. OPG-90-01.

Dubinsky, Z. and T. Berman, 1976. Light utilization efficiencies of phytoplankton in Lake Kinneret (Sea of Galilee). *Limnology and Oceanography*, **21**, 226–230.

Dubinsky, Z., T. Berman, and F. Schanz, 1984. Field experiments for in situ measurements of photosynthetic efficiency and quantum yield. *Journal of Plankton Research*, **6**, 339-349.

Dubinsky, Z., P.G. Falkowski, and K. Wyman, 1986. Light harvesting and utilization by phytoplankton. *Plant Cell Physiology*, **27**(7), 1335–1349.

Ducklow, H., 1986. Bacterial biomass in warm-core Gulf Stream ring 82-B: mesoscale distribution, temporal changes and production. *Deep Sea Research*, **33**, 1789–1812.

Dudani, S.A., K.A. Breeding, and R.B. McGee, 1977. Aircraft identification by moment invariants. *IEEE Transaction in Computing*, **C-26**, 39–45.

Duysens, L.M., 1956. The flattening of the absorption spectra of suspensions as compared to that of solutions. *Biochemica et Biophysica Acta*, **19**, 1–12.

Elterman, L., 1968. *UV, Visible and IR Attenuation for Altitudes to 50 km, 1968*. AFCRL, Bedford, MA, Report AFCRL-68-0153, April 1968.

Falkowski, P. G. and T. G. Owens, 1980. Light-shade adaptation: two strategies in marine phytoplankton. *Plant Physiology*, **66**, 592–595.

Falkowski, P.G., C.N. Flagg, G.T. Rowe, S.L. Smith, T.E. Whitledge, and C.D. Wirick, 1988. The fate of the spring phytoplankton bloom: export or oxidation. *Continental Shelf Research*, **8**, 457–484.

Fry, E.S. and G.W. Kattawar, 1981. Relationships between elements of the Stokes matrix. *Applied Optics*, **20**, 2811–2814.

Fukuda, M., 1960. Transparency measurements in the Baltic Sea. *Medd. Oceanogr. Inst. Gothenburg, Ser. B*, **8**(5).

Gardner, W.D., 1989. Periodic resuspension in Baltimore Canyon by focusing of internal waves. *Journal of Geophysical Research*, **94**, 18185–18194.

Gehrels, T., 1974. *Planets, Stars and Nebulae*. The University of Arizona Press, Tucson, Ariz.

Gershun, A., 1939. The light field. *Journal of Mathematics and Physics*. **18**, 51–151.

Goldman, J.C., 1988. Spatial and temporal discontinuities of biological processes in pelagic surface waters. *Towards a theory on biological and physical processes in the world ocean*. B. Rothschild, ed. Reidel, New York, pp. 273–296.

Gordon, H.R., 1973. Simple calculation of the diffuse reflectance of the ocean. *Applied Optics*, **12**, 2803–2804.

Gordon, H.R., 1979. Diffuse reflectance of the ocean: The theory of its augmentation by chlorophyll a fluorescence at 685 nm. *Applied Optics*, **18**, 1161–1166.

Gordon, H.R., 1986. Ocean color remote sensing: Influence of the particle phase function and the solar zenith angle. *EOS* (Transactions of the American Geophysical Union), **14**, 1055.

Gordon, H.R., 1987. A bio-optical model describing the distribution of irradiance at the sea surface resulting from a point source imbedded in the ocean. *Applied Optics*, **26**, 4133–4148.

Gordon, H.R., 1989a. Dependence of the diffuse reflectance of natural waters on the sun angle. *Limnology and Oceanography*, **34**, 1484–1489.

Gordon, H.R., 1989b. Can the Lambert–Beer law be applied to the diffuse attenuation coefficient of ocean water? *Limnology and Oceanography*, **34**, 1389–1409.

Gordon, H.R., 1991. Absorption and scattering estimates from irradiance measurements: Monte Carlo simulations. *Limnology and Oceanography*, **36**, 769–777.

Gordon, H.R. and D.K. Clark, 1980. Remote sensing optical properties of a stratified ocean: an improved interpretation. *Applied Optics*, **19**, 3428–3430.

Gordon, H.R. and A. Morel, 1983. Remote assessment of ocean color for interpretation of satellite visible imagery, A review. *Lecture Notes on Coastal and Estuarine Studies,* R.T. Barber, C.N.K. Mooers, M.J. Bowman, and B. Zeitzchel, eds. Springer-Verlag, New-York.

Gordon, H.R., O.B. Brown, and M.M. Jacobs, 1975. Computed relationships between the inherent and apparent optical properties of a flat homogeneous ocean. *Applied Optics*, **14**, 417–427.

Gordon, H.R., O.B. Brown, R.H. Evans, J.W. Brown, R.C. Smith, K.S. Baker, and D.K. Clark, 1988. A semi-analytical radiance model of ocean color. *Journal of Geophysical Research*, **93**, 10909–10924.

Greenberg, J.M., R.T. Wang, and L. Bangs, 1971. Extinction by rough particles and the use of Mie theory. *Nature Physical Science*, **230**, 110–112.

Hama, T., T. Miyazaki, Y. Ogawa, T. Iwakuma, M. Takahashi, A. Otsuki, and S. Ichimura, 1983. Measurements of photosynthetic production of marine phytoplankton population using a stable ^{13}C isotope. *Marine Biology*, **73**, 31–36.

Hamilton, M., T.C. Granata, T.D. Dickey, J.D. Wiggert, D.A. Siegel, J. Marra, and C. Langdon, 1990. Diel variations of bio-optical properties in the Sargasso Sea. *Ocean Optics X*, Society of Photo-Optical Instrumentation Engineers, **1302**, 214–224.

Hamner, W., E. Kristof, and A. Chandler, 1987. 3-D video and computer analysis of fish schooling. *IEEE Oceans*, **87**(3), 1232–1233.

Hawes, S.K., and K.L. Carder, 1990. Fluorescence quantum yields of marine humic and fulvic acids: application for in situ determination. *EOS* (Transactions of the American Geophysical Union), **71**(2), 136.

Hobson, L.A., D.W. Menzel, and R.T. Barber, 1973. Primary productivity and the sizes of pools of organic carbon in the mixed layer of the ocean. *Marine Biology*, **19**, 298–306.

Højerslev, N.K., 1974. *Inherent and apparent optical properties of the Baltic*. Report No. 23, University of Copenhagen, Copenhagen, Denmark.

Højerslev, N.K. and J.R.V. Zaneveld, 1977. *A theoretical proof of the existence of the submarine asymptotic daylight field*. University of Copenhagen Oceanography Series, Report #34.

Honey, R.C. and G.P. Sorenson, 1970. Optical absorption and turbulence-induced narrow angle forward scatter in the sea. *Electromagnetics of the Sea*, AGARD Conf. Proc., No.77: 39.1–39.7.

Honjo, S., K.W. Doherty, Y.C. Agrawal, and V. Asper, 1984. Direct optical assessment of large amorphous aggregates (marine snow) in the deep oceans. *Deep Sea Research*, **31**, 67–76.

Houssier, C. and K. Sauer, 1970. Circular dichroism and magnetic circular dichroism of the chlorophyll and protochlorophyll pigments. *Journal of the American Chemical Society*, **92**, 779–791.

Hu, M., 1962. Visual pattern recognition by moment invariants. *IRE Transaction on Information Theory*, **IT-8**, 179.

Hunt, J.R., 1980. Prediction of oceanic particle size distributions from coagulation and sedimentation mechanisms. *Particulates in water*, M.C. Kavanaugh and J.O. Leckie, eds. American Chemical Society, pp. 243–257.

Iturriaga, R., B.G. Mitchell and D.A. Kiefer, 1988. Microphotometric analysis of individual particle spectra. *Limnology and Oceanography*, **33**, 128–135.

Jerlov, N.G., 1951a. Optical studies of ocean water. *Report of the Swedish Deep-Sea Expedition*, **3**.

Jerlov, N.G., 1951b. Optical measurements of particle distribution in the sea. *Tellus*, **3**, 122–128.

Jerlov, N.G., 1953. Influence of suspended and dissolved matter on the transparency of sea water. *Tellus*, **5**, 59–65.

Jerlov, N.G., 1957a. A transparency-meter for ocean water. *Tellus*, **9**, 229–233.

Jerlov, N.G., 1957b. Improved instruments for optical studies of ocean water. Unpublished manuscript.

Jerlov, N.G., 1961. Optical measurements of the Eastern North Atlantic. *Medd. Oceanogr. Inst. Gothenburg, Ser. B*, **8**(11).

Jerlov, N.G., 1965. The evolution of the instrumental technique in the underwater optics. *Progress in Oceanography*, **3**, 149–154.

Jerlov, N.G., 1968. *Optical oceanography.* Elsevier Oceanography Series, 5. Elsevier, Amsterdam.

Jerlov, N.G., 1976. *Marine optics*, 2nd ed. Elsevier Oceanography Series, 14. Elsevier, Amsterdam.

Jerlov, N.G. and M. Fukuda, 1960. Radiance distribution in the upper layers of the sea. *Tellus*, **12**, 348–355.

Jerlov, N.G. and F. Koczy, 1951. Photographic measurements of daylight in deep water. *Report of the Swedish Deep-Sea Expedition*, **3**, 62–69.

Jerlov, N.G. and B. Kullenberg, 1953. The Tyndall effect of uniform minerogenic suspensions. *Tellus*, **5**, 306–307.

Jerome, J.H., R.P. Bukata, and J.E. Burton, 1988. Utilizing the components of vector irradiance to estimate the scalar irradiance in natural waters. *Applied Optics*, **27**, 4012–4018.

Johnson (Jerlov), N.G., 1944. A standard transparency meter. *Sven. Hydrogr.-Biol. Komm. Skr., Ny Ser. Hydrogr.*, **19**.

Johnson (Jerlov), N.G., 1946. On anti-rachitic ultra-violet radiation in the sea. *Medd. Oceanogr. Inst. Gothenburg, Ser. B*, **3**(11).

Johnson (Jerlov), N.G. and B. Kullenberg, 1946. On radiant energy measurements in the sea. *Sven. Hydrogr.-Biol. Komm. Skr., Ny Ser. 3, Hydrogr.*, **1**(1).

Johnson (Jerlov), N.G. and G. Liljequist, 1938. On the angular distribution of submarine daylight and the total submarine illumination. *Sven. Hydrogr.-Biol. Komm. Skr., Ny Ser. Hydrogr.*, **14**.

Kadyshevich, Y.A., 1977. Light-scattering matrices of inshore waters of the Baltic sea. *Izv. Acad. Sci. USSR Atmospheric Oceanic Physics*, **13**, 77–78.

Kadyshevich, Y.A., Y.S. Lyubovtseva, and I.N. Plakhina, 1971. Measurement of matrices for light scattered by sea water. *Izv. Acad. Sci. USSR Atmospheric and Oceanic Physics*, **7**, 557–561.

Kadyshevich, Y.A., Y.S. Lyubovtseva, and G.V. Rozenberg, 1976. Light-scattering matrices of Pacific and Atlantic ocean waters. *Izv. Acad. Sci. USSR Atmospheric and Oceanic Physics*, **12**, 106–111.

Kattawar, G.W., 1990. Irradiance invariance for scattering according to a Rayleigh phase function compared to a Rayleigh phase matrix for a plane-parallel medium. *Applied Optics*, **29**, 2365–2376.

Kattawar, G.W. and C.N. Adams, 1989. Stokes vector calculations of the submarine light field in an atmosphere-ocean with scattering according to a Rayleigh phase matrix: effect of interface refractive index on radiance and polarization. *Limnology and Oceanography*, **34**, 1453–1472.

Kattawar, G.W., G.N. Plass, and J.A. Guinn, Jr., 1973. Monte Carlo calculations of the polarization of radiation in the earth's atmosphere-ocean system. *Journal of Physical Oceanography*, **3**, 353–372.

Kattawar, G.W., G.N. Plass, and S.J. Hitzfelder, 1976. Multiple scattered radiation emerging from Rayleigh and continental haze layers. 1: Radiance, polarization, and neutral points, *Applied Optics*, **15**, 632–647.

Kattawar, G.W., C.N. Adams, and F.J. Tanis, 1988. Monte Carlo calculations of the complete Stokes vector for an inhomogeneous atmosphere-ocean system with a wind ruffled sea. *Ocean Optics IX*, Society of Photo-Optical Instrumentation Engineers, **925**, 398–406.

Kiefer, D.A., 1973. Fluorescence properties of natural phytoplankton populations. *Marine Biology*, **22**, 263–269.

Kiefer, D.A., 1986. Biological sources of optical variability in the sea. *Ocean Optics VIII*, Society of Photo-Optical Instrumentation Engineers, **637**, 25–34.

Kiefer, D.A. and B.G. Mitchell, 1983. A simple, steady state description of phytoplankton growth based on absorption cross section and quantum efficiency. *Limnology and Oceanography*, **28**, 770–776.

Kiefer, D.A. and R.A. Reynolds, 1992. Advances in understanding phytoplankton fluorescence and photosynthesis. *Primary productivity and biogeochemical cycles in the sea*, 37th Brookhaven Symposium in Biology. P. G. Falkowski, ed.

Kiefer, D.A. and J.B. SooHoo, 1982. Spectral absorption by marine particles of coastal waters of Baja California. *Limnology and Oceanography*, **27**, 492–499.

Kiefer, D.A., W.S. Chamberlin, and C.R. Booth, 1989. Natural fluorescence of chlorophyll *a*: relationship to photosynthesis and chlorophyll concentration in the western South Pacific gyre. *Limnology and Oceanography*, **34**(5), 868–881.

Kirk, J.T.O., 1975. A theoretical analysis of the contribution of algal cells to the attenuation of light within natural waters. I. General treatment of suspensions of living cells. *New Phytology*, **75**, 11–20; II. Spherical cells. *New Phytology*, **75**, 21–36.

Kirk, J.T.O., 1980. Spectral absorption properties of natural waters: contribution of the soluble and particulate fractions to light absorption in some inland waters of southeastern Australia. *Australian Journal of Marine and Freshwater Research*, **31**, 287-296.

Kirk, J.T.O., 1981a. *Monte Carlo procedure for simulating the penetration of light into natural waters*. CSIRO (Australia), Division of Plant Industry Technical Paper No. 36.

Kirk, J.T.O., 1981b. A Monte Carlo study of the nature of the underwater light field in, and the relationships between optical properties of, turbid yellow waters. *Australian Journal of Marine and Freshwater Research*, **32**, 517–532.

Kirk, J.T.O., 1983. *Light and photosynthesis in aquatic ecosystems*. Cambridge University Press, Cambridge.

Kirk, J.T.O. 1984a. Dependence of relationship between inherent and apparent optical properties on solar altitude. *Limnology and Oceanography*, **29**(2), 350–356.

Kirk, J.T.O., 1984b. Attenuation of solar radiation in scattering-absorbing waters: a simplified procedure for its calculation. *Applied Optics*, **23**, 3737–3739.

Kirk, J.T.O., 1991. Volume scattering function, average cosines and the underwater light field. *Limnology and Oceanography*, **36**, 455–467.

Kishino, M., C.R. Booth, and N. Okami, 1984. Underwater radiant energy absorbed by phytoplankton, detritus, dissolved organic matter and pure water. *Limnology and Oceanography*, **29**, 340–349.

Kishino, M. and N. Okami, 1984. Instrument for measuring downward and upward spectral irradiance in the sea. *La Mer*, **22**, 37–40.

Kishino, M., S. Sugihara, and N. Okami, 1984a. Influence of fluorescence of chlorophyll *a* on underwater upward irradiance spectrum. *La Mer*, **22**, 224–232.

Kishino, M., S. Sugihara, and N. Okami, 1984b. Estimation of quantum yield of chlorophyll *a* fluorescence from the upward irradiance spectrum in the sea. *La Mer*, **22**, 233–240.

Kishino, M., M. Takahashi, N. Okami, and S. Ichimura, 1985. Estimation of the spectral absorption coefficients of phytoplankton in the sea. *Bulletin of Marine Science*, **37**, 634–642.

Kishino, M., N. Okami, M. Takahashi, and S. Ichimura, 1986. Light utilization efficiency and quantum yield of phytoplankton in a thermally stratified sea. *Limnology and Oceanography*, **31**, 557–566.

Kitchen, J.C. and J.R.V. Zaneveld, 1990. On the noncorrelation of the vertical structure of light scattering and cholorophyll *a* in case I waters. *Journal of Geophysical Research*, **95**, 20237–20246.

Knudsen, M., 1922. *On measurements of the penetration of light into the sea.* Publ. Circonstance no. 76. Cons. Perm. Internat. Explor. Mer.

Kok, B., 1960. Efficiency of photosynthesis. *Handbuch der Pflanzenphysiologie*, vol. 5, p. 1, W. Ruhland, ed. Springer-Verlag, Berlin, pp. 535–633.

Kolber, Z.S. and P.G. Falkowski, 1991. The relationship between fluorescence and photochemistry on oxygenic photosynthesis: A steady state model based on kinetics of electron transfer. Unpublished manuscript.

Kolber, Z., J. Zehr, and P.G. Falkowski, 1988. Effects of growth irradiance and nitrogen limitation on photosynthetic energy conversion in photosystem II. *Plant Physiology*, **88**, 923.

Kolber, Z., K.D. Wyman, and P.G. Falkowski, 1990. Natural variability in photosynthethetic energy conversion efficiency: a field study in the Gulf of Maine. *Limnology and Oceanography*, **35**(1), 72–79.

Kondilenko, I.I., P.A. Korotkov, V.A. Klimenko, and O.P. Demyanenko, 1977. Transverse cross-section of Raman scattering of the u_1 vibration of the water molecule in the liquid and gaseous states. *Optical Spectroscopy*, **43**, 384–386.

Können, G.P., 1985. *Polarized light in nature.* Cambridge University Press, New York.

Krümmel, O., 1886. *Der Ozean.* Das Wissen der Gegenwart, vol. 52. Leipzing and Prag.

Kullenberg, G., 1968. Scattering of light by Sargasso Sea water. *Deep Sea Research*, **15**, 423–432.

Langdon, C., 1986. Dissolved oxygen monitoring system using a pulsed electrode: design, performance, and evaluation. *Deep Sea Research*, **31**, 1357–1367.

Laws, E.A. and T.T. Bannister, 1980. Nutrient- and light-limited growth of *Thalassiosira fluviatilis* in continuous culture with implications for phytoplankton growth in the ocean. *Limnology and Oceanography*, **25**, 457–473.

Lewis, M.R., R.E. Warnock, and T. Platt, 1985. Absorption and photosynthetic action spectra for natural phytoplankton populations: implications for production in the open ocean, *Limnology and Oceanography*, **30**, 794–806.

Lorenz, L.V., 1890. *Lysbevægelsen i og uden for en af plane lysbølger belyst kugle.* Vidensk. Selsk. Skr., 6. række. Naturvidenskab Matem. Afd. VI., 1.

Lorenzen, C.J., 1965. A method for the continuous measurement of *in vivo* chlorophyll concentration. *Deep Sea Research*, **13**, 223–227.

Maccio, M. and C. Langdon, 1988. Description of conversion of an EG&G VMCM into a MVMS (Multi-Variable Moored Sensor). *Proc. Oceans '88 Conference*, Washington D.C., pp. 1181–1187.

Marra, J. and E.O. Hartwig, 1984. BIOWATT: a study of bioluminescence and optical variability in the sea. *EOS* (Transactions of the American Geophysical Union), **65**, 732–733.

Marra, J. and C. Langdon, 1993 *Evaluation of in situ fluorometers for the estimation of chlorophyll a.* Lamont-Doherty Earth Observatory Technical Report LDEO-**93**-1, Palisades, NY.

Marra, J., R.R. Bidigare, and T.D. Dickey, 1990. Nutrients and mixing; chlorophyll and phytoplankton growth. *Deep Sea Research*, **37**, 129–143.

Marra, J., W.S. Chamberlin, and C. Knudson, 1993. Proportionality between *in situ* carbon assimilation and bio-optical measures of primary production in the Gulf of Maine in Summer. *Limnology and Oceanography*, **38**, 232–239.

Marshall, B.R. and R.C. Smith, 1990. Raman scattering and in-water ocean optical properties. *Applied Optics*, **29**(1), 71–84.

McGill, D.A. and T.J. Lawson, Jr., 1966. *The distribution of chlorophyll in the western Indian Ocean during the Northeast Monsoon period, Feb. 13 to July 16, 1965.* Woods Hole Oceanographic Institution Tech. Rep. no. 66–12.

Mie, G., 1908. Beitrage zur Optik truber Medien, speziell kolloidalen Metall-losungen. *Annalen der Physik*, **25**, 377–445.

Mitchell, B.G. and D.A. Kiefer, 1984. Determination of absorption and fluorescence excitation spectra for phytoplankton. In *Marine phytoplankton and productivity*, O. Holm-Hansen, L. Bolis, and R. Gilles eds. Springer-Verlag, Berlin, pp. 157–169.

Mitchell, B.G. and D.A. Kiefer, 1988a. Variability in pigment specific fluorescence and absorption spectra in the northeastern Pacific Ocean. *Deep Sea Research*, **35**, 665–689.

Mitchell, B.G. and D.A. Kiefer, 1988b. Chlorophyll a specific absorption and fluorescence excitation spectra for light-limited phytoplankton. *Deep Sea Research*, **35**, 639–663.

Mobley, C.D., 1989. A numerical model for the computation of radiance distributions in natural waters with wind-roughened surfaces. *Limnology and Oceanography*, **34**, 1473–1483.

Morel, A., 1973. Diffusion de la lumière par les eaux de mer. Résultats expérimentaux et approche theorique. *Optics of the Sea.* AGARD lecture series 61, pp. 31.1–31.76.

Morel, A., 1974. Optical properties of pure water and pure sea water. *Optical aspects of oceanography*, N.G. Jerlov and E. Steemann-Nielsen eds. Academic Press, New York, pp. 1–24.

Morel, A., 1978. Available, usable and stored radiant energy in relation to marine photosynthesis. *Deep Sea Research*, **25**, 673–688.

Morel, A., 1980. In-water and remote measurement of ocean color. *Boundary-Layer Meteorology*, **18**, 177–201.

Morel A., 1987. Chlorophyll-specific scattering coefficient of phytoplankton, a simplified theoretical approach, *Deep Sea Research*, **34**, 1093–1105.

Morel, A., 1988. Optical modeling of the upper ocean in relation to its biogenous matter content (Case I waters). *Journal of Geophysical Research*, **93**, 10749–10768.

Morel, A., 1991. Light and marine photosynthesis: a spectral model with geochemical and climatological implications. *Progress in Oceanography*, **26**, 263–306.

Morel, A. and Y.H. Ahn, 1990. Optical efficiency factors of free living marine bacteria : influence of bacterioplankton upon the optical properties and particulate organic carbon in oceanic waters. *Journal of Marine Research*, **48**, 145–175.

Morel, A. and J-F. Berthon, 1989. Surface pigments, algal biomass profiles and potential production of the euphotic layer: relationships reinvestigated in view of remote sensing applications. *Limnology and Oceanography*, **34**, 1545–1562.

Morel, A., and A. Bricaud, 1981. Theoretical results concerning light absorption in a discrete medium and application to specific absorption of phytoplankton. *Deep Sea Research*, Part A, **28**, 1375–1393.

Morel, A. and A. Bricaud, 1986. Inherent optical properties of algal cells including picoplankton : theoretical and experimental results. *Photosynthetic picoplankton*, T. Platt and W.K.W. Li, eds. Can. Bull. Fish. Aquat. Sci., **214**, 521–559.

Morel, A. and L. Prieur, 1977. Analysis of variations in ocean color. *Limnology and Oceanography*, **22**, 709–722.

Morrow, J.H., 1988. *Light absorption in naturally occurring marine phytoplankton communities*. Ph.D. Thesis. University of Southern California.

Mueller, H., 1948. The foundation of optics. *Journal of the Optical Society of America* 38, 661-663.

Mueller, J.L., 1991. *Integral method for irradiance profile analysis*. San Diego State University Center for Hydro-Optics and Remote Sensing Technical Memorandum 007-91.

Murray, J. and J. Hjort, 1912. *Atlanterhavet, fra overflaten til cont. on p. 3 havdypets mϕrke*. pt. 5. M. Aschehoug et Co. (W. Nygaard), Kristiania (now Oslo), p. 197.

Oishi,T., 1990. Significant relationship between the backward scattering coefficient of sea water and the scatterance at 120°. *Applied Optics*, **29**, 4658–4665.

Okami, N., M. Kishino, S. Sugihara, N. Takematsu, and S. Unoki, 1982. Analysis of ocean color spectra (III). Measurement of optical properties of sea water. *Journal of the Oceanographic Society of Japan*, **38**, 362–372.

Olson, R.J., S.W. Chisholm, E.R. Zettler, M.A. Altabet, and J.A. Dusenberry, 1990. Spatial and temporal distribution of prochlorophyte picoplankton in the North Atlantic Ocean. *Deep-Sea Research*, **37**(6), 1033–1051.

Olson, R.J., E.R. Zettler, S.W. Chisholm, and J. Dusenberry, 1991. Advances in oceanography through flow cytometry. *Particle analysis in oceanography*, Demers, S., and M. Lewis, eds. NATO ASI Series G: Ecological Sciences, **27**, 351–399.

Orellana, M.V. and M.J. Perry, 1992. An immunoprobe to measure Rubisco concentrations and maximal photosynthetic rates of individual phytoplankton cells. *Limnology and Oceanography*, **37**, 478–490.

Pak, H., D.A. Kiefer, and J.C. Kitchen, 1988. Meridional variations in the concentration of chlorophyll *a* and microparticles in the North Pacific Ocean. *Deep Sea Research*, **35**(7), 1151–1171.

Peacock, T.G., K.L. Carder, C.O. Davis, and R.G. Steward, 1990. Effects of fluorescence and water Raman scattering on models of remote sensing reflectance. *Ocean Optics X*, Society of Photo-Optical Instrumentation Engineers, **1302**, pp. 303–319.

Perry, M.J., and S.M. Porter, 1989. Determination of the cross-section absorption coefficient of individual phytoplankton cells by analytical flow cytometry. *Limnology and Oceanography*, **34**, 1727–1738.

Perry, M.J., M.C. Talbot, and R.S. Alberte, 1981. Photoadaption in marine phytoplankton: Response of the photosynthetic unit. *Marine Biology*, **62**, 92–101.

Peticolas, W.F., 1972. Inelastic laser light scattering from biological and synthetic polymers. *Advances in Polymer Science*, **9**, 285–333.

Pettersson, H., 1934. A transparency-meter for sea-water. *Medd. Oceanogr. Inst. Gothenburg, Ser. B*, **4**(4).

Pettersson, H., 1936. Das Licht im Meet. *Bioklimatische Beibätter*, pt. 1. Friedr. Vieweg and sons, Braunschweig.

Pettersson, H., 1939. *Oceanografi*. Vetenskapen om havet. Albert Bonniers Förlag, Stockholm.

Pettersson, H. and H.H. Poole, 1937. Measurements of submarine daylight. *Medd. Oceanogr. Inst. Gothenburg, Ser. B*, **5**(5).

Pettersson, H. and S. Landberg, 1934. Submarine daylight. *Medd. Oceanogr. Inst. Gothenburg, Ser. B*, **3**(7).

Pettersson, H., H. Höglund, and S. Landberg, 1934. Submarine daylight and the photosynthesis of phytoplankton. *Medd. Oceanogr. Inst. Gothenburg, Ser. B*, **4**(5).

Petzold, T.J., 1972. *Volume scattering functions for selected natural waters*. Scripps Institution of Oceanography, Visibility Laboratory, San Diego, CA, SIO Ref. 72–78.

Phinney, D.A. and T.C. Cucci, 1989. Flow cytometry and phytoplankton. *Cytometry*, **10**, 511–521.

Plass, G.N. and G.W. Kattawar, 1972. Monte Carlo calculations of radiative transfer in the earth's atmosphere-ocean system. 1. Flux in the atmosphere and the ocean. *Journal of Physical Oceanography*, **2**, 139–145.

Pospergelis, M.M., 1969. Spectroscopic measurements of the four Stokes parameters for light scattered by natural objects. *Soviet Physics – Astronomy*, **12**, 973–977.

Preisendorfer, R.W., 1959. On the existence of characteristic diffuse light in natural sea waters. *Journal of Marine Research*, **18**, 1–9.

Preisendorfer, R.W., 1961. *Application of radiative transfer theory to light measurements in the sea.* International Union of Geodesy and Geophysics Monograph (Symposium on Radiant Energy in the Sea) no. 10, pp. 11–30.

Preisendorfer, R.W., 1965. *Radiative transfer on discrete spaces.* Pergamon Press, New York.

Preisendorfer, R.W., 1976. *Hydrologic Optics* vol. 1: *Introduction.* NTIS PB-259 793/8ST. National Technical Information Service, Springfield, Ill.

Preisendorfer, R.W. and C.D. Mobley, 1984. Direct and inverse irradiance models in hydrologic optics. *Limnology and Oceanography*, **29**, 903–929.

Prieur, L., 1976. *Transfer radiatif dans les eaux de mer.* D.Sc. thesis. Université Pierre et Marie Curie, Paris.

Prieur, L. and A. Morel, 1971. Etude theorique du régime asymptotique: Relations entre caractéristiques optiques et coefficient d'extinction relatif à la pénétration de la lumière du jour. *Cahiers Oceanographie*, **23**, 35–48.

Prieur, L. and S. Sathyendranath, 1981. An optical classification of coastal and oceanic waters based on the specific absorption curves of phytoplankton pigments, dissoved organic matter and other particulate materials. *Limnology and Oceanography*, **26**, 671–689.

Richards, F.A. and T.G. Thompson, 1952. The estimation and characterization of plankton populations by pigment analysis. II. A spectrophotometric method for the estimation of plankton pigments. *Journal of Marine Research*, **11**, 156–172.

Roesler, C.S., M.J. Perry, and K.L. Carder, 1989. Modeling *in situ* phytoplankton absorption from total absorption spectra in productive inland marine waters. *Limnology and Oceanography*, **34**, 1510–1523.

Romanov N.P. and V.S. Shuklin, 1975. Raman scattering cross-section of liquid water. *Optical Spectroscopy*, **38**, 646–648.

Sakshaug, E., D.A. Kiefer, and K. Andresen. 1988. A steady-state description of growth and light absorption in the marine diatom *Skeletonema costatum*. *Limnology and Oceanography*, **43**(1), 198–205.

Sakshaug, E., G. Johnsen, K. Andresen, and M. Vernet, 1990. Modeling of light-dependent algal photosynthesis and growth: Experiments with the Barents Sea diatoms *Thalassiosira nordenskioeldii* and *Chaetoceros furcellatus*. *Deep Sea Research*, **38**, 415–430.

Sathyendranath, S., 1981. *Influence des substances en solution et en suspension dans les eaux de mer sur l'absorption et la reflectance. Modelisation et applications a'la teledetection*. Ph.D. thesis, 3d cycle, Université Pierre et Marie Curie, Paris.

Sauberer, F. and Ruttner, F., 1941. *Die Strahlungsverhältnisse der Binnengewässer*. Akadm. Verlag Becker and Erler Kom.-Ges., Leipzig.

Schuster, A., 1905. Radiation through a foggy atmosphere. *Journal of Astrophysics*, **21**, 1–22.

Secchi, P.A., 1866. Esperimento per determinare la transparanza del mare. *Sul moto ondoso del mare*. Cialdi (ed.) Rome, 258–288.

Shapiro, L.P., L. Campbell, and E. Haugen, 1989a. Immunochemical characterization of ultraplankton species. *Marine Ecology Progress Series*, **57**, 219–224.

Shapiro, L.P., E.M. Haugen, and E.J. Carpenter, 1989b. Occurrence and abundance of green-fluorescing dinoflagellates in surface waters of the Northwest Atlantic and Northeast Pacific Oceans. *Journal of Phycology*, **25**, 189–191.

Sheldon, R.W., A. Prakash, and W.H. Sutcliffe, Jr., 1972. The size distribution of particles in the ocean. *Limnology and Oceanography*, **27**(3), 327–340.

Shurcliff, W.A., 1962. *Polarized Light*. Harvard University Press, Cambridge, Mass.

Siegel, D.A. and T.D. Dickey, 1987. On the parameterization of irradiance for ocean photoprocesses. *Journal of Geophysical Research*, **92**, 14648–14662.

Siegel, D.A., T.D. Dickey, L. Washburn, M.K. Hamilton, and B.G. Mitchell, 1989. Optical determination of particulate abundance and production variations in the oligotrophic ocean. *Deep Sea Research*, **36**, 715–733.

Slusher, R.B. and V.E. Derr, 1975. Temperature dependence and cross section of some Stokes and anti-Stokes Raman lines in ice. *Applied Optics*, **14**, 2116–2120.

Smith, R.C. and K.S. Baker, 1978a. The bio-optical state of ocean waters and remote sensing. *Limnology and Oceanography*, **23**, 247–259.

Smith, R.C. and K.S. Baker, 1978b. Optical classification of natural waters. *Limnology and Oceanography*, **23**, 260–267.

Smith, R.C. and K.S. Baker, 1981. Optical properties of the clearest natural waters (200–800 nm), *Applied Optics*, **20**, 177–184.

Smith, R.C. and J.E. Tyler, 1967. Optical properties of clear natural water. *Journal of the Optical Society of America*, **57**, 589–595.

Smith, R.C. and J.E. Tyler, 1976. Transmission of solar radiation into natural waters. *Photochemistry and Photobiology Reviews*, Kendrick Smith, ed. Plenum Press, New York.

Smith, R.C., K.J. Waters, and K.S. Baker, 1990. Optical variability and pigment biomass in the Sargasso Sea as determined using deep sea optical mooring data. *Journal of Geophysical Research*, **96**, 8665–8686.

Sosik, H.M., 1988. *Analysis of chlorophyll fluorescence in marine phytoplankton: interpretation of flow cytometric signal.* M.S. thesis, MIT.

Sosik, H.M., S.W. Chisholm, and R.J. Olson, 1989. Chlorophyll fluorescence from single cells: Interpretation of flow cytometric signals. *Limnology and Oceanography*, **34**, 1749–1761.

Spinrad, R.W. and J.F. Brown, 1986. Relative real refractive index of marine microorganisms: a technique for flow cytometric estimation. *Applied Optics*, **25**, 1930–1934.

Spinrad, R.W., J.R.V. Zaneveld, and H. Pak, 1978. Volume scattering function of suspended particulate matter at near-forward angles: A comparison of experimental and theoretical values. *Applied Optics*, **17**, 1125–1130.

Spitzer, D. and R.W.J. Dirks, 1985. Contamination of the reflectance of natural waters by solar-induced fluorescence of dissolved organic matter. *Applied Optics*, **24**(4), 444–445

Stavn, R.H. 1990. Raman scattering effects at the shorter visible wavelengths in clear ocean waters. *Ocean Optics X*, Society of Photo-Optical Instrumentation Engineers, **1302**, pp. 94–100.

Stavn, R.H. and A.D. Weidemann, 1988a. Raman scattering effects in ocean optics. *Ocean Optics IX*, Society of Photo-Optical Instrumentation Engineers, **925**, pp. 131–139.

Stavn, R.H. and A.D. Weidemann, 1988b. Optical modeling of clear ocean light fields: Raman scattering effects. *Applied Optics* **27**:4002-4011.

Stavn, R.H. and A.D.Weidemann, 1989. Shape factors, two-flow models and the problem of irradiance inversion in estimating optical parameters. *Limnology and Oceanography*, **34**, 1426–1441.

Steemann-Nielsen, E., 1951. Conditions of light in the fjord. *Medd. Denmarks Fiskeri-og Havunders.*, **5**(4), 21–27.

Stramski, D. and D. Kiefer, 1990. Optical properties of marine bacteria. *Ocean Optics X*, Society of Photo-Optical Instrumentation Engineers, **1302**, 250–268.

Stramski, D., A. Morel, and A. Bricaud, 1988. Modeling the light attenuation and scattering by spherical phytoplankton cells: a retrieval of the bulk refractive index. *Applied Optics*, **27**, 3954–3956.

Sugihara, S., M. Kishino, and M. Okami, 1984. Contribution of Raman scattering to upward irradiance in the sea. *Journal of the Oceanographic Society of Japan*, **40**, 397–404.

Sverdrup, H.U., 1952. *Havlære.* Fagbφger for fiskere, Fabritius & sφnners forlag.

Swift, E. and C.R. Booth, 1988. Bioluminescence moored systems. *Ocean Optics IX*, Society of Photo-Optical Instrumentation Engineers, **925**, pp. 76–86.

Takematsu, N., M. Kishino, and N. Okami, 1981. The quantum yield of phytoplankton photosynthesis in Lake Fukami-ike, Japan. *La Mer*, **19**, 132–138 (in Japanese).

Teague, M.R., 1980. Image analysis via the the general theory of moments. *Journal of the Optical Society of America*, **70**, 920.

Timofeeva, V.A., 1974. Optics of turbid waters (results of laboratory studies). *Optical Aspects of Oceanography*, N.G. Jerlov and E. Steemann-Nielsen, eds. Academic Press, London, pp. 177–217.

Tyler, J.E., 1975. The *in situ* quantum efficiency of natural phytoplankton populations. *Limnology and Oceanography*, **20**, 976–980.

van de Hulst, H.C., 1948. *Journal of Astrophysics*, **108**, 220.

van de Hulst, H.C., 1957. *Light scattering by small particles*. Wiley, New York.

van de Hulst, H.C., 1980. *Multiple light scattering*, Academic Press, New York.

van de Hulst, H.C., 1981. *Light scattering by small particles*, Dover Publications, New York.

Voss, K.J. 1989. Use of the radiance distribution to measure the optical absorption coefficient in the ocean. *Limnology and Oceanography*, **34**, 1614–1622.

Voss, K.J. and E.S. Fry, 1984. Measurement of the Mueller matrix for ocean water. *Applied Optics*, **23**, 4427–4439.

Walrafen, G.F., 1964. Raman studies of water structure. *Journal of Chemistry and Physics*, **40**, 3249–3256.

Ward, B.B., 1990. A review of immunological methods for oceanography. *Oceanography*, **3**, 30–35.

Ward, B.B. and M.J. Perry, 1980. Immunofluorescent assay for the marine ammonium-oxidizing bacterium, *Nitrosococcus oceanus*. *Applied and Environmental Microbiology*, **39**, 913–918.

Warner, J.A., R.W. Austin, D. Bailey, G. Huszar, R.R. McConnaughey, K. Nealson, and E.A. Stephan, 1983. Scripps canyon sea structure: a design and deployment for the study of oceanic bioluminescence. *Marine Technology Society Journal*, **17**, 40–47.

Weidemann, A.D. and T.T. Bannister, 1986. Absorption and scattering coefficients in Irondequoit Bay. *Limnology and Oceanography*, **31**, 567–583.

Weller, R.A. and R.E. Davis, 1980. A vector measuring current meter. *Deep Sea Research*, **27**, 565–582.

Whitledge, T.E. and C.D. Wirick, 1986. Development of a moored in situ fluorometer for phytoplankton studies. *Tidal mixing and plankton dynamics*, M. Bowman, C. Yentsch, and W.T. Peterson, eds. Springer-Verlag, New York, pp. 449–462.

Wood, A.M., 1979. Chlorophyll a:b ratios in marine planktonic algae. *Journal of Phycology*, **15**, 330–332.

Yentsch, C.M. and R.W. Spinrad, 1987. Particles in flow. *Marine Technology Society Journal*, **21**, 58–68.

Yentsch, C.S. and D.W. Menzel, 1963. A method for the determination of phytoplankton chlorophyll and phaeophytin by fluorescence. *Deep Sea Research*, **10**, 221–231.

Yentsch, C.S. and D.A. Phinney, 1985a. Fluorescence spectral signatures for studies of marine phytoplankton. *Mapping strategies in chemical oceanography*, A. Zirino, ed. ACS Series no. 209, Washington, D.C., pp. 259-274.

Yentsch, C.S. and D.A. Phinney, 1985b. Spectral fluorescence: an ataxonomic tool for studying the structure of phytoplankton populations. *Journal of Plankton Research*, **7**, 617–632.

Yentsch, C.S. and D.A. Phinney, 1989. The bridge between ocean optics and microbial ecology. *Limnology and Oceanography*, **34**, 1698–1709.

Yentsch, C.S. and C.M. Yentsch, 1979. Fluorescence spectral signatures: The characterization of phytoplankton populations by the use of excitation and emission spectra. *Journal of Marine Research*, **37**, 471–483.

Yoder, J.A., 1979. Effect of temperature on light-limited growth and chemical composition of *Skeletonema costatum* (Bacillariophyceae). *Journal of Phycology*, **15**, 362–370.

Zaneveld, J.R.V., 1982. Remotely sensed reflectance and its dependence on vertical structure: a theoretical derivation. *Applied Optics*, **21**, 4146–4150.

Zaneveld, J.R.V., 1989. An asymptotic closure theory of irradiance in the sea and its inversion to obtain the vertical structure of inherent optical properties. *Limnology and Oceanography*, **34**, 1442–1452.

Zaneveld, J.R.V. and R. Bartz., 1984. Beam attenuation and absorption meters. *Ocean Optics VII*, Society of Photo-Optical Instrumentation Engineers, **489**, 318–324.

Zaneveld, J.R.V., D.M. Roach, and H. Pak, 1974. The determination of the index of refraction of particles suspended in the ocean. *Journal of Geophysical Research*, **77**, 2677–2680.

Zaneveld, J.R.V., R.Bartz, and J.C.Kitchen, 1990. Reflective-tube absorption meter. *Ocean Optics X*, Society of Photo-Optical Instrumentation Engineers, **1302**, 124–136.

Zerull, R.H. and K. Weiss, 1974. Scattering properties of irregular dielectric and absorbing particles. *Atmospheric aerosols: their optical properties and effect*. Optical Society of America.

This page intentionally left blank

INDEX